The Hamlyn Symposium on Medical Robotics

20-23 June 2015
The Royal Geographic Society and Imperial College London, UK

Proceedings

G.Z. Yang, A. Darzi Eds.

Proceedings

Guang-Zhong Yang and Ara Darzi (Eds.)

Karen Kerr, Valentina Vitiello, and Su-Lin Lee (Editorial Team)

The Hamlyn Symposium on Medical Robotics

20-23 June 2015
Imperial College London, UK

Proceedings of
The Hamlyn Symposium on Medical Robotics
20-23 June 2015, Imperial College London
London, UK
ISBN: 978-0-9563776-6-1

Preface

Robotics and autonomous systems continues to be an area of increasing interest and investment worldwide. On a national basis, this is demonstrated through the recent capital investment from the UK government through the EPSRC in 2014, which resulted in the creation of eight dedicated centres/facilities across the country covering key areas of transport, healthcare, manufacturing, and unmanned systems to ensure that the UK will maintain its leading engineering and research capacity in robotics and autonomous systems.

The 8th Hamlyn Symposium on Medical Robotics was held at the Royal Geographical Society on 20th to 23rd June 2015. The theme for this year's symposium was *'from whole body systems to micro-instruments'* with an impressive line-up of leading scientists and engineers in magnetic resonance (MR) and ultrasound imaging, image guidance, neurosurgery, and nanorobots, as some of our invited speakers. The keynote lecture was delivered by Professor Sylvain Martel, Polytechnique Montreal, who enlightened us on his experiences in using nanorobots and bacteria to fight cancer; Professor Andreas Melzer, from University of Dundee, spoke on recent developments in MR-image guided robotic-assisted interventions and focused ultrasound; Professor Nassir Navab of TUM, Germany and Johns Hopkins, shared his expertise and recent advances in robotics and control for patient specific imaging; Professor Garnette Sutherland, University of Calgary, outlined his experience with image guidance in neurosurgery, a new area of focus for the meeting this year. This year's Storz-Hopkins lecture was delivered by Professor Alex Mottrie, who provided his insight and vision on the emerging technologies that might influence the future of robotic surgery.

A total of 80 papers were submitted from 13 countries and 40 institutions, and after systematic peer review, 47 papers were selected for presentation at the Symposium. The topics covered ranged from MR and Ultrasound-guided Interventions, Continuum Robots and Navigation, to Training and Microsurgery Platforms.

We were delighted to see our workshop programmes continue to grow and flourish, held on the days pre- and post- the Symposium. Topics focused on some of the following areas: cognitive surgical robotics; MR-compatible robotics and interventions; paediatrics; imaging; flexible access surgery; microbots; additive manufacturing; and neurosurgery.

As with last year, two of the workshops were organised in conjunction with the EPSRC-NIHR Healthcare Technology Co-operatives (HTC) Partnership Award on Devices for Surgery and Rehabilitation. In collaboration with the Trauma HTC at University Hospital Birmingham NHS Foundation Trust, the Wearable and Assistive Robots workshop had an impressive line-up of international leaders in the field. The Augmented Reality and Surgical Imaging Guidance Workshop was supported by the Enteric HTC at Barts Health NHS Trust and Queen Mary University of London.

We were particularly excited to host the first Surgical Robot Challenge following on the Open Platforms for Medical Robots workshop at the 7th Hamlyn Symposium, in partnership with Intuitive Surgical, Kuka Robotics, and Applied Dexterity. The purpose of the Challenge was to foster collaboration, share resources and tackle some of the unmet technical/clinical challenges in robotic surgery. A large number of submissions were received, with 17 teams bringing their kit to London to compete over a 3-day competition, starting in the lab, followed by presentations to an esteemed judging panel and cumulating in the short-listed finalists presenting to the Hamlyn Symposium wider audience.

A lively debate was hosted, based on an opinion piece entitled '*Surgical Robotics: The Next 25 Years'*. This highlighted that despite the impressive feats of innovation to date, there is a need to continuously improve surgical robotics through advances in precision medicine, personalised healthcare, and quality-of-life improvements. It was noted that future clinical attention will likely be paid to the development of smart, miniaturized, mechatronically enhanced or robotically assisted surgical instruments. Such smart instruments will be integrated with advanced imaging and sensing techniques, combined with instrumentation passed through the device for performing early diagnosis and interventions.

We would like to thank the International and Local Programme Committees, the Workshop Organising Committee and the Local Organising Committee for giving up their valuable time to ensure timely review of the submitted papers, to shape an excellent symposium programme.

We are also grateful to the team who have worked behind the scenes and for their continuous effort in managing all aspects of the Symposium organisation. In particular, thanks to Valentina Vitiello, Su-Lin Lee, Raphaele Raupp, Robert Merrifield, Hawkeye King, Christos Bergeles, Benny Lo and Charence Wong.

Lastly, special thanks go to Lady Hamlyn. This would not be possible without the generous philanthropic support from both the Helen Hamlyn Trust and Lady Hamlyn herself.

It was our great pleasure to welcome attendees to the 8th Hamlyn Symposium in London.

June 2015, London
Karen Kerr, Guang-Zhong Yang, Ara Darzi

Organisation

General and Programme Co-Chairs
Guang-Zhong Yang
Ara Darzi

International Programme Committee

Darwin Caldwell	IIT, Italy
Howie Choset	Carnegie Mellon University, USA
Kevin Cleary	The Sheikh Zayed Institute, Washington, USA
Paolo Dario	Scuola Superiore Sant'Anna, Pisa, Italy
Simon DiMaio	Intuitive Surgical Inc, USA
Pierre Dupont	Children's Hospital Boston, USA
Hubertus Feussner	Technical University Munich, Germany
Gabor Fichtinger	Queen's University, Canada
Paolo Fiorini	University of Verona, Italy
Dennis Fowler	Titan Medical Inc., USA
Blake Hannaford	University of Washington, USA
Leo Joskowicz	The Hebrew University of Jerusalem, Israel
Jacques Marescaux	University Hospital Strasbourg, France
Arianna Menciassi	Scuola Superiore Sant'Anna, Pisa, Italy
Bradley Nelson	ETH Zürich, Switzerland
Vipul Patel	Global Robotics Institute, USA
Cameron Riviere	Carnegie Mellon University, USA
Ichiro Sakuma	University of Tokyo, Japan
Rick Satava	University of Washington, USA
Lee Swanstrom	University of Oregon, USA
Mark Talamini	University of California, San Diego, USA
Russ Taylor	Johns Hopkins University, USA
Kirby Vosburgh	Harvard University, USA
Steve Wexner	Cleveland Clinic Florida, USA

Local Programme Committee

Kaspar Althoefer	King's College London, UK
Thanos Athanasiou	Imperial College London, UK
Colin Bicknell	Imperial College London, UK
Nicholas Cheshire	Imperial College London, UK
Daniel Elson	Imperial College London, UK
Leonard Fass	Imperial College London, UK
Mohamad Hamady	Imperial College London, UK
Daniel Leff	Imperial College London, UK
Erik Mayer	Imperial College London, UK
Andreas Melzer	Dundee University, UK
Azad Najmaldin	St James University Hospital, Leeds, UK
Geoff Pegman	RU Robotics, UK
Ferdinando Rodriguez y Baena	Imperial College London, UK
Julian Teare	Imperial College London, UK
Justin Vale	Imperial College London, UK

Conference Organiser
Karen Kerr, Imperial College London

Local Organising Committee, Imperial College London
Javier Andreu
Ebubekir Avci
Christos Bergeles
Stamatia Giannarou
Petros Giataganas
Gauthier Gras
Michael Hughes
Hawkeye King
Su-Lin Lee
Konrad Leibrandt
Jindong Liu
Benny Lo
Hani Marcus
Elsie Mensah
Robert Merrifield
Chris Payne
Philip Pratt
Celia Riga
Carlo Seneci
Jianzhong Shang
Mikael Sodergren
Valentina Vitiello
Lin Zhang

Table of Contents

From Eyes to Hands to Needles

Poster Presentations

MR-Conditional Robot for Transcranial Focused Ultrasound in Infants

K. Price[1,2], V. Sin[1], C. Mougenot[3], T. Looi[1,2], S. Pichardo[4],
A. Waspe[1], J. Drake[1,2]

[1]*The Hospital for Sick Children, Canada*
[2] *University of Toronto, Canada*
[3]*Phillips Healthcare, Canada*
[4]*Thunder Bay Regional Research Institute, Canada*

karl.price@sickkids.ca

INTRODUCTION

Transcranial magnetic resonance-guided focused ultrasound (MRgFUS) involves the use of ultrasound energy to induce a bioeffect in a targeted area of the brain. An ongoing study at the Hospital for Sick Children proposes that intraventricular hemorrhagic (IVH) blood clots in premature infants can be treated with ultrasound-induced cavitation, and may result in better patient outcomes than current treatment methods. The procedure is performed inside a magnetic resonance imaging (MRI) machine. Precision positioning (±2 mm) of a focused ultrasound (FUS) transducer in five degrees of freedom (DOF) is required to perform the procedure within the contstraints of a neonatal incubator system.

Melzer has developed a 5 DOF MRI compatible arm that has been retrofitted for FUS applications [1, 2]. Yiallouras has developed a 3 DOF robot for FUS delivery to the prostate [3]. These robots lack the range of motion, payload capacity and/or dexterity required for transcranial FUS applications.

This paper describes an original 5 DOF, MRI conditional robot that has been developed to manipulate a FUS transducer for transcranial therapies.

MATERIALS AND METHODS

MRI-compatible materials are used for robot construction. These include plastics (Delrin, Ultem, ABS, Polycarbonate), brass, aluminum and 316 stainless steel for structural components. Custom designed parts were manufactured using CNC machining techniques. Nonmagnetic linear ball bearings (Del-Tron Precision Inc, CT, USA) are used as drive components for axes 1, 2 and 3 as shown in Figure 1. Glass ball bearings (Stock Drive Parts & Sterling Instruments, NY, USA) are used for rotational axes 4 and 5. Nonmagnetic piezoelectric motors (USR60-E3NT, Shinsei Corp, Japan) are used to drive all five axes. The motors are compatible with the drive electronics from a clinical Phillips Sonalleve MRgFUS system, facilitating installation of the system into any MRI facility already equipped with a Phillips MRgFUS system.

Robot components were tested for artifacts created during imaging. Individual robot components were placed immediately beside a cilindrical 4 L mineral oil phantom and imaged using T1-weighted, T2-weighted and spoiled gradient echo based thermal map sequences. Signal to noise ratio (SNR) was measured. Motors were moved farther away in increments of 1 cm and imaging was repeated. This process was performed both with the motors in motion and with the motors stationary.

A clinical FUS transducer (12cm focal length, 1.2 MHz, ImaSonic, France) is attached to a water-filled coupling bag to provide a consistent transmission media of ultrasound energy into the head of the patient. This assembly weighs 1.41kg, and defines the payload requirement.

Motion of the robot was tested under load to quantify payload capacity. Between 1 and 5, 1 kg brass weights were attached to the end effector of the robot in place of the FUS transducer. The robot was then moved through its full range of motions.

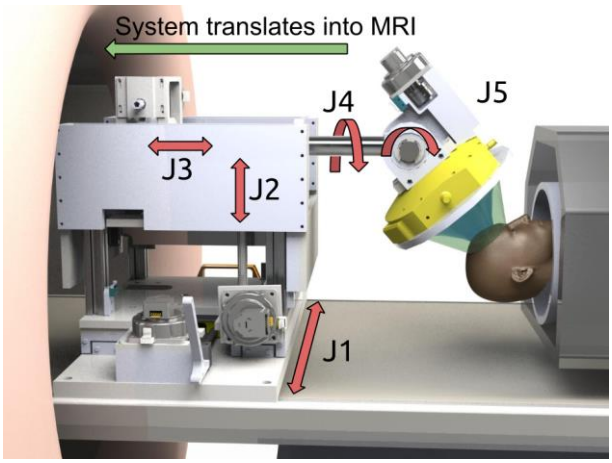

Fig. 1 - Robot design with joints labeled. Utrasound coupler (blue) provides an acoustic path to the skull.

Robot dexterous workspace was determined by calculating end effector position at each combination of joint limits. The smallest translational range of these values constitutes the dexterous workspace. The dexterous workspace for this application is defined as the volume the robot can target while maintaining a normal trajectory to the skull. An approximation of the brain volume of a 1 month old neonate was calculated based on a sphere of diameter equal to the major diameter taken from a computed tomography image (412 cm^3). Dexterous workspace results were compared to this worst-case volume approximation.

An inverse kinematic control scheme was implemented in MATLAB 2014b. A command in the form of an end effector pose (X, Y, Z, α, β) is entered into a console. The robot then moves to that pose.

Spatial accuracy data was acquired with the use of a Polaris infrared tracking system (Northern Digital Inc, ON, Canada, ±0.25 mm accuracy). A reference fiducal was placed on the stationary base of the robot, and another fiducial was placed on the end-effector of the robot. Equation 1 was applied to determine the end-effector pose in the robot's origin frame. Matrix T represents a 4x4 frame transformation, subscript *NDI* refers to the Polaris tracker origin, *ee* to the end effector, *org* to the robot's origin frame, and *ref* to the reference fiducial.

$$^{org}T_{ee} = (^{org}T_{ref})(^{NDI}T_{ref})^{-1}(^{NDI}T_{ee}) \quad (1)$$

The robot was commanded to move to 20 random points. The euclidean norm between the commanded position and the position measured by the Polaris tracker was calculated based on the average of 15 measurement readings. This process was then repeated with the tracker incorporated into the robot positioning feedback loop to improve system accuracy. The robot was moved to the commanded position, a position measurement was taken, and the robot position corrected. This experiment was first performed outside of the MRI magnetic field, then again inside the field.

The speed of each axis was determined by measuring the travel of each axis, commanding the robot to move through the full range of joint motion, and recording the time to complete the action.

RESULTS

The robot showed normal operation when placed inside the MRI bore indicating successful MRI-compatible construction.

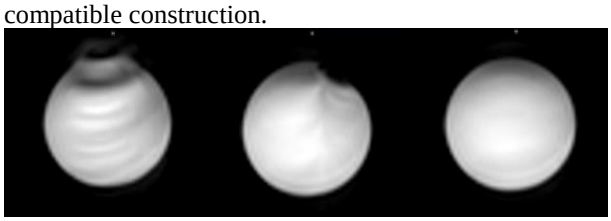

Fig. 2 – Image distortion created by motors on a 4 L MRI phantom at 0, 3 cm and 6 cm.

Distortions in the MR image due to large metal objects (such as the drive motors) were found to be negligible at distances longer 6 cm from the imaging field. Worst-case SNR recorded was 54% degredation (T2 weighted, motors in motion) compared to baseline. Figure 2 shows distortion as a result of the motors at varying distances.

The robot successfully moved through its full range of operation with a maximum payload of 5 kg.

Dexterous workspace volume was found to be a rectangular prism of dimensions 4.9 x 4.1 x 17.6 cm, covering 37.4% of the neonate skull volume, including significant coverage of the ventricular system (shown in Figure 3). Reachable workspace extends well beyond skull volume. When placed in the center of the MRI bore, the robot workspace was not affected.

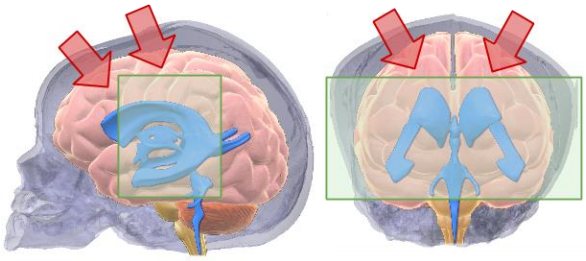

Fig. 3 – Dextrous workspace (green), covers 37.4% brain volume, and provides significant access to IVH-relevant anatomy (ventricular system, blue). Typical entry trajectories shown in red.

Intrinsic system accuracy was measured to be 4.2 ±1.4 mm. When the Polaris tracker was used to close the feedback loop, system accuracy was 0.7 ±0.8 mm. Table 1 shows the joint characterization results.

Table 1 - Robot joint characteristics

Axis	Type	Travel (mm, deg)	Resolution (μm, deg)	Speed (mm/s, deg/s)
J1	P	226	1.3	1.3
J2	P	152	2	2.0
J3	P	152	1	1.4
J4	R	360	8.18×10^{-3}	8.2
J5	R	90	8.18×10^{-3}	8.2

DISCUSSION

We have successfully designed and manufactured a 5 DOF, MRI-conditional robot capable of manipulating a FUS transducer for transcranial FUS delivery. The accuracy, dexterity, workspace, payload capacity and speed of the system have been shown to meet design requirements.

Future work will focus on additional system accuracy and repeatability characterization inside the MRI bore, improving the system control model, improving system accuracy, phantom and animal testing of robot controlled FUS sonications and continuing to improve integration of the control interface with the MRI console.

REFERENCES

[1] Melzer A, Gutmann B, Remmele T, Wolf R, Lukoscheck A, Bock M, Bardenheuer H, Fischer H. INNOMOTION for percutaneous image-guided interventions. IEEE Trans in Med and Bio Mag. 2008 May; 27(2):66-73.

[2] Krafft AJ, Jenne JW, Maier F, Stafford RJ, Huber PE, Semmler W, Bock M. A long arm for ultrasound: a combined robotic focused ultrasound setup for magnetic resonance-guided focused ultrasound surgery. Med Phys. 2010;37(5):2380-93.

[3] Yiallouras C, Ioannides K, Dadakova T, Pavlina M, Bock M, Damianou C. Three-axis MR-conditional robot for high-intensity focused ultrasound for treating prostate diseases transrectally. J Ther Ultrasound. 2015 Jan;3:2.

Needle-Guiding Robot for Percutaneous Intervention: Comparative Phantom Study in a 3T MRI Scanner

E. Franco[1], M. Rea[2], W. M. W. Gedroyc[2], M. Ristic[1]

[1]*Department of Mechanical Engineering, Imperial College London, UK*

[2]*St Mary's Hospital, London, UK*

ef1311@imperial.ac.uk

INTRODUCTION

Percutaneous intervention of liver tumours conducted under Magnetic Resonance Imaging (MRI) guidance offers better soft tissue contrast compared to the conventional ultrasound guidance [1]. While open MRI scanners have been employed for image-guided needle insertions in laser ablation (LA) procedures, their lower field strength limits image resolution and increases scan times [2]. Closed-bore scanners are more common; however the access to the patient is severely restricted. Consequently, image-guided needle insertions require repeatedly moving the patient bed in and out of the scanner bore, resulting in lengthy procedures. This paper introduces a new needle-guiding robot that operates in closed-bore MRI scanners in order to reduce procedure duration and increase targeting accuracy. The advantages of robot-assisted needle insertion are highlighted with a comparative phantom study.

MATERIALS AND METHODS

The needle-guiding robot builds upon our proof-of-concept [3] while introducing important new features. Firstly, a new design with four degree-of-freedom (DOF) results in a larger workspace and allows double inclined needle insertions, which are performed manually outside the bore (Fig. 1). Secondly, the robot registration in the MRI scanner is conducted using passive markers and an image processing method [4]. This approach does not require special imaging sequences and is therefore readily usable on different MRI scanners. Differently from other robots for liver intervention [5], [6], the prototype is designed for closed-bore scanners and employs pneumatic actuation which has negligible effects on the MR image quality [3]. This prototype is intended to operate within the established MRI-guided LA workflow, in which mechanical ventilation is briefly paused during needle insertion in order to minimize liver motion [7].

RESULTS

The potential benefits of the needle-guiding robot were evaluated with a comparative phantom study in a 3T closed-bore MRI scanner (GE, Discovery, MR750). The study employed a gelatine phantom containing four Vitamin-E capsules (Boots, UK), representing the target lesions. The phantom was positioned inside a plastic rib cage model, at the scanner isocenter. Silicone tape was attached to the ribs to make them visible on the MR images (Fig. 2). In the first part of the study, a coaxial needle (Somatex, Germany) was manually inserted in the phantom, outside the bore, based on the MR images. A grid of equally spaced cod-liver-oil capsules (Boots, UK) was positioned above the rib cage to provide a visual reference. Four sets of insertions were performed by two radiologist registrars aiming at different targets. Initial MR images (3Plane Loc SSFSE, TR = 1662.7 ms, TE = 78.9 ms, FA = 90°, FOV = 480 mm × 480 mm, Slice Thickness = 8 mm, Slice number = 65) were acquired to locate the lesions with respect to the capsule grid and to plan the needle insertion between the ribs.

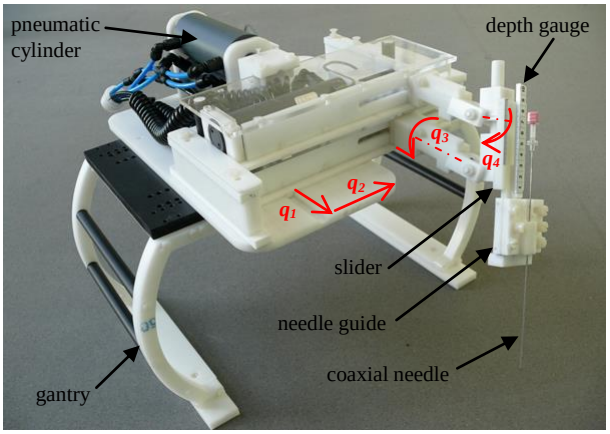

Fig. 1 Needle-guiding robot with 4 DOF (q_1, q_2, q_3, q_4).

The position of the inserted needle was confirmed with a verification scan: the insertion was repeated until the needle artefact intersected with the lesion (Fig. 3). The number of insertion attempts and the time elapsed from the start of the planning scan to the end of the verification scan is reported for each target in Table I.

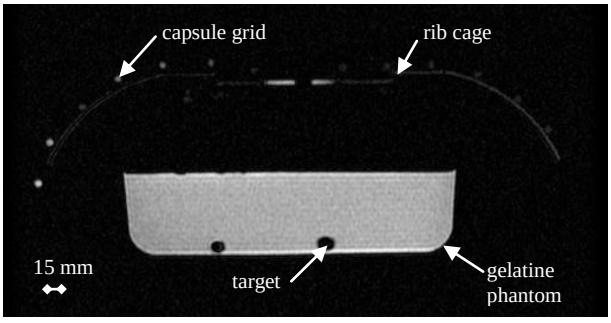

Fig. 2 Axial MR image of the phantom.

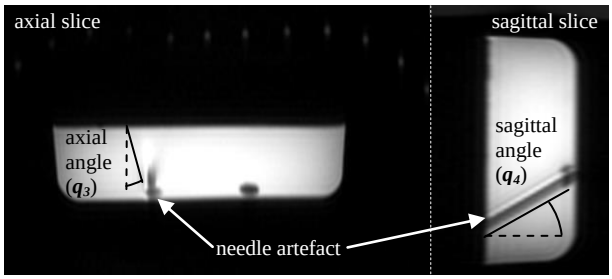

Fig. 3 MR images of a successful needle insertion.

The second part of the test involved using the needle-guiding robot to plan and assist the needle insertion. The robot was set up next to the plastic rib cage (Fig. 4), and automatically registered in the scanner coordinate system. Finally, a specially designed graphical user interface was employed to plan the needle insertion, which was performed manually outside the bore with the assistance of the needle guide. Although the robot setup took 30 minutes, it could be completed well before the clinical procedure and would therefore not affect its duration. The robot registration was completed in 5 minutes, which would be additional to the conventional LA procedure. Differently from the manual tests, all four targets were successfully punctured at the first attempt (Table II).

Table I Manual test

Target	Axial angle q_3	Sagittal angle q_4	Insertion attempts	Duration (minutes)
1	0°	30.0°	2	27
2	0°	28.3°	2	29
3	36.9°	21.5°	3	26
4	19.6°	-11.7°	4	35

Table II Robot-assisted test

Target	Axial angle q_3	Sagittal angle q_4	Insertion attempts	Duration (minutes)
1	-5°	7.9°	1	9
2	13.5°	-11.4°	1	12
3	-7.1°	-14.3°	1	15
4	-7.8°	17.2°	1	10

DISCUSSION

The results of the phantom study show that the needle-guiding robot allows targeting lesions of clinically representative size [2] in a shorter time compared to conventional manual insertions. In particular, in the robot-assisted test all targets were successfully punctured at the first attempt. This aspect could be particularly beneficial in clinical procedures since reducing the number of insertions also diminishes the risk of damaging blood vessels and healthy tissue, thus enhancing patient safety. Finally, the manual test showed that double inclined insertions are substantially more complex since they require considerable amount of training and 2D to 3D extrapolation skills. This suggests that the needle-guiding robot could be particularly beneficial for less experienced clinicians, allowing them to independently conduct MRI-guided LA procedures. Future work will include further tests with more experienced clinicians in preparation for the clinical trials.

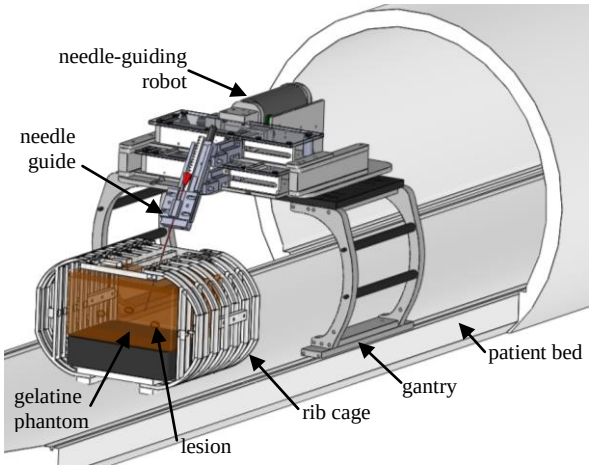

Fig. 4 CAD model of the robot setup in the MRI scanner.

ACKNOWLEDGEMENT

The authors wish to thank Wasim Hakim, St Mary's Hospital, for taking part in the experiments.
The support of the i4i Grant II-AR-1109-11011 is gratefully acknowledged.

REFERENCES

[1] W. M. W. Gedroyc, "Magnetic resonance guidance of thermal ablation.," Top. Magn. Reson. Imaging, vol. 16, no. 5, pp. 339–353, 2005.
[2] A. L. Gough-Palmer and W. M. W. Gedroyc, "Laser ablation of hepatocellular carcinoma--a review.," World J. Gastroenterol., vol. 14, no. 47, pp. 7170–7174, 2008.
[3] E. Franco and M. Ristic, "Design and control of needle positioner for MRI-guided laser ablation of the liver," in 2014 IEEE/ASME 10th International Conference on Mechatronic and Embedded Systems and Applications (MESA), 2014, pp. 1–6.
[4] J. Brujić, S. F. Edwards, D. V Grinev, I. Hopkinson, D. Brujić, and H. A. Makse, "3D bulk measurements of the force distribution in a compressed emulsion system.," Faraday Discuss., vol. 123, pp. 207–220; discussion 303–322, 419–421, 2003.
[5] N. Hata, R. Hashimoto, J. Tokuda, and S. Morikawa, "Needle guiding robot for MR-guided microwave thermotherapy of liver tumor using motorized remote-center-of-motion constraint," in Proceedings - IEEE International Conference on Robotics and Automation, 2005, vol. 2005, pp. 1652–1656.
[6] S.-E. Song, J. Tokuda, K. Tuncali, A. Yamada, M. Torabi, and N. Hata, "Design evaluation of a double ring RCM mechanism for robotic needle guidance in MRI-guided liver interventions," in 2013 IEEE/RSJ International Conference on Intelligent Robots and Systems, 2013, pp. 4078–4083.
[7] M. M. Arnolli, N. C. Hanumara, M. Franken, D. M. Brouwer, and I. A. M. J. Broeders, "An overview of systems for CT- and MRI-guided percutaneous needle placement in the thorax and abdomen.," Int. J. Med. Robot., Dec. 2014.

Magnetic Bi-component Millirobot for Targeted Drug Delivery

V. Iacovacci[1], G. Lucarini[1], L. Ricotti[1], P. Dario[1], P. E. Dupont[2], A. Menciassi[1]

[1] *The BioRobotics Institute, Scuola Superiore Sant'Anna, Italy*

[2] *Cardiovascular Surgery, Boston Children's Hospital, Harvard Medical School, USA*

v.iacovacci@sssup.it

INTRODUCTION

The goal of targeted delivery systems for therapeutic agents, e.g, drugs, nucleic acids and cells, is to overcome the limitations of conventional therapeutic strategies by avoiding the side effects of systemic administration. Most delivery systems under investigation, however, such as magnetic nanoparticles and smart triggerable materials, are affected by low controllability and the impossibility of retrieving the delivery system once the therapy has been completed, thus raising toxicity-associated risks [1]. Medical robotics and microsystem technologies can potentially contribute to the development of devices able to navigate a wide network of small-diameter canals and to controllably get in the hard-to-reach areas of the human body [2]. Several strategies have been proposed for microrobot locomotion and magnetic propulsion has emerged as one of the most promising approaches [3].

This paper deals with the design, prototyping and preliminary testing of a magnetically actuated robot able to navigate through relatively small diameter body canals (spine, urinary system, ovary, etc.), and to perform *in-situ* release of therapeutic agents. A bi-component system was developed, consisting of a carrier, in which the therapeutics are embedded, and a piston. External magnetic fields are used to propel and independently bring the robot components to the neighborhood of the target site, whereas intermagnetic attraction forces, acting when the carrier and the piston are in close proximity, are responsible for the docking between the parts that compress a drug-loaded hydrogel, thus activating drug release.

MATERIALS AND METHODS

The system consists of two millimeter-sized near-neutrally buoyant components (*i.e*. carrier and piston) both containing a spherical permanent magnet (NdFeB N45, 1 mm in diameter) (Fig. 1). The carrier consists of a polydimethylsiloxane shell (PDMS, SYLGARD® 184, Dow Corning) provided with holes to allow drug release and with NdFeB powder (Magnequench MQA-37-11, MolyCorp) embedded in its tip to increase magnetic heterogeneity thus enhancing independent control of the robot components [4]. Navigation of robot components can be performed by using an MRI scanner, a coil system or permanent magnets. The therapeutic strategy is articulated as following: *i*) the carrier is injected into the desired body lumen and navigated to the target site where it keeps its position; *ii*) the piston is subsequently injected, oriented and brought to the target area as well. Thanks to the geometric and magnetic differences between the piston and the carrier, independent control can be accomplished [4]; *iii*) when the distance between the two components falls below a critical threshold, the magnetic attraction between the carrier and the piston prevails over the external control force. Docking, compression of a hydrogel and drug release, occur; *iv*) at the end of the procedure the bi-component robot is magnetically retrieved and extracted from the body.

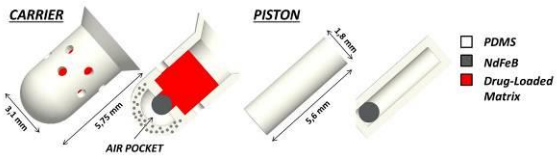

Fig. 1 Bi-component robot design and elements.

In the design of the millirobotic system, the selection of the drug-embedding material is challenging. Hydrogels based on agar and gelatin were selected for their biocompatibility and for the possibility to infuse them not only with drugs, but also with nucleic acids or cells, thus accommodating future therapeutic treatments. Different hydrogel compositions, with different agar concentration (4%, 2%, 1%, 0.75%, 0.5% and 0.25% w/w agar concentration with gelatin concentration fixed at 1% w/w) were fabricated and mechanically tested. In order to identify the best hydrogel composition, finite element model (FEM) simulations were carried out using Abaqus and MATLAB®. The aim was to calculate the deformation of the hydrogel cylinder due to the force exerted by the piston, which corresponds to the dipole-dipole interaction force between the embedded permanent magnets.

An anticancer drug (doxorubicin) commonly exploited for the treatment of different kinds of cancer was embedded into the hydrogel matrix at a concentration of 200 μg/ml. Piston and carrier components were fabricated in PDMS (monomer- curing agent ratio 10:1) by exploiting custom made 3D printed molds and a dedicated setup to orient and accumulate NdFeB powder on the carrier's tip. The polymeric shell components were assembled by embedding the permanent magnets; then, 10 μL of "hydrogel+drug" solution were injected into the carrier and let solidify *in situ* (Fig. 2).

Finally, the correct operation of the proposed platform was evaluated through magnetic locomotion, docking and drug release tests. The amount of doxorubicin

released by different prototypes (n=3) robot was assessed quantitatively through spectrophotometric analysis. *In vitro* tests were carried out by evaluating the effects that the devised procedure produced on human bladder cancer cells (T24, ATCC®, HTB-4™), both in the docked and undocked configurations.

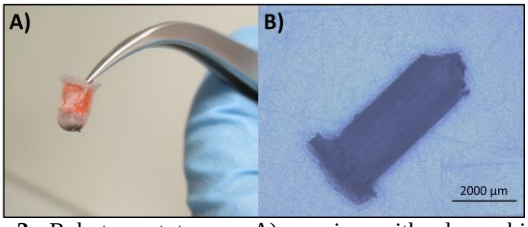

Fig. 2 Robot prototypes: A) carrier with doxorubicin-embedded hydrogel; B) piston.

RESULTS

At the initiation of hydrogel compression, the dipole-dipole attraction force between the embedded permanent magnets is 1.3 mN. FEM simulations revealed that, due to this compression force, a 0.25% agar - 1% gelatin hydrogel produced the best results, undergoing a deformation of about 38%. Further simulations and tests revealed that the embedded doxorubicin does not negatively affect hydrogel behavior, thus leading to the choice of this formulation as drug-loaded matrix. The locomotion of the robot components and the correct operation of the docking procedure were demonstrated in a liquid environment by exploiting a permanent magnets-based control (Fig. 3).

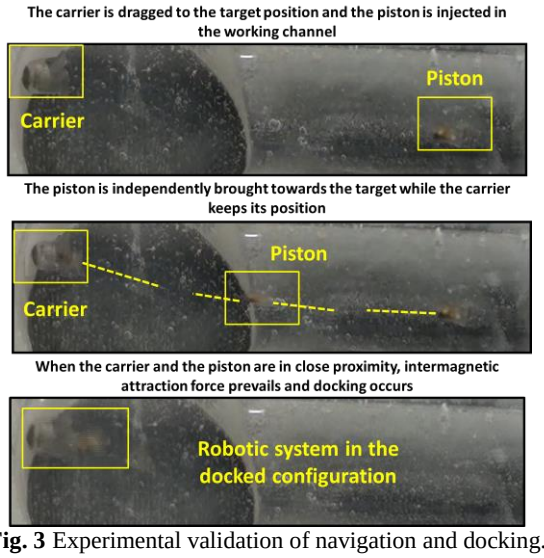

Fig. 3 Experimental validation of navigation and docking.

The efficacy of the drug release procedure was evaluated through spectrophotometric analyses, by measuring the amount of doxorubicin released by each robot prototype after docking. Results demonstrated that the spontaneous release without docking (control samples) is negligible, whereas 6.3±2.4 ng of drug were released by each robot prototype due to docking (Fig. 4A). Procedure efficacy was furtherly demonstrated by treating T24 cells with docking and undocking robots. *In vitro* tests revealed that the amount of doxorubicin released by the carrier is able to produce the desired toxic effect on cancer cells. Both reactive oxygen species (ROS) analysis, carried out 24 h after the docking procedure (fig. 4B), and DNA measurements, carried out 72 h after system testing, confirmed that the docking mechanism is highly effective to activate the drug release, thus damaging cancer cells.

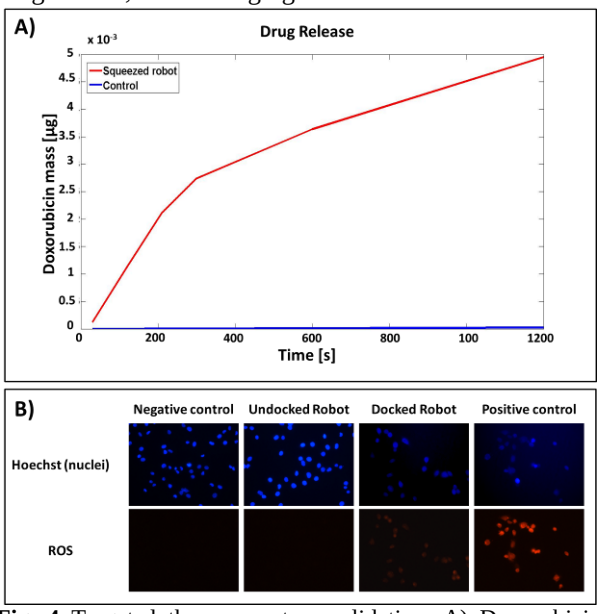

Fig. 4 Targeted therapy system validation. A) Doxorubicin temporal release profile in the docked (squeezed robot) and undocked configuration (control). Measures were performed in triplicate: average curves are reported; B) fluorescence images for the different sample types, 24 h after the treatment (nuclei in blue, ROS production in red). Negative control = no treatment; positive control = 10 µg/mL doxorubicin directly dispersed in the culture medium. Positive control is similar to the "docked robot" condition. Negative control is close to the "undocked robot" condition.

DISCUSSION

This paper reports a novel millirobot concept, enabling reliable targeted therapy in body regions currently reachable only by means of systemic drug administration or low-dexterity instruments. Magnetic locomotion and release tests were carried out, thus demonstrating that the proposed release mechanism, based on controlled squeezing of a drug-loaded matrix, is reliable and efficient and is able to produce a therapeutic effect on cancer cells.

REFERENCES

[1] Ricotti L, Cafarelli A, Iacovacci V, Vannozzi L, and Menciassi A. Advanced Micro-Nano-Bio Systems for Future Targeted Therapies. Curr. Nanosci. 2015; doi: 10.2174/1573413710666141114221246.

[2] Abbott, J, Nagy Z, Beyeler F, and Nelson B. Robotics in the small. IEEE Rob. Autom. Mag. 2007; 14: 92-103.

[3] Nelson BJ, Kaliakatsos IK, and Abbott J. Microrobots for minimally invasive medicine. Annu. Rev. Biomed. Eng. 2010; 12: 55-85.

[4] Panagiotis V, Akhavan-Sharif MR, and Dupont PE. Motion planning for multiple millimeter-scale magnetic capsules in a fluid environment. Proc. IEEE Int. Conf. Robot. Autom. 2012; 1927–1932.

Fused MRI-Ultrasound Guidance for Robot-Assisted Laparoscopic Prostatectomy: System Architecture and First Clinical Use

O. Mohareri[1,3], G. Nir[1], J. Lobo[1], R. Savdie[2], P. Black[2], S. E. Salcudean[1]

[1] *Department of Electrical and Computer Engineering, University of British Columbia, USA*

[2] *Department of Urological Sciences, University of British Columbia, USA*

[3] *Intuitive Surgical Inc., USA*

tims, omidm@ece.ubc.ca

INTRODUCTION

Robot-assisted laparoscopic radical prostatectomy (RALRP) using the da Vinci surgical system is the gold standard treatment option for organ confined prostate cancer. However, the rates of positive surgical margins (cancer left behind after surgery) still range between 9% and 30%, depending on the center [1]. The main reason why the best trade-off between achieving oncological success (cancer removal) and functional success (continence and potency) cannot be achieved is the inability to localize, intraopratively, the location and extent of cancer. Advances in MRI may provide spatially localized information to fill this void and aid surgical planning.

In this work, we present a novel MRI-Ultrasound guidance system for the da Vinci which involves a novel intraoperative segmentation-based MR-Ultrasound deformable registration method that is integrated into a clinically used robotic trans-rectal ultrasound (TRUS) imaging system [2], which in turn can be registered to the da Vinci system's coordinate frame. Using such a system, a 3D MR volume and the preoperative surgical plan can be mapped to the da Vinci system's coordinate frame. The surgical instrument can then be visualized, in real-time, with respect to the preoperative deformed MR volume. In addition, since the TRUS imaging system is robotic, it can track the tip of a da Vinci surgical instrument automatically, and is registered to the preoperative MR volume, the surgical instrument itself can be used as an intuitive and easy to use control device for the surgeon to manipulate both MR and TRUS images in real-time during the procedure. After initial testing and validation on a prostate phantom and a data-set of $n=6$ patients offline, the system was used with a clinical da Vinci surgical system inside a robotic operating room and tested on two patients undergoing RALRP. We outline the system architecture and present our experience with the system in the first two patients. The feasibility and application of fused MRI and TRUS during radical prostatectomy has not been demonstrated before. Given the significant rates of positive surgical margins still reported in the literature, the presented system has potentially significant clinical benefits.

MATERIALS AND METHODS

The components of our image-guided system are illustrated in Figure 1. The system comprises: (i) an ultrasound system with a motorized TRUS transducer mounted on a brachytherapy setup, (ii) an external PC for image registration and display on the da Vinci console, and (iii) registration and tracking software. A previously designed and clinically used robotic TRUS manipulator was used for automatic and remote rotation of the TRUS transducer during the procedure [2].

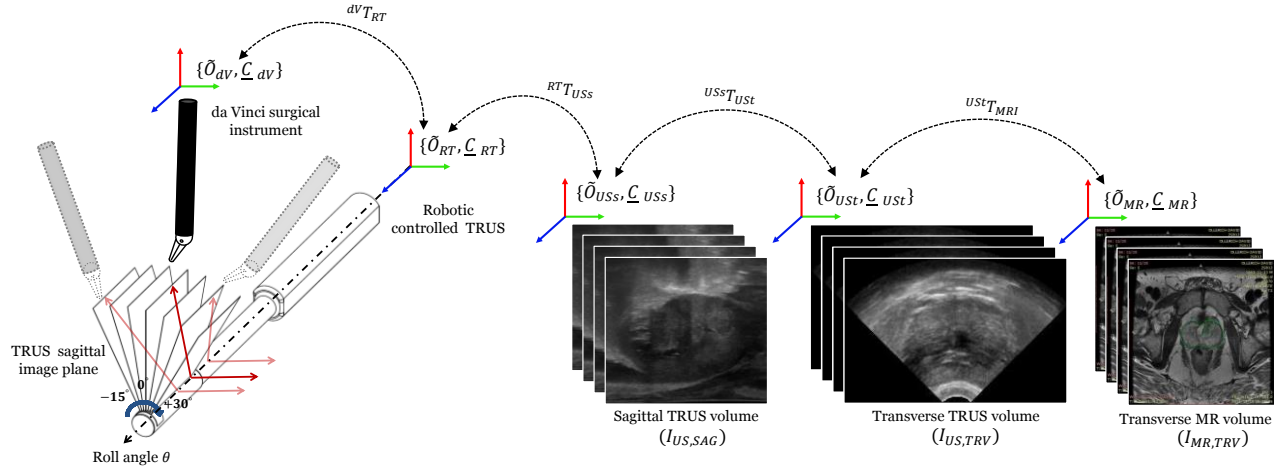

Fig. 1 Schematic figure of the system components. Dotted black arrows show the transformation between various coordinate systems involved in this system: da Vinci (dV), robotic TRUS (RT), ultrasound sagittal image (USs), ultrasound transverse image (USt) and MR volume (MR) .

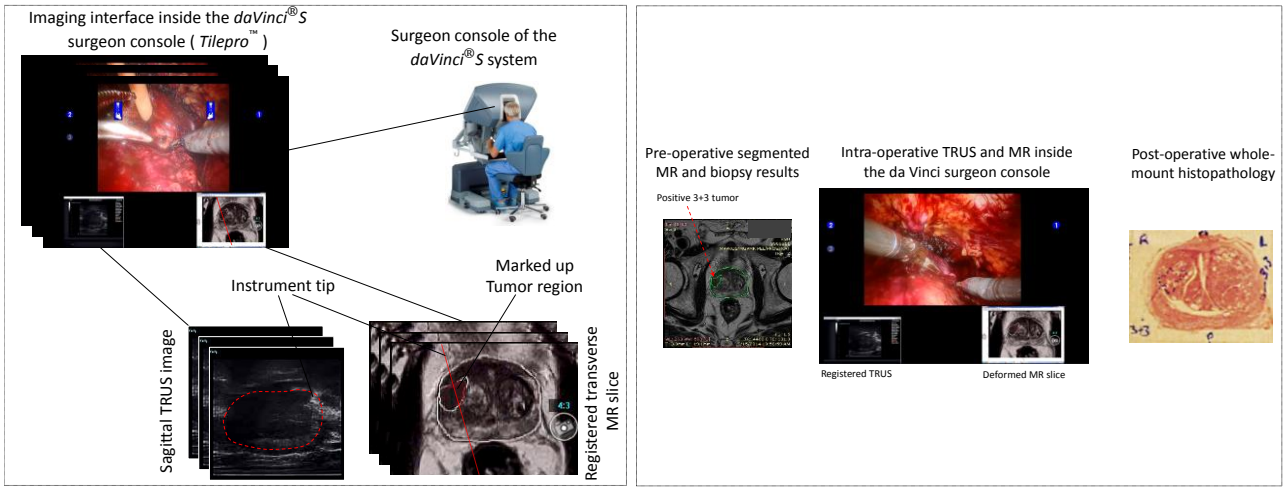

Fig. 2 (a) Real-time imaging interface using the da Vinci S TilePro feature and our custom MR imaging GUI. (b) An example image of the system in clinical use and imaging workflow. Both deformed MR and real-time TRUS are displayed to the surgeon. Post-operative whole-mount histopathology imaging is used to validate the cancer localization performance using MRI.

The sagittal TRUS imaging plane is automatically repositioned using the robot, so that the 2D ultrasound image continuously contains the tip of a specified da Vinci surgical manipulator. Automatic instrument tracking is achieved by means of a rapid, accurate and clinically feasible intraoperative registration technique that solves for the rigid homogeneous transformation between the da Vinci and the TRUS robot coordinate systems (Figure 1) [2].

The prostate gland on each transverse slice in the preoperative T2-weighted MR volume is segmented manually by a radiologist before surgery. After interpolating the intraoperative 3D TRUS B-mode images into a 3D grid in order to obtain transverse slices from the sagittal volume, we employed a real-time semi-automatic algorithm for 3-D segmentation of the prostate in the ultrasound volume. Based on the segmented surfaces of the prostate in the TRUS and MR volumes, we construct binary volumes. The two binary volumes can then be registered to each other in order to obtain a displacement map which can be applied to the MR volume. First, the MR binary volume is rigidly aligned (and scaled) to the TRUS binary volume using the principal axes transformation. Next, we deform the aligned MR volume to match the TRUS volume. The registration algorithm, based on the variational framework, minimizes the sum of squared differences between the two binary volumes with an elastic regularization of the displacement map.

RESULTS AND DISCUSSION

Two patients (ages 55 and 72; prostate specific antigen 13.5 and 28.5 ng/ml) with clinically organ confined prostate cancer undergoing RALRP agreed to participate in this institutional review board approved study. The imaging system interface and an example use case for intraoperative tumour localization is shown in Figure 2. For each case, after intraoperative TRUS to da Vinci and MR-TRUS registrations and activation of automatic tracking, the surgeon could examine the prostate anatomy and tumour locations by moving the registered surgical instrument around, placing it on the tissue surface in the area of interest and localizing the instrument tip with respect to anatomy seen in real-time sagittal TRUS images. The corresponding transverse MR slice is also displayed based on the position of the tool tip (shown in Figure 2). TRUS to da Vinci registration was performed successfully for both cases in less than 120 seconds and accuracy of less than 2 mm. MR-TRUS registration was performed for both cases in a mean time of 100 $second$ and registration accuracy of $2.1 \pm 0.3\, mm$ and $2.5 \pm 0.1\, mm$ for first and second case respectively.

The performed surgical procedures were the first in which a surgeon was able to see registered MR images intraoperatively, and to refine the surgical planes accordingly for achieving a better surgical margin and functional outcome. The intraoperative MR imaging allows surgeons to fine tune the procedure based on anatomy. Without MRI, they would just have a certain number and proportion of cores involved on one side or the other, but no other information on location - hence, relying mainly on intuition. Given the controversy on the "best" surgical approach in RALRP, as reflected in the literature, this MR-guidance could be a powerful tool to trade-off positive surgical margins against potency.

REFERENCES

[1] Ficarra V. Systematic review of methods for reporting combined outcomes after radical prostatectomy and proposal of a novel system: The survival, continence and potency (scp) classification. European Urology, 2012; 61(3):664-674.

[2] Mohareri O., et al. Intraoperative Registered Trans-Rectal Ultrasound Guidance For Robot-assisted Laparoscopic Radical Prostatectomy. The Journal of Urology, 2015; 193(1):302-312.

Comparison of Optimization Algorithms for a Tubular Aspiration Robot for Maximum Coverage in Intracerebral Hemorrhage Evacuation

Y. Guo[1], J. Granna[1], K. D. Weaver[2], R. J. Webster III[3], J. Burgner-Kahrs[1]

[1]*Center of Mechatronics (MZH), Leibniz Universität Hannover, Germany*

[2]*Department of Neurological Surgery, Vanderbilt University, USA*

[3]*Department of Mechanical Engineering, Vanderbilt University, USA*

burgner-kahrs@mzh.uni-hannover.de

INTRODUCTION

Non-aneurysmal intracerebral hemorrhage (ICH) is a significant burden to quality of life, society, and life itself. It comprises approximately 20% of all strokes with 40% and 55% median mortality rates at 30 days and 1 year, respectively [1]. The current standard of care consists of conservative medical management and treatment of any risk factors for repeat hemorrhage or progression (e.g. hypertension, coagulopathy). Many studies have addressed the role of surgery in intracerebral hemorrhage [1]. There appears to be a significant benefit in highly selected patients, especially those in which the hematoma comes close to the surface and is in the supratentorial compartment. Additional injury to the brain might occur in reaching the hemorrhage surgically as they are frequently in eloquent regions.

The ability to reach these hematomas through a trajectory that minimizes disruption of healthy brain and also allows for a dexterous aspiration within the hemorrhage is desirable. This may allow for decompression or removal of the hematoma and possibly salvaging the penumbra of at risk brain surrounding the lesion. A promising enabling technology are smaller, yet dexterous surgical manipulators and robots [2]. Tubular manipulators, also known as active cannulas [3], are particularly well suited for ICH surgery [4]. In this system, the needle-sized manipulator reaches the hemorrhage on a straight path. The curved inner tube allows debulking of the accumulated blood from within by coordinated motion during aspiration. By using differently curved aspiration tubes subsequently, the majority of the hemorrhage can be evacuated in a minimally invasive manner. Based on our initial results presented in [4], we introduce two new and less computationally intensive optimization methods to select aspiration tubes maximizing the volume coverage.

MATERIALS AND METHODS

The tubular aspiration robot is composed of a stiff guide tube, which is straight in order to reach the hemorrhage. An aspiration tube, which is superelastic (NiTi) with diameter 1mm, is inserted through the guide tube. It is composed of a straight section followed by a precurved section with constant curvature (see Fig. 1). The robot has 3 degrees of freedom (DOF): translation of the guide tube, translation and axial rotation of the aspiration tube. The kinematics of this robot has been described in [4] and allows computation of the shape of the robot for a given set of actuator values q=(α,β_1,β_2).

In this paper, we consider preoperative coverage planning. This planning problem is performed on 3D surface data representing the hemorrhage of the patient, obtained from computed tomography images and a straight entry path from the skull to the hemorrhage defined by the surgeon. We have shown that subsequent use of aspiration tubes with different curvatures leads to good coverage of the hemorrhage volume [4]. Thus, the optimal selection is performed from a set of potential tubes parameterized by the radius of the curved section $S = \{r_1, \dots, r_n\}$ and $L_c = r\pi$ (Fig 1). The goal of optimal coverage planning is to find a subset $S^* \in S$ with k aspiration tubes, which maximize the volume coverage of the hemorrhage. k can be predefined or incremented during planning until the clinically desired coverage is achieved. We quantify the covered volume as the ratio between the number of voxels (unit volume 1mm^3) reachable with the aspiration tube's tip and the overall number of voxels representing the hemorrhage (see [4]).

We previously presented a brute force algorithm [4], which determines the coverage for all possible combinations of k tubes in S and chooses S^* as the combination with maximum coverage. For large k and n this combinatorial optimization problem increases in complexity by $O(n) = n!\,(k!\,(n-k)!)^{-1}$. Thus, we propose two alternative algorithms in this paper.

The first is a greedy algorithm, which initially selects r_1 with the best coverage from S. In the second step, S is reduced to $n-1$ elements and r_2 with best coverage is selected out of S and so on. Thus, the number of combinations is reduced compared to the brute force

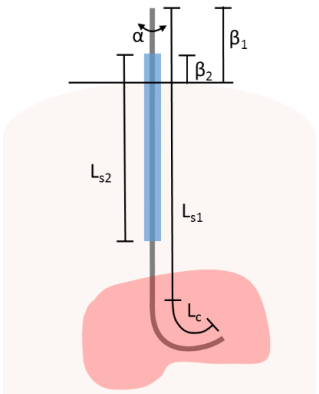

Fig. 1 Tubular aspiration robot with 3 DOF (α, β_1, β_2). Design parameters are tube lengths (L_{s1}, L_{s2}, L_c, and r).

algorithm with complexity $O(n) = \sum_{i=n-(k-1)}^{n} i$. For $k = 1$ the greedy algorithm achieves the same result as the brute force method.

Our second algorithm approximates the optimal tube radii based on our empirical results obtained with the brute force algorithm. This approximation algorithm does not involve computation of coverage during the selection as it uses a heuristic to determine the aspiration tubes radii. Here, we select the first tube with radius closest to half of the hemorrhage's extent in direction of the entry path. The second and third tube will be selected with smaller radii than the first aspiration tube (decremented in 1mm steps). The computational complexity is reduced to $O(n) = 1$.

We evaluated the performance of all 3 tube optimization algorithms on 8 representative patient ICH cases. Fig. 2 illustrates the 3D surface models of the hemorrhages. For each case we randomly generated 5 straight entry paths from a random position on the skull surface to the centroid of the hemorrhage volume. Thus, we obtained a total of 40 trials. For each trial, we determined the coverage achievable for an initial set of tubes $S = \{6,7,8,9,10,11,12,13,14,15,16\}$, L_{s1}=300, L_{s2}=140 (in mm), and for $k = \{1,2,3\}$ using each optimization algorithm.

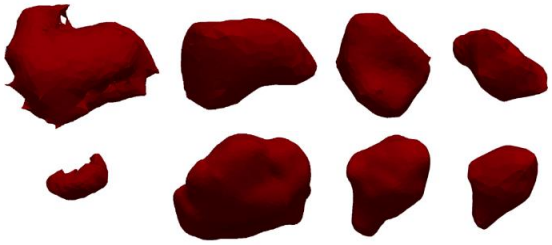

Fig. 2 Intracerebral hemorrhage geometries for 8 patient cases.

RESULTS

The coverage distribution over all 40 trials for the brute force, greedy, and approximation algorithms are summarized in histograms in Fig. 3-5 for 1, 2, and 3 tubes respectively. For all 40 trials, a volume coverage over 50% can be reached, which is considered clinically beneficial. It can be observed, that the concentration shifts significantly from 70-80% coverage with 1 tube to 80-90% with 2 tubes. The usage of 3 aspiration tubes allows for coverage mostly over 80%. The greedy algorithm leads to comparable results to the brute force method.

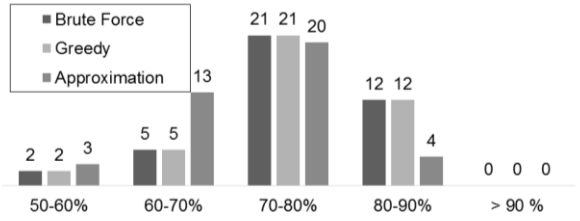

Fig. 3 Coverage distribution for $k = 1$ aspiration tube.

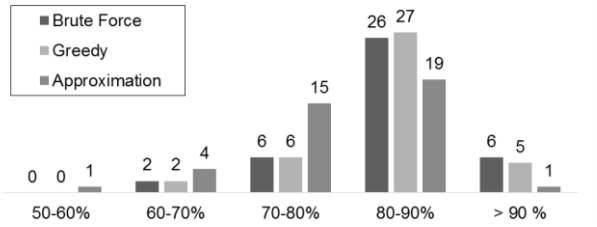

Fig. 4 Coverage distribution for $k = 2$ aspiration tubes.

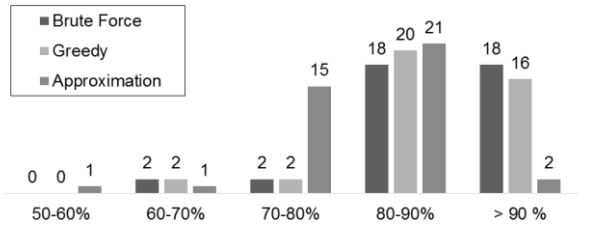

Fig. 5 Coverage distribution for $k = 3$ aspiration tubes.

In terms of computation time, brute force takes about 10 min, greedy about 22 s, and approximation algorithm about 6 s for one case on a regular PC (Matlab).

DISCUSSION

In this paper, we introduced two alternative optimization algorithms to determine a set of aspiration tubes, which maximizes coverage for evacuation of intracerebral hemorrhages. Our results indicate that 1 to 3 tubes selected from an overall set of 11 precurved aspiration tubes result in clinically significant coverage. The approximation algorithm may be favorable in those clinical cases with no time for preoperative planning.

Our current work focuses on computing an optimal motion plan (i.e. sequence of actuator values) for the selected aspiration tubes which allows for quick and safe evacuation of the hemorrhage in vivo. Extensive animal trials will be needed in the future to show clinical feasibility. Ultimately, we expect improved surgical outcome for patients suffering from intracerebral hemorrhages.

ACKNOWLEDGEMENT

This research was supported under NIH award R21 NS087796. The authors thank T.-D. Nguyen from the Center of Mechatronics for data processing.

REFERENCES

[1] van Asch CJ, Luitse MJ, Rinkel GJ, van der Tweel I, Algra A, Klijn CJ. Incidence, case fatality, and functional outcome of intracerebral haemorrhage over time, according to age, sex, and ethnic origin: a systematic review and meta-analysis. Lancet Neurol. 2010;9(2):167-76.

[2] Bergeles C, Yang G-Z. From Passive Tool Holders to Microsurgeons: Safer, Smaller, Smarter Surgical Robots. IEEE Trans Biomed Eng. 2014;61(5):1565-76.

[3] Gilbert HB, Rucker DC, Webster III RJ. Concentric Tube Robots: State of the Art and Future Directions. Proc Int Symp Robot Res. 2013;1-16.

[4] Burgner J, et al. Debulking from within: A robotic steerable cannula for intracerebral hemorrhage evacuation. IEEE Trans Biomed Eng. 2013;60(9):2567-75.

A Linearly Actuated Catheter Robot for Intelligent Steering Control based Tension and Catheter Shape Tracking

J. Back[1], R. Karim[2], K. Rhode[2], K. Althoefer[1], H. Liu[1]

[1]*Centre for Robotics Research, Department of Informatics, King's College London, UK*

[2]*Division of Imaging Sciences and Biomedical Engineering, King's College London, UK*

Junghwan.back@kcl.ac.uk

INTRODUCTION

Steerable catheter ablation therapies have been investigated for effective minimally invasive treatment of cardiac arrhythmia. Minimally invasive catheter ablation procedure promises attractive advantages, such as minimal incisions, quicker recovery time, less bleeding, and other economic effects However, the complex and delicate nature of the procedure makes it difficult to steer the catheter manually, causing an extension of surgery time. Thus, well-trained and skilled surgeons are required to treat a large number of patients in an effective manner. Moreover, extended procedure times increases the radiation burden of both surgeon and patient. In order to solve these problems, a tele steerable catheterization system has been developed. Currently, the proposed and improved robotized steerable catheter system has capabilities to provide tension sensing for safe steering and feedback of catheter position/force control, catheter-tip force estimation based on shape analysis, robotic image guidance for less radiation exposure, and tele-steering for easier steering.

MATERIALS AND METHODS

The catheter system is illustrated in Fig. 1. Four linear guides were installed to control four tendons, and these were controlled with a motion controller and user interface. The catheter was tracked using magnetic resonance image guidance. Also, shape analysis based the catheter-tip contact force estimation had been developed. In addition, the tension was measured using a custom-developed tension sensor with a strain gauge. This system was designed to allow the operator to operate away from patient, the proposed robotized steerable catheter system provides: 1) the actuator system which reacts to the measured tendon tension and input from operator, 2) contact-tip contact force estimation, and 3) 3D catheter magnetic tracking combined with image guidance.

CATHETER TIP

The MR-compatible catheter tip was made of twelve segments connected together. Each segment included a helical structure bended 4-way using four tendons, and the catheter-tip satisfied required dimensions used for cardiac catheterization, such as, the diameter was within 3mm; inner lumen diameter was 1.7mm to allow insertion of optional elements and irrigation. Each tendon guiding channel was 250μm in diameter, and the total length of the catheter tip is 112mm. In addition, a linear stage actuation was employed to provide axial movement of the catheter-tip, and also variable deflection curvature radius was achieved through sliding of a nitinol tube into the catheter tip. Thus, the catheter-tip provided a full 3D workspace.

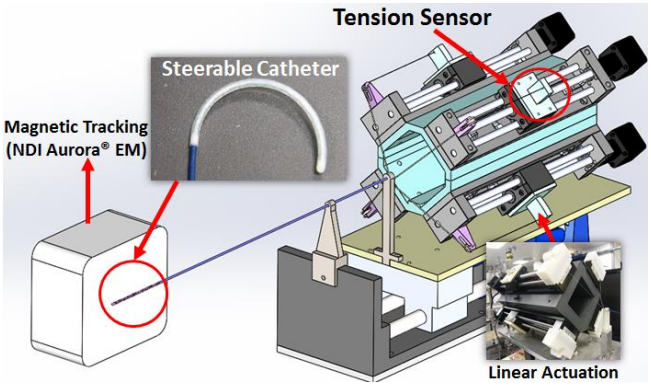

Fig. 1 Schematic diagram showing configuration of the proposed robotized tele catheterization system.

TENSION SENSING

The shape of the catheter tip is dictated by tension on the tendons. The tension is an essential parameter for safe and efficient steering, and preventing slack on the tendons. Additionally, during tele-control, the mechanical safety conditions are regulated with tendon tension measurements.

To this end, a simple cantilever beam structured tension sensor was developed as shown in Fig 2. Taking the linear stage of the beam deflection, the tension sensor had initial bending radius. A strain gauge attached to the middle surface of the cantilever beam measured the voltage difference depending on the applied tension. The tension sensor was calibrated, and it showed an accuracy of 96.5%.

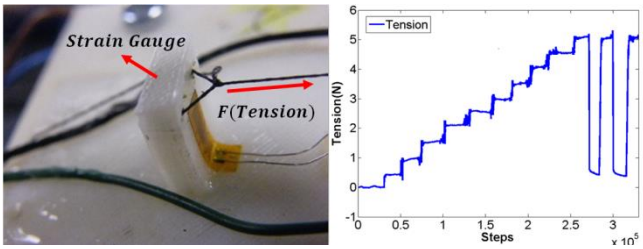

Fig. 2 The simple cantilever beam structured tension sensor, and tension sensor calibration result.

FORCE ESTIMATION

The importance of knowing the catheter-tip contact force is important due to risk of perforation during catheter insertion and this has motivated the development of numerous catheter-tip force sensors. However, many existing contact force designs cannot be easily integrated [1]. Moreover, existing force sensing devices employ fiber-optics, and strain gauge methods have difficulty in operating under small temperature changes. Therefore, we proposed a new contact force and angle estimation method based on the Cosserat rod theory which is suitable for the large non-linear deflection of a flexible body. To achieve real-time and analytical force estimation, we simplified the original Cosserat rod model and made several reasonable assumptions for solving it analytically. The force estimation was evaluated using several different scenarios such as the contact force due to internal tension and external contact as shown in Fig. 2. During these experiments, the configuration of catheter was extracted image processing. These result of the contact force calculation showed promise: The accuracy in estimating force magnitude was 89.86%, and for the force direction was 88.13%.

ROBOTIC IMAGE GUIDANCE

The image guidance platform consisted of the 3D CT reconstruction of an experimental phantom glass heart and its four chambers. Additionally, a 2D planar representation of one of its chambers (i.e. the left atrium) was also available from 3D to 2D flattening algorithm [2]. These planar representations provided a flattened map of the complex chamber anatomy on which the operator selected catheter targets for ablation. A commercial magnetic coil tracking system (NDI Aurora® EM) with a 5-DOF coil was used to measure the 3D position of the catheter tip in this experimental phantom glass heart setup.

FUTURE WORK & CONCLUSIONS

Tension sensing, catheter-tip contact force estimation and robotic image guidance have been developed, and we envisage that the fully-integrated proposed system has potential for safer and cost-effective left atrial chamber tele-catheterization procedures. Therefore, in the next step of work, the tele-catheterization system will be examined clinically, and compared with manual catheterization.

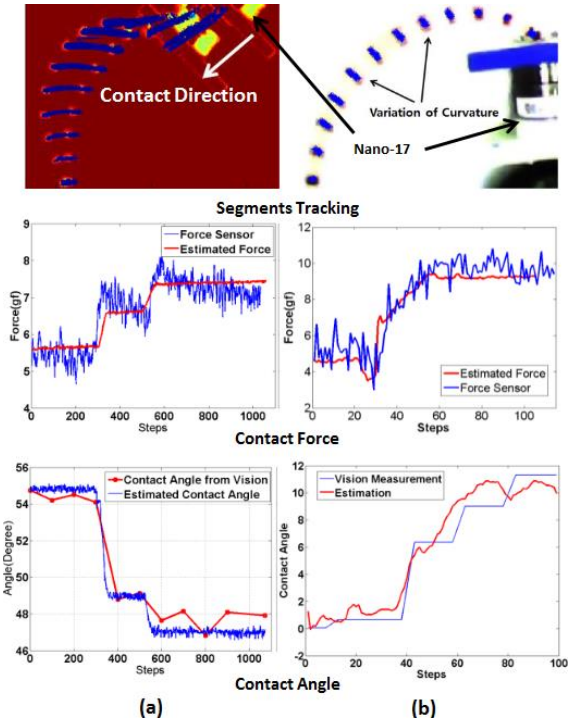

Fig. 3 Results of the contact-tip force estimation: (a) Due to internal tension, and (b) Due to external contact.

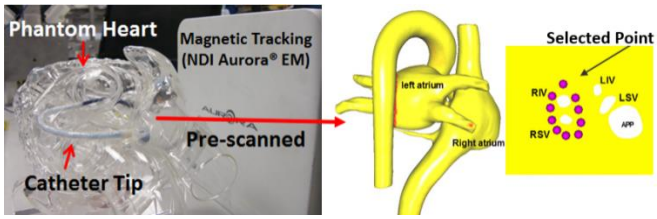

Fig. 4 3D and 2D Robotic Image Guidance.

Additionally, capabilities of the tele catheterization system satisfy necessary requirements of the proposed position/ force control algorithm described in [3, 4]. Therefore, future work will exploit these capabilities to improve the control of steering and of the interaction between heart tissue and catheter tip for robot-assisted catheter ablation procedures.

REFERENCES

[1] Di Biase, L. et al. "Relationship between catheter forces, lesion characteristics, "popping," and char formation: experience with robotic navigation system". Journal of Cardiovascular Electrophysiology. 2009.

[2] R. Karim, et al. Surface Flattening of the Human Left Atrium and Proof-of-Concept Clinical Applications, in Computerized Medical Imaging and Graphics, 38(4), pp.251-66, 2014

[3] J Back et al., "Control a Contact Sensing Finger for Surface Haptic Exploration", 2014 IEEE International Conference on Robotics and Automation (ICRA), pp.2736-2741, 2014.

[4] H Liu et al., "Finger Contact Sensing and the Application in Dexterous Hand Manipulation", Autonomous Robots, vol. 39, issue 1, pp 25-41, 2015.

Concentric Tube Robot Kinematics Using Neural Networks

C. Bergeles[1], F.-Y. Lin[1, 2], G.-Z. Yang[1]

[1]*Hamlyn Centre for Robotic Surgery, IGHI, Imperial College London, UK*

[2]*Medical Device Innovation DTP, University College London, UK*

c.bergeles@imperial.ac.uk

INTRODUCTION

Concentric tube robots (see Fig.1) are continuum robots that exhibit shape change through the insertion and rotation of pre-curved super-elastic tubes. Accurate control of the tip of a concentric tube robot requires thorough mechanics modelling that accounts for the individual tube parameters and their interaction. While extensive research has been performed on their highly non-linear modelling, no methodologies account for uncertainty in the parameters and actuation mechanism. This paper explores the application of neural networks for identification of the non-linear model of particular concentric tube robot mechanisms.

MATERIALS AND METHODS

Even though the research community has converged with regards to concentric tube robot mechanics modelling [1][2], all proposed methods rely on the underlying model of the robot and are susceptible to erroneous estimation of the multitude of parameters that govern the robot's behaviour, *i.e.* the stiffness, curvature, length, and Young's Modulus of individual tubes. Hence, a method to estimate the kinematics and inverse kinematics *in situ*, *i.e.* for a given robot but without requiring knowledge of its parameters, would be beneficial.

The approach explored here is based on machine learning, and, more specifically, neural networks. Until now, the demonstrations of neural networks for continuum manipulators is the neural network controller of [3], and limited work, [4], has explored inverse kinematics using neural networks. The current paper demonstrates that neural networks may be viable alternative to model-based kinematics approaches.

Multi-layer perceptrons (MLP) are used as the architecture of neural networks (NN). The basic building block is the perceptron, *i.e.* a multiple input and single output neuron (see Fig. 2(a)). The perceptron is characterised by the weights, w_i , of its inputs, p_i , a comparison element, b, and its activation function $F : x \in R \rightarrow [-1, +1]$. Sets of N perceptrons are cascaded in hidden layers to form MLP to map from $R^k \rightarrow R^m$, where k is the number of inputs and m is the number of outputs (see Fig. 2(b)).

The NN should possess the appropriate activation function F, together with the minimum number of neurons n and hidden layers N, to map inputs $x \in R$ n to outputs in $y \in R$ m with the required precision.

Using Matlab, these parameters are explored for the kinematics and inverse kinematics for a concentric tube robot comprising 3 tubes. Two tubes form a variable-curvature section, *i.e.* two tubes of identical stiffness, length, and pre-curvature that rotate independently to control the section's curvature but translate simultaneously, and the third tube of fixed pre-curvature. This robot possesses a total of 5 degrees-of-freedom - 3 in position and 2 in pointing orientation - and its parameters are given in the Table. Each tube has D-times larger stiffness k than its directly inner tube, thus following the "dominant stiffness" rule of [1]. The robot, illustrated in Fig. 1 is stable in its workspace.

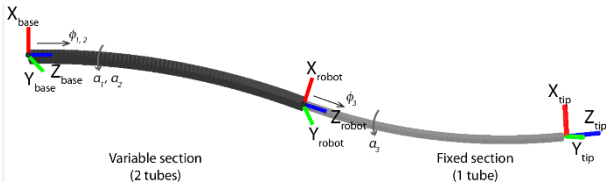

Fig. 1 A concentric tube robot with a variable-curvature section (2 tubes) and a fixed-curvature section (1 tube). Tube extensions and rotations control the tip. Angles α correspond to twist angles that vary along the robot's shape to account for robot torsion. (α_1, α_2, α_3, $\varphi_{1,2}$, φ_3) are the joint variables.

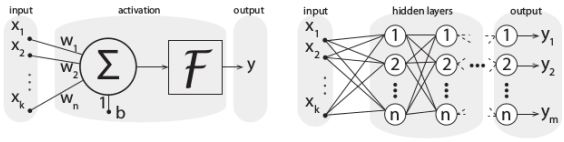

Fig. 2 (a) A single neuron acting as a perceptron. (b) The MLP architecture with k inputs and m outputs.

CONCENTRIC TUBE ROBOT PARAMETERS

Parameter	Value		
Base location [mm]	$[0, 0, 0]^T$		
Entry vector	$[0, 0, 1]^T$		
Section stiffness ratio	$D = 10$		
Section	$\mathbf{1/\kappa_i}$ **[mm]**	$\mathbf{\Phi_i}$ **[mm]**	$\mathbf{L_i}$ **[mm]**
proximal (two tubes)	242	150	150
distal (one tube)	194	100	250

The robot kinematics are solved using discretised versions of the Equations in [1], for arclength discretization of 1mm.

Forward Kinematics Network

Training set: By generating 1000000 robot shapes by uniformly sampling robot joint variables the set of tip poses of the robot and its workspace is covered.

Workspace calculation creates the tuples that form the training set of the NN. The 5 × 1 vector encoding the position and pointing orientation is used as the target, and the joint variables as input. To alleviate bias towards small total extensions and degenerate tip orientations, small tube translations, *i.e.* $\varphi < 0.3\Phi$, are ignored, where Φ is the maximum tube extension. The training set is split into training/testing/validation (60/20/20) to avoid overfitting.

Selection of MLP architecture: Kolmogorov's theorem states that any non-linear function can be approximated arbitrarily well using an MLP with a single hidden layer [5]. Hence, a single-layer MLP (N = 1) for the forward kinematics is sufficient.

Cardinality of training set: MLPs were trained for $|S| = 10 \times 10^3 \cdots 100 \times 10^3$, where $|S|$ is the number of training samples, with steps of 10×10^3, for N = 1 and n = 10 · · · 150, with steps of 10.

Inverse Kinematics Network

NN for inverse kinematics mapping has two differences:
1) The inputs to the MLP are now the three-dimensional position and pointing orientation of the tip, whereas the outputs are the joint variables;
2) It has been proved that approximating the inverse of a smooth non-linear mapping, e.g. the inverse of forward kinematics, require at least 2 hidden layers [6];

The increased complexity introduces the requirement of configuration-space splitting. To account for the behaviour of inverse trigonometric functions, *i.e.* arccos, arcsin, arctan, which will be implicitly modelled by the MLP to account for the torsional rotations of the tubes, the configuration space for α, *i.e.* the tube rotations, is split into 4 quadrants, $[0, \pi/2)$, $[\pi/2, \pi)$, $[\pi, 3\pi/2)$, $[3\pi/2, 2\pi)$. This, however, results in an uncertainty in the selection of the appropriate NN, since the joint variable interval is not known *a priori*.

This is tackled by using, for the target tip position and pointing orientation, all the trained IK NNs. This results in multiple joint variable estimates: a single estimate for each tube extension φ_i, and 4 estimates for each tube rotation α_i, *i.e.*, 16 joint variable sets for the robot under examination. The correct joint-variable tuple is selected as the one that returns the least forward kinematics error, since the desired tip pose is known.

RESULTS

Forward Kinematics Network

Figure 3 shows the average, and standard deviation of the errors for the tip position (estimated vs actual) and tip orientation (estimated vs actual, as the magnitude of the orientation vector difference). Increasing the number of neurons above 120 and the number of samples above 60×10^3 does not yield precision benefits. With these values, the mean tip error is 0.2mm, and the mean orientation vector magnitude difference is 0.002.

Inverse Kinematics Network

Similar simulations hold for the inverse kinematics networks: 10×10^3 samples, two layers, and 100 neurons per layer are sufficient. Then, using the described architecture for 1000 samples not considered for training results in errors in tube extension below 0.8mm, and errors in tube rotation below 0.1^o. Our Matlab implementation calculates the inverse kinematics at 50Hz. With hardware implementations possible, computational requirements can be trivial.

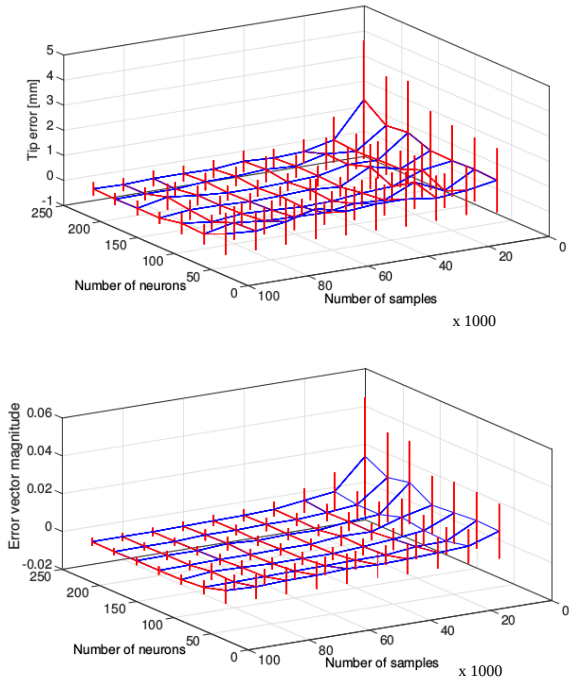

Fig. 3 Effect of training set cardinality and number of neurons on tip (a) position, and (b) orientation error (as vector-difference magnitude). Red vertical lines demonstrate the standard deviation of the error.

DISCUSSION

This paper presented in simulations the use of neural networks to model the forward and inverse kinematics of concentric tube robots. This experimentally allows the determination of the robot's motion model by observing the tip's behaviour for different actuator inputs, akin to system identification.

REFERENCES

[1] P. E. Dupont, J. Lock, B. Itkowitz, and E. Butler, "Design and control of concentric tube robots," IEEE Trans. Robotics, vol. 26, no. 2, pp. 209–225, 2010.

[2] R. J. Webster III, J. M. Romano, and N. J. Cowan, "Mechanics of precurved-tube continuum robots," IEEE Trans. Robotics, vol. 25, no. 1, pp. 67–78, 2009.

[3] D. Braganza, D. M. Dawson, and I. D. Walker, "A neural network controller for continuum robots," IEEE Trans. Robotics, vol. 23, no. 5, pp. 1270–1277, 2007.

[4] S. Tejomurtula and S. Kak, "Inverse kinematics in robotics using neural networks," Information Sciences, no. 116, pp. 147–164, 1999.

[5] R. Hecht-Nielsen, "Kolmogorov's mapping neural network existence theorem," Int. Conf. Neural Networks, vol. 3, pp. 11–14, 1987.

[6] E. D. Sontag, "Feedback stabilization using two-hidden-layer nets," IEEE Trans. Neural Networks, vol. 3, no. 6, pp. 981–990, 1992.

Cardioscopic Imaging to Guide Manual and Robotic Surgery Inside the Beating Heart

C. Kim, A. Ataollahi, I. Berra, P. E. Dupont

Pediatric Cardiac Bioengineering Lab, Boston Children's Hospital, Harvard Medical School
chunwoo.kim@childrens.harvard.edu

INTRODUCTION

The transcatheter approach is gaining popularity for many cardiac procedures that have previously been performed as open-heart surgery. One of the major hurdles of transcatheter interventions, however, is providing imaging of sufficient quality for procedure guidance and monitoring.

Ultrasound and X-ray fluoroscopy are the most common modalities utilized for the image guidance. While both are noninvasive, each has limitations in guiding interactions between the catheter and the tissue. Ultrasound images are of limited resolution and suffer from high noise. Fluoroscopy provides higher resolution, but the images are 2D and contain the catheter, but not the tissue. In short, both modalities lack ability to provide high-resolution images at the interventional site.

Optical imaging at the tip of the catheter can augment the image guidance of these modalities by providing intuitive local images of the intervention site. The challenge of optical imaging inside the heart, however, is seeing through the blood. Three approaches have been attempted to overcome this challenge: infrared imaging [1], flushing with clear liquid [2] and introducing an optical window [3]. In the latter, a transparent optical window is pressed against the tissue to displace the blood so that the tissue becomes visible. The advantages of this approach are that it does not require continuous fluid injection into the bloodstream and also stabilizes the imaging location through the contact force for subsequent tool delivery.

This abstract describes two of our cardioscope designs for intracardiac imaging. The first is a handheld instrument for tissue removal. The second smaller design, mounted on a robotic catheter, is being developed for transapical aortic paravalvular leak closure.

MATERIALS AND METHODS

Figure 1 shows the two cardioscopes. Their diameters are 13mm and 6mm, respectively. The main component of both cardioscopes is the transparent optical window cast from RTV-2 silicone rubber (QSil 216, Quantum Silicones LLC). The optical window encloses the camera and LED light sources and incorporates a tool channel. The handheld design has an additional channel for flushing saline to clear the field of view.

This work was supported by the the NIH under grant R01HL124020.

Imaging is performed using a 5mm CCD camera (Vividia Mini, Vividia Tech.) and 1mm CMOS image sensor (NanEye, Awiaba), respectively. The tool channels of the two systems were designed for passage of φ1.8 mm MEMS tissue removal tool [4] and 4Fr closure devices for sealing paravalvular leaks, respectively. The field of view of both cardioscopes is designed to enable visualization of devices extending from the tool channel.

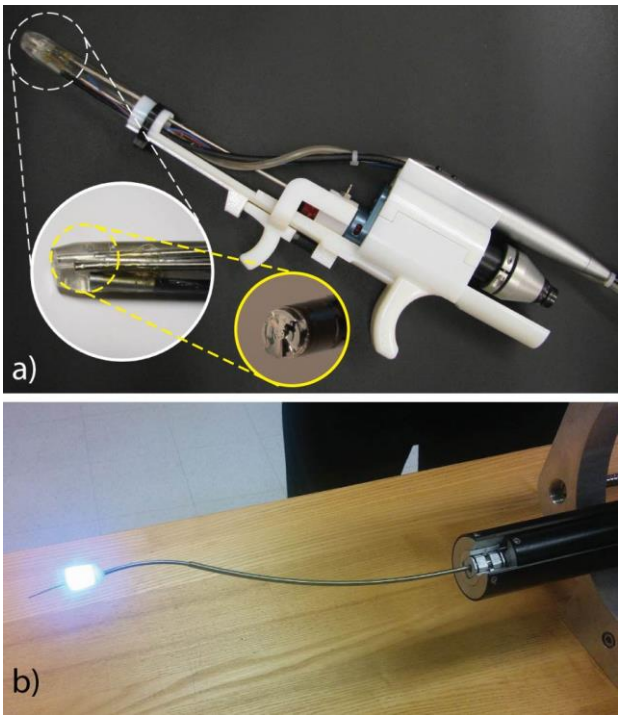

Fig 1. Cardioscope designs. a) Handheld tissue removal instrument. b) Robotic catheter for paravalvular leak closure.

RESULTS

The handheld cardioscope was tested in *ex-vivo* and *in-vivo* experiments. The goal of the both experiments was to remove tissue from the infundibulum region of the right ventricle, simulating the correction of pediatric outflow tract obstruction.

The *ex-vivo* experiments were performed on porcine hearts connected to a pulsatile pumping system to simulate the cardiac cycle. Prior to the experiments, a 15mm circle was marked on the tissue to specify the target for tissue removal, as shown in Figure 2a. The cardioscope was inserted through the free wall of the right ventricle and tissue was precisely removed from the target region as shown in Figure 2b.

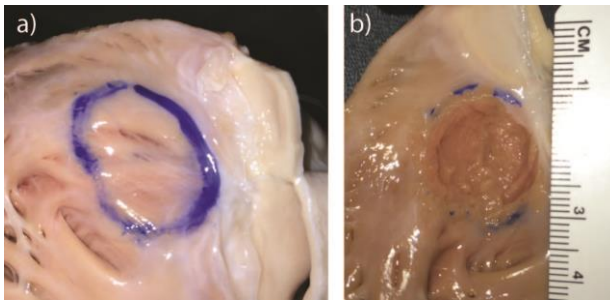

Fig 2. *Ex-vivo* experiment. a) Target region of interest marked on the inner surface of the heart. b) Target region after the experiment, showing precise removal of the tissue.

For the *in-vivo* experiment, a 65kg swine was anesthetized and the cardioscope was inserted through the right ventricular free wall. Figure 3 shows images of the ventricular wall during tissue removal. Clear visualization of the tissue was established as soon as the optical window contacted the tissue. Tissue was removed under visual guidance as shown in Figure 3c,d.

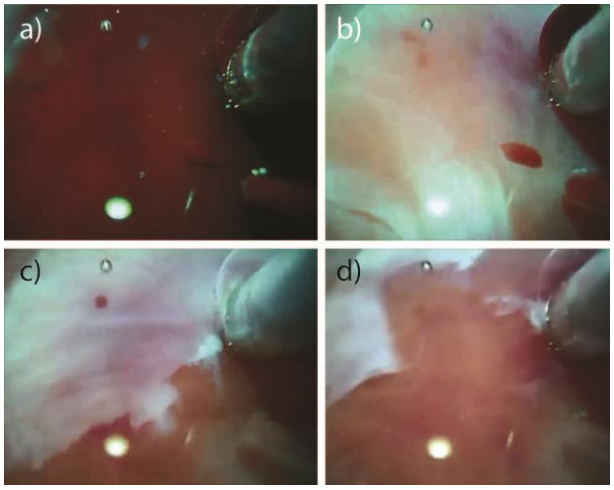

Fig 3. *In-vivo* View. a) Prior to tissue contact. b) At tissue contact. c) and d) Removal of the endocardium.

The robotic-catheter-mounted cardioscope has been tested in bench-top and *ex-vivo* experiments as shown in Figure 4. Figure 4a,b demonstrate navigation of the catheter tip inside a beaker of water to "read" lettering written on its exterior. In initial *ex-vivo* experiments, the catheter has been navigated inside a water-filled porcine heart (Figure 4c). As an on-going imaging demonstration project, current experiments involve constructing transcatheter valve models incorporating paravalvular leaks. The robotic catheter will be introduced transapically and the effectiveness of cardioscopically-guided navigation to each leak will be investigated.

DISCUSSION

This paper presents two cardioscope designs with the goal of providing tool-tip views inside the heart. The designs, which integrate camera, light source and tool channel as a single molded unit, are both simple and inexpensive to fabricate. As a milestone toward percutaneous robotic interventions, a handheld instrument was developed and demonstrated in the context of beating-heart tissue removal. It successfully addressed two key problems: visualization of tissue removal and precise control of tool-tissue contact.

As described, its miniaturization for deployment on a robotic catheter has been demonstrated. In combination with robotic steerability, cardioscopic navigation is currently being explored for paravalvular leak closure.

It is anticipated that cardioscopic imaging can be combined with X-ray fluoroscopy and ultrasound, the traditional imaging modalities of intracardiac procedures. The 'local' optical image of the intervention area from the cardioscope can augment the more 'global' picture of catheter position from fluoroscopy and ultrasound. Together, such imaging may provide sufficient additional information to broaden the range of transcatheter interventions that can be performed.

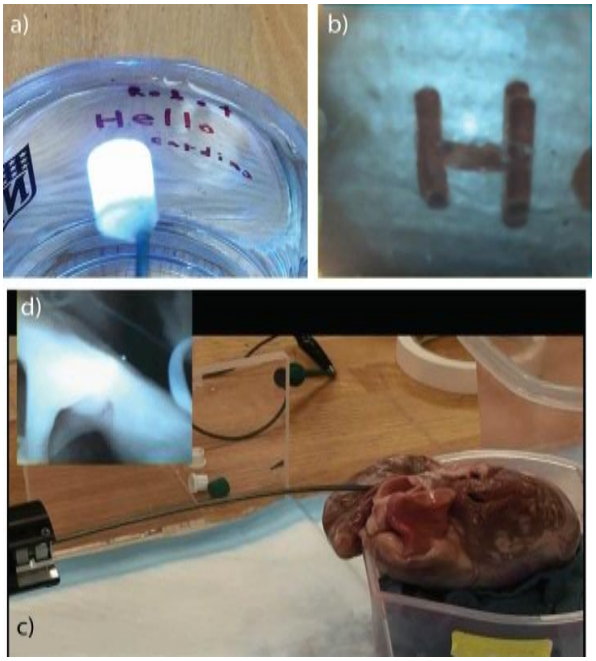

Fig 4. Initial testing of catheter-mounted cardioscope, a) Navigating to text on beaker, and b) Cardioscope image, c) *Ex-vivo* navigation into porcine heart, d) Image inside heart.

REFERENCES

[1] Grundfest, Warren S., et al. "Real-time percutaneous optical imaging of anatomical structures in the heart through blood using a catheter-based infrared imaging system." Seminars in thoracic and cardiovascular surgery. Vol. 19. No. 4. WB Saunders, 2008.

[2] Shiose, Akira, et al. "Cardioscopy-guided surgery: Intracardiac mitral and tricuspid valve repair under direct visualization in the beating heart." J thoracic cardiovasc surgery 142.1 (2011): 199-202.

[3] Padala, Muralidhar, et al. "Transapical beating heart cardioscopy technique for off-pump visualization of heart valves." J thoracic cardiovasc surgery 144.1 (2012):231-234.

[4] Gosline, A.H. et al. "Metal MEMS tools for beating-heart tissue removal," Robotics and Automation (ICRA), 2012 IEEE Int Conf, pp.1921-1926, 14-18 May 2012.

Development and Validation of a Training and Assessment Tool for Robot Assisted Radical Prostatectomy – A Multi-institutional Study

C. Lovegrove[1], G. Novara[2], K. Guru[3], A. Mottrie[4], B. Challacombe[5], M. Brown[5], J. Raza[3], R. Popert[5], H. Van der Poel[6], J. Peabody[7], P. Dasgupta[5], K. Ahmed[5]

[1]King's College London, UK, [2]University of Padua, Italy, [3]Roswell Park Cancer Institute, USA, [4]OLV Clinic, Belgium, [5]Guy's Hospital, London, UK, [6]Netherlands Cancer Institute, Netherlands, [7]Henry Ford Hospital, USA

Catherine.lovegrove@kcl.ac.uk

INTRODUCTION

Evidence has demonstrated manifold differences in technical and non-technical skill requirements between surgical modalities. With increasing use of Robot Assisted Radical Prostatectomy (RARP) for prostate cancer it is important that training and assessment be evaluated to ensure that they develop surgical skills required for safe, competent practice.

Surgical Safety

Adverse events arise from technical and non-technical skill deficiencies which training and assessment ought to rectify. Trainees must develop skills and knowledge of generic and procedure-specific techniques such as RARP. Adjusting training and assessment to ensure these outcomes ensures patient safety and maintains competent use of innovative surgical methods.

Checklists

Checklist can protect patient safety and measure surgical competence. Objective Structured Assessment of Technical Skills (OSATS) has been employed in training (gynaecology, ophthalmology), assessment and measuring procedural learning curves. To date non-specific measures have been designed. One example is the WHO Surgical Safety Checklist, acknowledging that any operation entails avoidable error. This is employed in a multitude of surgical settings (1). Other checklists for use in robotic surgery have been designed but do not assess specific procedures (2-4). The subjective and generic nature of existing assessments indicates the need for more specific, objective tools to ensure surgical competence in robotic techniques.

To address this paucity, this study sought to:

1. Develop and validate a checklist-based training and assessment score for RARP
2. Evaluate learning curve (LC) of trainees using the RARP score.

MATERIALS AND METHODS

Development & Validation

This multi-institutional, observational, prospective study used HFMEA to identify critical steps associated with RARP. HFMEA has been used in high-risk industries and employs pre-emptive risk assessment to minimize adverse events (Figure 1). Comprising five steps, HFMEA combines expert experience with brainstorming techniques to list failures and failure modes.

After building a process-map, failure modes and failure mode effects for each sub-process are brainstormed, constructing an HFMEA hazard analysis table. This underwent content validation by experts at a multi-institutional meeting in Buffalo, NY. Hazard analysis was conducted in an international, multi-institutional teleconference with experts to allocate hazard scores according to pre-defined definitions (5).

Content validation was undertaken at several stages throughout the process and by circulating the RARP Score for use by 17 mentors and trainees, construct validity, acceptability, feasibility and educational impact were appraised. Construct validity and inter-rater reliability was evaluated by two experts using trainees' footage and a video of RARP by an expert surgeon.

Learning Curves

15 surgical trainees were scored using the RARP Score while operating. Results were analyzed relative to RARP experience, examining sub-process learning curves. Information regarding the number of procedures required to attain competence in a step was uncovered.

RESULTS

Development & Validation

5 surgeons were observed for 42 console hours to map key steps of RARP (Fig. **2**).

3 of RARP were identified and consisted of 23 processes, 64 sub-processes:

1. Preparation of the Operative Field (9 processes, 12 sub-processes, 19 failure modes)
2. Dissection of the Bladder and Prostate (9 processes, 29 sub-processes, 37 failure modes)
3. Anastomosis and Closure (5 processes, 23 associated sub-processes, 27 failure modes)

HFMEA identified 46 potential causes of "Hazard score" ≥8 and incorporated them into the RARP Score. Content validation by multi-national experts (US, UK, Europe) developed the RARP Score comprising 17 stages, 41 steps (Fig. **3**). All participants deemed it to

encompass important procedural steps.
Construct validity showed a trend towards significance in steps 14, 15, 19, 20 and 28 (P=0.063, 0.093, 0.068, 0.073, 0.091 respectively). Inter-rater reliability demonstrated consistency in marking steps 5, and 27 ($p<0.001$). The RARP Score was acceptable, feasible and cost effective with educational impact.

Learning Curves

15 trainees were assessed for 8 months in 426 cases (Range 4-79) with all steps attempted. Most cases were T stage 2 (40.3%), N stage 0 (59.9%) and "Intermediate" D'Amico risk (36.1%).
Easier steps (for example patient preparation) are undertaken earlier during training and surgeons achieve "competence" within few procedures. Learning curves demonstrated several findings. There were plateaus for Anterior Bladder Neck Transection (16 cases), Posterior Bladder Neck Transection (18 cases), Posterior Dissection (9 cases), Dissection of Prostatic Pedicle and Seminal Vesicles (15 cases) and Anastomosis (17 cases). For other steps the LC did not plateau during data collection (e.g. Expose Prostatic Apex and Endopelvic Fascia; 31 cases, Stitching and Division of Dorsal Venous Plexus; 32 cases).

DISCUSSION

This multi-institutional, international study methodically designed the RARP Score using a validated risk assessment modality, HFMEA. Content validation formed an acceptable, feasible, cost-effective and educationally beneficial 17-stage assessment of technical competence for hazardous sub-steps of RARP. Analyses demonstrated varied LCs. Results can guide when surgeons should undertake steps, protecting against never events, promoting safety.

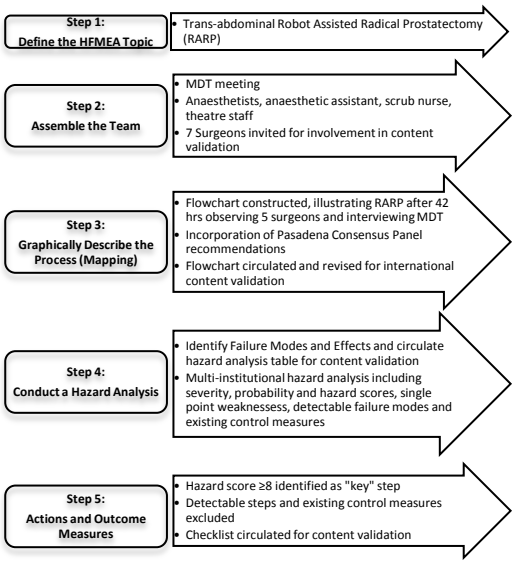

Fig. 1. HFMEA as applied to RARP.

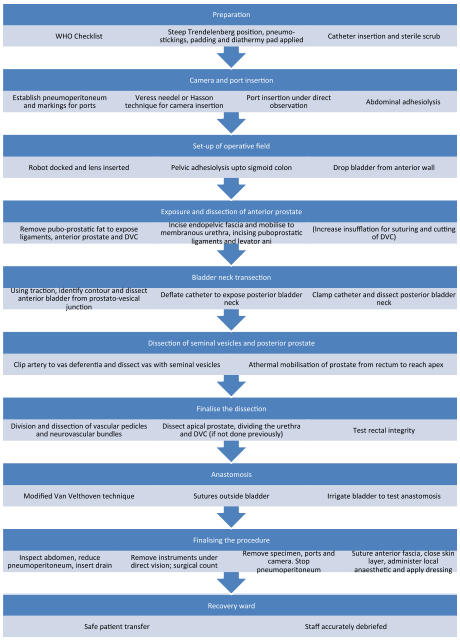

Fig. 2. Process map of RARP.

Fig. 3. RARP Score.

[1] Haynes AB, Weiser TG, Berry WR, Lipsitz SR, Breizat AH, Dellinger EP, et al. A surgical safety checklist to reduce morbidity and mortality in a global population. N Engl J Med. 2009;360(5):491-9.
[2] Song JB, Vemana G, Mobley JM, Bhayani SB. The second "time-out": a surgical safety checklist for lengthy robotic surgeries. Patient safety in surgery. 2013;7(1):19.
[3] Ahmed K, Khan N, Khan MS, Dasgupta P. Development and content validation of a surgical safety checklist for operating theatres that use robotic technology. BJU international. 2013;111(7):1161-74.
[4] ERUS. ERUS Pilot Study for European Robotic Curriculum 2013 [cited 2014 06.02.14]. Available from: http://www.uroweb.org/fileadmin/sections/ERUS/fellowship/docs/Curriculum.pdf.
[5] DeRosier J, Stalhandske E, Bagian JP, Nudell T. Using health care Failure Mode and Effect Analysis: the VA National Center for Patient Safety's prospective risk analysis system. The Joint Commission journal on quality improvement. 2002;28(5):248-67, 09.

Clinical Translation of Real Time Cautery Navigation for Breast Surgery

T. Ungi[1,2], G. Gauvin[2], A. Lasso[1], C. T. Yeo[1],
J. Rudan[2], C. J. Engel[2], G. Fichtinger[1,2]

[1]*School of Computing, Queen's University, Kingston, ON, Canada*

[2]*Department of Surgery, Queen's University, Kingston, ON, Canada*

ungi@queensu.ca

INTRODUCTION

Breast cancer is the most frequent surgically treated cancer in women. The recommended treatment for early stage breast cancer is breast-conserving surgery, which requires complete surgical excision of the tumor while conserving healthy breast tissue. If cancer is found at the excision margins (called positive margin), additional surgery is performed. Recent reported positive margins rates have been as high as 47% [1].

At the Hamlyn Symposium in 2014, we introduced the concept of a breast-conserving surgery navigation system using real time electromagnetic (EM) tracking [2]. The system features an EM-tracked tissue locking needle to serve as a local coordinate reference (Figure 1). Wire hooks lock the needle in the tumor, thereby achieving accurate tracking when the targeted tumor moves and deforms during surgery. The target is contoured in EM-tracked ultrasound and defined in the coordinate frame of the needle. The tracked surgical cutting tool (cautery device) is shown on the navigation display relative to the tumor margins. Phantom studies with this system have shown 50% reduction in positive tumor margins compared to conventional wire localization, while total excised tissue amount was equal in both groups [2]. In this paper, we present the clinical translation to breast-conserving surgery navigation and the outcomes of a clinical safety and feasibility study.

MATERIALS AND METHODS

Sterility is achieved by placing the EM field generator under the sterile drape (Figure 4) and by placing the EM sensors in sterile bags. Disposable 3D-printed fixtures house the EM sensors. The fixtures are clipped onto the needle and cautery (Figure 2). The needle tracking fixture is secured to the needle shaft and is compatible with a variety of needle brands. We use Sonic Touch GPS ultrasound scanner (Ultrasonix, Richmond, BC, Canada) with an L14-5gps probe that also includes an integrated EM sensor. The mechanical designs, editable printable models with user instructions are available on the PLUS software website (www.plustoolkit.org) [3].

For intra-operative segmentation of the tumor volume in tracked ultrasound, we model the tumors by an arbitrary number of margin points. A convex surface enclosing all tumor points is generated by Delaunay triangulation. Points are collected during systematic scanning of the tumor from multiple directions until the tumor in the ultrasound images is encompassed within the margins from all directions. Points can be added to update the tumor model at any time during the surgery. The cautery or any tracked pointer can be used to add points to the margin (Figure 3). This feature will be integrated with advanced intraoperative tumor detection methods such as mass spectrometry and optical coherence tomography in the future for tumors not completely visible in ultrasound.

The attention of the surgeons is usually focused on the surgical site, so the navigation display is out of their direct line of sight (Figure 4). The navigation system obtains the surgeon's attention when the tumor margin is breached. We developed a general purpose software module to provide visual and/or audio warning signals when the tools interfere with predefined tissue areas.

All software used in our navigation system is part of the

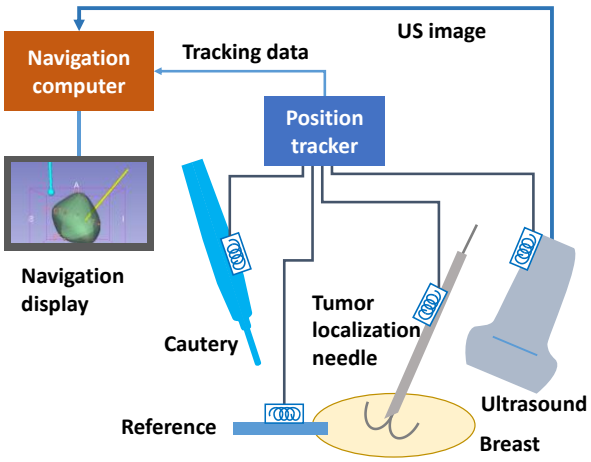

Fig. 1. Schematic view of the breast-conserving surgery navigation system. Blue coils represent EM tracking sensors.

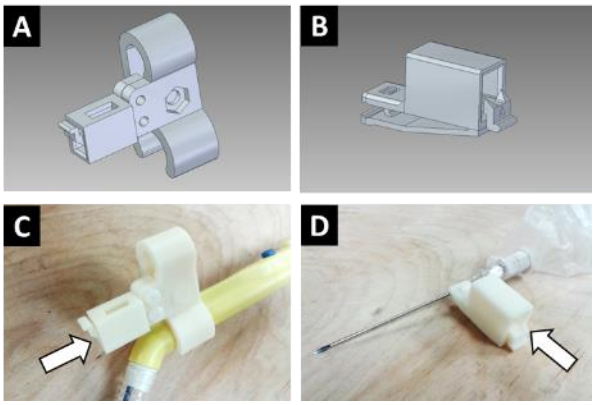

Fig. 2. Disposable tracking fixtures designed and 3D-printed for the cautery (A, C) and the needle (B, D). Arrows point at slots for EM tracking sensors.

SlicerIGT open-source framework. The source code is freely available from www.slicerigt.org, without any restriction of use. All modules are built on the 3D Slicer open source application framework (www.slicer.org) and they can be conveniently installed through the 3D Slicer extension manager. We provide online tutorials for the software modules on the SlicerIGT website. The tutorials do not require software coding knowledge. New features may be added by minimal Python scripting. Devices can be swapped out without programming by using PLUS [3]. The resulting navigation system was tested in a clinical safety and feasibility study on patients with palpable breast tumors. The study was approved by our institutional research ethics board, and written informed consent was obtained from all participating patients before surgery. We measured system setup time, calibration time, and the total procedure time. Surgeons were surveyed on the usability of the navigation system after the operations.

RESULTS

Six patients were included in the safety and feasibility study with stage IA to IIIA breast cancer. All margins were histologically confirmed as negative. There was no complication due to the navigation system, and no breach of sterility was detected in any of the cases. Clinical features and results of the study are shown in Table 1.

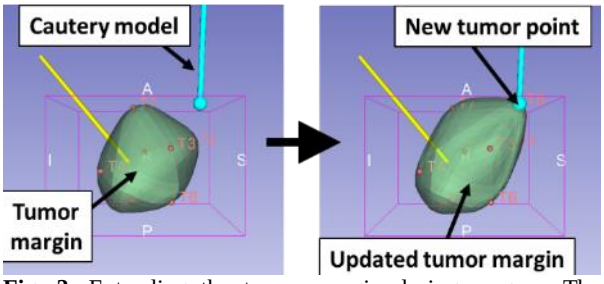

Fig. 3. Extending the tumor margin during surgery. The surgeon points at the tumor location with the cautery tip (left). The navigation software adds a new tumor point and extends the tumor margin with the new point set (right).

Fig. 4. The navigation system components (ultrasound and position tracker) are under the sterile draping. The navigation display is placed in front of the surgeons during the operation.

Questionnaires showed that the surgeons did not find the EM sensors to interfere with the procedure and the navigation system was generally easy to use. All surgeons rated the navigation system as "easy" or "very easy" to use, and considered it useful in maintaining safe and accurate tumor margins. The system setup and calibration time decreased from 15 minutes in the first case to only 6 minutes in the last case. Procedure times fell within the normal breast-conserving surgery times at our institution (Table 1).

Number of patients in study (N)	6
Age (range)	29 – 92 yrs.
Anesthesia (sedation / general)	3 / 3
Sentinel node biopsy in procedure (N)	4
Operation time (avg. ±SD)	51 ±16 min
Navigation setup time (avg. ±SD)	8.7 ±1.4 min
Margin histology (negative/positive)	6 / 0

Table 1. Clinical features and results of the clinical safety and feasibility study.

DISCUSSION

Our results suggest that real time navigation with EM tracking is safe and feasible in breast conserving surgery. No navigation system specific technical complications were experienced.

One person was needed in addition to the standard surgical staff to operate the navigation software. The surgeons indicated a strong need for sterile human-computer interface. We are planning to solve this problem by adding wireless touch-screen tablet in a sterile bag. With this, several workflow steps can be performed by the surgeons using the tablet device, such as tumor contouring and virtual viewpoint adjustment for the 3D navigation display. In one occasion the EM tracker slipped off of the needle and needed re-clamping, but tracking remained accurate because the fixture is clamped on the needle next to the hub reproducibly.

The breast surgery navigation system performed without any technical and clinical failure. A larger clinical study on non-palpable tumor cases is currently underway.

REFERENCES

[1] P. Ananthakrishnan *et al*., "Optimizing surgical margins in breast conservation. International Journal of Surgical Oncology, 2012, Article ID 585670."

[2] G Gauvin *et al.*, "Real-Time Electromagnetic Navigation for Breast Tumor Resection: Proof of Concept," in The 7th Hamlyn Symposium on Medical Robotics, London, UK, July 13-14 2014, Guang-Zhong Yang and Ara Darzi (Eds.) pp. 39-40.

[3] A Lasso *et al.*, "PLUS: open-source toolkit for ultra-sound-guided intervention systems." IEEE Trans Biomed Eng. 2014 Oct;61(10):2527-37.

Acknowledgements: The authors thank Dr. Ross Walker for help in the clinical study. G. Fichtinger is supported as Cancer Care Ontario Research Chair in Cancer Imaging.

Challenges in Multimodal Image-guided Targeted Prostate Biopsy

A. Shah[1], O. Zettinig[1,4], E. Storz[2], T. Maurer[2], M. Eiber[3], N. Navab[1,4], B. Frisch[1]

[1]*Chair for Computer Aided Medical Procedures, Technische Universität München*

[2]*Urologische Klinik und Poliklinik, Technische Universität München*

[3]*Nuklearmedizinische Klinik und Poliklinik, Technische Universität München*

[4]*Department of Computer Science, Johns Hopkins University*

amit.shah@tum.de

INTRODUCTION

The fusion of Magnetic Resonance Imaging (MRI) and Ultrasound (US) for targeted prostate biopsy can solve the diagnostic dilemma of patients with repeated negative prostate biopsies seen in the conventional Trans-Rectal UltraSound (TRUS) guided systematic biopsy. Recently, ^{68}Gallium labeled ligand of Prostate Specific Membrane Antigen (^{68}Ga-PSMA) Positron Emission Tomography (PET) was introduced that, in conjunction with MRI, provides combined molecular and structural information for the detection of Prostate Cancer (PCa) [1]. Hence, we developed an open source framework [2] that combines the preoperative PET/MRI images with TRUS and provides multimodal image guidance for targeted biopsy. In this paper, we present the technical challenges in the development of multimodal image guided prostate biopsy, especially in 3D TRUS acquisition and multimodal image registration. Further, we explain the steps to address these specific challenges and some unsolved problems. Finally, we discuss the clinical evaluation of the system.

MATERIALS AND METHODS

The multiparametric MRI and ^{68}Ga-PSMA PET were acquired on a combined PET/MR system (Siemens mMR) with 3T magnetic field strength. The 3D TRUS acquisition and biopsy were carried out in the urology department of our university hospital. We used a US system (Hitachi AVIUS) with a 2D front fire trans-rectal probe. However, our system is independent of the US machine as we are using a video frame grabber (StarTech) for image acquisition in HD (1280 × 1024 pixel). The US probe is tracked by an optical tracking system (NDI Polaris). We use a workstation with 2 Intel Xeon processors running at 2.13 GHz with 32GB RAM and a graphics card (Nvidia GeForce GTX Black Titan).

The clinical workflow has three steps – (i) pre-interventional ^{68}Ga-PSMA PET-MRI image acquisition, (ii) TRUS acquisition, 3D reconstruction and image registration, and (iii) biopsy as shown in Fig. 1. The acquisition of ^{68}Ga-PSMA PET-MRI for prostate cancer imaging is explained in [1].

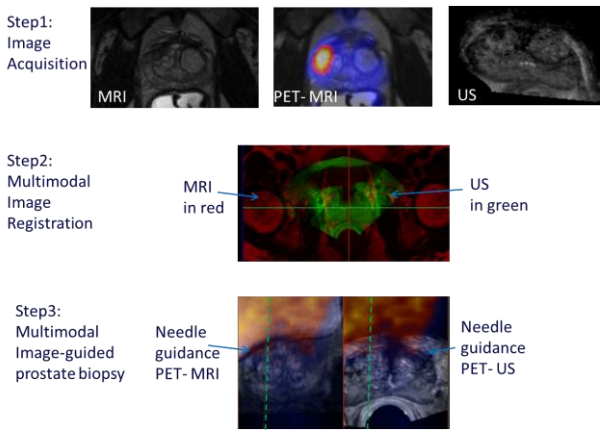

Fig. 1 Steps in clinical workflow.

3D TRUS acquisition

The challenges in 3D TRUS acquisition are precise tracking of the 2D US probe, accurate spatial calibration of the US probe for different depth settings, and reliable 3D compounding in the standard anatomical axes.

The spatial calibration of the ultrasound probe, acquisition of tracked ultrasound, and 3D compounding are done by the fCal application available in PLUS framework [3]. We use a reference target attached to the biopsy chair, as described in [2], that facilitates the free movement of tracking camera and reorientation of the 3D TRUS volume along the standard anatomical axes.

Multimodal image registration

The accurate modelling of the prostate deformation within clinically acceptable time limits is the main challenge for image registration and successfully targeting suspicious lesions. The review of various commercially available fusion devices is available in [4]. Most of these commercial devices use rigid image registration. The state of the art research on TRUS/MRI image registration is summarized in [5], wherein the typical approaches are either surface- or model-based. We use surface based deformable registration using Coherent Point Drift (CPD) algorithm [6] and compare it with rigid anatomical landmark based registration.

RESULTS

Phantom studies

For the evaluation of surface based elastic registration, we acquired MRI and TRUS images of a multimodality prostate phantom (model 053-MM, CIRS) that has visible structures such as urethra (7 mm) and three randomly placed lesions of approximately 5-10 mm. Six landmarks were annotated by an expert on images from both modalities.

The mean landmark registration errors (LRE) for surface based CPD method and rigid registration were 1.14 mm and 1.87 mm, respectively. The comparison of registration by both methods in the form of axial and coronal views is shown in Fig. 2.

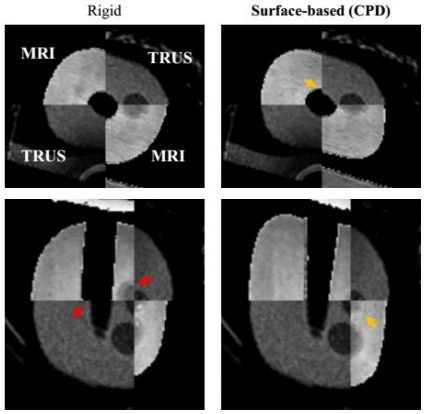

Fig. 2 Surface based elastic algorithm shows better alignment compared to rigid registration in phantom studies.

Retrospective study on patient dataset

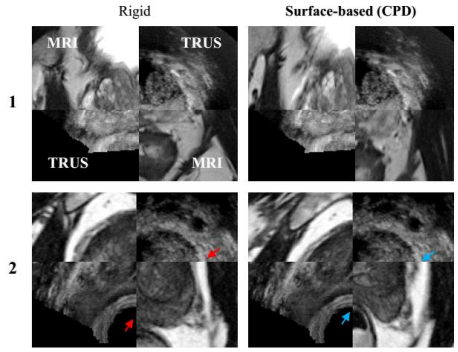

Fig. 3 Surface based elastic algorithm shows better alignment compared to rigid registration in patient data.

The 3D TRUS and ^{68}Ga-PSMA PET-MRI images were acquired as per the method described earlier. The expert performed manual segmentation on MRI and TRUS images for surface extraction and annotated four pairs of anatomical landmarks in each case for the evaluation of registration.

We evaluated our registration method on five patient datasets. The mean LRE for surface based elastic registration was 2.49 mm in comparison to 4.63 mm for rigid registration. The outcome of both registration approaches for two patient cases is shown in Fig. 3.

Exemplary clinical case

After validation of the system, we used it in one multimodal image-guided biopsy. A 65 year-old patient with previous negative biopsy and rising PSA was referred for ^{68}Ga-PSMA PET-MRI examination and follow-up biopsy. In addition to the 10-core systematic biopsy, two targeted biopsy were taken from a suspicious region in the left apical zone under multimodal image guidance.

The histology confirmed significant PCa with a Gleason score of 3 + 4 = 7. The targeted biopsy cores showed the highest percentage (90%) in pathological tissue.

DISCUSSION

The multimodal image guidance shows a value in the detection of significant PCa, especially in men with previous negative biopsy and rising PSA. Though we tried to address some of the challenges in 3D TRUS acquisition and multimodal image registration that can be done online within short time ~5 min, some other issues in the tracking and image registration still need further work. The tracking corruption can be improved by the preprocessing of tracking stream with kalman based estimation. The image based deformation models can improve the registration in comparison with surface based methods.

ACKNOWLEDGMENT

This research is partially supported by the EU 7th Framework Program projects Marie Curie Early Initial Training Network Fellowship (PITN-GA-2011-289355-PicoSEC-MCNet).

REFERENCES

[1] Eiber M., Nekolla S. G., Maurer T., Weirich G., Wester H. J., Schwaiger M. 68Ga-PSMA PET/MR with multimodality image analysis for primary prostate cancer. Abdominal imaging. 2014. 1-3.

[2] Shah A., Zettinig O., Maurer T., Precup C., zu Berge C. S., Weiss J., Frisch B., Navab N. An open source multimodal image-guided prostate biopsy framework. MICCAI Workshop on Clinical Image-based Procedures. LNCS Springer. 2014; 8680.

[3] Lasso A., Heffter T., Rankin A., Pinter C., Ungi T., Fichtinger G. PLUS: Open-source toolkit for ultrasound-guided intervention systems. IEEE Transactions on Biomedical Engineering. 2014; (10) 2527 - 2537.

[4] Sonn G.A., Margolis D.J., Marks L.S. Target detection: Magnetic resonance imaging ultrasound fusion–guided prostate biopsy. Urologic Oncology: Seminars and Original Investigations. Elsevier. 2013.

[5] Sparks, R., Bloch B. N., Feleppa E., Barratt D., Madabhushi A. Fully automated prostate magnetic resonance imaging and transrectal ultrasound fusion via a probabilistic registration metric. SPIE Medical Imaging. 2013 Mar; pp. 86710A - 86710A.

[6] Zettinig O., Shah A., Hennersperger C., Kroll C., Kübler H., Maurer T., Milletari F., Schulte zu Berge C., Storz E., Frisch B., Navab N. Multimodal Image-Guided Prostate Fusion Biopsy based on Automatic Deformable Registration. IPCAI. 2015.

Cognitive Camera Robot for Cognition-Guided Laparoscopic Surgery

M. Wagner[1,*], A. Bihlmaier[2,*], P. Mietkowski[1], S. Bodenstedt[2], S. Speidel[2], H. Wörn[2], B. Müller-Stich[1], H. G. Kenngott[1]

[1]*Department for General, Visceral and Transplantation Surgery, Heidelberg University Hospital, Germany*

[2]*Institute for Anthropomatics and Robotics, Karlsruhe Institute of Technology, Germany*

hannes.kenngott@med.uni-heidelberg.de

* Authors contributed equally

BACKGROUND

An optimal view on the operating field is important for high quality performance in laparoscopic surgery. Nevertheless, due to limited personal resources, inexperienced surgical staff members often perform the camera guidance. Therefore, research into camera robots began over 15 years ago [1]. However, until recently these camera robots were not used in clinical routine due to cumbersome human-machine-interfaces [2]. Up to now camera robots lack real cognitive capabilities. To address this need, we developed a robotic camera assistant that learns how to guide the camera based on the surgeon's preferences and acts as a cognitive surgical assistant (CoSA).

METHODS

With the OpenHELP phantom n=20 laparoscopic rectal resection with total mesorectal excisions were performed [3]. The laparoscopic video as well as the 3D position of the surgical instruments and the laparoscope, obtained with the Polaris® optical tracking system (NDI Inc., Waterloo, Canada), were recorded. Data annotation was performed with the s.w.an-Suite software (SWAN GmbH, Leipzig, Germany). Surgical experts classified the camera guidance quality of the human camera assistant as good, neutral or poor by rating each video frame. Furthermore, all parts of the surgical procedure were classified according to a surgical process model [4] comprising 5 phases and 15 steps. These semantic annotations as well as the 3D coordinate data were linked to each video frame to populate the knowledge base. Synthetic data was computed to provide additional learning examples of poor endoscope positioning for machine learning. This knowledge base was further expanded by using supervised machine learning (Random Forests) to train camera quality classifiers specific for each step [5].

The camera position was constrained by universal surgical requirements such as remote center of motion (respecting the trocar) and smoothness of movement. However, the actual robot movement was controlled solely through the learned camera quality classifiers. No additional movement rules were programmed. Thus, the movement was solely based on the instrument positions, providing flexibility during each step. Also, the different steps of the surgical procedure could be performed in flexible order. The software was developed within the ROS-framework [6].

Exemplarily two surgeons performed the mobilization of the descending hemicolon as a step in rectal resection using the OpenHELP phantom. As robotic platform two different systems were used, ViKY® (EndoControl S.A.S., Grenoble, France) and LWR (KUKA AG, Augsburg, Germany).

RESULTS

Altogether 151,598 video frames and 552,711 3D positions were recorded and semantically annotated. Additionally 154,018,480 synthetic 3D positions were computed. Based on the results of the camera quality classifiers (figure 1), the robot moved the camera to the optimal position in real time. Surgery could be performed by two different surgeons on both robotic platforms (figure 2). The surgeons were able to perform the surgery without any manual corrections in both cases.

CONCLUSIONS

For the first time our knowledge-based approach brought cognitive capabilities to laparoscopic camera robots. Both camera robots assisted the surgeons autonomously, their movement was smooth and the impression of the camera quality was good. A thorough evaluation of the camera guidance based on various subjective and objective criteria is underway.

The software worked independently of the robotic actuator and will be integrated in the framework of the CoSA envisioned in the Collaborative Transregional Research Center *Cognition-Guided Surgery*.

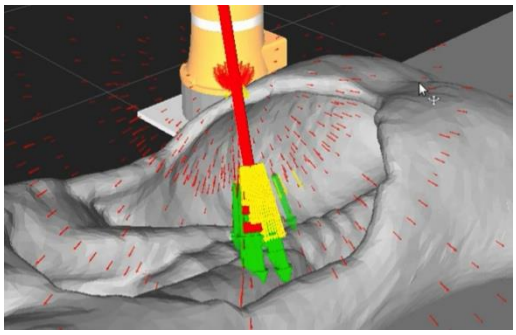

Fig. 1 Visualization of the camera quality classifiers results. Green, yellow and red arrows indicate good, neutral and poor camera positions, respectively.

Fig. 2 Surgeon performing a laparoscopic procedure with a cognitive camera robot based on the KUKA LWR-platform.

ACKNOWLEDGEMENTS

This work was carried out with the support of the German Research Foundation (DFG) as part of projects I05 and A01 in the SFB/TRR 125 Cognition-Guided Surgery.

REFERENCES

[1] Omote, K., et al., *Self-guided robotic camera control for laparoscopic surgery compared with human camera control.* Am J Surg, 1999. 177(4): p. 321-4.

[2] Pandya, A., et al., *A Review of Camera Viewpoint Automation in Robotic and Laparoscopic Surgery.* Robotics, 2014. **3**(3): p. 310-329.

[3] Kenngott, H.G., et al., *OpenHELP (Heidelberg laparoscopy phantom): development of an open-source surgical evaluation and training tool.* Surg Endosc, 2015 Feb 12. [Epub ahead of print].

[4] Lalys, F. and P. Jannin, *Surgical process modelling: a review.* Int J Comput Assist Radiol Surg, 2014. **9**(3): p. 495-511.

[5] Bihlmaier, A and H. Woern, *Automated Endos-copic Camera Guidance: A Knowledge-Based System towards Robot Assisted Surgery.* Proceedings of ISR/Robotics 2014, p.1-6

[6] Quigley, M., et al. *ROS: an open-source Robot Operating System*. in *ICRA workshop on open source software*. 2009.

Motorized 2-DOF Spherical Orienting Mechanism for Laser Micromanipulation in Trans-oral Laser Microsurgeries

N. Deshpande, L. S. Mattos, D. G. Caldwell

Department of Advanced Robotics, Istituto Italiano di Tecnologia, Genova, Italy

nikhil.deshpande@iit.it

INTRODUCTION

In state-of-the-art Trans-oral Laser Microsurgeries (TLM), laser aiming and surgical outcome rely on the skill and dexterity of the surgeon. A manual micromanipulator, consisting of a *beam-splitter* mirror and a small joystick, attached to the surgical microscope, aims the laser beam at the surgical area (the vocal fold, Fig. 1 (left)). Accurate laser aiming is critical in preserving healthy tissue while also removing the pathology. In recent years, motorized laser scanners have offered greater aiming accuracy and efficiency using automated incision patterns [1].

This paper proposes a novel design for motorized laser micromanipulation in TLM, based on a 2 degrees-of-freedom (DOFs) *spherical orienting* device for the beam-splitter mirror itself. The combination of this device with an integrated, computer-assisted surgical system provides precise aiming control and automated intraoperative planning, with dynamic active constraints, making it suitable to clinical applications.

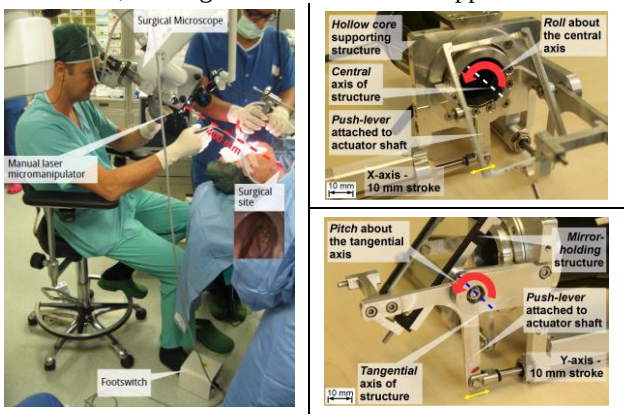

Fig. 1 Left: State-of-the-art TLM setup.
Right: The new micromanipulator – X and Y axes.

MATERIALS AND METHODS

The state-of-the-art TLM has a beam-splitter mirror aligning the beam from the laser focusing optics to the microscope's optical path and reflecting it towards the surgical site (Fig. 1 (left)). The motorized micromanipulator therefore had to allow: (i) compatibility with the laser focusing optics and coupling with the surgical microscope; and (ii) maintaining the surgical line-of-sight through the optical path of the microscope and the mirror. Therefore, the new design was based on actuating the beam-splitter mirror itself (Fig. 2).

New Micromanipulator Design

Two voice-coil linear actuators (SMAC CAL12, 24V, 1.5A) drive a 2-DOF spherical orienting mechanism, where the linear motions are converted into spherical orientations of the mirror (roll + pitch) resulting in 2-DOF motion of the laser at the surgical site (Fig. 2).

1. The design includes a *hollow core supporting* (HC) structure, having two revolute support joints. Their respective axes of rotation pass through the spherical center of rotation of the structure in mutually orthogonal disposition. Two actuation levers are attached to the structure through the revolute joints.
2. The back-n-forth motion of each lever generates a roll and pitch of a *mirror-holding* (MH) structure about the respective rotation axes.
3. For the 'X' axis, the mirror *rolls* about the central axis of MH, while for the 'Y' axis, the mirror *pitches* about the tangential axis of MH.

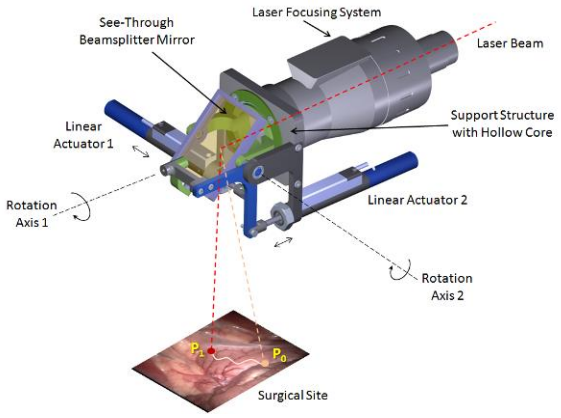

Fig. 2 The new motorized micromanipulator design rendering.

The light-weight linear actuators offer a 10 mm stroke length and a 1 µm encoder resolution. The actuators were sized to provide fast motion of the mechanism without high inertia. The actuators are controlled through a custom-designed motor control board which includes a velocity-based trajectory-control method for the programmable laser trajectories.

Integrated System

The prototype was fabricated and integrated into the surgical system, introduced in [2]. It consists of the following components and features:

1. Motorized laser manipulator: As described above.
2. Input: A graphics stylus with tablet interface for intuitive laser aiming and activation.
3. Visualization: Two HD cameras (Prosilica GT1910) attached to the surgical microscope

acquire stereoscopic video. They are displayed in a modified head-mount display, the *Virtual Microscope*, providing a comfortable and ergonomic visualization of the surgical site.

4. Configuration interface: A touchscreen interface to define types of surgical actions, view messages, and capture important procedural information.
5. Assistive features:
   a. Free-hand aiming and cutting with the laser
   b. Intraoperative planning: Virtual lines and shapes defined for automatic incisions.
   c. Virtual constraints: Virtual go / no-go zones defined to deactivate the laser for safety.
   d. Assistive techniques including optical magnification, and gesture / motion scaling.

System calibration for this new mechanism with the surgical system was adopted from [1].

RESULTS

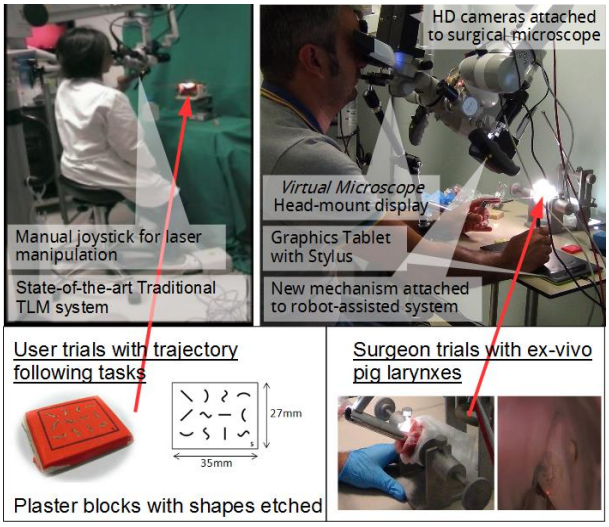

Fig. 3 The experimental setup for user and surgeon trials.

Characterization trials of the new system resulted in the values listed in Table I. The resolution offered by the new system is less than half the smallest laser spot size obtained from the focusing optics (110 µm), allowing for precise laser incisions.

Table I Characterization of the new system

Operating Distance	400 mm
Surgical Range	8640 sq. mm (64 x 135)
Maximum Speed	7.09 m/s
Resolution	12.8 µm (X-axis); 27.0 µm (Y-axis)

User accuracy trials with 10 non-medical subjects were conducted, where each subject traced 6 different randomized shapes (straight lines, S-curves, C-curves), comparing both systems – the traditional manual system and the new design (Fig. 3). The system accuracy was assessed using root-mean-square-error (RMSE) and Maximum Error metrics. The execution times metric provided a measure of the mental workload (Table II). The new design produces a statistically and significantly more accurate performance than the traditional manual system, showing a more than 57% improvement. The new design, in combination with the computer-assisted system, offers superior performance.

Table II Comparison of Accuracy Metrics

	Traditional System	New System
RMSE (mm)	0.3508 ± 0.1756	**0.1499 ± 0.0665**
Max. Error (mm)	1.5358 ± 0.8501	**0.4444 ± 0.1798**
Times (sec)	14.4031 ± 7.5778	**10.7226 ± 2.3306**

These results indicate that the new system reduces complexity from the user's perspective and its uniform and consistent integration into the surgical procedure could lead to its successful clinical acceptance.

Ex-vivo trials were conducted with 3 expert surgeons performing near-real surgical tasks (incisions and ablations) on pig larynxes. The surgeons were also encouraged to use the regular surgical instruments, e.g., forceps that are part of the surgery in the operating room (OR). The following qualitative feedback was received from the surgeons:

1. The mechanism allows a larger operating distance and surgical range, providing easier passage and maneuvering of surgical instruments.
2. The smooth control and accurate motion of the laser using the graphics tablet improves the cut quality and reduces carbonization. It is intuitive and easy to use.
3. The intraoperative planning mode is useful for quick and precise cuts. The ability to perform long incisions and spot ablations automatically is very useful.

DISCUSSION

An earlier prototype by the authors was based on a fast steering mirror (FSM) which allowed faster scans (10 m/s) and greater resolution (4 µm) , but had to be placed between the focusing optics and the beam-splitter mirror [1]. Additionally, the small diameter of the FSM, the allowable focal distance, and the type of focusing optics were important limitations in that design. These served as motivation for this new design based on motorizing the beam splitter mirror itself. The spherical orienting mechanism overcomes the earlier limitations, and offers a maximum speed of 7 m/s and a functional resolution between 12.8 and 27 µm, comparable to the FSM system [1]. It achieves greater than 57% improvement in accuracy indicating that the mechanism can greatly improve surgical safety, and comparing favorably to the FSM prototype (around 69%, [1]). The new system was evaluated positively in ex-vivo trials with expert surgeons pointing to its suitability in the OR.

REFERENCES

[1] L. Mattos, M. Dellepiane, and D. Caldwell, "Next-Generation Micromanipulator for Computer-Assisted Laser Phonomicrosurgery," in 33rd IEEE EMBS 2011, pp. 4555–4559.

[2] N Deshpande, J Ortiz, DG Caldwell, LS Mattos, "Enhanced Computer-Assisted Laser Microsurgeries with a "Virtual Microscope" based surgical system," in IEEE ICRA 2014, pp. 4194–4199.

Robust, Low-cost, Modular mm-scale Distal Force Sensors for Flexible Robotic Platforms

J. Gafford[1,2], R. Wood[1,2], C. Walsh[1,2]

[1]*Harvard School of Engineering and Applied Sciences, Cambridge, MA, USA*

[2]*Wyss Institute for Biologically-Inspired Engineering, Boston, MA, USA*

INTRODUCTION

Innovation in surgical robotics has seen a shift away from traditional rigid systems (such as Intuitive Surgical's *daVinci*^{TM} platform) towards flexible systems that can access remote locations inside the body. However, the flexible nature of these delivery systems, coupled with a lack of haptic feedback, could result in the application of unregulated forces that could damage or perforate tissue in delicate intraluminal spaces.

Several groups have recognized the need for distal force sensing in flexible surgical tools and robotics [1, 2]. However, a general reliance on conventional fabrication techniques ultimately limits the complexity and sophistication of distal implementations of such sensor systems, and poses a barrier to further innovation and widespread adoption. Herein we present a mm-scale force sensor manufactured using a composite lamination fabrication process, wherein linkages pre-machined in the laminate provide the required degrees-of-freedom and fold patterns to facilitate self-assembly. Using purely 2-dimensional batch fabrication techniques, energy contained within a planar elastic biasing element directly integrated into the laminate is released post-fabrication, allowing the sensor to `self-assemble' into its final 3-dimensional shape. The geometry of the sensor was selected based on size constraints inherent in minimally-invasive surgery, as well as with specific focus on optimizing the sensor's linearity. The sensor is unique from fiber-based force sensors in that the emitter and the detector are encapsulated within the sensor itself, allowing it to be retrofitted onto existing tools.

MATERIALS AND METHODS

The sensor operates by the principle of *light intensity modulation (LIM)*, a transduction method which has already been FDA-approved (St. Jude Medical's *TactiCath* force-sensing ablation catheter). The principle works as such: a light-emitting source (infrared LED) is separated from a detector (infrared phototransistor) by some distance as determined by an elastic mechanism. As a force is applied, the elastic mechanism deforms, bringing the source closer to the detector. By measuring the output current of the detector, the input force can be determined.

Up until now, due to difficulties in manufacturing and assembly of the requisite components, this modality has been practically realized by transmitting the light from a proximal source through optical fibers to the distal end of the tool where the force is being applied [3, 4]. Other light-based approaches (Fabry-Perot interferometry, fiber-Bragg gratings) also require optical fiber transmission as well as expensive interrogation hardware [5, 6]. The drawback of fiber-based approaches is that the tool must be designed 'around' the optical fibers and, as such, is not a modular solution.

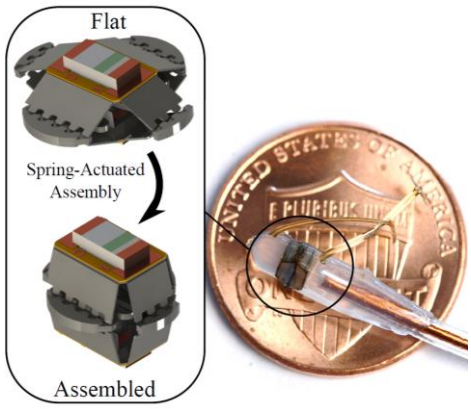

Fig. 1 Image of force sensor molded onto a 6F mock catheter, where the detail shows the sensor self-assembling as a result of a pre-stressed biasing spring contained within.

We have designed, fabricated and tested a modular LIM force sensor (see Fig. 1) that fully contains the emitter and detector and is compliant with the strict size requirements of endoscopic working ports (2.8mm OD). Using a manufacturing process based on printed circuit board fabrication, several layers of structural (304 Stainless Steel), flexible (Kapton polyimide), adhesive (DuPont FR1500 acrylic adhesive), and conductive (copper) material were laser-machined and laminated together. A pre-stretched spring (a) provides a restoring force that causes the sensor to 'self-assemble', much like a pop-up book, (b) serves as the elastic mechanism which deforms upon force application, and (c) serves as a grating which allows more light through as the spring is expanded to increase sensitivity. Fig. 2 shows an overview of the manufacturing process.

RESULTS

The sensor was calibrated using a reference load cell to generate the calibration curve shown in Fig. 3. The sensor exhibits linearity over 0-100mN range, after which, an exponential relationship more accurately describes sensor behavior. The calibrated behavior closely matches the predicted behavior based on a simple point-source emitter model. The sensor exhibits sub-mN resolution which was quantified by integrating the power spectral density of the sensor output given no

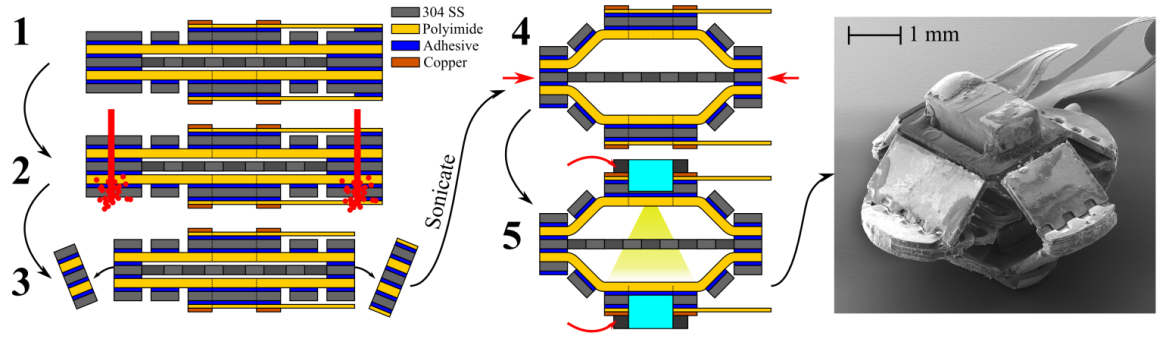

Fig. 2 Manufacturing process used to fabricate self assembling sensor: (1) multiple individually-machined layers of material are laminated to form a composite, (2) release cuts are made using a laser, (3) the alignment scaffold is discarded, (4) the sensor is submerged in an ultrasonic bath which causes assembly spring to retract and assemble the sensor, (5) pick-and-place components are reflow soldered to complete assembly. A scanning-electron microscopic (SEM) image shows sensor detail.

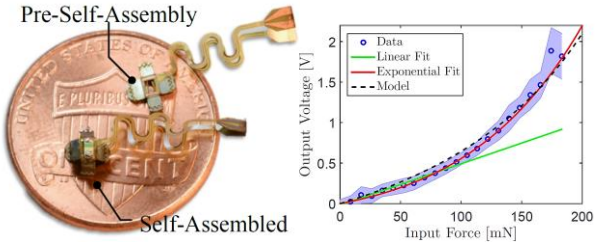

Fig. 3 *(left)* fabricated sensors, both pre- and post-assembly, *(right)* sensor calibration curve, compared with a linear and exponential fit, as well as a comparison with the deterministic model based on the optoelectronic properties of the system.

Table 1 Sensor Specifications

Parameter	Value	Unit	% FS
Sensitivity (0-100 mN)	5.0	V/N	N/A
Range	0-200	mN	N/A
Resolution	0.8	mN RMS	0.4
R^2 (Exponential)	0.99	N/A	N/A
R^2 (Linear, 0-100 mN)	0.97	N/A	N/A

input stimuli. The sensor's sensitivity can be controlled by selecting the appropriate thickness of the spring layer, and also by encapsulating the sensor in various polymers or rubbers which are IR-transparent. Sensor specifications are given in Table 1.

The sensor's efficacy was determined *in vitro* by encapsulating the sensor in silicone rubber, integrating the sensor onto the distal end of a 6F catheter and performing a palpation task on a block of silicone rubber (EcoFlex 00-50, Smooth-On) through a tortuous GI tract analog (rubber tubing bent at a 180-degree angle). A reference load cell measures the insertion force (a combination of the palpation force and frictional forces). The results are shown in Fig. 4. The distal sensor is necessary to discriminate distal forces at the proximal end due to friction in the system and other sources of contamination.

DISCUSSION

The results presented herein indicate a promising solution to developing robust, low-cost, modular, millimeter-sized force sensors with the resolution necessary for delicate MIS surgical interventions. Preliminary calibration tests have shown that the sensor

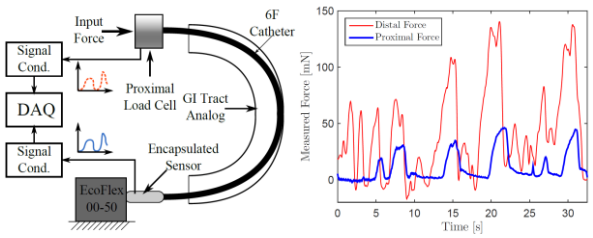

Fig. 4 In-vitro palpation test, showing a significant discrepancy between the haptic force surgeon-side and the distal force measured by the sensor.

can detect sub-mN forces over a range of 0-200 mN. An *in vitro* palpation simulation showed that the sensor has the sensitivity necessary to extract ~mN-level distal forces from an otherwise contaminated haptic profile, indicating the need for distal sensing modalities for obtaining accurate information from the tool-tissue interface. Future work will focus on optimizing the sensor design, improving methods of encapsulation and integration, and investigating multi-axis capabilities.

REFERENCES

[1] Y. Noh, E. Secco, S. Sareh, H. Wurdemann, A. Faragasso, J. Back, H. Liu, E. Sklar and K. Althoefer, "A Continuum Body Force Sensor Designed for Flexible Surgical Robotics Devices," in IEEE EMBS, Chicago, IL, 2014.

[2] S. Kesner and R. Howe, "Force Control of Flexible Catheter Robots for Beating Heart Surgery," in IEEE ICRA, Shanghai, China, 2011.

[3] P. Polygerinos, T. Schaeffter, L. Seneveratne and K. Althoefer, "A Fibre-Optic Catheter-Tip Force Sensor with MRI Compatibility: A Feasibility Study," in IEEE EMBS, Minneapolis, MN, 2009.

[4] P. Puangmali, H. Liu, L. Seneviratne, P. Dasgupta and K. Althoefer, "Miniature 3-Axis distal Force Sensor for Minimally Invasive Surgical Palpation," IEEE/ASME Transactions on Mechatronics, 2012.

[5] Z. Sun, M. Balicki, J. Kang, J. Handa, R. Taylor and I. Iordachita, "Development and Preliminary Data of Novel Integrated Optical Micro-Force Sensing Tools for Retinal Microsurgery," in IEEE International Conference on Robotics and Automation, Kobe.

[6] H. Song, K. Kim and J. Lee, "Development of optical fiber Bragg grating force-reflection sensor system of medical application for safe minimally invasive robotic surgery," Review of Scientific Instruments, vol. 82, 2011.

Micro-IGES Robot for Transanal Robotic Microsurgery

H. H. King, J. Shang, J. Liu, C. Seneci, P. Wisanuvej, P. Giataganas, N. Patel, J. Clark, V. Vitiello, C. Bergeles, P. Pratt, A. Di Marco, K. Kerr, A. Darzi, G.-Z. Yang

The Hamlyn Center for Robotic Surgery, IGHI, Imperial College London, UK

hawkeye.king@imperial.ac.uk

INTRODUCTION

Colorectal cancer is the third most common cancer for both men and women, and second leading cause of cancer death [1]. Traditional surgical treatment required complete anterior resection, i.e., removal of the lower rectum. Advances in endoscopic surgery allow local excision of rectal adenomas and early stage carcinomas through a transanal approach [2-4]. This is a technically demanding procedure since the surgeon must operate via the narrow opening of the anus; sometimes to a depth of 18cm or more.

The aim of the present work is to lower the technical barriers to surgeons' adoption of transanal excision. The solution is to perform the operation telerobotically. This delivers better visualization, access, and control of instruments to the surgeon. A previous study used a full daVinci robot [5], which has poor operating workspace, and form factor for transanal operation. This paper describes a robot specially designed to target this procedure.

The Micro-IGES (Microscopic Image Guided Endoluminal Surgery) robotic surgical system has been developed to perform transanal excision under teleoperative surgeon control. The high dexterity wristed 7-DoF (Degrees-of-Freedom) tools give the surgeon robust manipulation capabilities. System design is related to other snake-like systems, but to the authors' knowledge this is the first system designed and tested for colorectal surgery.

The remainder of this short paper introduces the Micro-IGES system and presents results from pre-clinical in-vivo and in-vitro tests.

SYSTEM DESIGN

Mechatronics - Seven DoF tools provide Cartesian position/orientation and grasping capability. Tools are 28cm long with 5mm diameter. Insertion along major axis of the rectum uses a rack and pinion mechanism. A rotational joint rotates the gripper-and-tool shaft. Lateral position of the end effector uses two snake-like joints with two segments each. A 3-DoF end effector provides two degrees of orientation plus grasping. Stainless steel cables transmit mechanical power from motor capstans to the tool end effector. Rack and pinion system is direct drive and tools ride on a rail mount so that they can slide in and out.

Actuation for the mechanism uses an "actuation pack" attached to the external end of the tool. It houses seven 13mm Maxon brushless motors with 67:1 gear ratios and quadrature encoders sensing 250 counts/rev. It uses custom designed, small form factor motor controllers that communicate with the host PC through a shared RS-485 bus. Motor controllers run a PID control loop to achieve a target motor angle (encoder count) specified by the host. Each pack also houses a cooling fan and DC/DC converter.

Robot Control - Robot is controlled from a standard Linux PC with PCIe RS-485 card. Eight mega-baud bandwidth provides 180-250 Hz input/output rate with fourteen motor controllers. Master-slave control uses direct joint mapping for insertion, tool roll, and wrist axes. A rotational transform ensures that up/down and left/right motions are preserved throughout tool rotation. Motion scaling is applied to tool translation.

Surgical master comprises two Force Dimension Omega.7 haptic devices and a footpedal. No force feedback is provided to the surgeon. Visual feedback is from an Olympus steerable 3D stereo endoscope.

Surgical Site Access - Transanal surgery requires access to and insufflation of the rectum. The Micro-IGES uses a port with four insertion points for a camera, two robotic tools, and a third robotic or manual tool. The robot mounts directly to the port. Both are held by a support arm. Pneumorectum is maintained by an airtight silicon gasket. The seal was able to maintain pressure of 20mm Hg with minimal leakage.

The supporting arm is a 6-DoF passive actuated serial link arm. Each of the six degrees of freedom is equipped with a brake and are together capable of holding up to 5Kg. A momentary pushbutton switch disables brakes and allows the surgeon to manually reposition the arm. Releasing the button engages the brakes, freezing the arm's configuration.

Fig. 1 Micro-IGES system CAD rendering.

Fig. 2 Surgical master station. Video shows rectal wall tissue under tension.

Operating Theatre Integration - The entire system was designed for use with medical equipment necessary for clinical use. A Karl Storz Electronic Insufflator connected to the port provides CO_2 insufflation. The surgical area can be ventilated through valves attached to the port; this is sometimes necessary to clear smoke from electrical diathermy operation. An Erbe VIO 200D powers the diathermy tool. Suction/irrigation can be applied through an integrated lumen in the robotic diathermy tool or using an additional, manual tool inserted through the fourth insertion point in the port.

Altogether this comprises a nontrivial OR footprint. However, the space requirements are still less than other commercial surgical robotic systems; much of the equipment is already present during conventional non-robotic operation; and the system was tested in theatre and proved it could be accommodated.

EVALUATION STUDIES

Benchtop testing - Initial testing of the system in benchtop dexterity tests showed capabilities for environment manipulation and suturing.

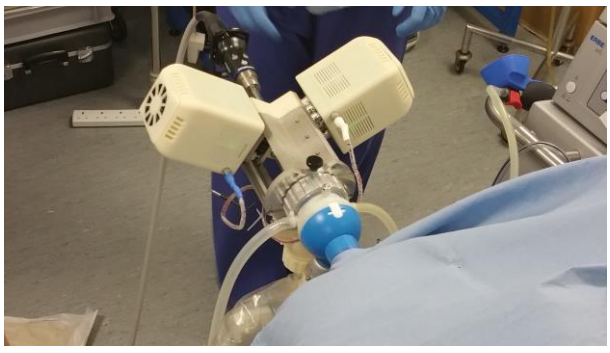

Fig. 3 In operating theater ready to operate on draped porcine patient. Shown are airtight port, tool mounting rails, actuation pack, and endoscope. Insufflation attachment at sides.

Fig. 4 Full thickness resection of rectal wall showing (left to right, top to bottom) preoperative rectum, circumferential marking with diathermy, resection under tension (2), and completed full thickness resection.

Suturing was carried out on a tissue phantom suturing pad. Using just the robot and endoscopic visual feedback two sutures were tied in twenty minutes. These were the first and second knots tied by the system.

In-vivo testing - The complete clinical system was deployed in animal theatre and a simulated tumor excision was performed. The TEMS clinical procedure protocol was followed, summarized as:

- Patient received general anesthesia;
- Patient positioned and draped;
- Insertion of port using obturator and positioned with positioning arm;
- Insertion of endoscope and robotic instruments;
- Circumference to be excised is marked with diathermy;
- Full thickness excision performed using grasper and diathermy;
- Removal of tools and scope;

The robot under surgeon control proved capable of excision of a simulated rectal wall tumor. Closure was not carried out.

DISCUSSION AND FUTURE WORK

The robot has proven capable of tumor excision and suturing. Work still remains to improve control so robot motion is more natural and easy for the surgeon.

ACKNOWLEDGEMENT

This work is supported by a Health Innovation Challenge Fund Award (HICF-T4-299) from the Wellcome Trust and the Department of Health.

REFERENCES

[1] Cancer Research UK (2014). Cancer Statistics Report: Cancer Incidence in the UK in 2011.

[2] MacFarlane, J. K. et al., "Mesorectal excision for rectal cancer." *The lancet*, 341.8843 (1993): 457-460.

[3] M. Ragupathi, E.M. Haas., "Transanal endoscopic video-assisted excision: application of single-port access." *J. Soc. Laparoendoscopic Surg.* 15.1 (2011): 53.

[4] Buess, G., et al. "Technique of transanal endoscopic microsurgery." *Surgical Endoscopy* 2.2 (1988): 71-75.

[5] Atallah, S., et al. "Robotic-assisted transanal surgery for total mesorectal excision (RATS-TME): a description of a novel surgical approach with video demonstration " *Techniques in Coloproctology* 17.4 (2013): 441-447.

Beware Credentialing Based on Fundamentals of Laparoscopy "The Eyes are Open, The Hands Move, But the Prefrontal Brain Has Not Departed"

K. Shetty, D. R. Leff, G.-Z. Yang, A. Darzi

Hamlyn Centre for Robotic Surgery, IGHI, Imperial College London, UK

d.leff@imperial.ac.uk

BACKGROUND

The Fundamentals of Laparoscopic Surgery (FLS)[1] is a training programme designed to equip residents with the requisite knowledge and technical skills to perform Laparoscopic Surgery (LS). Since FLS is a mandatory criterion for general surgery board certification in the United States, it sets the standard in an era when surgeons are increasingly expected to have documented evidence of competency. Clearly, if a surgeon fails the FLS test is it unlikely that he or she has acquired the necessary 'fundamentals' for safe LS performance, but what about those who pass the test? What does reaching expert-derived benchmarks say about one's level of familiarity with the skill or more specifically the degree to which the technique has been engrained? The prefrontal cortex (PFC) is a brain region known to be associated with attention and concentration and an area hypothesized to attenuate in-line with increasing technical skills acquisition and hence a useful surrogate for magnitude of task internalization[2-5].

METHODS

45 subjects of varying surgical experience were investigated using a 44-channel Optical Topography (OT) device (ETG-4000, Hitachi Medical Corp) to monitor changes in prefrontal responses during a laparoscopic suturing drill. To characterize frontal brain behaviour over the time of course from early learning to automation both cross-sectional and longitudinal studies were conducted as follows: (a) a cross-sectional study compared PFC excitation in 35 surgeons (novices with 2h training: n=12; registrars/residents: post-graduate year (PGY) 3-5, n=12; expert laparoscopists: n=11), and (b) a longitudinal study tracked changes in PFC responses across four time points as a second cohort of novices (n= 13) acquired suturing skills across a week of practice (8 hours). Laparoscopic suturing skill was objectively evaluated using the FLS framework (time, penalties, etc). Cortical haemodynamic data was analysed using a region of interest analysis (ROI).

RESULTS

Laparoscopic Technical Skills

Superior technical performance was observed in experts compared to residents (median FLS scores ± IQR: experts = 487±53, residents = 400±90, Mann-Whitney-U $p \leq 0.010$), who in turn outperformed novices (2 hours training=316±74, Mann-Whitney-U $p<0.001$). Deliberate practice led to significant improvements in technical performance (median FLS scores ± IQR: initial session (2 hours training = 302±128, mid session (5 hours training = 421±86, final session 8 hours training =471 ± 40, Friedman $p<0.001$) followed by skill stabilization when assessed at retention (1 month after cessation of practice = 468±56,Wilcoxon-Sign-rank p=0.808). At practice termination, technical skills amongst experts and trained novices could not be differentiated (p=0.014), based on a statistical threshold following Bonferroni correction $p<0.008$.

Cortical Brain Function

An inverse relationship was observed between the grade of the surgeon and PFC excitation [ΔHbO_2 (μM x cm) median ± IQR: novices = 10.19±21.75, residents = 7.46± 12.57, experts = 1.56±11.37, $p \leq 0.001$]. However, despite progression toward near expert levels of suturing skill, additional training failed to lead to progressive PFC attenuation [ΔHbO_2 (μM x cm) median ± IQR: initial = 8.08±19.95, mid = 7.67±21.12, final = 7.77±17.91; retention = 8.88±19.92, p=0.065]. As illustrated in Figure 1, at practice termination, suturing evoked a response that was on average four to five times greater among trained novices than expert laparoscopists, despite similarities in suturing skill.

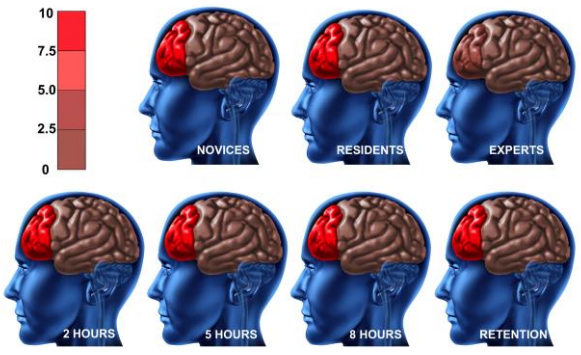

Fig. 1 Graphical illustration depicting the disparity in PFC activation associated with expertise (top row) and lack of progressive PFC attenuation associated with a week of practice (bottom row). Group median value (μM x cm) for intensity of activation is depicted on a colorimetric scale.

CONCLUSION

FLS proficiency criteria based on experts' motor behaviour or technical skill such as time and accuracy reflect a one-dimensional performance assessment. Current data suggests that despite attaining these benchmarks, trainees need significantly more attention and concentration than experts, and hence may not have internalized or automated the task.

REFERENCES

[1] Society of Gastrointestinal and Endoscopic Surgeon. FLS program hits new milestone 2015. Available at: http://www.sages.org/

[2] Dayan E, Cohen LG. Neuroplasticity subserving motor skill learning. Neuron 2011; 72(3):443-54.

[3] Leff DR, Elwell CE, Orihuela-Espina F, Atallah L, Delpy DT, Darzi AW, Yang GZ. Changes in prefrontal cortical behaviour depend upon familiarity on a bimanual co-ordination task: an fNIRS study. Neuroimage 2008; 39(2):805-13.

[4] Ohuchida K, Kenmotsu H, Yamamoto A, et al. The frontal cortex is activated during learning of endoscopic procedures. Surg Endosc 2009; 23(10):2296-301.

[5] Leff DR, Orihuela-Espina F, Atallah L, et al. Functional prefrontal reorganization accompanies learning-associated refinements in surgery: a manifold embedding approach. Comput Aided Surg 2008; 13(6):325-39.

Experimental Comparison of Force Feedback vs Tactile Sensory Substitution for Suture Tension Perception

A. Spiers[1], S. Baillie[2], C. Roke[3], A. Pipe[3]

[1]*Dept. Mechanical Engineering, Yale University, USA*

[2]*School of Veterinary Sciences, University of Bristol, UK*

[3]*Bristol Robotics Laboratory, University of the West of England, UK*

adam.spiers@yale.edu

INTRODUCTION

Suturing is an essential part of surgical procedures, yet tension regulation is difficult when using tele-operator systems [1]. Incorrect tension application can lead to various complications. It has been suggested that the use of haptic feedback to allow tension perception would reduce such errors [1]. Many groups have highlighted the benefit of haptic feedback in robot assisted minimally invasive surgery (RMIS) and bi-lateral, kinesthetic 'force feedback' solutions have been proposed. However, instability issues have prevented such solutions from reaching clinical implementation [2]. An alternative to bi-lateral force feedback is the use of sensory substitution to represent haptic information to the surgeon without influencing system stability [1][2]. Examples of sensory substitution include visual and vibrotactile feedback, though it has been suggested that such techniques, which do not represent forces by natural methods and/or channels, may lead to higher cognitive loading [2]. In our work, the use of fingertip surface deformation (also known as tactile skin stretch) is considered as a method of representing tangential (shear) and normal (indenting) interaction forces through a natural haptic feedback method. Skin stretch feedback avoids the controller instability issues of bi-lateral force feedback and may be achieved via relatively simple, compact and low cost technology [2].

In this work we investigate the capability of tactile skin stretch feedback (SSF) to aid novice participants in perceiving the tension of simulated sutures during a 'grasp and pull' task. The experiment is also conducted with force feedback (FF) and combinations of FF and SSF to permit comparative evaluation between feedback modalities and changes in perceptual capability.

MATERIALS AND METHODS

To investigate user 'tension perception capability' related to the SSF and FF haptic modalities under investigation, a novel multi-modal haptic interface (Fig. 1) was combined with classic experimental methods of psychophysics. In the study, participants used the haptic interface to 'grab and pull' virtual suture threads, as if they were performing the last stages of tying a knot or pulling the thread through tissue. The study method was based on the classic psychophysics '*Method of Limits*' protocol [3] and had ethical approval from the University of Bristol (application 4201).

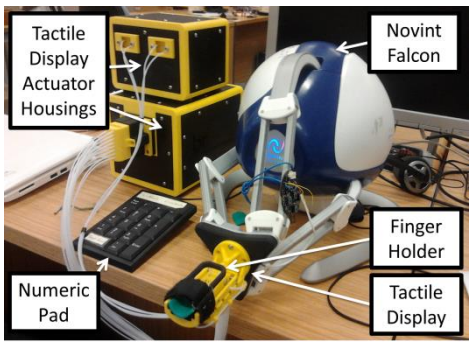

Fig. 1: Novint Falcon and Tactile Display used in this study.

By this method, in each trial, two virtual suture threads were presented to the participants, via display on a computer monitor. By moving the haptic interface with their finger, participants manipulated an on-screen cursor to 'grab' virtual objects attached to the end of the suture threads and laterally 'pull' the objects and threads towards themselves. The goal was to manipulate both threads and use the presented haptic feedback to determine the relative tension of a green, *comparison* thread to a red, *reference* thread. The participant selected *greater* or *less* using labelled buttons on a numeric pad. The red thread had a constant reference tension of 4N. The green thread began each trial either high (7, 7.5 or 8N) or low (0, 0.5 or 1N) and increased or decreased accordingly in 0.5N increments. For more details on the *Method of Limits* protocol see [3].

Facilitating realistic two finger suture thread grasping motions and the tactile sensations of thin-diameter thread is technically difficult in a multi-modal (FF and SSF) haptic interface and beyond the scope of this investigation. As such, large wedge shaped objects (Fig. 2) were implemented to facilitate grabbing the thread. The following description of objects, motions and forces is represented in Fig. 2. The threads were biased with different tensions T, which acted in opposition to the pulling force of the user F_P. Motion of the object and thread, X (constrained to one dimension and direction) would only occur if $F_P > T$. In addition, a downwards force F_G was required to 'grab' the thread (via the connected wedge object). As a user exerted F_P and F_G, opposing reaction forces F_{PR} and F_{GR}, were calculated. Both reaction forces could be rendered by SSF and / or FF haptic feedback modalities. They were therefore felt by the user via the *Tactile Display* and / or *Novint Falcon* haptic device respectively. The tactile display features a 4×4 variable height tactile pin array mounted

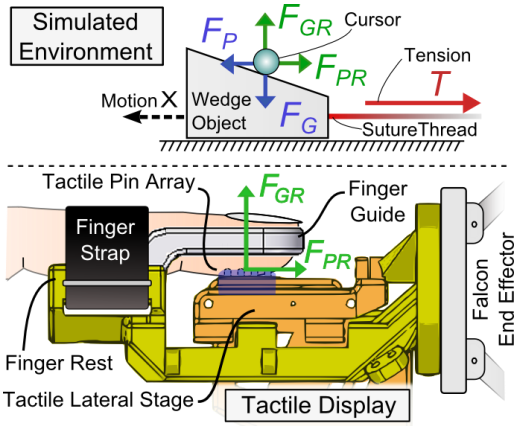

Fig. 2: Simulated environment and tactile display. Reaction forces (F_{PR}, F_{GR}) may be rendered by tactile display or Falcon

on an actuated 'lateral stage' to permit the generation of skin stretch sensations both normal and lateral to the user's finger pad. In this work lateral deformation is proportional to the suture pulling reaction force F_{PR}, while the height of the pins, which are actuated as a whole in this study, are proportional to the grasping reaction force F_{GR} (both via a 0.32mm/N ratio). Such indenting and shearing finger pad deformations are present in natural, every day interactions with real world objects in proportion to exerted forces [2]. Details of the tactile display are shown in Fig. 2, with more information available in [4]. F_{PR} and F_{GR} can also be represented, directly as kinesthetic forces, by the *Novint Falcon* haptic device. The tactile display is attached to the end effector of the Falcon (Fig. 1). To maintain constant position between the user's finger pad and tactile stimulus, the second phalanx of the user's dominant index finger is strapped to a finger rest with the distal phalanx held in place by a finger guide, available in various sizes. To keep the system lightweight and easy to move, the tactile display is remotely actuated via Bowden cables (Fig. 1). In order to compare the effect of different stimulus rendering, four feedback modalities (A-D) were presented to users:

	FF	SSF
A – Force	F_{PR} & F_{GR}	–
B – Tactile	–	F_{PR} & F_{GR}
C – Combined	F_{PR} & F_{GR}	F_{PR} & F_{GR}
D – Hybrid	F_{GR}	F_{PR}

For each feedback modality, 8 (random and balanced) sequences of comparison stimuli (trials) were completed per participant. Familiarisation with comparison tensions of 0N and 8N was completed before the study.

RESULTS

11 participants (9 male, ages 23-45) took part in the study and completed several feedback modalities each. Modes A and C both had 7 completed trials while modes B and D had 6. Combined psychometric functions [3] were generated for each modality by combining the results of all individual trials for that modality. These combined functions are presented in Fig. 3. In this figure, steeper gradients around 4N (the reference stimulus) indicate a greater sensitivity of

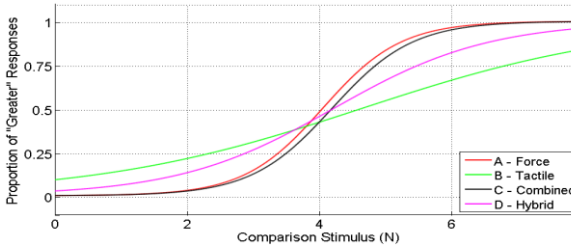

Fig. 3 - Combined Pyschometric Functions.

participants to a change in stimulus. It may be seen that the force feedback modalities A and C provide better perception of tension. B and D, which both used skin stretch feedback for representing F_{PR} (and therefore tension) provided relatively reduced sensitivity, though D (the hybrid mode) is superior to B (SSF only). These results are numerically presented in the following table, which illustrates Point of Subjective Equality (PSE – where two tensions appear equal), Just Noticeable Difference (JND – the smallest change in tension that may be reliably detected) and Weber Fraction (stimulus change that can be reliably detected) for all modalities. Two tailed t-test comparisons for individual participants found statistically significant ($p<0.02$) differences in JND and WF between modalities A & B and B & D.

	Force	Tactile	Combined	Hybrid
PSE(N)	4.032	4.592	4.176	4.184
JND(N)	0.656	2.32	0.672	1.304
WF (%)	16.4	55.8	16.8	32.6

DISCUSSION

The results indicated superior tension perception for force feedback (A) compared to skin stretch feedback (B). However, FF stability is presently too unreliable for commercial RMIS, despite considerable research efforts [2]. Combining SSF with FF (C) had little effect on FF only (A) results. SSF alone (B) led to relatively poor perception but the *hybrid* mode (D) significantly improved perception over B ($p<0.02$). In D, F_{PR}, which related to tension, was displayed by SSF, while FF represented only the grasping force, F_{GR}. More reliable grasping via FF improved SSF tension perception. Although our study used an abstracted component of suturing, it seems that SSF has potential, especially when compared to the current clinical standard of no haptics in RMIS.

REFERENCES

[1] B. T. Bethea, A. M. Okamura, M. Kitagawa, and D. D. Yuh, "Application of Haptic Feedback to Robotic Surgery," *J. Laparoendosc. Adv. Surg. Tech.*, vol. 14, no. 3, pp. 191–195, 2005.

[2] S. Schorr, Z. Quek, and R. Romano, "Sensory substitution via cutaneous skin stretch feedback," *ICRA*, pp. 2333–2338, 2013.

[3] G. A. Gescheider, *Psychophysics: The Fundamentals*, vol. 435. 1997, p. 435.

[4] C. Roke, A. Spiers, T. Pipe, and C. Melhuish, "The effects of laterotactile information on lump localization through a teletaction system," *2013 World Haptics Conf.*, pp. 365–370, Apr. 2013.

Development of a High-Fidelity Pediatric Cleft Palate Phantom and Feasibility Testing using a da Vinci ® Surgical System

D. Podolsky[1,2], D. Fisher[2], K. Wong[2], T. Looi[1], R. Patel[4], J. Drake[1,3], C. Forrest[1,2]

[1]Center for Image Guided Innovation and Therapeutic Intervention, The Hospital for Sick Children, Canada

[2]Department of Plastic and Reconstructive Surgery, University of Toronto, Canada

[3]Department of Neurosurgery, University of Toronto, Canada

[4]Canadian Surgical Technologies & Advanced Robotics, University of Western Ontario

dale.podolsky@mail.utoronto.ca

INTRODUCTION

Cleft palate is the most common congenital defect and requires surgical repair between 6-12 months of age to ensure proper speech development [1]. Surgical repair of a cleft palate is a challenging procedure due to the small confines of the infant oral cavity, and the delicate tissue handling and dissection required [2-4]. Access, visualization, instrument manipulation, ergonomic factors and teaching opportunities are all limited during the procedure.

Previously described cleft palate simulators are very low fidelity and do not incorporate the majority of the relevant anatomy [2-4]. We propose developing a high-fidelity cleft palate phantom for training purposes.

In addition, the surgical approaches used in cleft palate repair have remained unchanged over the last century [5]. The limited access, space and delicate tissue handling make cleft palate surgery an ideal candidate for robotic application.

MATERIALS AND METHODS

Cleft Palate Phantom Development

A high-fidelity cleft palate phantom (patent pending 62/100150 and 62/118306) was developed from a normal infant computed tomography (CT) scan. A three-dimensional (3D) representation of the palate, the relevant components of the cranial base and the oral cavity were segmented from the CT. A bony cleft was created using 3D modeling software. Computer animation software was utilized to develop the detailed musculature of the palate based off the anatomy in the literature [6] and discussion with expert cleft palate surgeons. The bony palate and molds of the muscles and oral cavity were created with a Makerbot® Replicator™ 2 (Makerbot Industries, New York, United States) 3D printer. The musculature and oral cavity were casted with silicone. The musculature, bony component and mucosa were assembled using medical grade adhesive. The model was developed with a cartridge that can be replaced after each use.

Three staff surgeons and two fellows in Plastic and Reconstructive Surgery performed a von Langenbeck cleft palate repair using standard surgical instruments on the phantom model.

Robotic Testing

The feasibility of utilizing the da Vinci® Surgical System to perform a cleft palate repair using the phantom was conducted. Testing was performed using a first generation da Vinci ® Surgical System with 5 mm Endowrist® instruments at the Canadian Surgical Technologies & Advanced Robotics Center (CSTAR) at the University of Western Ontario.

RESULTS

Phantom Model

The complete cleft palate phantom model can be seen in Fig. 1 and Fig. 2 with the specific features described in Table 1. The three staff surgeons and two fellows reported the model replicated the critical components of cleft palate repair in a realistic fashion. The surgeons were successful in 1) creating lateral relaxing incisions, 2) elevating mucoperiosteal flaps, 3) exposing the pedicle, 4) exposing the posterior cleft margin (Fig. 3A), 5) releasing the palatopharyngeus from the cleft margin (Fig. 3A), 6) release of the palatopharyngeus from anterior fibers of the tensor muscle, 7) exposure of the levator muscle travelling through the levator tunnel, 8) suturing the nasal mucosa (Fig. 3B), 9) suturing the levator muscles together, and 10) suturing the oral mucosa together.

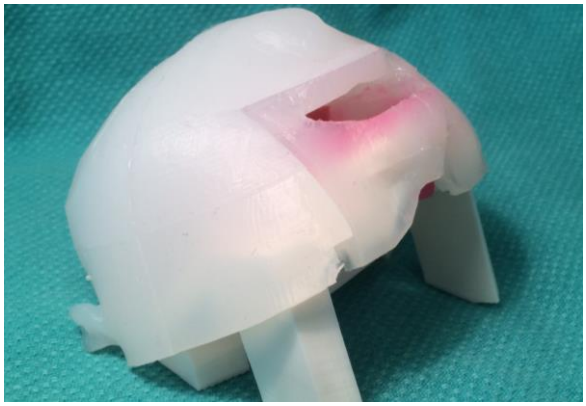

Fig 1. Perspective view of cleft palate phantom.

Table 1. Muscles, bony landmarks and oropharyngeal structures incorporated into cleft palate phantom.

Muscles	Bony Landmarks	Oropharyngeal structures
Superior constrictor Levator veli palatini Tensor veli palatini -Anterior fibers -Aponeurosis Palatopharyngeus -Oral head -Nasal head Palatoglossus	Foramen magnum Foramen lacerum Foramen ovale Foramen spinosum Carotid canal Levator origin Tensor origin Hamulus Greater palatine foramen	Soft palate mucosa Hard palate mucosa Oropharynx mucosa Eustachian tube

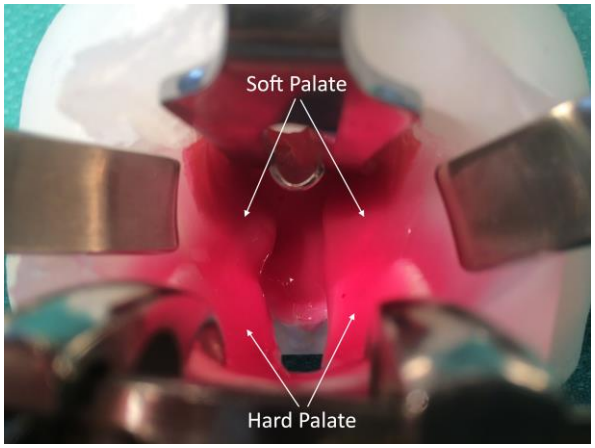

Fig 2. Multi-layered silicone cleft palate phantom close-up surgical view with mouth retracted using the Dingman oral retractor.

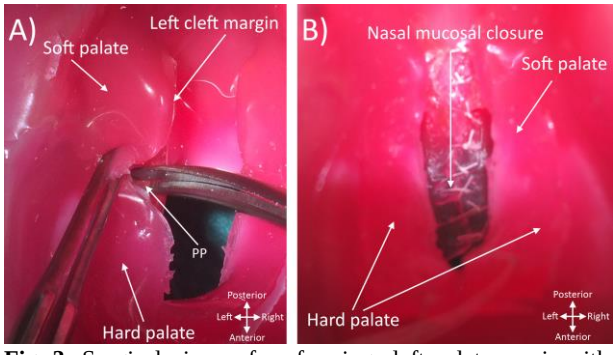

Fig. 3: Surgical views of performing cleft palate repair with phantom. A) Releasing palatopharyngeus (PP) from left cleft margin. B) Suturing nasal mucosa together.

Robotic Testing

An evaluation of the 3D workspace (3 cm by 3 cm aperture, depth 6.5 cm, suggested 5 mm Endowrist® instruments on the da Vinci ® Platform as a potential robotic solution. Close positioning of the patient side manipulators (PSM's) allowed accessing both the soft and hard palate and a 30 degree endoscope positioned distal to the oral aperture resulted in excellent visualization of the hard and soft palate.

Testing was successful in dissection of the mucosa from the hard and soft palate, elevation of mucoperiosteal flaps, releasing the musculature from the hard palate as well as suturing the nasal mucosa, muscles and oral mucosa together (Fig 4). However, frequent collisions between the PSM's and oral aperture made the procedure challenging.

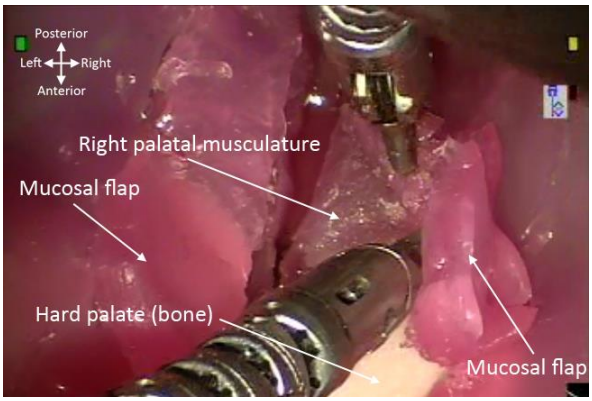

Fig. 4: dissection of mucosal layer from right palatal musculature using phantom with 5 mm Endowrist® instruments and 30 degree endoscope.

DISCUSSION

We have successfully developed a highly realistic, functional cleft palate phantom that can be used as both a training tool and to test a robotic approach to cleft palate repair. Utilization of the da Vinci ® Surgical System for cleft palate repair using 5 mm Endowrist® instruments is feasible and robotic repair may have many advantages over standard instruments. Given the smaller size of the infant oral cavity compared to adults, the frequency of collisions was not surprising.

Optimization of path planning, collision alerts, alternate tool configurations, and customized retractors would improve the efficiency and safety of the robotic procedure.

REFERENCES

[1] Joseph E. Losee REK. Comprehensive Cleft Care: The McGraw-Hill Companies; 2009.

[2] Vadodaria S, Watkin N, Thiessen F, Ponniah A. The first cleft palate simulator. Plastic and reconstructive surgery. 2007;120(1):259-61.

[3] Senturk S. The simplest cleft palate simulator. The Journal of craniofacial surgery. 2013;24(3):1056.

[4] Nagy K, Mommaerts MY. Advanced s(t)imulator for cleft palate repair techniques. The Cleft palate-craniofacial journal : official publication of the American Cleft Palate-Craniofacial Association. 2009;46(1):1-5.

[5] Smartt JM, Jr., Gerety P, Serletti JM, Taylor JA. Application of a robotic telemanipulator to perform posterior pharyngeal flap surgery: a feasibility study. Plastic and reconstructive surgery. 2013;131(4):841-5.

[6] Huang MH, Lee ST, Rajendran K. Anatomic basis of cleft palate and velopharyngeal surgery: implications from a fresh cadaveric study. Plastic and reconstructive surgery. 1998;101(3):613-27; discussion 28-9.

Transoral Steerable Needles in The Lung: How Non-Annular Concentric Tube Robots Can Improve Targeting

P. J. Swaney[1], H. B. Gilbert[1], R. J. Hendrick[1], O. Commichau[2], R. Alterovitz[3], R. J. Webster III[1]

[1]*Mechanical Engineering, Vanderbilt University, USA*
[2]*Hannover Center of Mechatronics, Leibniz Universität Hannover, Germany*
[3]*Computer Science, University of North Carolina at Chapel Hill, USA*
philip.j.swaney@vanderbilt.edu

INTRODUCTION

Lung cancer is one of the most profound current public health challenges, with more than 150,000 lives lost to it each year in the United States alone [1]. A major challenge is early diagnosis, since life expectancy drops precipitously as the tumor grows. While small nodules (which may or may not be cancerous) are being identified with increasing frequency due to better imaging and new guidelines that dramatically increase the frequency of screening, many cannot currently be biopsied. Surgeons have a low diagnostic yield rate (< 52%) with nodules less than 1.5 cm in size using hand-held needles [2]. Furthermore, traditional percutaneous approaches risk lung collapse, which is a serious complication that can even be fatal to patients with various co-morbidities.

Transoral targeting for biopsy and therapy delivery is a better approach, since the lung's outer wall is not punctured, reducing the risk of lung collapse. While a few academic and commercial systems exist for this purpose (e.g. Medtronic's superDimension system http://superdimension.com/), they are typically limited to nodules that occur in or near the bronchial tree. We recently described a robotic system designed to exit the bronchial tree and steer through the soft tissue of the lung [3]. The system, shown in Fig. 1, combines three steerable surgical devices: a tendon-driven redundant mechanism (the bronchoscope), a concentric tube robot [4], and a flexure-based bevel tip steerable needle [5]. Concentric tube robots have been used to augment the dexterity of rigid [6] and flexible endoscopes [7] in prior work, but this is the first time all three steering technologies have been combined into one system. The intended workflow for our system is (1) deploy the bronchoscope manually to the desired location in the bronchi, (2) use a puncture mechanism [3] to make a small opening in the bronchial wall, (3) deploy the concentric tube robot through it into the soft tissue of the lung, and (4) deploy the bevel tip needle and steer it to the desired target under closed loop control [8].

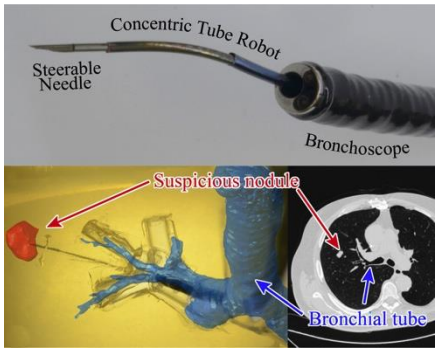

Fig. 1. Our transoral lung access system consists of three stages: a tendon-actuated bronchoscope, a concentric tube robot, and a steerable needle. The system was designed to target hard-to-reach nodules in the peripheral lung.

In this paper we focus on improving step (3). Our objective is to provide a way for the concentric tube stage to use high curvatures, while minimizing tissue damage and deformation. We aim to achieve this via follow-the-leader deployment, in which the shaft of the device remains perfectly in the path traced out by the device's tip as it advances through tissue. See [9] for a discussion of this as it relates to concentric tube robots. Achieving follow-the-leader deployment with our system is a challenge, because the long transmission lengths required for the tubes to pass through the bronchoscope are subject to substantial torsional windup as the curved tubes elastically interact. This can cause elastic instabilities and snap-through, in which the tubes suddenly snap from one configuration to another [10,11]. This makes a range of axial tube rotation angles inaccessible, unless tubes are only gradually curved, or are deployed such that their curved sections do not overlap when relative axial tube rotations are applied.

Non-annular tube cross sections provide a way to achieve follow-the-leader deployment with higher tube curvatures, or at currently inaccessible relative angles. Non-annular tubes prevent relative rotation of the tubes with respect to one another, avoiding the snapping behavior caused by elastic instabilities. This idea was first developed in a collaboration between the last author and Philips, Inc. Yet to date, it has only been described conceptually in the patent literature [12]. Thus, the contribution of this paper is the first physical realization of non-annular concentric tubes.

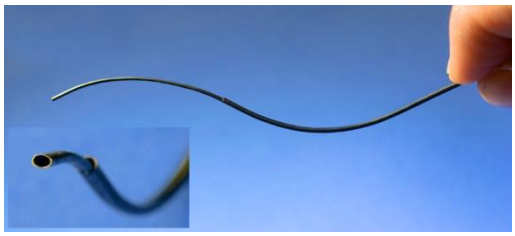

Fig. 2. Our prototype concentric tube robot with elliptical cross sections. This design can achieve configurations that would be unstable for annular tubes, facilitating follow-the-leader deployment with higher curvatures.

MATERIALS AND METHODS

To create a set of non-annular tubes, we modified a set of annular tubes. We used an outer tube with an outside diameter (OD) of 1.60 mm and an inside diameter (ID) of 1.40 mm, and an inner tube with an OD of 1.16 mm and an ID of 0.99 mm. Mandrels made from nitinol wire (0.79 mm and 0.48 mm, respectively) were inserted into each tube, and a hot air gun was used to heat each tube to approximately 600° C. We then mechanically deformed the tube onto the mandrel with a set of pliers, yielding an elliptical cross section. We then precurved the tubes (curvature of 31.5 m^{-1}, curved length ≈55 mm). Fig. 2 shows the tubes placed concentrically. The elliptical cross sections prevent relative tube rotation.

RESULTS

The complete system introduced in the previous section, and described in [3], is illustrated in Fig. 3. The enhancement to the system that is the main result of this paper is the prototype shown in Fig. 2. The elliptical cross sections enable tubes to deploy with curvatures opposed to one another (see Fig. 2), in configurations that would be unstable for annular tubes [10,11]. For example, annular tubes of the same dimensions, precurvatures, and curved lengths, with transmission lengths long enough to pass through a bronchoscope (e.g. 735 mm and 835 mm), would wind up torsionally and be unable to achieve this configuration. In fact, the maximum overlapped arc length of the precurved portions of these annular tubes for which stable opposed curvatures could be maintained would be 0.9 mm [10]. Furthermore, when the precurved sections of these annular tubes are fully overlapped and extended from the bronchoscope, the maximum stable rotation angle of the inner tube relative to the outer is 53°, and this requires a tube base angle of approximately 3083°, more than 8.5 revolutions! In contrast, the use of non-annular tubes enables higher curvatures and previously inaccessible relative tube angles (e.g. the 180° case shown in Fig. 2) to be employed.

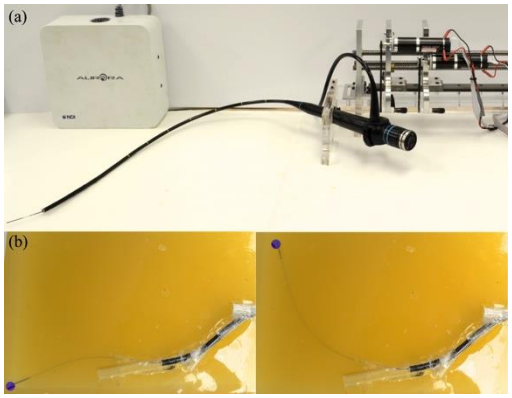

Fig. 3. (a) Our complete system, in which the concentric tube robot and steerable needle pass through the bronchoscope port. (b) Photographs of phantom targeting experiments with the system, in which magnetic tracking feedback was used to steer the needle to targets [3].

CONCLUSION

While non-annular tube cross sections would not be useful in contexts where the concentric tube robot is intended to act as a manipulator (see [4]), they can be a good option when one desires the concentric tube robot to act like a steerable needle. By locking the relative axial rotation of the tubes, elastic instability is prevented, and configurations inaccessible to annular tubes become possible. This is potentially useful in any procedure where the robot acts like a steerable needle.

REFERENCES

[1] American Cancer Society. Cancer facts & figures 2014. Accessed Oct. 21, 2014.

[2] N. Kothary, et al. "Computed tomography–guided percutaneous needle biopsy of pulmonary nodules: impact of nodule size on diagnostic accuracy." Clinical Lung Cancer, vol. 10, no. 5, pp. 360-363, 2009.

[3] P. J. Swaney, A. Mahoney, et al., "Tendons, concentric tubes, and a bevel tip: Three steerable robots in one transoral lung access system", IEEE Int. Conf. on Robotics and Automation, 2015. In Press.

[4] H. B. Gilbert, D. C. Rucker, and R. J. Webster III, "Concentric tube robots: state of the art and future directions", Int. Symposium on Robotics Research, 2013. Springer Tracts in Advanced Robotics, In Press.

[5] P. J. Swaney, J. Burgner, H. B. Gilbert, and R. J. Webster III, "A flexure-based steerable needle: high curvature with reduced tissue damage", IEEE Trans. on Biomedical Engineering, vol. 60, no. 4, pp. 906-909, 2013.

[6] R. J. Hendrick, et al., "A multi-arm hand-held robotic system for transurethral laser prostate surgery", in IEEE Int. Conf. on Rob. Autom., pp. 2850-2855, 2014.

[7] E. J. Butler, et al., "Robotic neuroendoscope with concentric tube augmentation," IEEE/RSJ Int. Conf. Intel. Rob. and Sys., pp. 2941–2946, 2012.

[8] D. C. Rucker, J. Das, et al., "Sliding mode control of steerable needles", IEEE Trans. on Robotics, vol. 29, no. 5, pp. 1289-1299, 2013.

[9] H. B. Gilbert, et al., "Concentric tube robots as steerable needles: achieving follow-the-leader deployment", IEEE Transactions on Robotics, In Press.

[10] R. J. Hendrick, et al., "Designing snap-free concentric tube robots: A local bifurcation approach", IEEE Int. Conf. on Robotics and Automation, 2015. In Press.

[11] J. Ha, F. Park, P. E. Dupont, "Achieving elastic stability of concentric tube robots through optimization of tube precurvature", in IEEE/RSJ Int. Conf. Intelligent Robots and Systems, pp. 864-870, 2014.

[12] E. Greenblatt, et al. "Interlocking nested cannula", US Patent Application Number 20110201887. 2011.

Vision-guided Learning by Demonstration for Adaptive Surgical Robot Control

H. Rafii-Tari[1*], A. Vandini[1*], L. Zhang[1*], A. Hughes-Hallett[2], G.-Z. Yang[1]

[1]*The Hamlyn Centre for Robotic Surgery, Imperial College London, UK*

[2]*Department of Surgery and Cancer, Imperial College London, UK*

{h.rafii-tari11, a.vandini12, lin.zhang11}@imperial.ac.uk

[*]H. Rafii-Tari, A. Vandini and L. Zhang are joint first authors

INTRODUCTION

Autonomous robot-assisted execution of repetitive surgical tasks has the potential to reduce fatigue, whilst improving surgical navigation, procedure times and workspace usage. The increased use of tele-surgical robots and development of open-source platforms offers new opportunities for autonomous navigation which has led to a growing interest in applying the learning-by-demonstration (LbD) framework used in robotics towards complete automation of repetitive tasks [1, 2]. While vision information has been used towards towards tool tracking and target detection for autonomous task execution [3], the combination of LbD with vision-based 3D landmark recognition and tool tracking towards adaptive trajectory transfer has not been explored. This paper proposes a LbD framework for automating surgical robotic execution of subtasks under stereo vision guidance, using the da Vinci Research Kit (DVRK). The approach consists of learning optimum motion trajectories for different subtasks of a suturing task, and using stereo vision for 3D anatomical landmark recognition and needle tracking, to allow adaptation of learned trajectories to different clinical scenarios with moving camera views.

MATERIALS AND METHODS

This paper made use of the DVRK development platform provided by Intuitive Surgical with the software implementation based on the cisst/SAW libraries [4]. Two large needle driver tools were used at the patient side manipulator (Fig. 1). A custom-made PVA cryogel phantom (providing similar elastic and tensile properties as normal tissue) with customized built-in wounds (width=6mm) was made for these experiments. Motion models were learned from multiple experienced demonstrations (n=6,>10 simulator/surgical procedures) performing a running suture with three needle insertions. The suturing task is considered to consist of a set of subtasks to be modeled individually and executed by the robot automatically in a sequential order. However, the focus of this study is "**Subtask 1**: needle insertion through the wound with the right instrument", which for this task can be considered the more dexterous subtask. This subtask is preceded by an initialization step involving moving the needle to the correct insertion point by the right instrument.

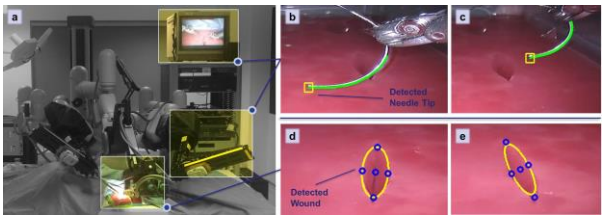

Fig. 1 Experimental setup of the da Vinci system with the DVRK (a), needle tracking for moving the needle from initial position (b) to desired target insertion point (c), wound detection under different camera views (d, e).

Each demonstration consisting of the 3D Cartesian positions and the rotations (represented as 4D quaternions) of the needle driver tip was manually segmented and trajectories from multiple demonstrations were temporally aligned using a combination of dynamic time warping and spherical linear interpolation. For learning the movement patterns and reproducing trajectories that capture the main features of the training data, this work makes use of Hidden Semi-markov Models (HSMM) [5], a form of explicit-duration Hidden Markov Model (HMM), where the self-transition probability of the standard HMM is replaced with a parametric model of the state duration, thereby providing a better balance between temporal and spatial constraints than a standard HMM. As a result, a smooth generalized form of the motion for the desired subtask was learned.

The proposed vision algorithm is used for two main purposes: 1) wound detection for extracting the geometry and orientation of the wound under different anatomical variations/camera views 2) needle tracking in order to provide real-time 3D positioning of its tip.

In order to move the needle from an arbitrary initial position to desired target insertion point (Fig. 1), after which automatic execution of the learned trajectories for Subtask 1 can be performed, the inverse kinematics of the robot is used. The transformation between the coordinate system at the base of the robot and at the stereo endoscopic camera was calculated offline through hand-eye calibration.

Initially, the wound is detected in the stereo images through a semi-automatic algorithm that asks the user to provide two input points and geometrically models the wound with an ellipse, while a feature image based on the analysis of the eigenvalues of the Hessian matrix is computed to enhance the borders of the wound. Once

the 3D pose of the wound is estimated through triangulation, the needle is driven towards the desired target insertion point using the robot's inverse kinematics. Needle tracking is achieved through an algorithm that detects small straight segments on a feature image and only considers segments close to the detected needle in previous frames and with similar orientation. The segments are combined to create a continuous curve that represents the needle shape in the current frame. Using these results the 3D needle tip position is estimated through triangulation.

RESULTS

Fig. 2 shows the running suture task (a) as well as the HSMM structure for Subtask 1, as learned from multiple experienced demonstrations, and the smooth generalized version of the motion extracted (b), with different colors corresponding to the different states of the HSMM. The optimum number of states was selected using the Bayesian information criterion.

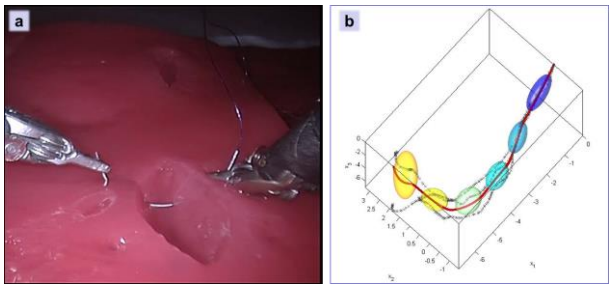

Fig. 2 The running suture task (a) and the learned motion for "Subtask 1" (b) as reproduced from multiple demonstrations using the HSMM. The ellipses correspond to the covariances for each state of the HSMM.

The proposed method has been validated by automating the needle initialization towards the target insertion point, using the vision system, followed by automated playback of the learned trajectory for Subtask 1. The whole execution was considered successful if the needle tip passed through the wound, and exited on the other side, enough to be grasped by the left instrument. The automation has been tested with the wound under different camera views, ranging from a viewing angle of -10 degrees to +10 degrees with respect to the camera, as well as different initial poses and distances of the needle with respect to the wound. The algorithm vas validated multiple times (n=7) under these different initial conditions. In each case the wound detection algorithm estimates the 3D pose of the anatomy which was used to drive the needle towards the desired target insertion point. Fig. 3 shows examples of the needle driver tip trajectory for automated initialization of the needle at the desired insertion point in the robot base coordinate system (depicted in orange), followed by automated playback of the learned motion for Subtask 1 (depicted in blue). The initialization step is sensitive to the accuracy of the wound detection, the robot kinematics, and the hand-eye calibration. The results depict successful and smooth execution of the desired motion under different initial conditions.

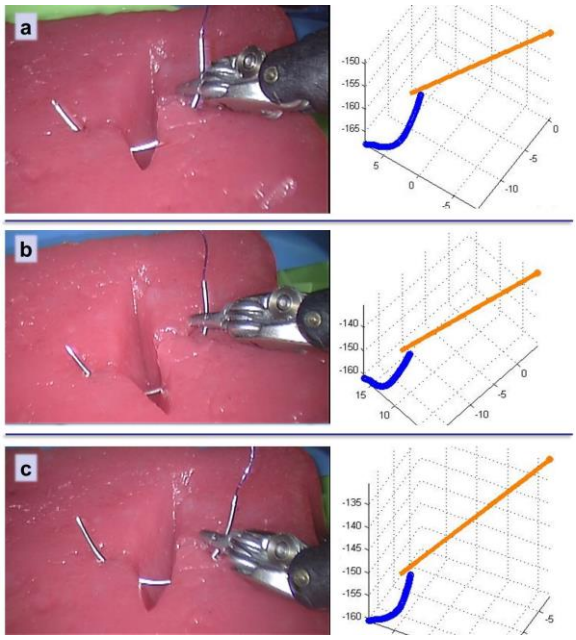

Fig. 3 Examples of the needle driver tip trajectory for automated initialization of the needle at the desired insertion point (orange) followed by automated playback of the learned motion for the first subtask (blue) under different initial conditions in the robot base coordinate system [mm].

DISCUSSION

This paper proposes a LbD approach, using the DVRK framework, for learning and automating motion trajectories for different subtasks of a suturing task under vision guidance. By using stereo vision for 3D perception, anatomical landmark detection and needle tracking, the approach addresses different clinical scenarios under varying initial conditions and camera views, thereby allowing for subject-specific variability and tissue deformation. Future work will further extend the framework for adapting the learned trajectories to more complex anatomical variations by combining the needle tracking with visual servoing, to further overcome the inherent errors in the needle initialization.

REFERENCES

[1] Berg JVD, et. al. Superhuman performance of surgical tasks by robots using iterative learning from human-guided demonstrations. IEEE International Conference on Robotics and Automation. 2010; 2074-2081.

[2] Padoy N, Hager G. Human-machine collaborative surgery using learned models. IEEE International Conference on Robotics and Automation. 2011; 5285-5292.

[3] Kehoe B, et. al. Autonomous multilateral debridement with the raven surgical robot. IEEE International Conference on Robotics and Automation. 2014; 1432-1439.

[4] Kazanzides P. et al. An open-source research kit for the da vinci surgical system. IEEE International Conference on Robotics and Automation. 2014: 6434-6439.

[5] Calinon S, Pistillo A, Caldwell DG. Encoding the time and space constraints of a task in explicit-duration hidden markov model. IEEE/RSJ International Conference on Intelligent Robots and Systems. 2011; 3413-3418.

Design of a Novel Flexible Endoscope

Z. Li[1], M. Z. Oo[3], V. D. Thang[3], V. Nalam[2], T. Kofidis[3], H. Ren[2], H. Yu[2]

[1]*Institute of Digestive Disease and Chow Yuk Ho Technology Centre for Innovative Medicine, the Chinese University of Hong Kong*
[2]*Department of Biomedical Engineering, National University of Singapore*
[3]*Department of Cardiac, Thoracic, and Vascular Surgery, National University of Singapore*

INTRODUCTION

Minimally invasive surgery (MIS) brings multiple benefits to patients, such as shorter hospital stay, lower incidences of intra- and post-operative complications, and better cosmesis. The growing popularity of MIS leads to a vast adoption of endoscopy devices, of which the market is $28.2 billion in 2013 and is expected to reach $37.9 billion by 2018 [1]. Existing endoscopes fall into three categories, i.e. the rigid endoscope (RE), the flexible endoscope (FE) and the capsule endoscope (CE). Among them, REs are most frequently used in the minimally invasive cardiac surgery (MICS), in which the endoscope enters via an incision on the chest wall much smaller than that used in conventional cardiac surgery. Since the tip of the RE cannot be steered, it is difficult to view the entire surgical site with one RE. Also, some regions cannot be viewed due to the blockage of tissues. To solve these drawbacks, it is desired that the tip be flexible and can be steered. Hence, a FE with a rigid shaft and a steerable section is in favor, e.g. Endoeye Flex by Olympus [2]. However, in this type of FE, the length of the bending section is fixed. This results in the flexible section sweeping a large area to view from side to side. In cardiac surgery, the sweeping action is often limited by the heart and surrounding vital structures, and hence the field of view remains restricted. To solve these problems, a new cardioscope design is needed.

The biomimetic wire-driven mechanism (WDM) is well suited to developing flexible devices [3-6]. It comprises of a flexible backbone and a set of controlling tendons/wires. Its motion is similar to that of the flexible endoscope. However, by using a constraint, bending of the flexible section is controllable and the workspace is expanded [7, 8]. This can increase the scope of vision.

MATERIALS AND METHODS

In this paper, we present a novel flexible endoscope which is well suited to MICS. It is named 'the Cardioscope'. It is composed of a handle, a rigid shaft, a flexible section and the camera. The flexible section is composed of an elastic tube, a number of spacing discs and four tendons. The spacing discs are evenly distributed along the elastic tube. The tendons pass through the pinholes on the spacing discs and are fixed at the end of the flexible section. The other end of the tendons is attached to the tendon driving module, which is inside the handle. The flexible section is connected to the handle by the rigid shaft, which contains two concentric tubes, one is the shaft and the other is the overtube as shown in Fig. 1(a). The overtube can slide along the shaft by a sliding knob in the handle. It serves as a constraint to the flexible section. By adjusting the position of the overtube, the flexible section is constrained so that only the part outside the overtube can bend. The flexible section can bend in all directions by controlling four tendons and hence, the angulation of the bending section is also steerable. The bending motion is shown in Fig. 1(b)-(d): Fig. 1(b) shows the regular bending motion, in which the length of the bending section is fixed; Fig. 1 (c) shows the bending motion, in which the length of the bending section is controlled. The four positions (i-iv) of the constraint and the corresponding bending are given.

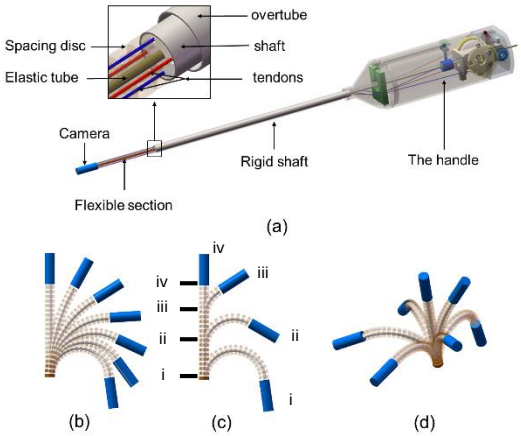

Fig. 1 Design of the flexible cardioscope: (a) the system overview; (b) bending of the flexible section – by controlling the bending angle (traditional way); (c) bending of the flexible section – by controlling the length of the bending section; (d) 2D bending of the flexible section.

A prototype is developed and *ex-vivo* tests are carried out to evaluate the design. The experimental setup is shown in Fig. 2. In the test, a pig heart is suspended by sutures and the endoscopes enter from the side holes, which mimic the incisions in the MICS. Two sets of tests are performed. In the first test, a mitral valve ring is placed in the pig heart and three different endoscopes are used to view the ring from a side pinhole mimicking the incision in the MISC. The first is a 0° RE and the second is a 30° RE, both from Karl Storz; the third is 'the Cardioscope'. Three tasks are assigned to the endoscopes: task A – find the ring; task B view the full ring; task C – view the full ring in a single view. In the second test, the Cardioscope is used to explore the whole heart.

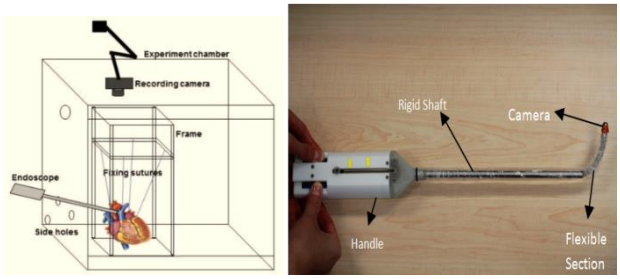

Fig. 2 The *ex-vivo* experiment setup and cardioscope in one of the bending configurations.

RESULTS

Results of the first test are summarized in Table 1. In the first test, all three endoscopes can find the ring successfully. However, for the 0° RE and 30° RE, due to the restricted scope of vision, they cannot view the full ring. The best views of the two REs are shown in Fig. 3 (a) and Fig.3 (b). The Cardioscope is tested in three configurations: the first is straight configuration; the second is bending with long bending section; the third is bending with short bending section. At the straight configuration, the best view of the Cardioscope is shown in Fig. 3 (c). It successfully finds the ring, however, the scope of vision is much smaller than the two commercial REs. The quality of the image is poorer. Considering this is the first prototype, the quality of image is not a key performance index. When the bending section is long, the Cardioscope successfully find the ring and can view the full ring. The views obtained at different bending length configurations are shown in Fig 3.

Table 1 – Summary of the results of test 1

		Task A	Task B	Task C
Olympus 0° RE		Yes	No	No
Karl Storz 30° RE		Yes	No	No
Cardioscope	Straight	Yes	No	No
	long bending length	Yes	Yes	No
	short bending length	Yes	Yes	Yes

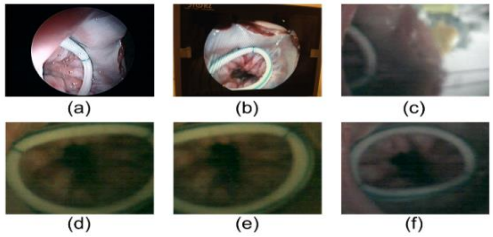

Fig. 3 Results of test 1: (a) best view of the 0° RE; (b) best view of the 30° RE; (c) best view of the cardioscope at straight configuration; (d) and (e) first and second view of the cardioscope with long bending section; (f) view of the cardioscope with short bending section.

In the second test, the pig heart is placed in a position similar to that in the MICS. The Cardioscope is controlled to explore the entire heart. Twelve snapshots are shown in Fig. 4. In the test, the surgeon successfully identifies the mitral valve, the aortic valve, the aorta, the pulmonary artery, the wall of the ventricles, and even the apex of the heart from a retrograde bending position.

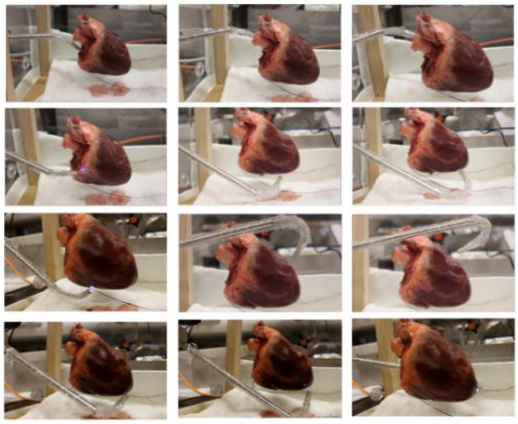

Fig. 4 Results of test 2: Cardioscope is controlled to explore the entire heart posed in the surgical position.

DISCUSSION

The presented Cardioscope shows the ability to provide much wider scope of vision than traditional endoscopes. By controlling the length of bending, the scope of vision is also tunable. In the test, the Cardioscope successfully explores the full heart through a single hole, which shows the design is promising. Although designed for MICS, the Cardioscope can also be applied to other MIS, such as laparoscopy, and neurosurgery.

REFERENCES

[1] M. A. MARKETS. (2014, 1st, Nov.). *Endoscopy Equipment Market by Endoscopes*. Available: http://www.marketsandmarkets.com/PressReleases/endoscopy.asp

[2] Olympus. (2014, 1st, Nov.). *Endoeye Flex HD*. Available: http://www.olympus.co.uk/medical/en/medical_systems/products_services/product_details/product_details_17285.jsp

[3] Z. Li, R. Du, M. C. Lei, and S. M. Yuan, "Design and Analysis of a Biomimetic Wire-Driven Robot Arm," in *Proceedings of the ASME 2011 International Mechanical Engineering Congress & Exposition*, Denver, Colorado, USA, 2011, pp. 11-17.

[4] Z. Li and R. Du, "Design and Analysis of a Bio-Inspired Wire-Driven Multi-Section Flexible Robot," *International Journal of Advanced Robotic Systems*, vol. 10, pp. 1-11, 2013.

[5] B. Liao, Z. Li, and R. Du, "Robot fish with a novel biomimetic wire-driven flapping propulsor," *Advanced Robotics*, vol. 28, pp. 339-349, 2014.

[6] Z. Li, R. Du, and Y. Yao, "Flying Octopus - A LTAV with Wire-Driven Flapping Wings," in *International Mechanical Engineering Congress & Exposition (IMECE 2012)*, Houston, Texas, USA, 2012.

[7] Z. Li and R. Du, "Expanding Workspace of Underactuated Flexible Manipulator by Actively Deploying Constrains," in *IEEE International Conference on Robotics and Automation (ICRA 2014)*, Hong Kong, China, 2014, pp. 2901-2906.

[8] A. Ataollahi, R. Karim, A. S. Fallah, K. Rhode, R. Razavi, L. D., *et al.*, "3-DOF MR-Compatible Multi-Segment Cardiac Catheter Steering Mechanism," *IEEE Biomedical Engineering, IEEE Transactions on*, vol. PP, pp. 1-11, 2013.

Shoulder-Mounted Robot for MRI-Guided Arthrography Procedure; Second Prototype and Accuracy Study

R. Monfaredi[1,2], E. Wilson[1], R. Sze[1], K. Sharma[1], I. Iordachita[3], K. Cleary[1]

[1]*Sheikh Zayed Institute for Pediatric Surgical Innovation, CNMC, Washington, DC, USA*

[2]*Industrial Department, Azad University-South Tehran Branch, Tehran, Iran*

[3]*Laboratory for Computational Sensing and Robotics (LCSR), Johns Hopkins University*

rmonfare@cnmc.org

INTRODUCTION

A novel, small, and lightweight patient-mounted MRI-compatible robot has been developed for MRI image-guided interventions. Arthrography, biopsy, facet joint injection, and other percutaneous interventions which typically require radiation-based imaging guidance, could benefit from using this new robotic system. In typical manual image-guided interventions, the physician guides the needle using cross-sectional images to reach the desired position. Traditional needle manipulation often requires multiple passes to reach the target which prolongs the procedures and exposes the patient to undesired ionizing radiation. MRI-compatible robots may be enabling for radiation free procedures, which is especially important for pediatrics.

The envisioned use of our prototype robot is as follows: after placing and securing the robot on the patient, and performing robot to scanner coordinate system registration, the radiologist will select a target and entry point from the MR images; the robot will then align a needle guide along this trajectory; and the radiologist will then insert the needle to the desired depth. The system configuration is shown in Fig. 1.

A few research groups have reported related work in the field of patient-mounted robots for percutaneous interventions. Walsh *et al.* [1] developed a patient-mounted robot called Robopsy. This was a system with 4 degree of freedom (DOF) for needle holding, guidance, and insertion. A 2 DOF MRI coil-mounted robotic positioner for cryoablation was developed in [2]. The needle entry point had to be found and marked before attaching the robot to the patient, since this robot did not have translational DOFs. Bricault *et al.* [3] developed a light (1Kg) and compact (15x23cm) robot with 5 DOFs to perform abdominal and thoracic punctures under CT or MRI guidance for diagnostic or therapeutic purposes. Song *et al.* developed a 2 DOF MRI-compatible double ring remote center of motion (RCM) mechanism for MRI-guided liver interventions. This device was a passive mechanism which was manually operated [4].

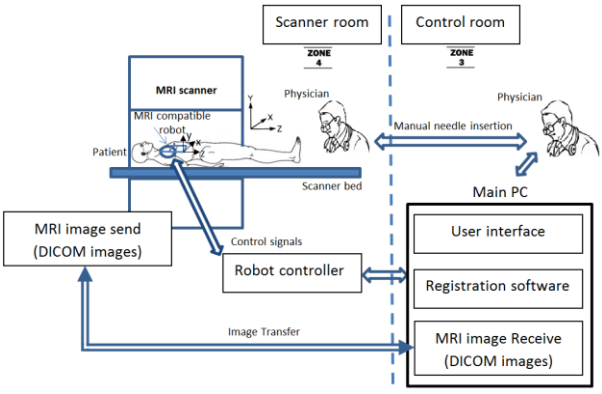

Fig 1 System configuration.

In this paper, we introduce a second version of our prototype robot [5]. An overview of control architecture and hardware is provided. The results of a recent accuracy study are reported.

MECHANICAL SYSTEM

Fig. 2 shows the new design and prototype of our patient-mounted robot created using an Objet 500 rapid prototyping machine. This robot is a 4 DOF robot, 2 for needle translation (r1 and d1 in Fig. 2), and 2 for needle rotation (r3 and r4). Some modifications were done from the previous design [5] to reduce the friction and backlash, and to increase the accuracy of the system. MRI-compatible piezo-motors (Piezo LEGS® Upsala, Sweden), and MRI-compatible Encoder: E8P OEM Optical Kit Encoder, 512 CPR, 1/8 bore, differential, hole in (US digital, Vancouver, Washington, USA) were used for robot's joint actuation and measurement. A full ceramic ball bearing (ID=90 mm, Boca Bearing Inc., FL, U.S.A) was used for the base rotation to eliminate the backlash and friction associated with a sliding rotary bearing.

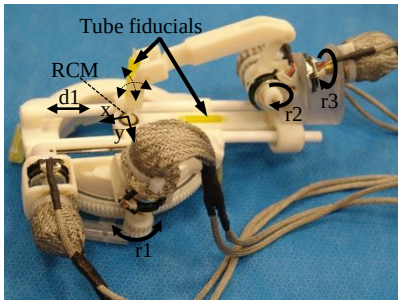

Fig. 2 Prototype of our 4DOF robot.

SYSTEM IMPLEMENTATION

As shown in Fig. 1 the control system consists of four components: 1) robot controller, 2) robot/scanner

registration software, 3) user interface software, and 4) a communication channel to transfer MRI DICOM images and control signals between the scanner room and the control room. As shown in Fig. 3 the robot controller is located inside the MRI room, while the user interface software and image registration software run on a computer located in the control room. All cables between the scanner room and the control room are passed through the patch panel. Fiber optic cables were used to minimize the RF noise inside the MRI room. Preliminary tests in the MRI environment showed that the robot introduces some noise when activated. However, we do not anticipate this to be a crucial concern as MRI images will only be acquired when the motors are in an 'OFF' state. As part of our ongoing work, we are investigating quantitative metrics of image distortion under various use scenarios.

ACCURACY STUDY

Goal: To investigate needle positioning and orienting accuracy.

Experiment Setup: To track the position and orientation of the robot's needle guide, a rigid body, as shown in Fig. 3, was attached to the needle guide. This rigid body consisted of 8 active embedded markers. An optical tracker (Certus, NDI, Waterloo, ON, Canada) was used to track the rigid body (See Fig. 3). The manufacturer's stated accuracy is 0.1 mm. The optical tracker was placed 2m away from the markers.

Experiment Workflow and Data Collection: The robot was moved in the xy plane in 5 mm increments along both axes, and the position of the rigid body recorded. The robot was commanded to move to 48 different positions throughout the workspace. The orientation accuracy study was performed with 1 degree increments along both orientational DOFs. At each location, the position and orientation of the rigid body was recorded for 1 second at a sample rate of 120Hz, and averaged.

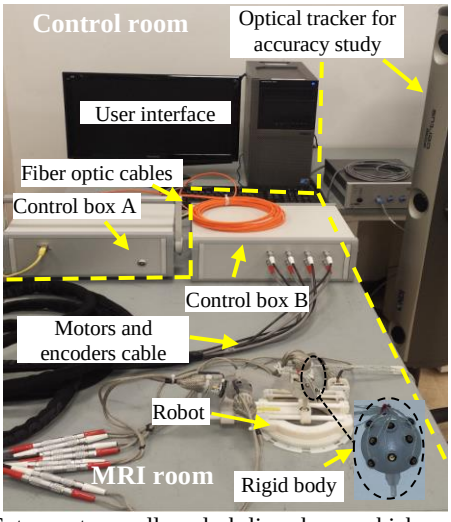

Fig. 3 Sytem setup; yellow dash line shows which part of the setup is placed in MRI control room. Optical tracker was used for accuracy study in the lab environment.

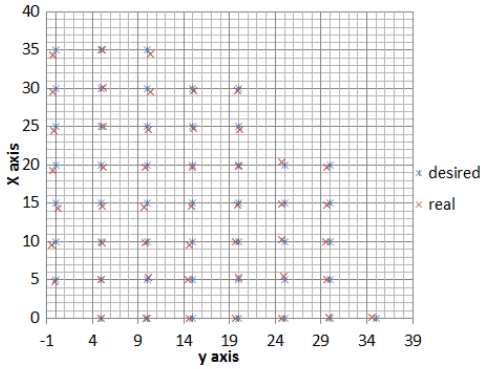

Fig. 4 Position accuracy study results for a quarter of the workspace.

The root mean square (RMS) for rigid body definition was between 0.08 to 0.20mm during these experiments.

Results: The maximal position and orientation errors for the robot were ±0.6 mm and ±0.5 degree. Fig. 4 shows the position accuracy study results for a quarter of the robot's workspace. Based on clinician feedback, overall needle placement accuracy under 3 mm is considered sufficient for a conventional shoulder arthrography procedure. For the intended clinical procedure, this robot should be accurate enough.

DISCUSSION

This paper presented the second prototype of our patient-mounted MRI-compatible robot. The robot is intended to provide better targeting ability, improve the clinical workflow, and allow better access within the MRI scanner bore for needle-based percutaneous interventions. The robotic system architecture and an accuracy study were presented. In the next phase of our work, we will continue with MRI imaging studies, and evaluate the clinical accuracy in a phantom study in the MRI suite.

REFERENCES

[1] C. Walsh et al., "A Patient-Mounted, Telerobotic Tool for CT-Guided Percutaneous Interventions", *J. of Med. Devices*, vol. 2, no. 1, pp. 011007.1–011007.10, 2008.

[2] F. Y. Wu et al., "An MRI Coil-Mounted Multi-Probe Robotic Positioner For Cryoablation", *Proceedings of the ASME International Design Engineering Technical Conferences & Computers and Information in Engineering Conference*, Portland, Oregon, USA, pp. 1-9, 2013.

[3] I. Bricault et al., "A Light Puncture Robot for CT and MRI Interventions", *Engineering in Medicine and Biology Magazine, IEEE*, vol. 27, no. 3, pp.42-50, 2008.

[4] S. E. Song et al., "Design Evaluation of a Double Ring RCM Mechanism for Robotic Needle Guidance in MRI-guided Liver Interventions", *2013 IEEE/RSJ Int. Conf. on Intelligent Robots and Systems (IROS)*, Tokyo, Japan, pp. 4078-4083, 2013.

[5] R. Monfaredi et al., "A prototype body-mounted MRI-compatible robot for needle guidance in shoulder arthrography", *5th Int. Conf. on Biomedical Robotics and Biomechatronics*, Sao Paulo, Brazil, pp. 40 – 45, 2014.

Dynamic Non-Continuous Virtual Fixtures for Operations on a Beating Heart using the da Vinci® Research Kit

A. Ruszkowski[1], Z. F. Quek[2], A. Okamura[2], S. E. Salcudean[1]

[1]*Robotics and Control Laboratory, University of British Columbia, Canada*
[2]*Department of Mechanical Engineering, Stanford University, USA*
{angelicar, tims}@ece.ubc.ca

INTRODUCTION

Virtual fixtures, or active constraints, are a controls concept that enable robots to intelligently collaborate with human users to complete tasks that are too complex for the robot to complete autonomously and too challenging for the user to complete unassisted. The body of work on *dynamic* active constraints is not extensive, but combinations of guidance and forbidden-region dynamic virtual fixtures for teleoperation have been studied. [1] Fixture evaluation methods in previous work include potential fields determined from pre-operative images, predicted and current positions of the environment surface location, and streaming point clouds. Some of these do not allow the slave to penetrate the forbidden region, which is impractical in surgical situations. This work proposes an impedance-controlled regional 3D dynamic virtual fixture generated based on dynamics of the heart motion. This virtual fixture has been added to the heart motion compensation system implemented on the da Vinci Research Kit (dVRK) described in [2]. In this work it was noted that while a user was operating on a virtually stabilized heart, the dynamics of the heart target were not accurately perceived. This resulted in additional, inadvertent perforations. To augment the surgeon's perception, we propose a novel non-continuous, strobe-like virtual fixture whose enforcement is conditional upon the kinematics of a beating heart's trajectory.

MATERIALS AND METHODS

A. Virtual Stabilization System overview

The heart motion compensation system from [2] was implemented on the dVRK at the Collaborative Haptics and Robotics in Medicine Laboratory at Stanford Univeristy (Fig 1). In the heart motion compensation system, the Patient Side Manipulators (PSMs) are programmed to follow the trajectory of a point on the heart surface, with superimposed teleoperation commands issued from the Master Tool Manipulators (MTMs). This results in a virtual stabilization of the heart motion from the perspective of the surgeon. The 3D printed plastic heart target is controlled by one PSM while the surgeon controls the other PSM. The camera is attached to the plastic target at a fixed location relative to the simulated heart surface, emulating perfect camera motion tracking.

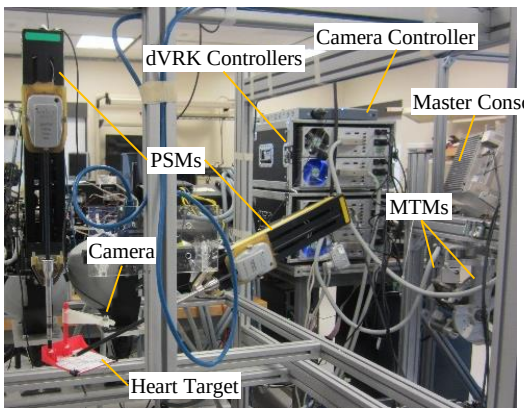

Fig. 1 dVRK set up for virtual fixture experiments for beating heart applications at Stanford University.

B. Virtual Fixture Design

In previous user studies for the heart motion compensation, it was difficult to see when the heart surface is accelerating upwards. This strobe fixture thus provides pulsing haptic feedback, active during periods of high acceleration in the heart trajectory. A 2nd order Butterworth Filter is used to calculate the z-acceleration, a_z, of the heart using joint velocity readings from the position sensors in the PSMs. It was experimentally determined that, for the trajectory (as in [2]) with a z-displacement of 11mm at 1.5Hz, the virtual fixture strobe pulse commences when $a_z > 0.39 m/s^2$ and terminates when acceleration falls below $a_z < -0.145 m/s^2$. The force feedback on the master is displayed only in the positive z direction. The magnitude of the feedback is calculated using the relative position of the slave tool tip and a proxy following the heart surface (similar to the concept in [3]). The tool tip and proxy follow an elastic linkage model:

$$\Delta_z = z_{heart} - z_{tool\ tip}$$

$$F_{MTM_z} = \begin{cases} VF_{scale} \times (\Delta_z + VF_{margin}) & if\ \Delta_Z > 0 \\ 0 & otherwise \end{cases}$$

A virtual margin of 5mm is added to the surface of the heart so the imperceptibly low F_{MTM_z} occurs before collision between the tool tip and the heart surface. The dynamics and inertia of the MTMs guarantee a smooth transition across the $F_{MTM_z} = 0$ threshold. $VF_{scale} \approx 150$; Δ_z is usually only a few millimeters so large scaling values are needed to generate perceptible haptic feedback. The torque applied to the MTM motors to display the haptic feedback is clipped to 1.0 Nm to avoid instabilities. The virtual fixture control loop runs at a frequency of 1kHz.

C. User Studies

Seven right handed subjects completed two one-handed tasks in an IRB-approved study with informed consent: drawing a circle (relevant to the standard Fundamentals

of Laparoscopy circle cutting task), and a simulated suturing task (piercing printed targets with a needle) (Fig 2). Heart motion compensation was active for both.

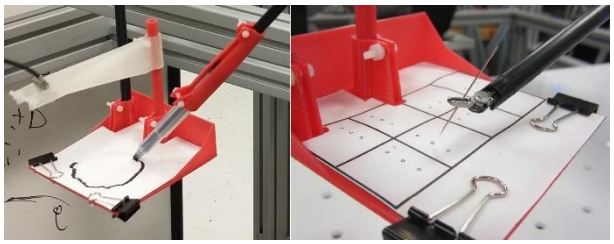

Fig. 2 Tasks completed for user studies. Left: drawing a circle. Right: simulated suturing.

For drawing a circle, a 3D printed adapter was used to attach the marker coaxially to the instrument shaft. For suturing, a straight needle and 6 pairs of dots were used. Each dot is a circle 1mm in diameter and the needle is 0.5mm in diameter; high accuracy (similar to actual anastomosis) is required for this task. A target is "hit" if the needle perforation is completely within the printed dot, "missed" if the perforation is completely outside the printed dot, and "almost" otherwise. The subjects had varying levels of expertise with the robot and haptic devices. Each task was performed under four conditions; the subjects completed practice and three test trials for each. The conditions were *(C1)* no feedback; *(C2*) basic moving wall virtual fixture: feedback is calculated using the elastic linkage model (described in B). This has been implemented in previous work [4], and is the baseline for comparing the effect of the non-continuity of the proposed virtual fixture; *(C3)* haptic pulse feedback: the pulse is active during high acceleration periods, irrespective of the relative positions of the tool tip and heart surface *(C4)* pulsing moving wall virtual fixture: based off C2 with additional dependencies on the dynamics of the target.

RESULTS

The performance of the subjects under the various conditions was evaluated based on four indicators:

i. Efficiency – time of completion
ii. Accuracy – how many times the marker tip left the surface (circle task); how many hit/missed/almost targets (suture task)
iii. Damage – the "collision extent" or time under the surface multiplied by the distance under the surface
iv. Safer Motion – to evaluate the efficacy of the non-continuity, we compare the motion of the teleoperated slave during the high-risk periods of the trajectory to the motion during lower-risk periods.

The results shown in Fig 3 (except for the circle results in row II) depict the average over the 7 users. Efficiency and accuracy measures are normalized relative to the results for C1, showing the effect of the feedback.

DISCUSSION

Based on the efficiency results, C2 was comparable to C4. However in the accuracy results for the circle task, C4 was the only condition with improved performance over C1. The collision extent results show the benefits

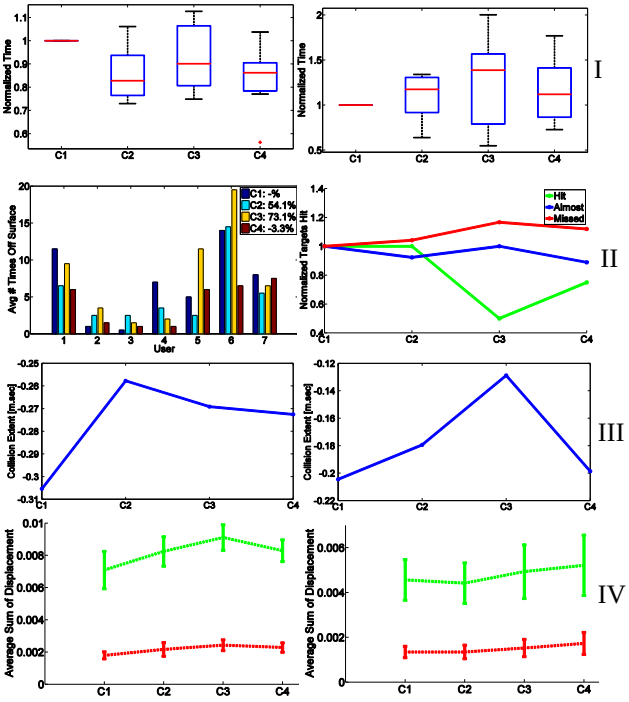

Fig. 3 Results for user studies. Left column shows circle task results, right column shows suture task results. Row I shows efficiency; row II shows accuracy; row III shows damage; and row IV shows safe motion results (green: low-risk periods, red: high-risk periods).

of virtual fixtures, where all conditions with haptic feedback surpassed the results from C1. The ranking of the feedback conditions varied depending on the task. The advantage of the non-continuity is seen in the safe motion results, where in C3 and C4 the users performed a greater portion of the total displacement during the low-risk periods of the heart trajectory. There was high variance in performance between the different users; the tasks may have been too difficult for the skill levels of the participants, particularly the suturing task. Overall, the results show that the pulsing virtual fixture succeeds in relaying to the user the ideal times at which they should perform their tasks. The pulsing virtual fixture also improves completion time and accuracy of simpler tasks such as circle drawing.

ACKNOWLEDGEMENTS

I would like to thank Intuitive Surgical, NSERC and NSF grant #1227406 for their support of this work.

REFERENCES

[1] S. Bowyer et al., "Active Constraints/Virtual fixtures: A survey." IEEE Trans. Robotics. 2014 30(1): 138-157.
[2] A. Ruszkowski et al., "On the Feasibility of Heart Motion Compensation on the da Vinci® Surgical Robot for Coronary Artery Bypass Surgery: Implementation and User Studies," in Proc. ICRA 2015, in press.
[3] S. Nia Kosari et al. "Forbidden region virtual fixtures from streaming point clouds." Advanced Robotics. 2014 28(22): 1507-1518.
[4] S. Park et al., "Virtual fixtures for robotic cardiac surgery," in Proc. MICCAI 2001, pp. 1419-1420.

6-D Localization of a Magnetic Capsule Endoscope Using a Stationary Rotating Magnetic Dipole Field

K. M. Popek[1], J. J. Abbott[2]

[1]*School of Computing,* [2]*Dept. of Mechanical Engineering, University of Utah, USA*
{katie.popek, jake.abbott}@utah.edu

INTRODUCTION

Since the introduction of passive commercial capsule endoscopes, researchers have been pursuing methods to control and localize these devices, many utilizing magnetic fields [1, 2]. An advantage of magnetics is the ability to both actuate and localize using the same technology. Prior work from our group [3] developed a method to *actuate* screw-type magnetic capsule endoscopes in the intestines using a single rotating magnetic dipole located at any position with respect to the capsule. This paper presents a companion *localization* method that uses the same rotating dipole field for full 6-D pose estimation of a capsule endoscope embedded with a small permanet magnet and an array of magnetic-field sensors. Although several magnetic localization algorithms have been previously published, many are not compatible with magnetic actuation [4, 5]. Those that are require the addition of an accelerometer [6, 7], need *a priori* knowledge of the capsule's orientation [7], provide only 3-D information [6], or must manipulate the position of the external magnetic source during localization [8, 9]. Kim et al. presented an iterative method for use with rotating magnetic fields, but the method contains errors [10]. Our proposed algorithm is less sensitive to data synchronization issues and sensor noise than our previous non-iterative method [11] because the data from the magnetic sensors is incorporated independently (rather than first using sensor data to estimate the field at the center of the capsule's magnet), and the full pose is solved simultaneously (instead of position and orientation sequentially).

MATERIALS AND METHODS

Localization is performed relative to the robot's frame, $\boldsymbol{O}_R$, which we place at the location of the rotating dipole (i.e., the center of the actuator magnet). The capsule's coordinate frame origin, $\boldsymbol{O}_C$, which resides at the center of the capsule's magnet, is described by the vector $\boldsymbol{p}_C$ (Fig. 1). The rotation matrix, R, describes the capsule's coordinate frame relative to the robot's. Our goal is to solve for $\boldsymbol{p}_C$ and R.

This method assumes the capsule is free to move, but that the dipole-field rotation is well beyond the "step-out" frequency, where the field is rotating too quickly for the capsule to rotate synchronously, such that we can assume no net motion and decouple the localization and actuation of the capsule. In our setup, the field source is

This material is based upon work supported by the National Science Foundation under Grant No. 0952718.

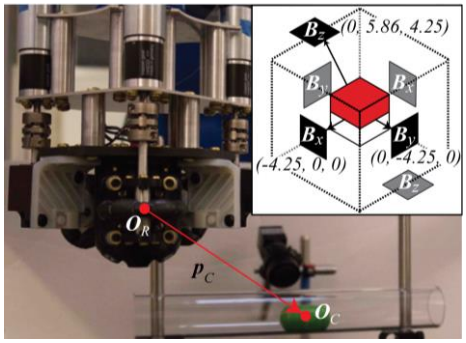

Fig. 1 Experimental setup with a spherical-actuator-magnet manipulator [12], mounted on the end of a 6-DOF robot. A prototype capsule freely rotates and slides in a clear, acrylic, lubricated tube. The inset depicts the capsule's sensor layout [11]. Each sensor is labeled with the field component it measures and its offset, $\boldsymbol{\delta}_i$ in mm, from the internal magnet's center. The grey sensors are not visible from this angle, but are at symmetric offsets.

a spherical permanent magnet, which is accurately modeled by the point-dipole equation [3]:

$$\boldsymbol{B}(\boldsymbol{p}) = \frac{\mu_0}{4\pi\|\boldsymbol{p}\|^3}\left(3\hat{\boldsymbol{p}}\hat{\boldsymbol{p}}^T - \boldsymbol{I}\right)\boldsymbol{M} \qquad (1)$$

where $\boldsymbol{B}(\boldsymbol{p})$ is the field at location $\boldsymbol{p}$, $\hat{\boldsymbol{p}}$ is the unit-normalized $\boldsymbol{p}$ vector, $\boldsymbol{M}$ is the dipole moment of the magnet, $\boldsymbol{I}$ is the identity matrix, and μ_0 is the permeability of free space.

We previously developed an array of six Hall-effect sensors to surround the magnet inside the capsule to estimate the applied field at its location [11] (Fig. 1). The sensors are placed at known offsets, $\boldsymbol{\delta}_i$, as noted in Fig. 1. The position vector, $\boldsymbol{p}_i$, describing sensor i in the robot frame, is $\boldsymbol{p}_i = \boldsymbol{p}_C + R\boldsymbol{\delta}_i$. The scalar magnetic-field projection measured at each sensor is:

$$B_i(\boldsymbol{p}_i) = \boldsymbol{s}_i^T R^T \frac{\mu_0}{4\pi\|\boldsymbol{p}_i\|^5}\left(3\boldsymbol{p}_i\boldsymbol{p}_i^T - \boldsymbol{I}\|\boldsymbol{p}_i\|^2\right)\boldsymbol{M} \qquad (2)$$

where $\boldsymbol{s}_i$ is the sensor's measurement axis in the capsule frame, which is known. The nonlinear least-squares Levenberg-Marquardt algorithm in MATLAB was implemented to estimate the capsule's pose by comparing the sensor data to the estimated field at each of the sensor positions using Eq. 2.

The spherical-actuator-magnet manipulator (Fig. 1) uses three omniwheels to provide a singularity-free rotating dipole field [12]. It is mounted on the end of a 6-DOF robot. A prototype capsule, 50.5 mm in length and 25 mm in diameter, was placed in a lubricated acrylic tube in which it is free to move, at a known position and orientation with accuracy of 2 mm and 10°, respectively, based on visual inspection.

The actuator magnet was rotated at 2 Hz around the **x**, **y**, and **z** axes, which resulted in step-out, with the actuator magnet's position held stationary. Data was collected at 100 Hz and wirelessly transmitted, in batches, at 20 Hz to a computer. Two rotations about each axis were combined, for a total of 3 s of data (1800 sensor measurements) to localize at a given position. For positions to test, we chose two orthogonal planes as depicted in Fig. 2.

RESULTS

The localization results are shown in Fig. 2. The total position error in mm and the orientation error in degrees are shown next to their corresponding position. The orientation error is in terms of the angle-axis representation. The average error across all points was 6.9 mm and 10.7°, the average computation time for the least-squares algorithm was 3.4 seconds. As expected, the position error tends to increase as the magnet is moved farther away from the capsule, due to reduced signal-to-noise. For both planes, the radial positions (along the **r** axis) result in more accurate position estimates than the axial positions (along the -**x** axis). We do not observe any clear trends in orientation error, but this could be partially due to our ground-truth orientation error having comparable values. Note that the two axial positions are the same in planes *A* and *B*, so the differences in the localization estimates give an indication of the variance that can be expected. This method assumes that the capsule has no net motion; some of the error is due to our experiments not respecting this assumption, as would be true in practice.

DISCUSSION

The accuracy obtained is likely to be sufficient for use with our previously published magnetic-actuation method [13]. It performs comparable to other 6-D localization methods; [7] has an average error of 5 mm in a slightly smaller 15 cm sphere. This localization method is not capable of localizing a synchronously rotating capsule because of the assumption that the capsule has no net motion. However, a simple control scheme involves pausing actuation at periodic intervals, and either increasing the rotation speed of the dipole field or rotating it around an orthogonal axis, either of which will cause the capsule to stop rotating synchronously, and after collecting a few rotations of data, continue propelling the capsule in a desired manner. No additional movement of the external dipole source is necessary. For the reported experiments, we arbitrarily chose to use two rotations about three orthogonal axes. Further investigation needs to be done to determine the relationship between the amount of data collected and the resulting accuracy. Subsequent to the reported experiments, we built a smaller version of the prototype capsule that is 36 mm in length and 13.5 mm in diameter. Although it is conceivable that the hardware size could be further reduced, we believe this will be sufficient for clinically realistic trials in future work.

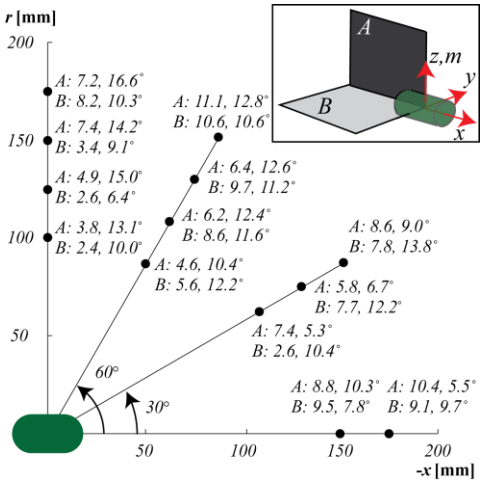

Fig. 2 The inset shows the two orthogonal planes tested. The capsule's **z** axis is aligned with its magnet's dipole axis **m**. On each plane, dots show positions tested. The position (mm) and orientation errors are shown next to the corresponding dot. The radial distance **r** refers to the **z** axis in plane *A* and the –**y** axis is plane *B*.

REFERENCES

[1] P. R. Slawinski, et al. Emerging issues and future developments in capsule endoscopy. *Tech Gastro Endo*, doi: 10.1016/j.tgie.2015.02.006, 2015.

[2] T.D. Than, et al. A review of localization systems for robotic endoscopic capsules. *IEEE Trans. Bio. Eng.*, 59(9):2387–2399, 2012.

[3] A.W. Mahoney and J.J. Abbott. Generating rotating magnetic fields with a single permanent magnet for propulsion of untethered magnetic devices in a lumen. *IEEE Trans. Robotics*, 30(2):411-420, 2014

[4] S. Song, et al. 6-D magnetic localization and orientation method for an annular magnet based on a closed-form analytical model. *IEEE Trans. Mag.*, 50(9):5000411, 2014.

[5] D. M. Pham and S.M. Aziz. A real-time localization system for an endoscopic capsule. In *IEEE Int. Conf. ISSNIP*, 1-6, 2014.

[6] M. Salerno, et al. Magnetic and inertial sensor fusion for the localization of endoluminal diagnostic devices. *I J CARS.*, (S1):229-235, 2012.

[7] C. Di Natali, et al. Real-time pose detection for magnetic medical devices. *IEEE Trans. Mag.*, 49(7):3524-3527, 2013.

[8] M. Salerno, et al. A discrete-time localization method for capsule endoscopy based on on-board magnetic sensing. *Meas. Sci, Technol.*, 23(1):015701, 2012.

[9] S. Yim and M. Sitti. 3-D localization method for a magnetically actuated soft capsule endoscope and its applications. *IEEE Trans. Robotics*, 29(5):1139-1151, 2013.

[10] M. Kim, et al. Position and orientation detection of capsule endoscopes in spiral motion. *Int. J. Prec. Eng. & Manu.*, 11(1):31-37, 2010.

[11] K. M. Popek, et al. Localization method for a magnetic capsule endoscope propelled by a rotating dipole field. *IEEE Int. Conf. Robotics & Auto.*, 5328-5333, 2013.

[12] S. E. Wright, et al. A spherical-magnet end-effector for robotic magnetic manipulation. *IEEE Int. Conf. Robotics & Auto.*, 2015, to appear.

[13] A. W. Mahoney and J. J. Abbott. Control of untethered magnetically actuated tools with localization uncertainty using a rotating permanent magnet. *IEEE Int. Conf. Biomedical Robotics & Biomech.*, 1632-1637, 2012.

Google Glass Guidance: First Clinical Experience in Open Abdominal Aortic Aneurysm Repair

P. Pratt[1], C. D. Bicknell[2], S. Dindyal[3], A. Darzi[1,2]

[1]*Hamlyn Centre for Robotic Surgery, IGHI, Imperial College London, UK*

[2]*Department of Surgery and Cancer, Imperial College London, UK*

[3]*Imperial Vascular Unit, Imperial College Healthcare NHS Trust, London, UK*

p.pratt@imperial.ac.uk

ABSTRACT

To date, applications of Google Glass in the operating theatre, including video streaming for training and telementoring [1], can be characterised by the outward flow of information from the device. No precedents have been set where the platform acts as the delivery mechanism for patient-specific 3D images, providing anatomical guidance at key stages during surgical procedures. In laparoscopic and robotic surgery, the natural destination for such information is the existing display device. Most operating theatres for open interventions have fixed imaging displays, but there is a compelling case for equipping the surgeon with a personal navigation feed, manipulatable in real time, always within the field of view, delivered unobtrusively through a wearable device, so that attention is never diverted away from the surgical field.

Fig. 1 (clockwise from top) First deployment of Google Glass for surgical guidance; Myo gesture control armband; open palm gesture used to engage orientation control.

Under an existing ethical protocol (REC reference 07/Q0703/24), informed and written consent was obtained from a 65 year old male patient requiring open aortic and bilateral common iliac aneurysm repair. Preoperative contrast-enhanced CT imaging was segmented manually to demonstrate the spatial relationship of each ureter to the dilated aneurysm sacs. These mesh-based models were complemented by real-time volumetric renderings of the raw DICOM data, provided by the Fovia HDVR® engine. Powerful hardware facilitated creation of a video stream on-the-fly. This underwent GPU-based H.264 encoding and was served as a RTSP stream to the Google Glass client over a local wireless network.

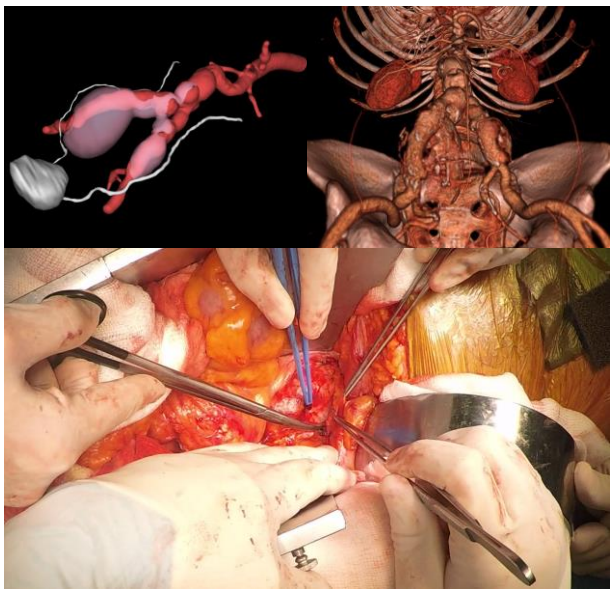

Fig. 2 (clockwise from bottom) Vessel preparation prior to placement of graft; segmented preoperative CT scan showing distorted path of ureters; volumetric rendering of main vessels demonstrating tortuosity and internal iliac origins.

Manipulation of the image viewpoint and orientation was made possible through a wireless Myo gesture control armband worn underneath surgical scrubs. In tandem with a 9-axis inertial measurement unit, proprietary electromyography (EMG) sensors measured electrical activity from forearm muscles, detecting up to five command poses. Auxilliary control was also provided via an existing iPad gesture interface [2] managed by the assistant. Figure 2 (top) illustrates typical images viewed in the display.

ACKNOWLEDGMENTS

The authors are grateful for support from the Hamlyn Centre, BBC News Click, Fovia Inc., and the NIHR Biomedical Research Centre funding scheme.

REFERENCES

[1] Muensterer O, Lacher M, Zoeller C, Bronstein M, Kübler J. Google Glass in Pediatric Surgery: An Exploratory Study. Internation Journal of Surgery 2014 12(4):281-289.

[2] Hughes-Hallett A, Pratt P, Mayer E, Martin S, Darzi A, Vale J. Image Guidance for All – TilePro Display of 3-Dimensionally Reconstructed Images in Robotic Partial Nephrectomy. Urology 2014 84(1):237-243.

Hybrid Actuation for a Bio-inspired Continuum Robotic Manipulator for Surgical Applications

A. Stilli, H. A. Wurdemann, K. Althoefer

Department of Informatics, King's College London, UK

k.althoefer@kcl.ac.uk

INTRODUCTION

Robot-assisted minimally invasive surgery is a research area of continuous evolution. A number of continuum robotic manipulator has been designed to overcome the limitation of traditional rigid instruments. The high number of degrees of freedom of these kinds of robots provides superior redundancy and allows reaching further inside the abdominal cavity of a patient avoiding organs in the way [1], [2]. This capability has been proven to consistently increase the workspace inside the patient body, and, hence, to enhance the efficiency at which the surgeon can conduct minimally invasive surgery (MIS) tasks [3] with a great potential of improving the operation's outcome for the benefit of the patient.

STIFF-FLOP is an EU-FP7 project which aims to create novel soft continuum manipulators taking inspiration from the octopus arm [4] [5]. The soft manipulation concept proposed here is based on an antagonistic actuation mechanism combining extrinsic (tendon-driven) and intrinsic (pneumatic) actuation [6]. This principle is used by nature in various ways, e.g., in the octopus arms which have longitudinal and transversal muscles. Activating both sets of muscles increases the arm's stiffness [7]. A similar behaviour is achieved with the hybrid manipulation principle presented here. By fusing the advantages of both actuation types, the stiffness of the soft manipulator can be varied. The manipulator is able:

- to change its configuration depending on the number of actuated tendons (see Figures 1),
- to vary its length by changing the air pressure in the robot's main body, and
- to vary its stiffness and configuration through the controlled interplay of applied pressure and tendon displacement.

The combination of intrinsic and extrinsic actuation principles has been investigated in a number of works [6]. An example of hybrid actuation is presented in [8] where a combination of pneumatic and electro-mechanical actuation is described proving an enhanced manipulation capability. The idea of a tendon-driven actuation combined with a pneumatic one has been investigated in [2], where each robot segment is composed of a pressurisable chamber divided from the adjoining ones by an aluminium disk to which a set of tendons are attached. In our earlier paper [6], we presented a novel model tendon-driven and pneumatic-actuated soft manipulator.

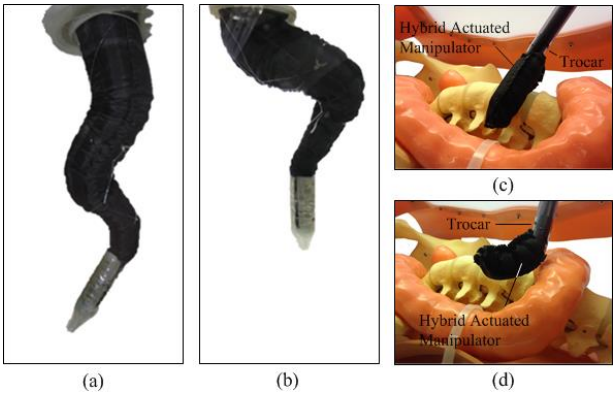

Fig. 1 (a) and (b) Examples of achievable configurations of the manipulator. (c) and (d) Application in minimally invasive surgery .

This paper proposes an evolution of our previously presented manipulator with a novel design conceived specifically for robotic surgery applications (see Figure 1(c) and (d)). Section II presents the overall bio-inspired system and its actuation architecture. Tendons are integrated to tele-operate each section, pressure control and the combination of tendon and pressure actuation is implemented to change the length and stiffness of the robot working antagonistically as in the octopus muscles. The experiments conducted are described along with results in Section III. Section IV summarises the achievements of this paper and presents future works.

MATERIALS AND METHODS

Figure 2 (a) shows the conceptual system architecture of our hybrid-actuated manipulator. 3D and section views of the manipulator are shown in Figures 2(b) and (c), respectively. The geometric structure can be described as a frustum of a cone (truncated cone). The diameter of the manipulator is 40mm at the base and narrows down to 10mm at the tip. The robot is composed of three main components: an inner air-tight and stretchable latex bladder, an outer, non-stretchable (but foldable) polyester fabric sleeve and 12 nylon tendons. The stretchable cylindrical latex bladder is inserted into the cylindrical polyester sleeve. The outer sleeve is 30cm in length when fully inflated. As the fabric material is non-stretchable, the outer sleeve prevents any ballooning of the inner bladder in radial direction beyond its maximum diameter. Whilst morphing from a deflated to

an inflated state, the robot can only expand along its longitudinal axis (elongation). The stiffness of the arm can be controlled adjusting the tendons - e.g., tightening the tendons at a fixed air volume in the sleeve will reduce the robot's length and increase the stiffness. The nylon tendons are guided along the outside of the manipulator sleeve within polyester channels, 90° spaced apart along the perimeter of the outer sleeve (Figure 2(c)). In our three-section prototype, four tendons are fixed to the top of each section of the manipulator (Figure 2 (a)). As Figure 2 shows, the soft manipulator is mounted inside a phantom dome. The 12 tendons that are connected to the three sections are controlled by a system of 12 pulleys. Each pulley is fixed onto the shaft of a stepper motor (Soyo SY57ST56-0606B Unipolar Stepper Motor). By controlling the angular position of the pulley system, it is possible to vary the length of each tendon separately and, hence, the bending of the manipulator.

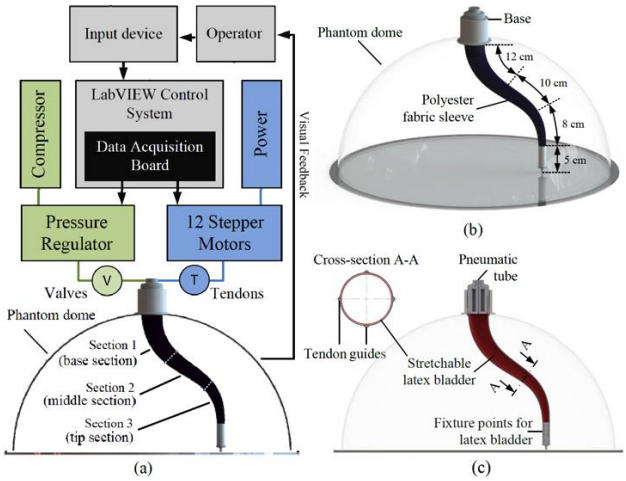

Fig. 2 (a) Conceptual system architecture of the manipulator with three sections and a combination of tendon-driven and pneumatic actuation. CAD drawings of the soft manipulator: (b) 3D and (c) section view.

The stepper motors are connected to bi-polar micro-stepping drivers (Sparkfun Big Easy Driver ROB-11876). The inner latex bladder is connected to one pressure regulator (SMC ITV0010-3BS-Q). The regulator is able to control the air pressure from 0.001MPa to 0.1MPa. An in-built pressure sensor ensures to maintain the desired pressure inside the bladder. The motor drivers and pressure regulator are interfaced via three DAQ cards (NI USB-6211) to LabVIEW software. A joystick (Logic 3 JS282 PC Joystick) is utilized as an input device for the operator.

EXPERIMENTS AND RESULTS

A series of experiments has been conducted in order to explore the stiffness of manipulator. Lateral forces F_1, F_2, F_3 have been exerted to the manipulator, see Figure 3. The experimental results were recorded and are plotted (Figure 3). The internal pressure of the bladder was altered from 0.015 MPa to 0.055 MPa and, hence, the stiffness increased. The maximum force held by the robot was defined as a displacement at the tip of 5 mm was reached. The manipulator is able to hold up to 5.2 N at the tip.

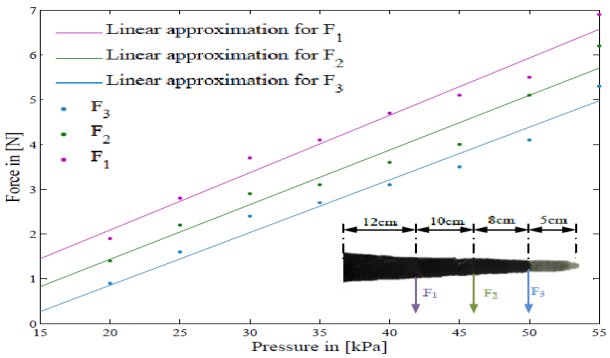

Fig. 3 Experimental results of lateral forces F_1, F_2 and F_3.

DISCUSSION AND FUTURE WORKS

We have presented here our new hybrid and antagonistic actuation system for a continuum soft robotic manipulator fusing pneumatic with tendon-driven actuation. Being inspired by the biological role model, the octopus, our antagonistic actuation system aims at modelling the octopus way of using its longitudinal and transversal muscles in its arms: activating both types of muscles, the octopus can achieve stiffening of its arms – this concept is realised here using tendons and pneumatics to configure the arm and to adjust its stiffness, as shown by the experimental study. In future works, we will explore ways to utilise the empty space within the air-filled bladder, to integrate sensors and actuators for additional tools as may be required in the surgical context.

REFERENCES

[1] R. Buckingham, "Snake arm robots," Industrial Robot: An International Journal, vol. 29, no. 3, p. 242245, 2002.

[2] B. Jones, W. McMahan, and I. Walker, "Design and analysis of a novel pneumatic manipulator," in IFAC Symposium "Advances in Automotive Control", 2004.

[3] J. Shang, D. Noonan, C. Payne, J. Clark, M. Sodergren, A. Darzi, and G.-Z. Yang, "An articulated universal joint based flexible access robot for minimally invasive surgery," in ICRA, pp. 1147-1152, 2011.

[4] M. Cianchetti, T. Ranzani, G. Gerboni, I. de Falco, C. Laschi, and A. Menciassi, "Stiff-flop surgical manipulator: Mechanical design and experimental charaterization of the single module," in IROS, 2013.

[5] J. Fras, J. Czarnowski, M. Macias, J. Glowka, M. Cianchetti, and A. Menciassi, "New STIFF-FLOP module construction idea for improved actuation and sensing," in ICRA, 2015

[6] A. Stilli, H. Wurdemann, and K. Althoefer, "Shrinkable, stiffness controllable soft manipulator based on a bio-inspired antagonistic actuation principle," in IROS, 2014.

[7] F. Maghooa, A. Stilli, K. Althoefer, H. Wurdemann "Tendon and pressure actuation for a bio-inspired manipulator based on an antagonistic principle", in ICRA 2015.

[8] Y. Gutfreund, T. Flash, G. Fiorito, and B. Hochner, "Patterns of arm muscle activation involved in octopus reaching movements," The Journal of Neuroscience, vol. 18, no. 15, p. 5976598, 1998.

Adaptive Filtering of Fibre-optic Fetoscopic Images for Fetal Surgery

E. Maneas[1], G. Sato dos Santos[1], J. Deprest[2], R. Wimalasundera[3], A. L. David[4], T. Vercauteren[1], S. Ourselin[1]

[1]*Translational Imaging Group, Centre for Medical Imaging Computing, UCL, UK*

[2]*University Hospital KU Leuven, Leuven, Belgium*

[3]*Fetal Medicine Unit, University College London Hospital, UK*

[4]*Institute for Women's Health, UCL, UK*

efthymios.maneas.14@ucl.ac.uk

INTRODUCTION

Intrauterine interventions currently rely on the use of a fetoscope as the main intraoperative imaging modality [1]. Fetal surgery could benefit from computational processing of fetoscopic images, such as image mosaicking. However, images from fibre-optic fetoscopes contain a "honeycomb" pattern due the camera oversampling the irregular fibre bundle image guide. This honeycomb pattern distracts the clinician and will adversely affect any subsequent image computing algorithm; thus, a crucial first step in the image-processing pipeline is the removal of the honeycomb pattern.

Previously published methods for the removal of the honeycomb structure include adaptive spectral masking [2] and spatial interpolation methods [3-5]. We chose the spectral masking filter approach because, as opposed to spatial interpolation, it can cope with defocused images where individual fibres cannot readily be distinguished in the honeycomb pattern, and because, once the method is validated, spatial filtering can be readily optimised by GPU implementation. To filter out the honeycomb structure without over-blurring the image, it is important to estimate the optimal cut-off frequency f_c for the filter mask. The optimal f_c depends on the fibre intercore distance and also on the camera focus and zoom levels, which may change during the procedure. We test three different approaches for estimating the optimal f_c from fetoscopic images: (1) by direct measurement of the intercore distance; (2) by estimating the fibre density; or (3) by estimating the honeycomb frequency spectrum. Here we demonstrate that the honeycomb pattern can be robustly filtered using the f_c estimated from any of the three approaches.

MATERIALS AND METHODS

Data. Test images were obtained using a fibre-optic fetoscope and an imaging system (Karl Storz, Germany). The test images include a set of *in vivo* images obtained during an intrauterine procedure.

Estimating f_c from the intercore fibre distance. The locations of the fibres were identified by finding the regional maxima in the image. Then the median distance between adjacent fibres d_{ic} was used to determine f_c as: $f_c = 0.4/d_{ic}$.

Estimating f_c from the fibre density. The imaged fibre density was estimated by measuring the area of the imaged bundle and using the number of fibres in the bundle, n_{fibre}, supplied by the manufacturer. Then the average distance between adjacent fibres d_{ic} was calculated by relying on a hexagonal circle packing assumption as: $d_{ic} = \sqrt{(2 * area)/(n_{fibre} * \sqrt{3})}$. As in the first approach, f_c was then set as: $f_c = 0.4/d_{ic}$.

Estimating f_c in the frequency domain. The FFT of the fetoscopic image was computed and its log amplitude was used to estimate the frequency of the honeycomb pattern. The honeycomb frequency f_{comb} was detected by integrating the log amplitude of the FFT over rings of varying radius, and finding the non-zero radius with the largest average amplitude (Fig. 1). f_c was then determined as: $f_c = 0.4 * f_{comb}$.

Spectral mask filtering. Using the f_c estimated with either spatial or frequency method, fetoscopic images were filtered by applying a smoothed spectral mask in the frequency domain. A circle mask of radius f_c was smoothed with a Gaussian filter to avoid ringing artefacts (std. dev. = 10) and multiplied with the FFT of the image (Fig. 1d). The filtered image was then recovered by taking the inverse FFT of the masked spectrum, and then examined for the removal of the honeycomb pattern.

RESULTS

The optimal f_c was estimated using all three approaches, and the resulting values were within 15.68±2.96% (mean ± std. dev., n=28 images) of one another. The estimates from the first and the third approach differed by 11.04±2.51%. No one method was systematically overestimated or underestimated the f_c.

Images of the USAF-1951 test pattern at different zoom and focus levels were filtered with the spectral mask

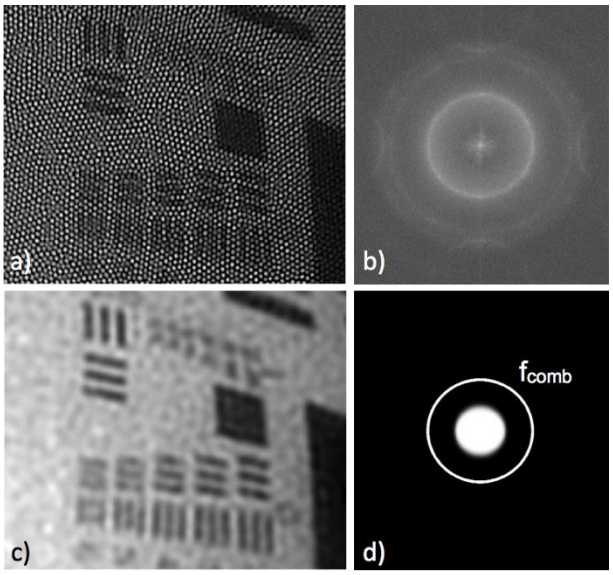

Fig. 1 a) Magnified fetoscopic image of the USAF-1951 test pattern showing the honeycomb pattern, b) Fourier power spectrum of the whole fetoscopic image (logarithmic grey scale), c) Filtered image using estimated f_c = 0.068, d) Ring used for the detection of f_{comb} (inset) and the smoothed mask used for spectral filtering.

using the f_c estimated in the frequency domain, which was generally the median value of the three estimates.

All filtered images had the honeycomb pattern removed while not over-blurring the small structures in the image (Fig. 1).

In vivo images filtered using the estimated f_c also had their honeycomb patterns removed while preserving the finer anatomical details in the image (Fig. 2).

Finally, a comparison between the adaptive spectral filtering and the Gaussian filtering shows that the Gaussian filtering slightly over-blurs the image, while the spectral filtering maintains the edges (Fig. 3).

DISCUSSION

Our results suggest that the honeycomb pattern can be robustly removed from fetoscopic images at different focus and zoom levels by estimating the optimal cut-off frequency and applying a filter. The cut-off frequency for the filter mask could be estimated using any of the three proposed approaches. Future work will focus on speed optimisation by re-estimating f_c only when a change in zoom or focus is detected, and designing a fast filter as done in [6] but with spectral characteristics that are closer to an ideal circular band-pass filter without the ringing artefacts.

ACKNOWLEDGMENTS

This work was supported through an Innovative Engineering for Health award by the Wellcome Trust [WT101957]; Engineering and Physical Sciences Research Council (EPSRC) [NS/A000027/1].

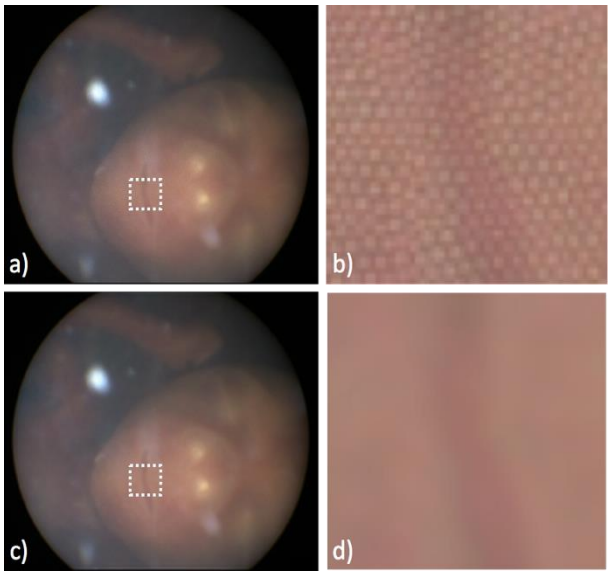

Fig. 2 a) *In vivo* fetoscopic image (dashed rectangle: ROI), b) Magnified ROI showing the honeycomb pattern, c) Filtered fetoscopic image using estimated f_c = 0.064, d) Magnified ROI of the filtered image.

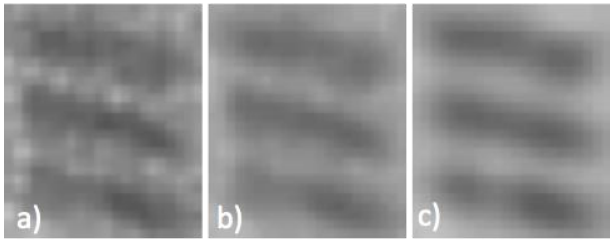

Fig. 3 a) Filtered image using a Gaussian filter with $\sigma = 0.4*d_{ic}$, b) The same as in a) but with $\sigma = 0.5*d_{ic,}$ c) Filtered image using the estimated f_c as in Fig. 1c.

REFERENCES

[1] Gratacós E., Ville, Y., and Deprest J. Obstetric Endoscopy. In *Ultrasound and Endoscopic Surgery in Obstetrics and Gynaecology*, pp. 332-340. 2003, Springer London.

[2] Winter C., Rupp S., Elter M., Munzenmayer C., Gerhauser H. and Wittenberg T. Automatic Adaptive Enhancement for Images Obtained With Fiberscopic Endoscopes. IEEE Trans Biomed Eng. 2006 Oct; 53(10):2035-46.

[3] Elter M., Rupp S., and Winter C. Physically motivated reconstruction of fiberscopic images. Proc of 18th Intl Conf on Pattern Recognition 2006:(3)599-602.

[4] Le Goualher G., Perchant A., Genet M., Cave C., Viellerobe B., Berier F., Abrat B., and Ayache N. Towards optical biopsies with an integrated fibered confocal fluorescence microscope. In Proc. of MICCAI '04, 2004, pp. 761–768.

[5] Savoire N., André B., and Vercauteren T. Online blind calibration of non-uniform photodetectors: Application to endomicroscopy. In Proc. of MICCAI'12, 2012, pp. 639–646.

[6] Vidal-Migallón I., Commowick O., Pennec X., Dauguet J., and Vercauteren T. GPU & CPU implementation of Young-Van Vliet's Recursive Gaussian Smoothing Filter. Insight Journal (ITK) 2013, 16.

SmartLiver Image Guidance System for Laparoscopic Liver Resection

S. Thompson[1], J. Totz[1], Y. Song[1], S. Johnsen[1], D. Stoyanov[1], S. Ourselin[1], K. Gurusamy[2], C. Schneider[2], B. Davidson[2], D. Hawkes[1], M. J. Clarkson[1]

[1]*Centre for Medical Image Computing, University College London, United Kingdom*

[2]*Division of Surgery and Interventional Science, UCL Medical School, United Kingdom*

s.thompson@ucl.ac.uk

INTRODUCTION

Minimally invasive surgery, both robotic and laparoscopic, has demonstrable benefits for the patient [1]. However, inability to distinguish different tissues and target lesions reduces eligibity for laparoscopic surgery. Image guidance using previously acquired imaging has the potential to mitigate these effects increasing eligibity for minimally invasive surgery. We present the "SmartLiver" image guidance system for image guided laparoscopic and robotic liver resection.

Existing image guidance systems for the liver [2,3] rely on separate probes to locate points on the liver surface relative to the theatre coordinate system. With sufficiently long digitizing probes these systems can be used for laparoscopic as well as open surgery. However, as well as requiring an additional tool in theatre they do not locate the laparoscope relative to the liver, precluding the use of augmented reality on the laparoscope's display. The SmartLiver guidance system addresses these two short comings by using a tracked stereo laparoscope to locate the liver surface.

This paper describes the system, results of validation experiments on porcine and phantom models and initial results from first use in humans.

MATERIALS AND METHODS

Prior to surgery, contrast enhanced CT images of the patient are segmented[1] to surface models of the relevant anatomy. During surgery the HD stereo laparoscope (Viking HD) acquires image pairs of the liver surface. Fast feature matching [4] and triangulation are used to reconstruct surface patches relative to the laparoscope.

In practice the size of these patches is limited to less than 40 cm^2 by the narrow stereo separation (4.5 mm) of the stereo laparoscope. A patch of this size is insufficient to enable registration of the liver surface, so multiple patches are composited using the position of the laparoscope determined by an Optotrak Polaris Spectra tracking system. Figure 1 shows 9 such patches overlaid on a silicone phantom used for development and validation.

[1]Segmentation by http://www.visiblepatient.com/

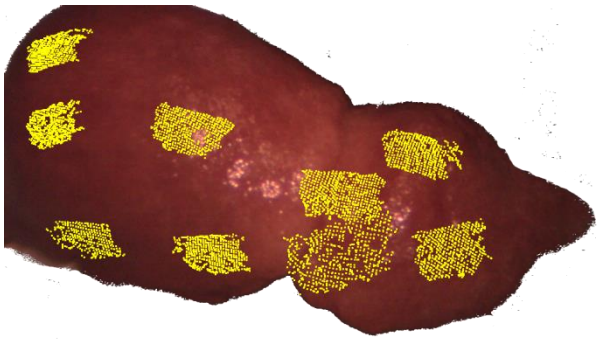

Fig. 1 Reconstructed Patches up to 40 cm^2 are composited using tracking data to enable rigid ICP registration.

Registration of the composited patches to the segmented liver surface is performed using a rigid iterative closest point algorithm. Initialisation of the registration is performed manually. An initial estimate of the liver position is refined by using a second object tracked by the Spectra to move the liver in six degrees of freedom. Any tracked object can be used for this. We use an off the shelf sterile object so the alignment can be performed by the surgeon.

The software is implemented using the NifTK[5] platform. The system has been tested and the accuracy assessed on a silicone phantom and 3 pigs. Accuracy was measured by picking landmarks on the video and model, and measuring the distance between the landmarks on a plane parallel to the video screen, see Figure 2.

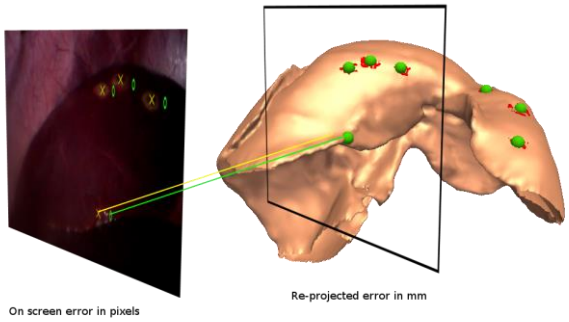

Fig. 2 System errors were calculated by manually picking landmark points in the video, and measuring their distance to the model points on a plane parallel to the screen.

RESULTS

On the phantom the system achieved RMS errors of 2.9 mm based on 791 samples of 9 subsurface landmarks. The 3 porcine experiments gave an average RMS error of 9.4 mm based on between 234 and 483 samples of 4 to 6 surface landmarks.

Registration was achieved in under 5 minutes on the phantom, and in under 15 minutes on the pigs. The longer time taken on the pigs was due to the increased difficultly in performing initial manual registration under the influence of non-rigid and dynamic deformation, mainly due to breathing motion.

The system has been used on four human cases to date with more ongoing. The human cases have demonstrated that the system can be used practically within current clinical practice. There appears to be less dynamic deformation (breathing) in the human cases and the liver anatomy is significantly simpler, indicating that the accuracy on human cases could be better than in the pigs. However, we are currently having to adapt the system to cope with the smaller human liver and less available landmarks for accuracy assessment.

DISCUSSION

The SmartLiver system presented here enables image guidance during laparoscopic liver resection. The current system has been tested in-vivo on pigs and on humans and shown to enable registration and visualisation in theatre. The system accuracy is currently around 9 mm on pigs, but is likely to be slightly better on humans.

Human trials are ongoing with the current system. We are measuring the clinical outcomes together with Likert Scale based questionnaires to assess the system performance during the human trials. By correlating these measures with assessment of the system accuracy and user interface design, we hope to show how these parameters could affect clinical outcomes.

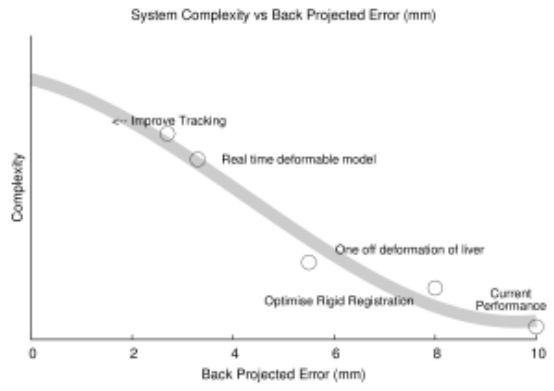

Fig. 3 The results can be used to isolate sources of error and create a development road map for this and other abdominal image guidance systems.

The results of the pig and phantom experiments were analysed to determine the contribution of different error sources to the overall system error. Understanding the error sources enables the construction of a system development road map, Figure 3, showing how ongoing developments should impact the system performance.

Using the NifTK software platform we have developed several pluggable modules to improve the system performance. We have implemented a deformable registration algorithm though at present the surface patches do provide sufficient constraints for this to work. We are also investigating using subsurface landmarks imaged using laparoscopic ultrasound. Development of these novel algorithms is ongoing in parallel to the clinical implementation of the basic system.

ACKNOWLEDGEMENTS

This publication presents independent research commissioned by the Health Innovation Challenge Fund (HICF-T4-317), a parallel funding partnership between the Wellcome Trust and the Department of Health. The views expressed in this publication are those of the authors and not necessarily those of the Wellcome Trust or the Department of Health. The authors also thank NVIDIA for the kindly donated Quadro K5000 and SDI capture card. We also thank CONMED and IRCAD for their support.

REFERENCES

[1] K. Nguyen, J. Marsh, A. Tsung, J. Steel, T. Gamblin, and D. Geller, “Comparative benefits of laparoscopic vs open hepatic resection: A critical appraisal,” Archives of Surgery 146(3), pp. 348–356, 2011.

[2] M. Peterhans, A. vom Berg, B. Dagon, D. Inderbitzin, C. Baur, D. Candinas, and S. Weber, “A navigation system for open liver surgery: design, workflow and first clinical applications,” Int J Med Robot. 7(1), pp. 7–16, Mar 2011.

[3] N. C. Buchs, F. Volonte, F. Pugin, C. Toso, M. Fusaglia, K. Gavaghan, P. E. Majno, M. Peterhans, S. Weber, and P. Morel, “Augmented environments for the targeting of hepatic lesions during image-guided robotic liver surgery,” Journal of Surgical Research 184(2), pp. 825 – 831, 2013.

[4] J. Totz, S. Thompson, D. Stoyanov, K. Gurusamy, B. Davidson, D. J. Hawkes, and M. J. Clarkson, “Fast Semi-dense Surface Reconstruction from Stereoscopic Video in Laparoscopic Surgery,” in Information Processing in Computer-Assisted Interventions, Lecture Notes in Computer Science 8498, pp. 206–215, Springer International Publishing, 2014.

[5] M. J. Clarkson, G. Zombori, S. Thompson, J. Totz, Y. Song, M. Espak, S. Johnsen, D. Hawkes, and S. Ourselin, “The NifTK software platform for image-guided interventions: platform overview and niftylink messaging,” International Journal of Computer Assisted Radiology and Surgery , pp. 1–16, 2014.

Pediatric Surgical Robot (PSR) – MRI-guided Bone Biopsy System

T. Looi[1,2], L. Ma[3], Y. Yi[3], A. Goldenberg[2,3], J. Amaral[1,2], J. Drake[1,2]

[1]*The Hospital for Sick Children, Canada*
[2] *University of Toronto, Canada*
[3]*Engineering Services Inc, Canada*

thomas.looi@sickkids.ca

INTRODUCTION

Magnetic resonance imaging (MRI) provides high resolution soft and hard tissue imaging where its' non-ionizing radiation property is ideal for paediatric patients. However, despite these advantages, it remains primarily a diagnostic device because of the challenges in developing non-ferrous tools that can work in the magnetic field without impacting image quality and tool performance. MRI-compatiable robots have been developed in the areas of neurosurgery, prostate and breast biopsy but they are not capable of imaging and treating bone conditions. [1-4]

Bone tumours account for 6% of paediatric patients where they are most common between ages 10-20. [5] A bone biopsy involves taking a core sample (~4.4mm diameter) of the bone with a manual hollow serrated needle. Clinicians have used MRI to target the lesion and avoid injuring critical vessels and nerves but it requires moving the patient in/out of the MRI scanner and using an adhoc needle placement. The biopsy procedure is complex as it requires a significant amount of force and coordination to manually obtain the core sample in the MR environment.

To address this problem, we have developed a modular MRI-guided paediatric surgical robot (PSR) for bone biopsy. The system is designed to allow the clinician to simultaneously image and perform the procedure with greater precision and less time.

MATERIALS AND METHODS

The PSR is developed as a collaborative effort between interventional radiology, neurosurgery and private sector (Engineering Services Inc). The major system requirements for PSR included: 3T MRI compatibility, in-bore intra-operative capability, mechanical rigidity and strength sufficient for bone drilling. The system diagram is shown in Figure 1.

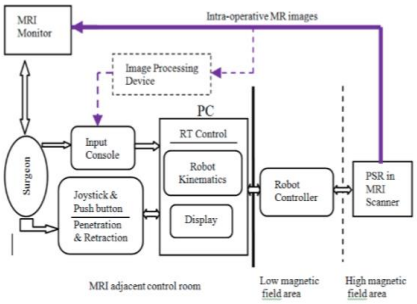

Fig. 1 – PSR System Diagram.

The goal is to allow the clinician to select the bone target from pre-operative imaging and then allow the PSR to take the core sample while simultaneously imaging to track the needle location.

The system is designed to be modular and reconfigurable to accommodate for a variety of pediatric patient sizes and potential applications. There are 5 generic modules: linear motion module, turret module, elbow roll module, wrist tilt module and penetration module. The module casings were created in plastic using stereo lithography (SLA) and ultrasonic motors. Non-ferrous metal brass was used as fasteners and gearboxes. The linear module provides a translation stroke motion of up to 30mm with a mass of 0.3 kg. The turret and elbow roll module are rotational modules that provide up to 360 degree rotation with a mass of 0.25 kg. The wrist tilt module is design a "horseshoe" where it secures and rotates a tool. The penetration module provides linear translation for up to 90mm and it has a flexible force sensor (FlexiForce A201) mounted.

For the bone biopsy procedure, a tool module is a designed to mimic the manual bone biopsy procedure. It carries a clinical serrated hollow titanium biopsy needle (Invivo) with three concentric cylinders: a pointed solid rod for initial anchoring, hollow serrated cutting drill bit and a solid protective sleeve. This allows the system to take 25 mm bone core sample. See Figure 2 – Right.

A mobile arch system has been developed that translates the PSR along the axis of the MR table. The modules can be secured in a variety of orientations such as on the MRI table or arch to reach different clinical targets. The PSR has up to 5 degrees of freedom with an additional separate tool actuation. See Figure 2 – Left.

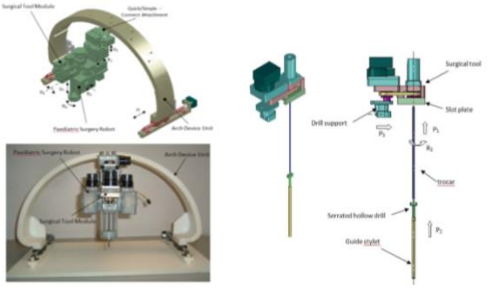

Fig. 2 – Left: PSR System, Right: Surgical Tool Module.

The robot controller box is designed to be placed within the MR room beyond the 5 Gauss field line. It is interfaced to the control PC through a penetration panel.

For MRI compatibility testing, the system was mounted on the MR bed in a Philips Achieva 3.0T MRI scanner and two phantoms (Philips mineral oil phantom

and a watermelon) were used for imaging testing. The phantoms were scanned with a Flex-M coil. A series of interventional T1-w, T2-w and T2*-w imaging sequences were conducted in both axial and coronal planes (2D fast spin echo (FSE), 2D fast gradient echo (GRE), 2D FIESTA and 3D fast spoiled gradient (FSPGR)). Each of the sequences were conducted under 3 states (system – power on, system – power on, system – motors in motion).

For drilling performance, PSR drilling tests were conducted on polyurethane foam blocks (density 15-40) that simulated human cancellous bone and chicken bone.

RESULTS

The workspace of the system is described in table 1 (joint limits). The system is capable of translation linearly along the MR table bed up to 100mm and the surgical biopsy needle can be detached and sterilized separately from the robotic system. The system can be driven in joint and Cartesian space.

Table 1 – PSR Joint Workspace

Vertical linear module	30 mm
Turret roll module	140 degrees
Elbow roll module	140 degrees
Wrist tilt module	40 degrees
Arch linear motion	100 mm
Drill penetration module	90 mm
Biopsy tool module	25 mm

MR imaging testing showed that the PSR did not adversely impact the MR scan sequences (Figure 3) with minimal change to the image quality and signal to noise ratio for the all the imaging sequences. This was for PSR present (no power), PSR present (powered on) and PSR moving.

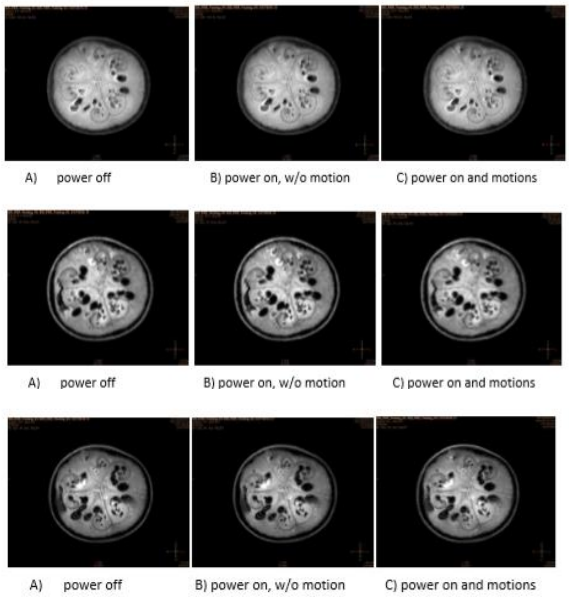

Fig. 3 – Top: FSE, Middle: FGRE, Bottom: FIESTA.

Results from drilling testing showed that the PSR is capable generating sufficient force to drill through simulated bone phantoms with 15-40 density as well as fresh chicken bone samples. See Figure 4. For the bone testing, core samples were successfully retrieved from flat regions of the bone.

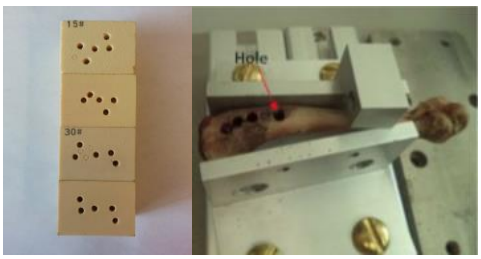

Fig. 4 – Left: Bone phantom, Right: Chicken Bone.

DISCUSSION

During drilling, it was noted that if the PSR was attempted to drill a narrow cylindrical sample (diameter of bone < drill), the serrated needle would not be able to "catch" the bone and slip off the surface. This problem also appeared during off-centre insertion where the PSR drill bit was not completely on the surface. In these scenarios, it appeared the overall system stiffness of the PSR was not sufficient to hold the system in place during an off-centre or high curveature drilling. Additional work is being conducted to analyze and improve the overall system focusing on gearbox backlash and the plastic frame. In addition, the drilling algorithm is being refined with clinician input to mimic the circular and axial insertion motion to account of off-centre bone sampling.

To improve the range of motion, a motorized rotational arch mechanism is being designed that will allow the PSR to rotate around the MRI bore. From an integration prospective, pre- and intra-operative software is being developed to allow the clinician to image, plan and execute the procedure from a dedicated console using the forward and inverse kinematics.

The PSR demonstrated that it can be operated within the MR bore during imaging with minimal impact to image quality. The system is able to able drill and take core samples from simulated bone samples and chicken bone while simultaneously imaging the target. Further invivo animal testing is being planned to validation its' performance.

REFERENCES

[1] Sutherland GR, McBeth PB, Louw DF. NeuroArm: An MR Compatible Robot for Microsurgery. Computer Assisted Radiology and Surgery 1256: 504-508, 2003

[2] Su H, Iordachita I, Yan X, Cole GA, Fischer GS. Reconfigurable MRI-Guided Robotic Surgical Manipulator: Prostate Brachytherapy and Neurosurgery Applications. Proc. of 33rd Int. Conf. IEEE Engineering in Medicine and Biology, Boston, USA, August 2011.

[3] IGAR Breast System: MRI Breast Biopsy and Ablation [Online]. http://csii.ca/robotic_development/igar

[4] Melzer A, Gutmann B, Remmele T, Wolf R, Lukoscheck A, Bock M, Bardenheuer H, Fischer H. INNOMOTION for Percutaneous Image-Guided Interventions. IEEE Engineering in Medicine and Biology, May/June 2008.

[5] Bone cancer stats (http://www.ped-onc.org/diseases/SOCC.html#bone cancer)

Calibration-free Gravity Compensation for Cooperative Manipulation

P. Wisanuvej, J. Liu, K. Leibrandt, G.-Z. Yang
The Hamlyn Centre for Robotic Surgery, IGHI, Imperial College London, UK
piyamate.w12@imperial.ac.uk

INTRODUCTION

Direct manipulation of a robot is a common approach in human robot cooperative settings, furthermore it is ideal for human intervention in safety critical situations. For direct manipulation of compliant robotic arms, two critical issues must be resolved: weight compensation and compliant control. Weight compensation minimises the payload on the operator's hand by compensating the mass of tools and robot. Compliant control accurately senses the operator's manipulation intention and moves the arm accordingly. A number of design strategies have been proposed to address these two issues. The Baxter robot (Rethink Robotics, USA) has elastic joints with springs for weight compensation. However, these non-rigid joints have problems of low accuracy and low stiffness over the arm. When using rigid joints on robotic arms, in the Lightweight Robot (LWR) (Kuka Roboter, Germany) and the MIRO (DLR, Germany), multiple single-axis torque sensors are fixed on all joints to sense the torque raised from the distal end-effector side or the other part of the arm body. Precise weight calibration of the tool and the robot is required to conduct the weight compensation and to prevent motion drift when the operator leaves the robot arm with the tool alone. Changing tools may incur system instability due to the weight difference or moment of inertia difference among different tools. It is practically inconvenient to re-calibrate the system for each time changing the tool.

In this paper, we propose a calibration-free cooperative manipulation method. In brief, a force sensor is mounted between the tool and a manipulation knob held by the operator. Tools with different weight can be freely exchanged during the manipulation without tool recalibration or change of settings. The sensitivity range for the manipulation force can be adjusted in a wide range according to the specific requirements. From the experimental results with a tool insertion task, this method has a similar outcome compared to the joint level torque sensing method implemented on the LWR.

MATERIALS AND METHODS

The proposed calibration-free cooperative manipulation method is designed to be suitable for most robotic manipulators since it only relies on the robot's position controller. A force sensor is installed to the end-effector to measure the hand manipulation force. Unlike conventional methods that have the sensor mounted between the robot and the tool, the force sensor is placed such that the manipulation force is decoupled from the tool's weight. An example setup is shown in Fig. 1. The control scheme for cooperative manipulation is implemented by commanding the robotic end-effector position according to the force measurements of the sensor. First, the sensor's raw reading is subtracted with the initial force to account for force offset readings and the weight of the knob. To generate motion from the manipulation force, the force reading $\boldsymbol{F}$ is converted to velocity by multiplying it with a constant gain value K_v. This gain can be adjusted depending on the desired sensitivity. In order to reduce the noise during an idle state, a threshold $\boldsymbol{F}_t$ is applied beforehand. This threshold also provides stability by imposing an initial force required to move the tool.

$$\boldsymbol{V}_v = K_v(\boldsymbol{F} - \boldsymbol{F}_t) \tag{1}$$

$$\boldsymbol{F}_t = \begin{cases} \boldsymbol{F}, & \boldsymbol{F} \leq \boldsymbol{Th} \\ \boldsymbol{Th}, & \boldsymbol{F} > \boldsymbol{Th} \end{cases} \tag{2}$$

where $\boldsymbol{Th}$ is the initial force parameter.

$\boldsymbol{V}_v$ is then fed as an input for a trajectory generator to produce a position command for the robot. A maximum acceleration parameter, is used to limit the acceleration of the robot at this stage.

An experiment is setup to evaluate the performance of the proposed method as well as to compare it with the joint torque sensor based approach. The setup is illustrated in Fig. 2, which consists of a light-weight Hamlyn Arm and a Mini40 Force/Torque Sensor by ATI Industrial Automation (NC, USA). The Hamlyn Arm is a 6 degrees-of-freedom robotic arm incorporating harmonic drive gears with a new magnetic absolute angular position encoder. It is also equipped with a motion controller that performs PID position control on-board.

An asynchronously running inverse kinematic solver, using the damped-least-square (DLS) Jacobian based algorithm [3], converts the desired pose in task space to a position command in joint space.

The control software is implemented in C++ running on Scientific Linux 6.6 with a real-time kernel. Reflexxes Velocity-based Type II On-Line Trajectory generator [2] is used in task-space to convert a velocity command to a position command. The same setup can also be applied to the LWR.

RESULTS

A tool insertion task is used to validate the proposed methods on the LWR. The task for each participant is to pick-up and move the tool tip from a starting point P_0 to the entry point of the tube P_1 by holding only the knob with one hand. The tool should be guided along the centreline of the tube until the tooltip reaches the exit

point P_2. Participants are asked to perform the task three times, with different tool weights and control scheme between tasks.

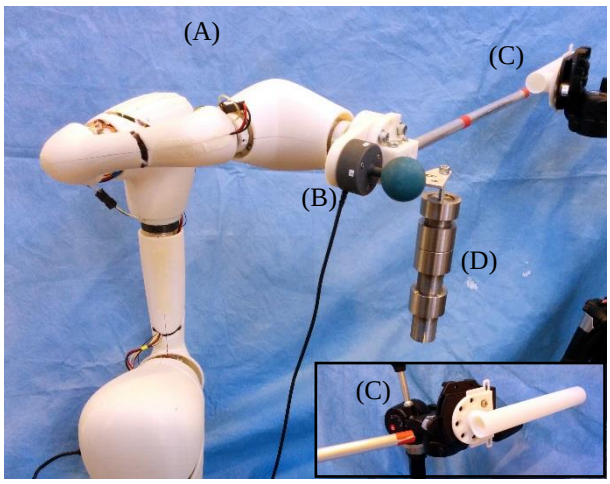

Fig. 1 System Overview: (A) Arm, (B) Force Sensor, (C) Tools for the insertion task, (D) Variable tool weight

The light and heavy tool are weighted 0.8kg and 1.4kg respectively. The control methods used are the LWR's gravity compensation and our force sensor based control method. Therefore, there are four variations of parameters for this experiment in total. They are denoted as *LWR-Light*, *LWR-Heavy*, *FT-Light*, and *FT-Heavy*.

Fig. 2 Hamlyn Arm, with enlarged view of its joint

In order to evaluate the effects of manipulating an un-calibrated tool, the LWR is only calibrated with the light tool. Hence, the user is expected to perceive 0.6 kg-equivalent tool weight with *LWR-Heavy* manipulation task. The orientation of the arm is always maintained in the horizontal pose by setting its rotational stiffness to the maximum. In case of the proposed methods, the LWR runs in position control mode.

Table I Experimental results showing the mean values ± SD and minimum–maximum values in parenthesis.

	LWR-Light	**LWR-Heavy**	**FT-Light**	**FT-Heavy**
Time (s)	**4.33** ± 1.94 (2.67–9.47)	5.30 ± 3.06 (2.25–12.54)	4.91 ± 1.51 (3.17–7.85)	5.08 ± 2.19 (2.99– 9.48)
Deviation (mm)	3.89 ± 1.84 (0.14–9.27)	3.83 ± 1.90 (0.06–9.63)	3.47 ± 1.70 (0.04–10.14)	**3.22** ± 1.53 (0.06–7.43)
Force (N)	7.32 ± 0.91 (3.88–11.66)	11.98 ± 1.53 (6.20–15.28)	1.44 ± 0.43 (0.0–4.81)	**1.42** ± 0.35 (0.01–3.72)

Each participant is given 10 minutes to get familiar with the system in all task variations. There are total of 5 participants who took part in the experiments, resulting in 60 recorded tasks. The results are summarised in Table I. Only the manipulation within the tube region (between P_1 and P_2) is analysed while the rest is discarded. Three performance metrics for each are calculated: completion time, position deviation from the tube centreline, and manipulation force. A demonstration video of the control scheme implemented on the Hamlyn Arm and LWR is available online at http://goo.gl/MU9nB3.

DISCUSSION

In this paper, we presented a calibration-free gravity compensation method based on tool mounted force sensor. It has a wide range of manipulation sensitivity settings to account for manipulation tasks where some friction is required for motion steadiness. In tasks where small manipulation forces are preferred, a sensitivity as low as 0.03 N is achieved.

Implementing gravity compensation with joint torque sensors, requires complex joint construction as well as complex low level-joint torque control algorithms. The proposed methods achieve similar functionality with comparable performance for simple manipulation tasks. Additionally, the manipulation force can be adjusted down to a lower level. All these can be implemented on any robotic arm with a position controller, which is simple in terms of hardware and software.

One disadvantage of our method is that contact forces between the tool and the environment are not detectable. In applications where the contact force must be limited, direct positioning of a force sensor at the tool tip or active constraints can be implemented to overcome this issue.

REFERENCES

[1] Hvilshøj, M.; Bøgh, S.; Skov Nielsen, O. & Madsen, O. "Autonomous industrial mobile manipulation (AIMM): past, present and future." Industrial Robot: An International Journal, 2012, 39, 120-135.

[2] Kroger, T. "Opening the door to new sensor-based robot applications—The Reflexxes Motion Libraries." Robotics and Automation (ICRA), 2011 IEEE International Conference on. IEEE, 2011.

[3] Y. Nakamura and H. Hanafusa, "Inverse kinematic solutions with singularity robustness for robot manipulator control," J. Dynamic Systems, Measurement, and Control, vol. 108, pp. 163–171, 1986.

Occupational Radiation Exposure During FEVAR: A Stage-By-Stage Analysis; Targets for Robotic Intervention

M. M. Li[1], C. D. Bicknell[1,2], S. Cheung[1], N. Burfitt[2], R. Thomas[2], M. Jenkins[2], N. Cheshire[1,2], M. Hamady[2], C. V. Riga[1,2]

[1] *Division of Surgery, Department of Surgery and Cancer, Imperial College London, United Kingdom,*

[2] *Imperial Vascular Unit, Imperial College Healthcare NHS Trust, London, United Kingdom*

mimi.li10@imperial.ac.uk

BACKGROUND

The last two decades have witnessed a paradigm shift to an endovascular, minimally invasive approach in treating diseases of the aorta and its branches, with clear advantages in terms of morbidity and mortality [1,2]. All endovascular procedures are currently performed under fluoroscopic X-ray guidance; radiation exposure is therefore important to consider. Technically complex cases inevitably take longer to perform, increasing radiation exposure. Complex patient anatomy and suboptimal fluoroscopic imaging can make endovascular manipulation challenging. Conventional endovascular catheter technology contributes to these technical impediments; with a limited repertoire of shapes, they are difficult to steer and lack active manoeuvrability. This can hinder overall stability and control at key target areas requiring frequent catheter changes, risking loss of access. Relatively inaccessible anatomical targets may lead to prolonged instrumentation carrying significant risks to the patient (embolization, stroke, vessel wall trauma) with increased fluoroscopic exposure and long overall procedure times for both patients and staff. Endovascular robotic technology in the arterial tree is a novel concept, however pre-clinical outcomes are encouraging and clinical experience is growing [3,4,5].

METHODS

Radiation exposure data was collected prospectively during 19 consecutive FEVAR cases over a 14-month period at a tertiary referral centre. 10 of these cases involved robotic manipulation of the renal arteries. Robotic manipulation is a new technology and a novel concept in endovascular intervention, entailing an inherent learning curve. Previous work has shown this learning curve to be shorter than conventional manual techniques [6]. Operators in this study were experienced in both conventional (n>300) and robotic (n>30) approaches.

Digital over-lead dosimeters measured operator exposure (OE) during pre-defined procedural stages. Patient exposure (PE) for the entire procedure was also measured. Cannulation technique (robotic/manual), operator positioning, c-arm angulation, procedure and fluoroscopy times were noted. Non-parametric tests were used for comparisons. The robotic system is remotely-operated, however it should be noted that "negligible" readings were recorded as the dosimeter sensitivity threshold (0.03mSv cases 1-10; 0.01mSv cases 11-19) rather than 0.

RESULTS

Median OE per case was 0.37mSv[IQR(0.23–0.65)] compared with 1.68mSv (0.98–2.84) for PE. OE readings per stage were: stent alignment [0.03(0.03–0.27)], renal cannulation [0.03(0.03–0.03)], visceral cannulation [0.08(0.03–0.22)], completion [0.11(0.03–0.26)]. OE during visceral cannulation was significantly higher compared to renal cannulation ($p<0.001$).

There were no significant differences in procedure time and OE between manual and robotic techniques, despite the robot being used for more anatomically challenging cannulations. OE was significantly affected by operator positioning, with the highest doses observed in the cephalad position [0.09(0.03–0.27)] during visceral vessel manipulation via the axillary/brachial approach ($p<0.001$).

CONCLUSIONS

Operator and patient radiation exposure for FEVAR is considerable and higher than reported figures for conventional EVAR. With increasing caseloads and anatomical complexity, a significant cumulative OE is likely. Radiation awareness and staff education is therefore essential. Alternative approaches such as remote robotic navigation for high-risk stages should be explored.

FEVAR = Fenestrated Endovascular Aneurysm Repair
EVAR = Endovascular Aneurysm Repair

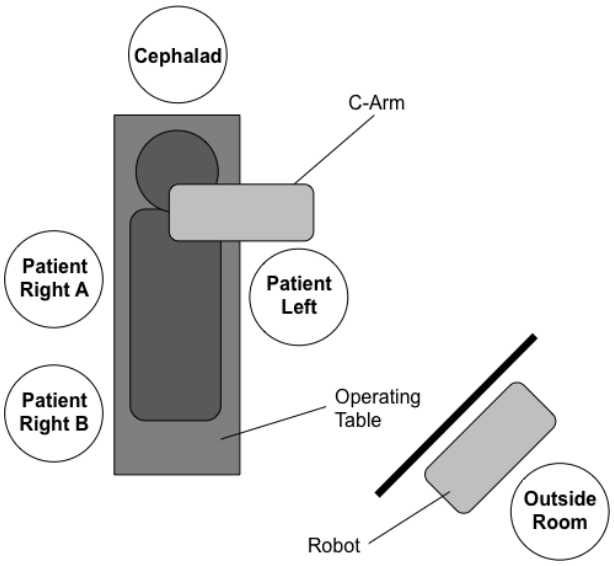

Fig. 1 Classification of operator positioning.

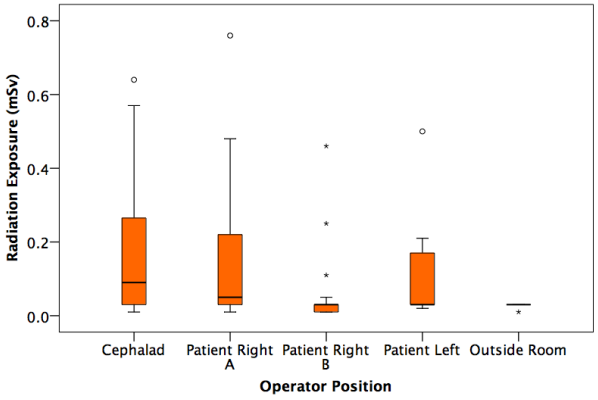

Fig. 2 Occupational exposure by position: OE was significantly affected by positioning (p=0.005), with the highest being at "Cephalad" and "Patient Right A" positions.

REFERENCES

[1] Schermerhorn ML, O'Malley AJ, JhaveriA, Cotterill P, Pomposelli F, Landon BE. Endovascular vs. open repair of abdominal aortic aneurysms in the Medicare population. N Engl J Med 2008; 358: 464–474.

[2] Greenhalgh RM, Brown LC, Kwong GP, Powell JT, Thompson SG. Comparison of endovascular aneurysm repair with open repair in patients with abdominal aortic aneurysm (EVAR trial 1), 30-day operative mortality results: randomised controlled trial. Lancet 2004; 364: 843–848.

[3] Riga CV, Cheshire NJ, Hamady MS, Bicknell CD. The role of robotic endovascular catheters in fenestrated stent grafting. J Vasc Surg. 2010;51(4):810-9; discussion 819-20.

[4] Riga CV, Bicknell CD, Rolls A, Cheshire NJ, Hamady MS. Robot-assisted Fenestrated Endovascular Aneurysm Repair (FEVAR) Using the Magellan System. J Vasc Interv Radiol. 2013 Feb;24(2):191-6.

[5] Bonatti J, Vetrovec G, Riga C, Wazni O, Stadler P. Robotic technology in cardiovascular medicine. Nat Rev Cardiol. 2014 May;11(5):266-75.

[6] Riga CV, Bicknell CD, Sidhu R et al. Advanced catheter technology: is this the answer to overcoming the long learning curve in complex endovascular procedures. Eur J Vasc Endovasc Surg. 2011;42(4):531-8.

Augmented Visualization for Robotic Prostatectomy

X. Luo[1], U. L. Jayarathne[1], S. E. Pautler[2], T. M. Peters[1]

[1]*Robarts Research Institute, Western University, London, Canada*

[2]*Department of Urology, St. Joseph's Hospital, London, Canada*

{xluo, ujayarat, tpeters}@robarts.ca, stephen.pautler@sjhc.london.on.ca

INTRODUCTION

Nowadays robotic prostatectomy is widely performed for minimally invasive prostatic tumor resection. It uses stereoscopic laparoscopes to intuitively visualize the organ surface in the body and manipulate various surgical tools. Unfortunately, the insufficient light sources and the relatively narrow field of view of the binocular stereoscopic laparoscope usually limit the high-quality visualization on the organ being operated on and its anatomical surroundings. Moreover, these limitations affect surfuce structures (e.g., neurovascular bundle) and disable surgeons to accurately perceive the surgical field (e.g., subtle bleeding areas), potentially increasing risks in robotic prostatectomy.

This study aims to accurately recognize subtle surface structures and visualize regions of interest in prostate surgery. Based on color constancy [1], the human visual system has a relatively constant awareness of the color of objects under illumination differences. This implies that the human color perception generally depends on the reflectance of objects but not the scene illumination. Hence, the fidelity and quality of images or videos can be augmented by removing the illumination component.

This work is basically motivated by color constancy. To model human color constancy, Retinex is currently a popular and effective approach [2]. This paper proposes Retinex processing to deal with the aforementioned limitations occurred in robotic prostatectomy. Retinex-augmented visualization enables surgeons to accurately identify subtle surface details and plainly perceive the anatomical surroundings of the organ being operated on.

MATERIALS AND METHODS

The Retinex-augmented visualization approach consists of three main steps: (1) Gaussian convolution, (2) color restoration, and (3) histogram equalization. Fig. 1 shows the flowchart of Retinex processing for augmentation.

Gaussian convolution. Suppose that (x, y) is a pixel on a color image I_c with three channels of red, green, and blue $c \in \{R, G, B\}$. For each pixel $I_c(x, y)$ in each channel, we perform the Gaussian convolution and the logarithmic transformation and obtain $\phi_c(x, y)$:

$$\phi_c(x, y) = \log I_c(x, y) - \log(G_m(x, y) * I_c(x, y)), \quad (1)$$

$$G_m(x, y) = K_m \exp[-(x^2 + y^2)/2\sigma_m^2], \quad (2)$$

where m indicates the Gaussian scale level, σ_m denotes the scale, and K_m guarantees $\int G_m(x, y)dxdy = 1$.

Gaussian convolution and logarithmic transformation in Eq. (1) aim at accurately separating the reflectance and illumination components on image I_c. Based on the definition of Retinex model, the output $R_c(x, y)$ is the sum of weighted $\phi_c(x, y)$ in different Gaussian levels

$$R_c(x, y) = \sum_{m=1}^{M} \omega_m \phi_c(x, y), \quad (3)$$

where ω_m is the weight in various levels and the level number M. Typically, we set $M = 3$ and $\omega_m = 1/M$.

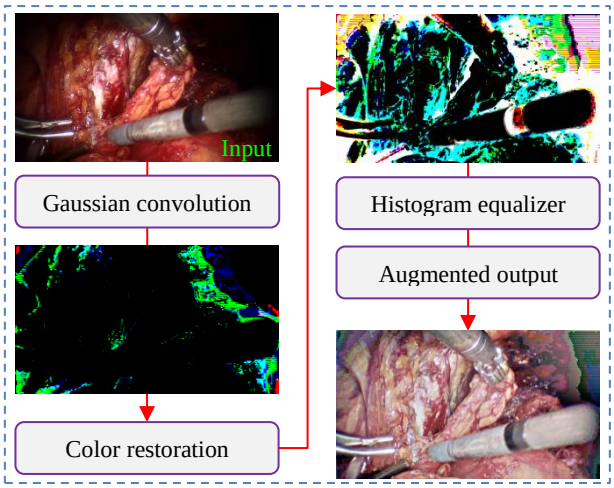

Fig.1 Retinex processing for augmented visualization.

Color restoration. Since the processing of Gaussian convolution and logarithmic transformation deteriorates the color saturation and generates a grayish image, a color restoration step is necessarily performed to obtain the color restoration coefficient $\gamma_c(x, y)$

$$\gamma_c(x, y) = \alpha \left[\log \beta I_c(x, y) - \log \sum_{c \in \{R,G,B\}} I_c(x, y) \right], \quad (4)$$

where α is a gain factor and β controls the nonlinearity. After that, the output becomes to be $\gamma_c(x, y)R_c(x, y)$.

Histogram equalization. Although the restoration step corrects the color saturation, it usually results in a problem of pixel inversion, i.e., the pixel intensity close to 0 in color channels can jump to 255 while the pixel intensity near 255 also potentially change to 0. The histogram equalization is used to tackle this problem.

Blind quality assessment. As it is somewhat difficult to generate ground truth for clinical video visualization, a blind video quality measure is used to quantitatively evaluate augmented video visualization. The Shannon entropy is widely employed to blindly assess the quality of images without any reference, and is given by [3]

$$E(I_c) = -\sum_{c \in \{R,G,B\}} \sum_{i=1}^{N} H(L_i) \log H(L_i), \quad (5)$$

which calculates the image entropy by characterizing its histogram (L_i is the frequency of i-th intensity level).

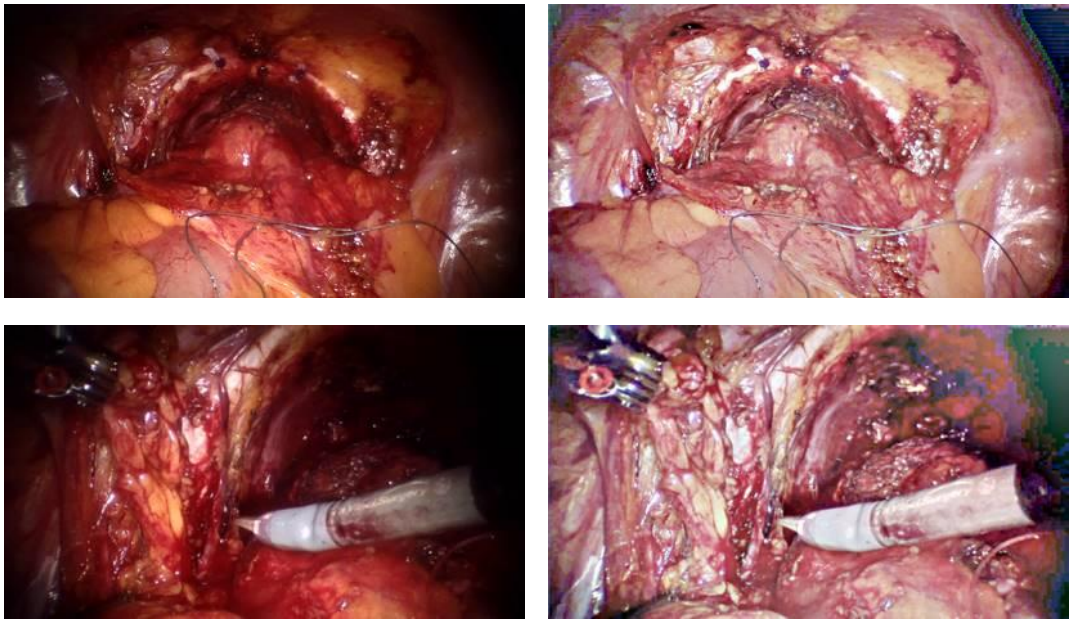

Fig.2 Examples of augmented visualization by Retinex processing: Original (*left*) and augmented (*right*) images.

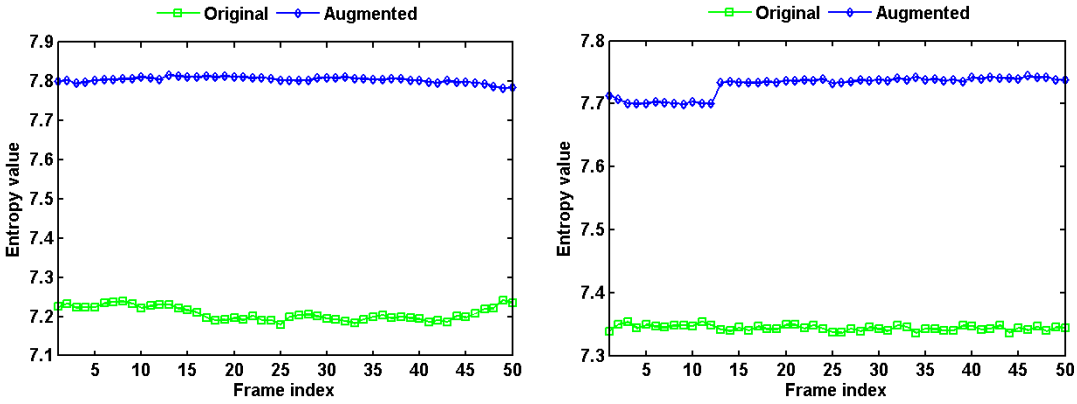

Fig.3 Information entropy comparison of original and augmented videos recorded from robotic prostatectomy.

Validation. The Retinex augmentation was evaluated on clinical videos that were collected from the robotic prostate surgery using a da Vinci surgical Si system.

RESULTS

Fig. 2 illustrates surgical video images with and without the Retinex augmentation. The image visual quality was obviously improved and more subtle structure details were visible after the Retinex augmentation. Fig.3 quantitatively compares the entropies of original and augmented images and proves Retinex effective.

DISCUSSION

This work showed the first study on augmented surgical filed visualization for releasing subtle surface structures and anatomical surroundings of the prostate. In robotic prostatectomy, the organ sub-structures or surroundings are hidden and hardly perceived by surgeons due to limited illumination and narrow endoscopic view of the surgical field. Based on the color constancy theory, the Retinex augmentation strategy was proposed to address the limitations. The Retinex processing uses Gaussian convolution and logarithmic transformation to separate the reflectance and illumination components. By removing the illumination component, the visual fidelity was augmented. The experimental results prove that this study is effective to enhance the surgical vision, improving a surgeon's awareness of various structures.

ACKNOWLEDGEMENTS

This work was supported in part by the Canadian Institutes for Health Research (CIHR) Team Grant on Prostate Imaging, the Canadian Foundation for Innovation, and the Ontario Research Fund.

REFERENCES

[1] A. Gijsenij, T. Gevers, J. van de Weijer, Computational color constancy: survey and experiments. IEEE Trans. Image Processing 20(9): 2475-2489, (2011)

[2] J. Morel, A. Petro, C. Sbert. A PDE formalization of Retinex theory. IEEE Trans. Image Processing 19(11): 2835-2837, (2010)

[3] D. Tsai, Y. Lee, E. Matsuyama. Information entropy measure for evaluation of image quality. Journal of Digital Imaging 21(3): 338-347, (2008)

Computer Assisted Laparoscopy Robot — A Low-cost Lightweight Design

D. Á. Nagy[1,2], Á. Takács[2], I. J. Rudas[2], T. Haidegger[2,3]

[1] *Department of Surgical Research and Techniques, Semmelweis University, Budapest, Hungary*

[2] *Antal Bejczy Center for Intelligent Robotics, Óbuda University, Budapest, Hungary*

[3] *Austrian Center for Medical Innovation and Technology, Wiener Neustadt, Austria*

denes.nagy@irob.uni-obuda.hu

INTRODUCTION

High quality surgical education has long been in the focus of medical associations throughout the world. Between 2000 and 2002, the Accreditation Council for Graduate Medical Education of the United States defined six fields of competency for physicians that were later implemented in the surgical field by the American College of Surgeons (ACS). These competencies included basic knowledge, clinical competence, interpersonal skills, professionalism, patient-based learning, system based learning and surgical simulation [1, 2]. In the past years, computer assisted surgery (CAS) has also become part of the everyday surgical practice, leading to a dramatic decrease in the time required for carrying out the actual surgical procedure, especially when the medical professionals receive training in robotic surgery [3]. However, most of the commercially available surgical robots do not provide features for surgical training, leaving university hospitals to solve this issue by alternatives, e.g., using retired robots as educational platforms.

Camera handling, along with many other laparoscopic procedures, lacks standardization background in general surgical practice and training. While today's training in this field is mostly based on learning-along-the-way methods, untrained medical students may compromise the success of surgery and reduce the effectiveness of the procedure in terms of communication and dynamics. There are numerous robotic solutions existing for camera handling, including the ones equipped with a separate hand panel [4], driven by voice control [5] or navigated by the movements of the surgeon's head [6], although up until now there is no general 'best' solution for the issue of separate handling of the camera(s) in laparoscopic surgery. The aim of this research is to develop a complete system for education of robotic minimally invasive surgeries, and surgical skills assessment. The primary focus is the camera handling during laparoscopic interventions, where a novel design of a camera holding robotic arm is presented that may be integrated into the da Vinci Surgical System of Intuitive Surgical Inc.

MATERIALS AND METHODS

The da Vinci Surgical System has undoubtedly become the most successful complete surgical system available in commercial distribution. As of December 31, 2014, there were 3,266 units installed worldwide, and the manufacturing company is employing almost 3,000 people in total [7]. In order to enhance research in surgical robotics, the da Vinci Research Kit (dVRK) was developed at Johns Hopkins University (and partner institutions) that allows researchers to access all levels of control of the da Vinci system or its modules [8]. The retired da Vinci Surgical System at Óbuda University, Budapest does not provide endoscopic camera handling, which motivated this research to develop a novel system, the Computer Assisted Laparoscopy (CALap) for overcoming this issue, leading to the design of a low-cost robotic arm used for holding laparoscopic cameras. The used training environment was developed at the Semmelweis University, Budapest in 2008, called the Apollo box trainer [9]. The environment follows the classical layout of laparoscopic box trainers, including a non-opaque cover, four input ports in order to manipulate the trocars and an aperture for camera installments.

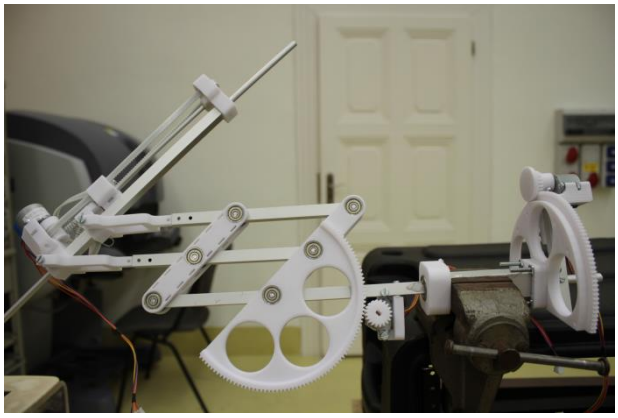

Fig. 1 The assembled Computer Assisted Laparoscopy robot (CALap) at the Antal Bejczy Center for Intelligent Robotics, Óbuda University.

COMPUTER ASSISTED LAPAROSCOPY ROBOT

Due to the lack of functional camera handling at the dVRK and da Vinci systems available at our laboratory, a new low-cost assembly was created that would be used in education and skill assessment. The prototype of the CALap system is shown in Fig. 1. The first prototype was created in a short period of time. The hardware was designed as follows. Aluminum profiles were used to hold the main weight of 1 kilogram, which provide the necessary stability of the construction without significantly increasing the total weight of the system. Special shaped parts for gears and bearing holders were also custom designed and 3D printed. The electronic implementation of the CALap system is based on the master–slave design, which allows low-level electronic and high level programming approach. Low-cost lightweight stepper motors were used for driving the assembly, keeping it as lightweight as possible. Communication between the master side computer and the slave robot was achieved by a custom-designed serial protocol, transferred over USB connection.

The programming of the system constitutes of two phases: the dVRK programming and creating the software for the CALap system. The da Vinci boards use the IEEE-1394 FireWire communication lines for data transfer. The protocol allows a high bandwidth for the dVRK, resulting in a near real-time communication speed. The created software on the dVRK side is built up from 5 layers: the hardware interface, the low-level control, the high-level control, teleoperation and application. The CALap software was utilizing the master–slave concept. The custom-designed serial communication protocol incorporates driving commands from the master side computer to the slave robot, while position and status data are received and transmitted back to the program. The software at the slave side runs on an Arduino Uno board using an ATmega328 microcontroller, attached to the CALap robotic arm, interpreting serial communication, executing low level motor driving commands and reporting back to the master computer. The full experimental setup and environment of the CALap system is shown in Fig. 2.

DISCUSSION

Computer assisted and robotic laparoscopic surgical procedures are relatively new, rapidly developing fields of general surgery. The new approaches to surgical interventions require surgeons with psychomotor adaptations, which are not part of the classical surgical curriculum. Due to the new requirements in the field, there is an increasing need of revolutionizing surgical education, including special training methods and skill assessment. The introduced laparoscopic camera handling system is a useful tool for the above mentioned topics, while its lightweight and low-cost (~$100) design allows one to apply it in many different types of surgical interventions and environments.

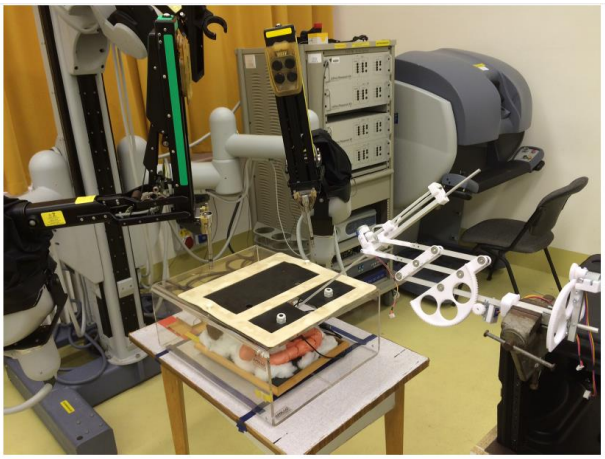

Fig. 2 The experimental setup of the CALap system with the da Vinci Surgical System and Research Kit in the background.

In the future, the CALap system would be a great tool for providing robotic background for surgical training in the field of minimally invasive surgery. Further plans include complete integration with the dVRK system. This prototype would also open up opportunities for bringing low-cost and lightweight robotic tools into the operating room.

REFERENCES

[1] B. J. Palmer, V. Stams, T. Russel, “ACS promotes the six competencies of the accreditation council for graduate medical education,” *Bull Am Coll Surg*, vol. 94, pp. 16–22, 2009.

[2] R. G. Williams and G. L. Dunnington, “Accreditation Council for Graduate Medical Education core competencies initiative: the road to implementation in the surgical specialties,” *Surg. Clin. North Am.*, vol. 84, no. 6, pp. 1621–1646, xi, Dec. 2004.

[3] W. R. Chitwood, L. W. Nifong, W. H. H. Chapman, J. E. Felger, B. M. Bailey, T. Ballint, K. G. Mendleson, V. B. Kim, J. A. Young, and R. A. Albrecht, “Robotic Surgical Training in an Academic Institution,” *Ann Surg*, vol. 234, no. 4, pp. 475–486, Oct. 2001.

[4] J. M. Sackier and Y. Wang, “Robotic assisted laparoscopic surgery,” *Surg Endosc*, vol. 8, pp. 63–66, 1994.

[5] J. A. Long, P. Cinquin, J. Troccaz, S. Voros, P. Berkelman, J. L. Descotes, C. Letoublon, and J. J. Rambeaud, “Development of miniaturized light endoscope-holder robot for laparoscopic surgery.," *J Endourol*, vol. 21, pp. 911–914, Aug 2007.

[6] J. M. Gilbert, “The endoassist robotic camera holder as an aid to the introduction of laparoscopic colorectal surgery," *Ann R Coll Surg Engl.*, vol. 91, no. 5, pp. 389–393, 2009.

[7] Investor FAQ, Intuitive Surgical Inc. [Online] Available: http://phx.corporate-ir.net/phoenix.zhtml?c=122359&p=irol-faq

[8] S. DiMaio and C. Hasser. (2008) “The da Vinci research interface,” *The MIDAS Journal—Systems and Architectures for Computer Assisted Interventions*, 2008.

[9] B. Lengyel, “Education of minimally invasive surgery in the digital age,” MSc Thesis, Semmelweis University, Budapest, Hungary, 2009.

Towards Robotic Needle Steering for Percutaneous Radiofrequency Ablation in the Liver: Procedure-Specific Workspace Analysis

T. K. Adebar[1], J. D. Greer[1], P. F. Laeseke[2], G. L. Hwang[2], A. M. Okamura[1]

[1]*Mechanical Engineering Department, Stanford University, USA*
[2]*Radiology Department, Stanford University, USA*
tadebar@stanford.edu

INTRODUCTION

Needle steering robots—robotic systems that insert flexible needles along controlled curved paths through tissue—have been discussed extensively in the research literature. Although significant work on modeling, control, path planning, and image guidance has been completed, no practical needle steering system has been evaluated for efficacy in a specific clinical application. The goal of our current work is to apply robotic needle steering to radiofrequency ablation (RFA) of liver tumors, by steering electrodes along curved paths to previously inaccessible regions of the organ.

Multiple needle steering techniques have been described, including needle-base manipulation, tissue manipulation, active cannulas, programmable bevels, and bevel-tip or bent-tip needles [1]. While these methods have shown promising initial results, they have been validated almost exclusively in artificial tissue simulants. Based on the limited results reported, the same needle steering techniques perform worse (*i.e.*, they result in less tightly curved paths) in *ex vivo* and *in vivo* biological tissues [2].

As part of our ongoing work, we are currently developing methods to improve the curvature of bent-tip steerable needles in liver tissue. This necessitates a specific design requirement. In other words: How much curvature is enough? The goal of the work described in this paper was to establish the curvature requirements for steerable needles in percutaneous RFA of liver tumors, by combining analysis of medical images with knowledge of existing clinical techniques and needle steering models.

MATERIALS AND METHODS

Medical Image Analysis

An open-source contrast-enhanced abdominal CT scan of a healthy 36-year-old male was analyzed [3]. The segmented liver capsule was exported from 3D SLICER, refined using MESHLAB, and imported into MATLAB to serve as a workspace boundary. Similarly, large-diameter portions of the internal vasculature which represent a significant bleeding risk (specifically the hepatic and portal veins with diameter over approximately 5 mm) were imported to serve as obstacles. These models are shown in Fig. 1.

Two entry vectors $v^{(i)}$ were defined based on typical introducer placement for percutaneous RFA of liver tumors. Vector $v^{(1)}$ represents an intercostal approach into the right liver. Vector $v^{(2)}$ represents an anterior subcostal approach under the costal margin into the left liver. Both orientations reflect insertion under ultrasound guidance with the needle at 45° to the transducer axis.

Reachable Workspace

For each $v^{(i)}$, the corresponding reachable workspace $R^{(i)}$ was measured by discretizing the liver volume L (excluding the vasculature) into 4-mm voxels, and determining if each voxel could be reached by a permissible path. Paths that crossed the liver boundary (capsule) or vasculature were excluded to decrease risk of bleeding and other complications. Paths were also restricted to have one or two constant-curvature sections. Although insertion and rotation of a bent-tip steerable needle can theoretically generate more complex needle paths, in practice the mechanical properties of liver cause these complicated paths to relax into simpler paths. Demonstrating this, Fig. 2(a) shows ultrasound segmentation results from switching a steerable needle on a straight path to a maximally curved path in *ex vivo* porcine liver. After the direction change, rather than forming a path with distinct tangent sections as predicted, the needle relaxed by 10.3 mm to a constant curvature path. Two-section paths were excluded if the waypoint was already beyond the target (*i.e.*, if the dot product of the vector from the waypoint to the target and the tangent vector at the waypoint was negative) to avoid impractical looping behavior. Finally, paths were excluded if they required radius of curvature ρ below threshold $\rho_{\min}$, which was varied as a parameter from 10-200 mm. Fig. 2(b) shows examples of permissible and excluded paths.

RESULTS

Fig. 3 shows the size of the reachable set—specified by the ratio of the set sizes $|R^{(i)}|/|L|$—as a function of minimum radius of curvature $\rho_{\min}$. With $\rho_{\min}$ = 100 mm, paths starting at $v^{(1)}$ were able to reach approximately 8% of L, while paths starting at $v^{(2)}$ were able to reach approximately 41% of L.

Fig. 4 shows a frontal slice near the center of the liver, with color indicating radius of curvature ρ required to reach each voxel from $v^{(1)}$. The needle was not able to reach areas behind the hepatic veins and surrounding the insertion. Most of the slice was reachable using single-section paths, except for the area blocked by the vessels.

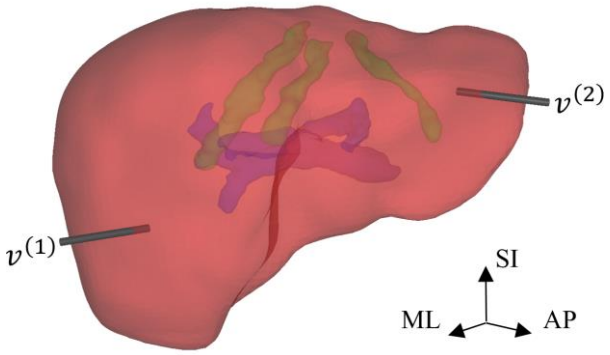

Fig. 1 Models of the liver boundary (capsule), large hepatic veins (green) and large portal veins (blue). The entry vectors are also indicated. The superior-inferior (SI), medial-lateral (ML), and anterior-posterior (AP) directions are shown.

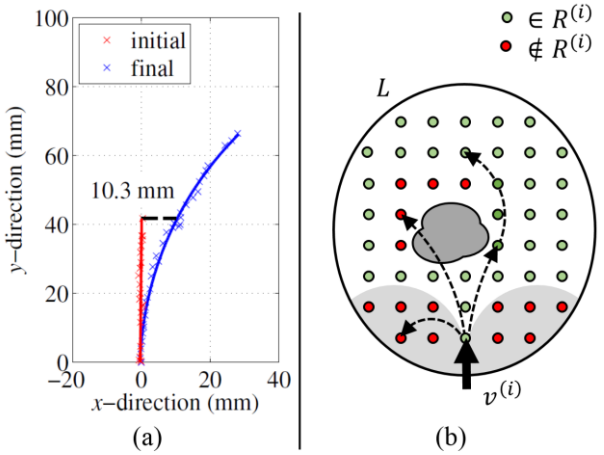

Fig. 2 Needle paths: (a) Ultrasound segmentation results showing a steerable needle before and after a direction change in *ex vivo* porcine liver. Rather than forming a path with distinct arc sections, the needle relaxed into a single arc. (b) Reachable and unreachable voxels within L, and lines showing, from left to right, an excluded path that violates $\rho_{\min}$, an excluded path that passes through an obstacle, and a permissible two-part path.

DISCUSSION

Results shown in Fig. 3 reveal the gap between current needle steering methods and our clinical application. The tightest steerable needle curvatures $\rho_{\min}$ reported in biological tissue are between 100-200 mm [2]. Even combining the intercostal and anterior subcostal approaches, such needles would only permit access to 50% of the liver at best. Since the distribution of tumor sites is approximately uniform throughout the liver, current steerable needles would be unable to access many targets. Although angling the introducer could change the results shown in Fig. 4, interference from the ribs and potential for tissue injury limit this degree of freedom after the initial insertion.

An important potential advantage of needle steering in RFA of liver tumors is the ability to reach targets in the dome of the liver (on the right-lateral superior surface), which can be very difficult in some patients using traditional RFA probes due to interference from the ribs.

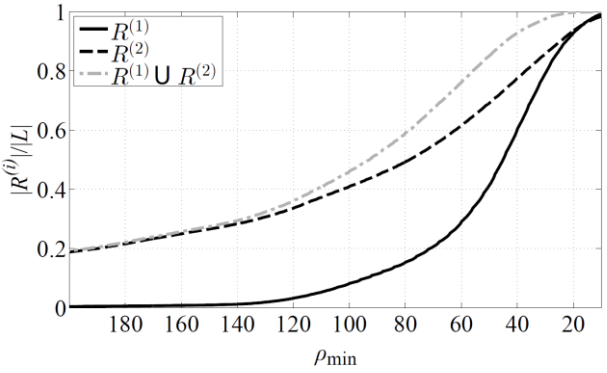

Fig. 3 Ratio of reachable set size to total liver size as a function of minimum radius of curvature $\rho_{\min}$. Results for intercostal ($v^{(1)}$) and anterior approaches ($v^{(2)}$) are shown.

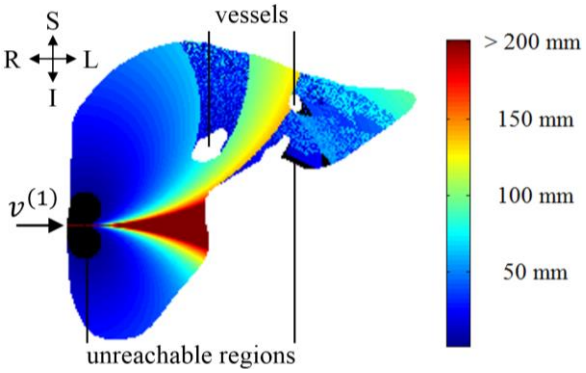

Fig. 4 Frontal slice of L. Colors indicate the radius of curvature ρ required to reach each voxel. Black voxels were not reachable with any curvature in the examined range (10-200 mm). White voxels, including the vessels inside the liver, were outside L.

As seen in Fig. 4, a radius of curvature of approximately 50 mm is necessary to reach the right-lateral aspect of the liver dome. We believe $\rho_{\min}$ = 50 mm is thus a reasonable curvature requirement for future development, since it allows the needle to access the liver dome, and reach approximately 85% of the liver volume from the entry points we have described. Improvement of needle curvature to this level will require significant refinement of needle steering techniques.

This work was supported in part by the National Institutes of Health through R01 EB018849.

REFERENCES

[1] van de Berg NJ et al. Design choices in needle steering—a review. IEEE Trans Mechatronics, in press.

[2] Majewicz A et al. Behavior of tip-steerable needles in ex vivo and in vivo tissue. IEEE Trans Biomed Eng. 2012; 59(10): 2705-15.

[3] Pieper S et al. 3D SLICER. Proceedings of the 1st IEEE International Symposium on Biomedical Imaging: From Nano to Macro. 2004; 632-635.

Validation of the RobotiX Mentor Robotic Surgery Simulator

G. Whittaker, A. Aydin, N. Raison, F. Kum, B. Challacombe, M.S. Khan, P. Dasgupta, K. Ahmed

MRC Centre for Transplantation, King's College London; Department of Urology, Guy's and St. Thomas' NHS Foundation Trust, London, United Kingdom

george.whittaker@kcl.ac.uk

INTRODUCTION

With robotic-assisted surgery becoming more common practice in urology, effective training remains a challenge. There is a considerable learning curve associated with robotic training, though this has been reported as gentler than for laparoscopic training[1]. Simulation has gained wide acceptance as a method of reducing the initial phase of the learning curve. The RobotiX Mentor™ is a new virtual reality simulator which mimics the interface of the da Vinci® Surgical System, with integrated training modules including Fundamentals of Robotic Surgery (FRS) and Robotic Suturing. Face and content validity of the suturing module have been confirmed in a previous study[2], though this was performed on a different platform. This study aims to assess face, content and construct validity of the RobotiX Mentor™. It also aims to assess its acceptability as a training tool and feasibility of its use in training.

MATERIALS AND METHODS

This prospective, observational and comparative study recruited novice (n=20), intermediate (n=15), and expert (n=11) robotic surgeons as participants from institutions across the United Kingdom and at the 30th European Association of Urology Annual Meeting. Each participant completed nine surgical tasks across two modules on the simulator, followed by a questionnaire to evaluate subjective realism (face validity), task importance (content validity), feasibility, and acceptability. Outcome measures of novice, intermediate, and expert groups were compared using Mann-Whitney *U*-tests to assess construct validity. Outcome measures of novice, intermediate, and expert groups were compared using Mann-Whitney *U*-tests to assess construct validity.

RESULTS

Construct validity was demonstrated in a total of 17/25 performance evaluation metrics ($p<0.001$). Experts performed better than intermediates in regard to time taken to complete the first ($p=0.002$) and second ($p=0.043$) module, number of instrument collisions ($p=0.040$), path length ($p=0.049$), number of cuts >2mm deep ($p=0.033$), average distance from suture target ($p=0.015$), and number of suture breakages ($p=0.038$). Participants determined both the simulator console and psychomotor tasks as highly realistic (mean: 3.7/5) and very important for surgical training (4.5/5), with system pedals (4.2/5) and knot tying task (4.6/5) scoring highest respectively. The simulator was also rated as an acceptable (4.3/5) tool for training and its use highly feasible (4.3/5).

CONCLUSIONS

Construct, face, and content validity were established for the RobotiX Mentor and feasibility and acceptability of incorporation into surgical training was ascertained. The RobotiX Mentor shows potential as a valuable tool for training and assessment of trainees in robotic skills and may reduce the initial learning curve if utilised as an adjunct to operating-room training. Investigation of concurrent and predictive validity is necessary to complete validation and evaluation of learning curves would provide insight into its value for training.

REFERENCES

[1] Goldstraw MA, Challacombe BJ, Patil K, Amoroso P, Dasgupta P, Kirby RS. Overcoming the challenges of robot-assisted radical prostatectomy. Prostate cancer and prostatic diseases. Mar 2012;15(1):1-7.

[2] Abboudi H, Khan MS, Aboumarzouk O, et al. Current status of validation for robotic surgery simulators-a systematic review. BJU international. Feb 2013;111(2):194-205.

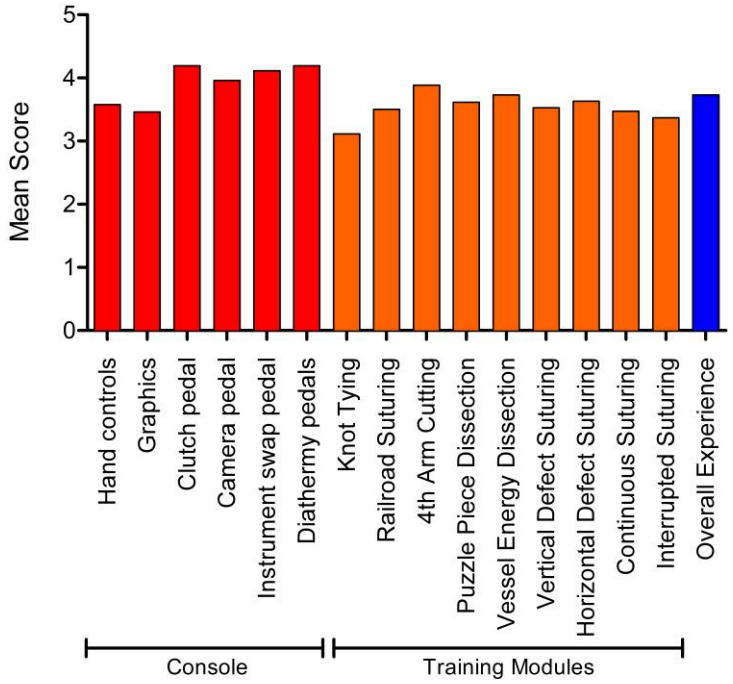

Figure 1. Assessment of face validity by novice, intermediate, and expert groups. Each element was scored on a numerical scale between 1 (not realistic) and 5 (very realistic). The diathermy pedals and '4th Arm Cutting' task were rated as most realistic, whereas graphics and 'Knot Tying' task were judged as least realistic.

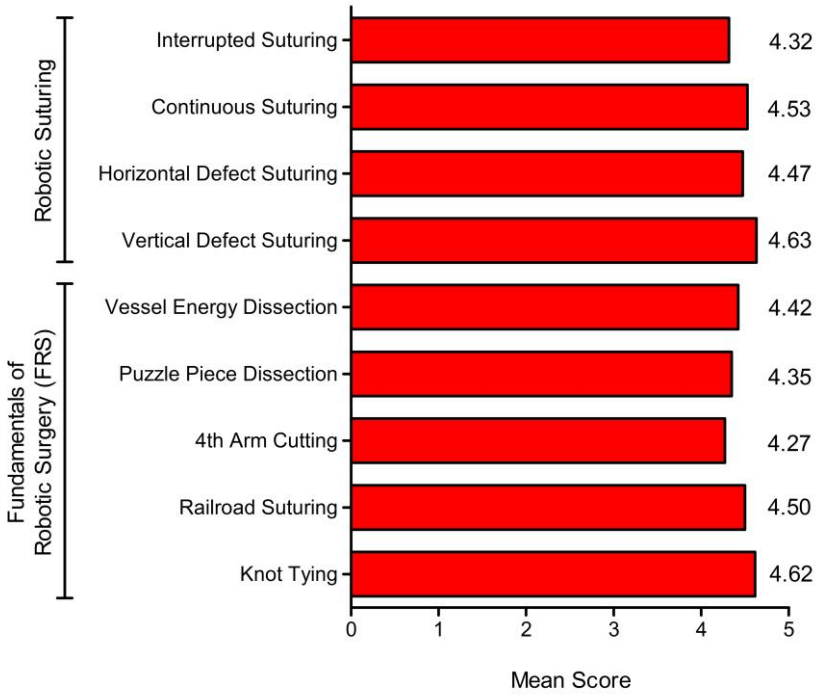

Figure 2. Assessment of content validity by intermediate and expert groups. Each task was scored on a numerical scale between 1 (not important) and 5 (very important). 'Knot Tying' and 'Vertical Defect Suturing' tasks were rated as most important, whilst 'Puzzle Piece Dissection' was judged as least important.

Re-Thinking Patient Specific Instrumentation and Robotics in Orthopaedics: A New Mechatronic Approach

A. Darwood[1], R. Emery[2], R. Richards[3], P. Reilly[2],
F. Rodriguez y Baena[2], A. Dawood[1], A. Tambe[4]

[1]*Prometheus Surgical Ltd., London, UK, alastairdarwood@hotmail.com*
[2]*Imperial College, London, UK, r.emery@imperial.ac.uk*
[3]*Cavendish Implants, London, UK,* [4]*Derby Hospital NHS Trust, UK*

INTRODUCTION

It is well known that the accurate placement of orthopaedic hardware such as arthroplasty prostheses into a biomechanically derived optimum position is of paramount importance in the long term success of these interventions[1,2,3]. Similarly, in many orthopaedic procedures it is advantageous or even essential to know the exact placement of hardware such as screws or pins, for example in spinal surgery or complex fracture reduction. Two main technologies have been developed to facilitate accurate placement: bespoke patient specific instrumentation such as rapid manufactured guides and orthopaedic surgical robots. Both technologies enable good results but are hindered by well-known significant drawbacks such as high cost, complex logistical chains, poor versatility and long set up times[4,5].

This paper presents a radically new technology developed to overcome many of the drawbacks of existing approaches whilst providing a means to accurately place orthopaedic hardware according to a pre-operative plan. The approach allows accurate bespoke drill/cutting guides to be rapidly produced intraoperatively at minimal per patient cost using a simple low cost hardware element and disposable consumables. In this paper, the technology is described in the context of total shoulder arthroplasty, more specifically, the placement of the glenoid component according to a pre-operative plan.

MATERIALS AND METHODS

The method comprises two main intraoperative components: A mechatronic apparatus and disposable sterile consumables. The apparatus is made up of an optical 3D scanner (HDI 120, LMI Technologies, Delta, BC Canada), a 2 axis Computer Numerical Control (CNC) drill with replaceable sterile drill bit and a 3 axis CNC receptor assembly for the sterile disposables. The sterile disposables comprise a plastic element with standard geometry coated on one side with a body of mouldable material able to be rapidly solidified, for example by exposure to air, heat or light and a carrier element to allow an interface with the non-sterile surfaces of the receptor assembly. The disposable component is inserted into the receptor assembly in a known way, by virtue of its standard geometry. With the exception of the mouldable element, all elements of both components remain spatially and positionaly calibrated with respect to one another.

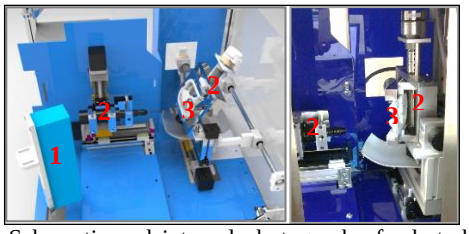

Fig. 1: Schematic and internal photograph of robot showing surface scanner (1) and CNC apparatus (Drill and gimbal 2) with disposable components (3).

The approach consists of 6 steps to produce an intraoperative guide.

1. Planning is carried out on CT or MRI patient data. This process defines e.g. a guide wire position as a vector within the coordinate frame of reference of the digital scapula model. This plan may be carried out pre-operatively or intra-operatively.

2. The surgeon exposes the surgical site in the conventional manner. In this case, exposing the osseous anatomy of the glenoid cavity.

3. The sterile disposable consumable is prepared. The mouldable side of the component is pressed into the surgical site (the glenoid cavity) and quickly solidifies forming a mould of the glenoid cavity and exposed portions of its rim. The component is removed and placed within the sterile carrier which in turn is placed into the corresponding receptor assembly of the apparatus.

4. The optical scanner scans the surface of the mould, containg the detail of the glenoid cavity geometry. The scan data is inputted into a software registration module based on the classical Iterative Closest Point (ICO) algorithm, which registers the glenoid surface mould scan with its corresponding position on the CT/MRI imaging derived digital patient anatomy. In this way, the scanned glenoid surface model is automatically placed into the same coordinate frame of reference as the original 3D patient scapula data. As a result, the vector describing the location of the guide wire may now intersect the digital glenoid surface mould model.

5. From this data, a CNC drilling path is now created. The CNC drill fitted with a sterile drill bit and the CNC receptor assembly is repositioned according to the output of the planning module, which is based on the registered scan data, in order to drill through the mould and carrier such that the hole drilled matches the geometry of the guide wire vector passing through the digital glenoid surface mould model.

6. The sterile moulded part is removed from the

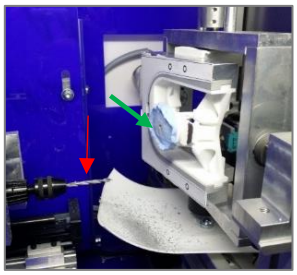

Fig. 2: Internal robot photograph – Following registration the sterile drill (red arrow) has cut a guide hole through the mouldable component (Green arrow). It may now be removed from the robot ready for use.

machine and returned to the operative site. Its solidified moulded geometry constrains it to the identical positon from where the mould was taken. The prepared guide hole may now be drilled through by the surgeon placing a guide wire into the pre-planned position. Once this is complete, the disposable may be slid off the guide wire and discarded, leaving the wire in the pre-operatively planned position. Surgery may then continue in the conventional manner.

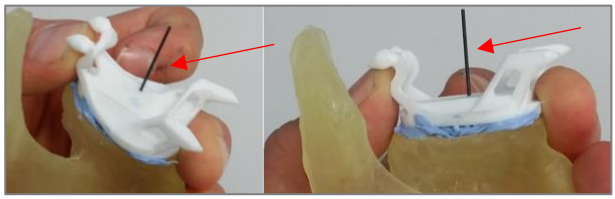

Fig. 3: The modified disposable element 'locks' into place by virtue of the solidified impression on its underside. A guide wire (indicated by red arrow) can now be drilled through the guide hole.

A prototype device was constructed from a combination of 'off the shelf' components and specifically designed 3D printed parts. Bespoke software was created to control the above steps to be carried out in one computer program. The prototype is controlled either with the use of a built in touch screen PC or an external desktop computer. The prototype is able to demonstrate a full operative surgical workflow including the maintenance of sterility of all parts that come into contact with the patient and operated by scrubbed personnel. A dental mould material was used for prototype testing however it is conceived that any sterile, non-toxic rapidly setting mouldable material may be used in its place. Full ex-vivo testing was carried out to assess the feasibility of the approach in terms of accuracy, manufacture time and ease of use.

10 anonymized shoulder CT scans of patients requiring arthroplasty were collected and thresholded to produce a 3D model of patient anatomy. A consultant orthopaedic surgeon with arthroplasty experience planned the ideal guide wire position in each scapula in order to place the glenoid component into an ideal position. Three planar markers were also added to each glenoid model so as to create a reference plane upon which to compare guide wire placement accuracy. A pair of each scapula glenoid was 3D printed (Objet Eden, Stratasys company USA) to produce two groups of 10 identical models: a guided group and a conventional group. The surgeon manually placed a guide wire into all glenoids in the conventional group according to the bespoke plan created for each glenoid. The prototype was then used in the guided group to place guide wires according to identical bespoke plans for each glenoid. Guide wire placement was subsequently analysed in both groups and compared to the pre-operative plan. Accuracy was measured in two ways: minimum distance between planned glenoid entry coordinate and achieved vector axis of physical guide wire (mm) and absolute angle (º) between planned guide wire axis and achieved physical guide wire axis.

RESULTS

Full guide manufacture was completed in approximately 5 minutes including planning, molding and device set up. In the conventional group, average placement accuracy was 1.580mm (3.22-0.4mm) and 6.815° (16.63-1.19°) in comparison to the guided group achieving 0.47mm (1.31-0.12mm) and 1.572º (1.77-0.06º). Student's t-tests were applied to the minimum distance and the absolute angle metrics and they were both shown to be statistically significantly affected by the method (manual vs. automatic) at the 95 % confidence interval ($p < 0.05$).

DISCUSSION

With a total guide manufacture time of 5 minutes, cheap consumables, a simple hardware unit and the ability to accurately place orthopaedic hardware into a pre-planned position it is evident that this approach overcomes many of the drawbacks of existing orthopaedic guidance technologies. The approach may be used in the guidance of other arthroplasty operations with minimal re-configuration of the disposable components. Work in these areas is ongoing at time of writing. In conclusion, this paper describes a new approach and validation for the intraoperative rapid production of bespoke patient specific cutting guides. In removing many of the drawbacks of existing technologies and significantly reducing costs, it is hoped that the technique may open up orthopaedic guidance so that a greater number of patients may benefit from a fully computer guided orthopaedic intervention.

REFERENCES

1. Krishnan, S. P. et al. A review of rapid prototyped surgical guides for patient-specific total knee replacement. *J. Bone Joint Surg. Br.* **94,** 1457–61 (2012).

2. Choong, P. F. et al. Does accurate anatomical alignment result in better function and quality of life? Comparing conventional and computer-assisted total knee arthroplasty. *J. Arthroplasty* **24,** 560–9 (2009).

3. De Haan, R. et al. Revision of metal-on-metal resurfacing arthroplasty of the hip: the influence of malpositioning of the components. *J. Bone Joint Surg. Br.* **90,** 1158–63 (2008).

4. Lang, J. E. et al. Robotic systems in orthopaedic surgery. *J. Bone Joint Surg. Br.* **93,** 1296–9 (2011).

5. Beringer, D. C. et al. An overview of economic issues in computer-assisted total joint arthroplasty. *Clin. Orthop. Relat. Res.* **463,** 26–30 (2007).

Design of a Robotic Implant for in-vivo Esophageal Tissue Growth

D. D. Damian, S. Arabagi, P. E. Dupont

Boston Children's Hospital, Harvard Medical School, USA
dana.damian@childrens.harvard.edu

INTRODUCTION

Robotic devices in medicine have yielded numerous benefits from advanced diagnostic tools to instruments that augment surgeons' physical capabilities [1,2]. With smaller and safer technologies, medical technology is advancing from interventional robotic medicine to personalized robotic medicine with the aim of reducing clinical assistance, hospitalization, or the repetitive need for surgeries. Robotic implants, as a new category of medical robots, are implanted in the body to autonomously regulate biological processes for long periods of time. An example of their clear benefit is long-gap Esophageal Atresia (LGEA) in which a section of the esophagus longer than 3cm is missing [3,4]. Long-gap EA afflicts over 100 babies per year in the USA and Europe. One effective procedure to repair this congenital defect is Foker's technique [5,6], in which growth-inducing traction forces are applied to the esophageal segments using suture that is tied off outside the child's back. The traction is manually maintained for an average of 14 days to induce sufficient elongation to close the gap. While producing superior outcomes to alternative procedures, the child is sedated and kept on a ventilator for the duration of the treatment. It would be extremely beneficial to these patients if (1) multi-week sedation could be avoided so as to eliminate any effect on long-term neurocognitive development, (2) the need for re-operation due to suture tear-out could be reduced, and (3) the duration and cost of hospitalization could be reduced.

We present a robotic implant that has the potential to resolve these shortcomings. The implant operates in the thoracic cavity attached to the two esophageal segments using attachment rings, thus localizing the elongation procedure. In contrast to the standard Foker technique, the implant's configuration is not affected by infant motion and, consequently, the child does not need to remain paralyzed and sedated in the ICU during traction. Equipped with force and position sensors, the motorized implant allows controlled and precise tissue traction, eliminates the risks of suture tear-out due to the ring attachment that distributes forces around the esophagus, and enables traction monitoring. The design concept of the robot was introduced in [7].

In this paper, we present the robotic implant, which has been designed and tested for in vivo animal experiments. The following are the paper's contributions: (1) a robotic implant design featuring a biocompatible encapsulation, (2) an integrated system for remote implant monitoring and control, and (3) position and force control of esophageal tissue.

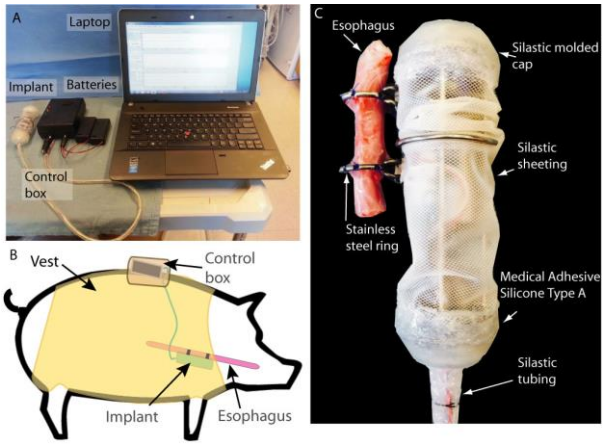

Fig. 1 Robotic implant. A. Implant and monitoring system. B. Schematic for testing in swine. C. Implant shown attached to length of porcine esophagus. Note: initial tests induce growth of esophageal segment between rings.

IMPLANT DESIGN FOR SURVIVAL TESTS

The entire system, shown in Fig. 1A, consists of the robotic implant, a control box, battery pack, and a laptop. An animal protocol, approved by IACUC (Institutional Animal Care and Use Committee), provides for two types of experiments. In this first, the robotic implant is mounted on an intact esophagus and growth is induced in the segment between the rings over a 7-day period (Fig. 1 BC). In subsequent experiments, a section of esophagus is removed to mimic actual atresia and the rings move to close the gap.

The robotic implant applies traction on the esophageal segments using a motor, which displaces the rings relative to each other. The implant is also equipped with force and position sensors to measure and control tissue forces and displacements [7]. The implant is sealed with a biocompatible encapsulation. We designed the implant encapsulation with the following properties: (1) biocompatible; (2) anti-fouling; (3) impermeable to air and water; and (4) abrasion resistant. It is fabricated from silastic (Fig. 1C), which satisfies the first three properties. The silastic (Bentec Medical) embeds a polyester mesh to satisfy the forth requirement. Silastic caps were fabricated using a molding process (Dow Corning Corp.). Thorough sealing was ensured using medical adhesive silicone Type A (Dow Corning Corp.). The tubing protecting the electric wires was also made of silastic (Bentec Medical).

The attachment rings were fabricated from stainless steel by TIG welding to preserve the material properties and avoid corrosion. The rings are detachable and adjustable in order to allow easy implantation and suturing, depending on the diameter of the esophagus.
The control box contains an Atmel controller (Baby Orangutan B-328, Pololu), force sensor amplifier, and Bluetooth module (BlueSMiRF, Sparkfun Electronics). The control box is worn in a vest pocket by the animal during the survival experiments. The laptop is used to launch a graphical interface for visualizing real-time sensor data, inputting controller commands and data logging via Bluetooth. A low-level controller generates traction forces using either force or position set-point control. Set points can be set manually or using a high-level controller to produce a desired waveform, e.g., adjustment once per day or every few minutes. Automated adjustment during animal studies enables controlled comparison of traction histories and their effect on tissue growth rate and properties.

IMPLANT CONTROL

The controllers were tested in 36-hour *ex vivo* studies with swine esophagus during which the implant and esophageal segment were submerged in saline. The saline kept the tissue wet while also testing the impermeability of the encapsulation. The esophageal segments were taken from swine weighing 43 kg on average. The initial relaxed length of the esophagus segment was 20 mm (Fig. 1C). The laptop was used to command the implant and to log position and force data during testing. There were no liquid leaks inside the robotic implant during and after these experiments, as observed from the signals of the electronic components and from visual inspection of the interior of the robot.
Figure 2 shows implant signals corresponding to automatic position control. Position and force signals are reported for a 1200s duration during which the commanded displacement was a square wave of amplitude 10mm and a period of 130s.

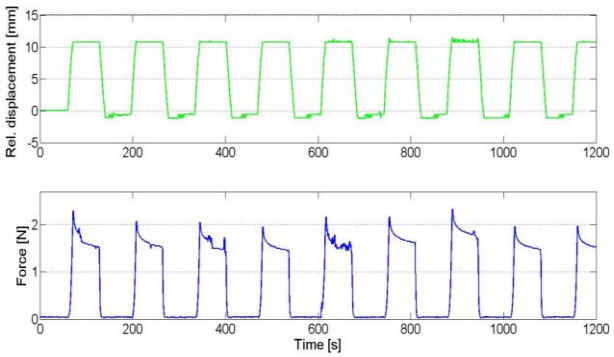

Fig. 2. Robot position set-point control. Response to commanded 10mm position square wave.

Under position control, the implant generated a peak force in the tissue of about 2N, which reduced to about 1.5N after one minute due to relaxation of the tissue.

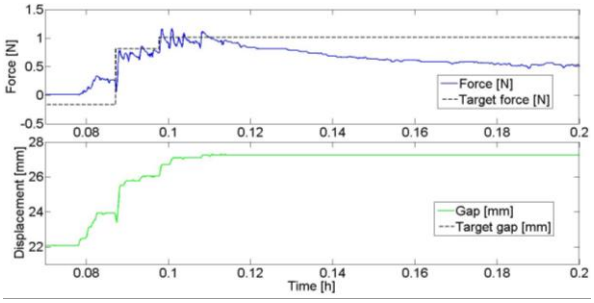

Fig. 3. Robot force set-point control. Response to force-control set points of 0.8N and 1.0N.

Figure 3 presents the response to force set-point commands of 0.8N and 1.0N obtained during long-term testing. The plots also show the response after the controller was turned off at 0.1138h. Force fluctuations occur due to relaxation of the tissue.

IN VIVO TESTING

The implant is sterilized using the Ethylene Oxide (EtO) sterilization process in order to protect the electronic components. It is implanted through a right thoracotomy, which provides access to the esophagus while keeping a safe distance from the heart. The cable from the implant is tunneled to the control box in the vest through the skin. The animal is fed a semi-solid diet for the duration of the experiment. Traction is applied every day. The tissue growth is assessed by comparing the stretched segment with a control segment, and by histological analysis.

ACKNOWLEDGEMENTS

This project is supported by Boston Children's Hospital's Translational Research Program, Manton Center for Orphan Disease Research, and the Swiss National Science Foundation.

REFERENCES

[1] B.J. Nelson, I.K. Kaliakatsos, and J.J. Abbott. Microrobots for minimally invasive medicine, *Annual Review of Biomedical Engineering*, 12:55–85, 2010.
[2] C. Bergeles and Y. Guang-Zhong, From Passive Tool Holders to Microsurgeons: Safer, Smaller, Smarter Surgical Robots, *IEEE Trans. Biomed. Eng.*, 61(5):1565-76, 2014.
[3] P.F. Martins Pinheiro, A.C. Simoes e Silva, and R.M. Pereira. Current knowledge on esophageal atresia. *World Journal of Gastroenterology*, 18(28):3662–72, 2012.
[4] R. Sfeir, L. Michaud, J. Salleron, F. Gottrand, Epidemiology of esophageal atresia, *Dis. Esophagus*, 26(4):354-5, 2013.
[5] J.E. Foker, B.C. Linden, E.M. Boyle, and C. Marquardt. Development of a true primary repair for the full spectrum of esophageal atresia. *Annals of Surgery*, 226:4:533–543, 1997.
[6] J.E. Foker, T.C. Kendall Krosch, K. Catton, F. Munro, and K.M. Khan. Long-gap esophageal atresia treated by growth induction: the biological potential and early follow-up results. *Seminars in Pediatric Surgery*, 18:23–29, 2009.
[7] D.D. Damian, S. Arabagi, A. Fabozzo, P. Ngo, R. Jennings, M. Manfredi, and P.E. Dupont. Robotic Implant to Apply Tissue Traction Forces in the Treatment of Esophageal Atresia, *IEEE International Conference on Robotics and Automation* (ICRA), pp. 786-792, 2014.

Analysis of the Instrument Vibrations and Contact Forces caused by an Expert Robotic Surgeon doing FRS Tasks

J. D. Brown, C. O'Brien, K. W. Miyasaka, K. R. Dumon, K. J. Kuchenbecker

University of Pennsylvania, Philadelphia, Pennsylvania, USA

brownjer@seas.upenn.edu, kuchenbe@seas.upenn.edu

INTRODUCTION

The widespread growth of robotic minimally invasive surgery has led to the need for a standardized training curriculum. Toward that end, the Institute for Surgical Excellence is conducting the Fundamentals of Robotic Surgery (FRS) validation trial. This multi-site study is testing both novice and experienced surgeons using Intuitive Surgical da Vinci robots and robot simulators. While a standardized curriculum will increase training consistency, the tasks performed on the robot itself will still rely heavily on expert observation of a trainee's performance. While common in traditional surgical skill assessment, observation-based ratings are both subjective and time consuming for the expert reviewers.

Thus, there is also a growing need for more objective and automatic approaches to surgical skill assessment during robot-based training [1]. Although several studies have assessed surgeon performance by analyzing the robot arm motions, e.g., [2], these analyses do not account for the quality of the physical interaction between the instruments and their environment. Our work on VerroTouch, a system that provides real-time haptic feedback of instrument vibrations [3], has shown that instrument vibrations are a construct-valid measure of surgical skill during robotic *in vitro* training tasks such as suturing and peg transfer [4]. While instrument vibrations can capture rough interactions between the instruments and with stiff tissue, some contacts with soft tissue do not produce measurable instrument vibrations [5]. We hypothesize that the quality of these interactions can be monitored by examining the forces that the robotic instruments exert on the tissue; we can measure such forces during *in vitro* and *ex vivo* training tasks but not during *in vivo* surgery.

To better understand how instrument vibrations and contact forces may elucidate the skill level of a surgeon during various tasks, we have recorded surgeon interactions with the *ex vivo* avian tissue model used during the robot-based portions of the FRS validation trial at our institution. This paper provides a descriptive analysis of the vibrations and forces caused by a single expert robotic surgeon in this study.

MATERIALS AND METHODS

One experienced colorectal surgeon (>50 robotic cases on human patients) performed a series of psychomotor tasks with a da Vinci Si robot as part of the FRS validation trial taking place at the University of Pennsylvania. The five tasks included knot tying, suturing, fourth-arm cutting, pattern cutting, and vessel energy dissection. The tasks were performed on an avian tissue model (a turkey leg quarter) as a post-test to the FRS training curriculum.

The da Vinci Si was augmented with our system for measuring instrument and camera vibrations, as well as the forces applied to the tissue (Fig. 1). A three-axis accelerometer (LIS344ALH) measured the vibrations of the left tool, the right tool, and the camera; each sensor was attached using a plastic bracket on the shaft. A force sensor (ATI Mini40) was mounted under the plate holding the tissue model; the three vibration axes were combined into a single magnitude, and the force measurement was separated into normal and tangential components. We also recorded the camera video feed.

We measured the vibrations and forces during three selected FRS tasks. Their instructions were as follows:

A. **Suturing:** Close the incision using a continuous horizontal mattress suture pattern, with the needle entering and exiting through the marks placed on the skin. The suture is already anchored on one side

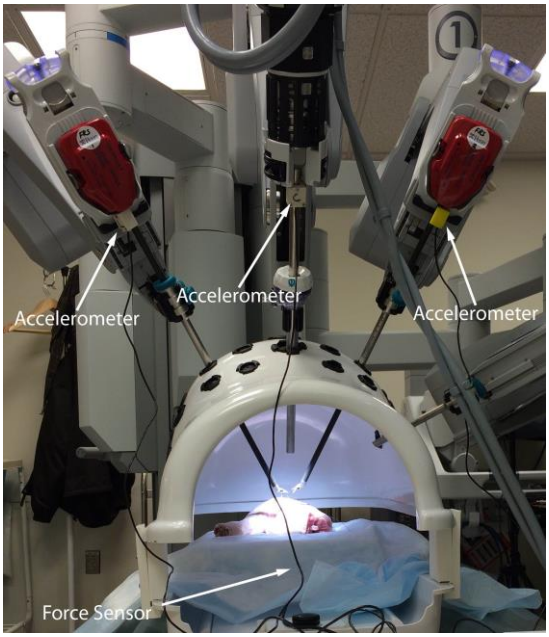

Fig. 1 A da Vinci Si robot augmented with accelerometers that measure instrument and camera vibrations. The avian tissue model is resting on top of a draped plate that is equipped with a three-axis force sensor.

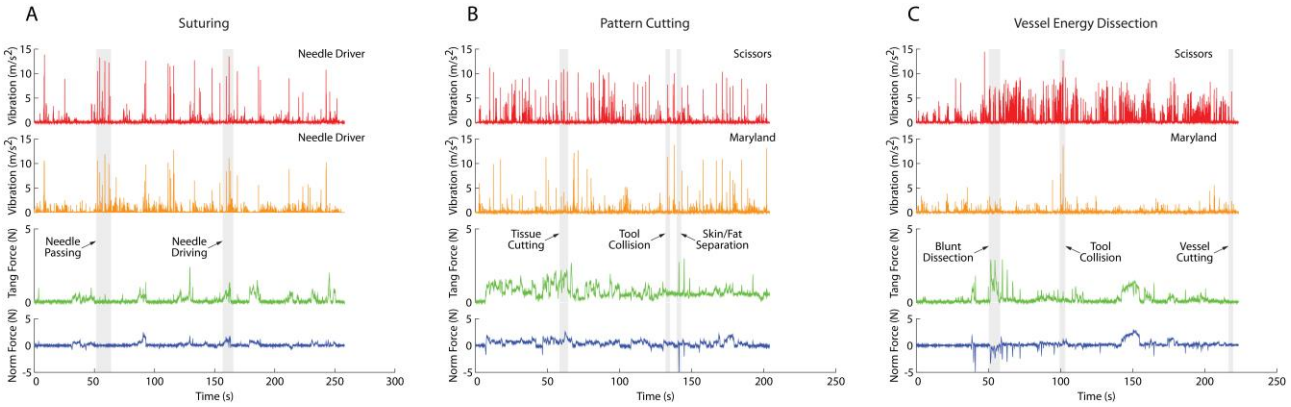

Fig. 2 Vibration and force recordings for the (A) suturing, (B) pattern cutting, and (C) vessel energy dissection tasks performed on the avian tissue model. Shaded grey regions highlight key events that are visible in the vibration and/or force data.

of the incision. At the end of the closure, tie the suture to itself using a surgeon's knot – a double throw, followed by two single throws. Tools: (2) Large Needle Drivers.

B. **Pattern Cutting:** Cut and peel the skin off exactly along the marked line, avoiding damage to the underlying muscle tissue. Tools: (1) Maryland Bipolar Forceps, (1) Curved Scissors.

C. **Vessel Energy Dissection:** Dissect down to the turkey femoral artery or vein. Liberate a (>3 cm) segment of the vessel from the surrounding tissue, cauterize at two points (>0.5 cm apart), and cut the vessel in between those points. Tools: (1) Maryland Bipolar Forceps, (1) Curved Scissors.

To provide an analysis of time-synced events in the force and vibration data, the experimenter considered the time-series signals alongside the recorded video.

RESULTS

The Suturing task data shows large vibration spikes on both tools when the needle is passed from hand to hand (see Fig. 2A). The normal and tangential force exerted on the tissue increases when the surgeon pulls up on the tissue to drive the needle or pulls tight on the suture to close the incision. A negative normal force can also occur when the surgeon pushes on the tissue with one tool while pulling on the suture with the other.

The Pattern Cutting task generates more vibrations than Suturing, especially from the scissors (see Fig. 2B). With sufficient counter-tension, the vibration caused by the cut is also transmitted to the Maryland forceps. A few large vibration spikes are caused by collisions between the instruments. Both the tangential and normal forces exhibit peaks when the surgeon pulls on the tissue to create counter-tension for the cut. The negative normal forces typically stem from the surgeon pushing on the tissue to separate the skin from the fat.

The Vessel Energy Dissection task shows the strongest vibrations of the studied tasks (see Fig. 2C); these vibrations occur when the surgeon bluntly dissects the tissue, cuts tissue during the dissection, and cuts the vessel near the end of the task. Large vibrations also result from instrument collisions. There are both positive and negative normal forces exerted on the tissue, with corresponding tangential forces; these forces are the result of the surgeon pressing and pulling on the tissue to locate and dissect out the vessel.

DISCUSSION

This paper described the instrument vibrations and contact forces generated by one expert surgeon performing three FRS tasks on an avian tissue model. These recordings are consistent with those from other surgeons in the FRS trial. However, with further analysis, we do expect to find variation between subjects in different surgical specialties, especially when novice surgeons are considered. These results will hopefully unravel the unique signatures within the vibration and force data that can be used to not only identify a given task, but also automatically evaluate how skilled a surgeon is at performing that task.

REFERENCES

[1] H. W. R. Schreuder, R. Wolswijk, R. P. Zweemer, M. P. Schijven, and R. H. M. Verheijen, "Training and learning robotic surgery, time for a more structured approach: A systematic review," *BJOG*, vol. 119. pp. 137–149, 2012.

[2] R. Kumar, A. Jog, A. Malpani, B. Vagvolgyi, D. Yuh, H. Nguyen, G. Hager, and C. C. G. Chen, "Assessing system operation skills in robotic surgery trainees," *Int J Med Robot Comput Assist Surg*, vol. 8, pp. 118–124, 2012.

[3] W. McMahan, J. Gewirtz, D. Standish, P. Martin, J. A. Kunkel, M. Lilavois, A. Wedmid, D. I. Lee, and K. J. Kuchenbecker, "Tool contact acceleration feedback for telerobotic surgery," *IEEE Trans Haptics*, vol. 4, no. 3, pp. 210–220, 2011.

[4] K. Bark, E. D. Gomez, C. Rivera, W. McMahan, A. Remington, K. M. Murayama, D. I. Lee, K. R. Dumon, N. N. Williams, and K. J. Kuchenbecker, "Surgical instrument vibrations are a construct-valid measure of technical skill in robotic peg transfer and suturing tasks," in *Hamlyn Symp on Medical Robotics*, 2012, pp. 50–51.

[5] K. Bark, W. McMahan, A. Remington, J. Gewirtz, A. Wedmid, D. I. Lee, and K. J. Kuchenbecker, "In vivo validation of a system for haptic feedback of tool vibrations in robotic surgery.," *Surg Endosc*, vol. 27, no. 2, pp. 656–64, Feb. 2013.

Practical Dry Calibration with Medium Adaptation for Fluid-Immersed Endoscopy

F. Chadebecq[1], T. Vercauteren[1], R. Wimalasundera[2], G. Attilakos[2], A. L. David[3], J. Deprest[4], S. Ourselin[1], D. Stoyanov[1]

[1]*Centre for Medical Image Computing, University College London, UK*

[2]*Fetal medicine Unit, University College London Hospital, UK*

[3]*Institute for Women's Health, University College London, UK*

[4]*Department of Development and Regeneration, Katholieke Universities Leuven, Belgium*

f.chadebecq@ucl.ac.uk

INTRODUCTION

A few endoscopic procedures are performed with a fluid-immersed endoscope. Fetoscopy is one such minimally invasive procedure that allows observation and intervention within the amniotic sac during pregnancy. The fetoscope is inserted through the uterus and immersed in amniotic fluid. Fluid has a strong influence on the image formation process due to refraction at the interface of the fetoscopic lens. It is determined by the optical properties of the amniotic medium (Fig. 1).

Fig. 1 Images of a calibration target acquired with a fetoscope. Left: calibration setup. Right: images of the calibration target respectively in the air and in water.

Accurate calibration is critical to vision-based methods for providing image-guided surgery and real-time information from the surgical site [1]. It consists of recording images of a calibration target of known geometric pattern in order to estimate optical properties of a camera. In the case of a fetoscope, calibration should be realised in the amniotic fluid which currently cannot be practically achieved. A fluid-immersed calibration is also impractical for sterilisation purposes. Few computer vision methods address this issue and most of them are not adapted to the wide field of view as well as the severe distortion effect of a fetoscope [2]. We experimentally show a direct link between dry and fluid-immersed camera parameters that can compensate for the optical properties of amniotic fluid as well as radial distortion effects.

ENDOSCOPIC CAMERA MODEL

Endoscopic cameras generally embed large field of view optical systems. We chose to rely on the unifying model of central catadioptric system proposed in [3] to handle severe distortion effects and assume optical parameters remain fixed. This model unifies under a common mathematical formalism central catadioptric optical systems with a single projection centre. It has also been proved that the unified model can suit perspective as well as certain fish-eye optical systems which makes it flexible.

The image formation model, illustrated in figure 2, consists of four mappings. A projective ray joins a 3D point *Q* of the scene with the effective projection center *O* intersecting the unit sphere in a single point *Qs*. The second mapping is equivalent to projecting the point *Qs* into the normalized plane from a novel projection center $O'=(0,0,-\xi)T$. This non-linear mapping intrinsically handles severe radial and tangential distortions. However, a fourth degree function based on a Brown-Conrady model was considered to compensate for lens aberration and model approximations. The last transformation maps the distorted point *qd* to the point *q* observed in the image plane. It is expressed by the internal camera parameter matrix K which embeds the parameter γ (directly related to the focal length *f* of the camera), a skew parameter (pixel ratio) and the position of the principal point in the image plane. It is worth to note that γ is directly related to ξ according to the real shape of the omnidirectional camera considered [4].

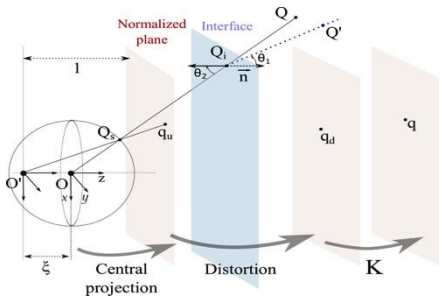

Fig. 2 Unifying model of central catadioptric system.

We now consider a thin interface, planar and fronto parallel to the image plane, which separates the optical system of the endoscope from the external medium (as it appears to be in practice). Because it is difficult to accurately calibrate the depth of the interface we

arbitrarily fixed it above the normalized plane. According to Snell's law the refraction angle of the incoming light ray is expressed by:

$$n_1 \sin\theta_1 = n_2 \sin\theta_2 \quad (1)$$

Where n_1, n_2 represent the refractive index of each medium at either end of the interface and θ_1, θ_2 represent the angles between the incoming ray and the normal $\vec{n}$ to the interface. We approximate the refractive index of the amniotic fluid by the refractive index of water $n_1 \simeq 1.33$. According to the unified model, we expect to estimate a new value ξ' and a new focal length γ' to compensate for the refractive properties of fluid. The new ξ' is obtained thanks to:

$$\xi' = arg\min_{\xi} \sqrt{(q_{ux} - \frac{Q'_x}{Q'_z + \|Q'\|\xi})^2 + (q_{uy} - \frac{Q'_y}{Q'_z + \|Q'\|\xi})^2} \quad (2)$$

where q_u corresponds to the coordinates of a 2D point on the normalized plane and Q' is an immersed 3D point casting on the normalized sphere on point Qs. According to Snell's law (1), Q' lies on the light ray belonging to the plane defined by $\overrightarrow{(Q_i, Q_s)}$ and $\vec{n}$ and forming an angle θ_2 with $\vec{n}$ at Qi. The unifying model of central catadioptric system allows to derive the value of γ' according to ξ' and the shape of the catadioptric mirror. This relationship cannot be applied to a fetoscope which does not embed a real catadioptric system. However, our experiments, presented in the last section, show that an appropriate value of γ' can compensate for the refraction effects without the need to estimate other camera parameters.

METHOD

The calibration method can be decomposed in the following steps. We first realize a dry calibration of the fetoscope using [4]. We use one of the calibration image to estimate the light paths inside the optical system from each pixel of the image plane to the 3D points Qi belonging to the interface plane. We then use equation (1) to compute new incoming light paths considering the refractive index of the external fluid. We randomly define 3D point Q' lying on each of these light rays. Finally we use (2) to estimate the new value of ξ'. The back ray tracing algorithm require to convert each mapping of the image formation model. However, the distortion function is not directly invertible. We used [5] to estimate the inverse distortion function.

RESULTS

We conduct experiments with three Storz fetoscopes model 26120a (33-degree angle of view), 27020aa and 26003aga (0-degree angle of view). Each dataset is composed of 15 dry and underwater calibration images as amniotic fluid is mainly made up of water. We compared underwater calibration results with the results obtained by estimating fluid-immersed camera parameters form a dry calibration. We used previously defined algorithm to compute ξ'. We used a single underwater observation to compute γ' by minimising the reprojection error for the last mapping of the image formation process. We used underwater images to compare the two methods. Results are illustrated in figure 3 and synthesised in the following table.

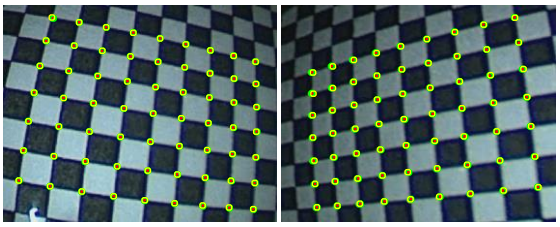

Fig. 3 Reprojection error. Red dots: ground truth, yellow and green circles: 3D points projected in the images using underwater calibration parameters and estimated parameters. Left: 33 degree fetoscope. Right: 0 degree fetoscope.

Reprojection error (pixel)	Fetoscope 1 (0 degree)	Fetoscope 2 (33 degree)	Fetoscope 3 (0 degree)
underwater calibration	0.46 ± 0.06	0.43 ± 0.43	0.52 ± 0.21
Estimated calibration	0.69 ± 0.14	0.70 ± 0.12	0.75 ± 0.12

The results show that estimated calibration is less accurate than a proper underwater calibration but the reproduction error is less than a pixel for all the fetoscope used for experiments. As most of the distortion effects are corrected underwater, a proper calibration of the fetoscopes using a central catadioptric model was difficult to obtain [3].

DISCUSSION

We presented promising results which show that fluid-immersed endoscope parameters could be directly inferred from a dry calibration using the unifying catadioptric model. Investigations will be conducted in order to establish a proper link between ξ and γ. This could lead to a fast calibration process adapted to the constraints of fluid immersed endoscopy.

ACKNOWLEDGMENT

This work was supported through an Innovative Engineering for Health award by Wellcome Trust [WT101957], Engineering and Physical Sciences Research Council (EPSRC) [NS/A000027/1]. A.L David is supported at UCL/UCLH by funding from the Department of Health NIHR Biomedical Research Centres funding scheme.

REFERENCES

[1] Wengert C, Reeff M, Cattin P, Székely G. Fully Automatic Endoscope Calibration for Intra operative Use. Bildverarbeitung für die Medizin. 2006; 419-423.

[2] Lavest JM, Rives G, Laprest J. Dry Camera Calibration for Underwater Applications. MVA. 2003; 245-253.

[3] Barreto JP. A unifying geometric representation for central projection systems. CVIU. 2006; 208–217.

[4] Mei C, Rives P. Single View Pont Omnidirectional Camera Calibration from Planar Grids. ICRA. 2007.

[5] Heikkila J, Silven O. A four-step camera calibration procedure with implicit image correction. CVPR. 1997.

Label-based Optimization of Dense Disparity Estimation for Robotic Single Incision Abdominal Surgery

V. Penza[1,2], S. Bacchini[2], A. Ciullo[2], E. De Momi[2], A. Forgione[3], L. S. Mattos[1]

[1]*Department of Advanced Robotics, Istituto Italiano di Tecnologia, Italy*

[2]*Department of Electronics Information and Bioengineering, Politecnico di Milano, Italy*

[3]*AIMS Academy, Milano, Italy*

veronica.penza@iit.it

INTRODUCTION

Minimally invasive surgical techniques have led to novel approaches such as Single Incision Laparoscopic Surgery (SILS), which allows the reduction of post-operative infections and patient recovery time, improving surgical outcomes. However, the new techniques pose also new challenges to surgeons: during SILS, visualization of the surgical field is limited by the endoscope field of view, and the access to the target area is limited by the fact that instruments have to be inserted through a single port.

In this context, intra-operative navigation and augmented reality based on pre-operative images have the potential to enhance SILS procedures by providing the information necessary to increase the intervention accuracy and safety [1]. Problems arise when structures of interest change their pose or deform with respect to pre-operative planning, as usually happens in soft tissue abdominal surgery. This requires online estimation of the deformations to correct the pre-operative plan, which can be done, for example, through methods of depth estimation from stereo endoscopic images (3D reconstruction). The denser the reconstruction, the more accurate the deformation identification can be.

This work presents an algorithm for 3D reconstruction of soft tissue, focusing on the refinement of the disparity map in order to obtain an accurate and dense point map. This algorithm is part of an assistive system for intra-operative guidance and safety supervision for robotic abdominal SILS [2].

MATERIALS AND METHODS

3D shape reconstruction using stereo-images is a process composed of two main steps: the disparity estimation and the stereo-triangulation. Using the left and right images (im_l, im_r) captured by a stereo camera, the disparity is estimated searching corresponding points between images. These are the projection of the same world point into two image planes. The relative distance between the corresponding pixels is described by the disparity map. Stereo-triangulation consists in exploiting the detected correspondence and the geometry of the cameras to extract the 3D measurement of the observed scene [3].

In this section, the steps of an improved algorithm for surface reconstruction are described (Fig. 1).

Disparity Estimation

Images are rectified in order to simplify the stereo-correspondence analysis. An intensity pixel-based algorithm is used for local similarity searching. A sparse modified census transform [4] is applied to im_l and im_r before matching. This method is robust against non-stationary exposure and illumination variations. It converts each pixel inside a moving window (nxn) into a bit vector, representing which neighbor pixels have an intensity above or below the central pixel and the mean of the pixels inside the window.

The similarity between the two census transformed images is done using the sum of Hamming Distance (HD) measure applied on a moving window. HD compares bit strings representing the pixels and identifies the number of positions at which the corresponding bits are different. These values are summed within a window (mxm) and a "winner-takes-all" strategy is used to find the minimum, and thus the disparity associated to the best similarity. The HD is computed only for a chessboard pattern of pixels inside the window in order to decrease the computational time.

Since using only pixel precision the reconstructed surface would consist of separated layers, a sub pixel refinement is applied using a parabola fitting. To invalidate wrong pixels on texture-less surfaces, the disparity is defined invalid if the two minimum values of HD are within a threshold. Additionally, a Left-Right Consistency (LRC) check is performed to invalidate half-occluded pixels, i.e. object views in one image and not in the other. A speckle removal filter is also applied in order to invalidate regions of large and small disparities that can be generated near the boundaries of the objects.

Dense Disparity Optimization

The pixels of the disparity map defined invalid lead to holes in the point cloud, compromising the usefulness of the reconstructed surface. Here, we exploit the segmentation of the reference image im_l to optimize the disparity map (Alg. 1). In literature, these techniques segment the images and then label each region with a disparity value, preserving the boundaries of the objects. However, finding gradually changing disparities can be a problem since all pixels in a region have the same disparity. Moreover, segmentation algorithms are computationally expensive.

Algorithm 1 *Label-based Disparity Optimization*

Require: D disparity map
L_i labeling of im_l segmented with SLIC Superpixel
M mask of invalid disparity values
τ threshold of number of valid points

1: associate L_i to D $\rightarrow$ DL_i
for each DL_i $i \in \{1,..nSuperPixel\}$
3: **compute** plane parameters p with LO-RANSAC of
4: $DL_i(i,j)$ with $i = n_{cols}$, $j = n_{rows}$
5: **compute** median m of $DL_i(i,j)$
end for
for each i and j of D
if $M(i,j) = true$
if $(nValidPoints \in DL_i) > \tau$
6: replace $D(i,j)$ with m (DL_i)
else
7: replace $D(i,j)$ with a point on $p(DL_i)$
end if
end if
end for
return disparity map $D_{refined}$

To overcome these drawbacks, im_l is segmented using a Simple Linear Iterative Clustering (SLIC) super pixel algorithm [5]. Each super-pixel is an homogeneous area with similar or at least continuous depth. A label L is assigned to each super-pixel, being $im_l(L)$ a group of pixels with the same label, i.e. belonging to the same super-pixel. Only the invalid values of disparity map are corrected using the information of the pixels belonging to the same label. Depending on the valid values inside a label, we apply two different strategies:

- *Plane fitting*: if the found plane can be considered a reliable plane, the invalid disparity values are fitted to that plane. The plane parameters are estimated using the Locally Optimized RANSAC method.
- *Constant fitting*: otherwise, the invalid disparity values are replaced by the median of the valid ones.

After the stereo-triangulation step, a Moving Least Square algorithm is applied in order to smooth the point cloud, using PCL library.

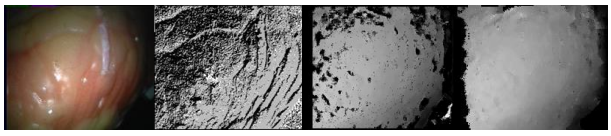

Fig. 1 Main steps of the presented algorithm. From left to right: RGB image, census transformed image, disparity map, dense refined disparity map.

RESULTS

The point clouds obtained are validated using 10 frames from a video dataset (*heart 1*) available online from the Hamlyn Centre [6], the closest available datasets to the application of this work. The error is defined as the median of Euclidean distances between the point cloud and the ground truth. We calculated this error for different window sizes of census transform and Hamming Distance to show the correlation between the accuracy and the computational time, as shown in Fig. 2. We considered also the percentage of valid points to evaluate the density of the point cloud (Fig. 2 – black line). Results show how the smoothing improves the accuracy of the reconstruction, giving a median error between $1.50mm$ and $2.27mm$ in the worst case.

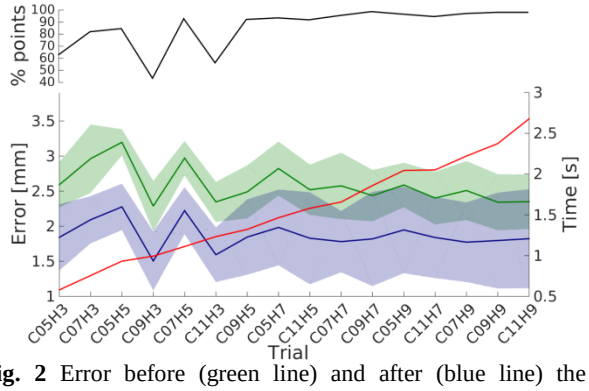

Fig. 2 Error before (green line) and after (blue line) the smoothing, and the pre-smoothing computational time (red line) with the corresponding interquartile range. C*nHm* represents the dimension of a squared window used in census transform (C) and in HD (H), ordered increasingly with time.

DISCUSSION

The presented work provides a dense surface reconstruction to be used in an enhanced vision system for robotic abdominal SILS. The strength of this method is the usage of SLIC Super Pixel algorithm for obtaining a high density valid disparity map (over the 90% of the total number of points), which can be exploited for augmented reality applications. Comparing our method with state-of-the-art CPU implementations [7] evaluated on *heart 1*, the percentage of valid points obtained with our method is 40% higher while providing a slightly lower accuracy (mean error 2.38 mm). Future research will focus on the development of a real-time implementation of the proposed algorithm, potentially based on a hybrid CPU-GPU processing framework.

REFERENCES

[1] Nicolau S, Soler L, Mutter D, Marescaux J. Augmented reality in laparoscopic surgical oncology. Surgical Oncology. 2011; 20(3):189-201

[2] Penza V, Ortiz J, De Momi E, Forgione A, Mattos L. Virtual assistive system for robotic single incision laparoscopic surgery. 4th Joint Workshop on Computer/Robot Assisted Surgery. 2014; 52-55

[3] Szeliski R. Computer vision: algorithms and applications. Springer Science & Business Media. 2010.

[4] Ma L, Li J, Ma J, Zhang H. A Modified Census Transform Based on the Neighborhood Information for Stereo Matching Algorithm. Image and Graphics (ICIG). 2013.

[5] Achanta R, Shaji A, Smith K, Lucchi A, Fua P, Susstrunk S. SLIC superpixels compared to state-of-the-art superpixel methods. Pattern Analysis and Machine Intelligence. 2012; 34(11): 2274-2282.

[6] Stoyanov D, Scarzanella M V, Pratt P, Yang G Z. Real-time stereo reconstruction in robotically assisted minimally invasive surgery. MICCAI. 2010; 275-282

[7] Röhl S, et al. Dense GPU-enhanced surface reconstruction from stereo endoscopic images for intraoperative registration. Medical Physics. 2012; 39(3): 1632-1645.

Recognition of Intentional Violations of Active Constraints in Cooperative Manipulation Tasks

M. Aricò[1], S. A. Bowyer[2], E. De Momi[1], G. Ferrigno[1], S. Pastorelli[3], F. Rodriguez y Baena[2]

[1]*Department of Electronics, Information and Bioengineering, Politecnico di Milano, Italy*
[2]*Department of Mechanical Engineering, Imperial College London, UK*
[3]*Department of Mechanical and Aerospace Engineering, Politecnico di Torino, Italy*
f.rodriguez@imperial.ac.uk

INTRODUCTION

Active Constraints (ACs) are high-level control algorithms deployed to assist a human operator in man-machine cooperative tasks [1], and define regions within which it is safe for the robot to move and cut [2]. To enhance the performance in cooperative surgical tasks, adaptive constraints have been exploited to optimally adjust the provided level of assistance according to some knowledge of the task, hardware or user. In [3] Hidden Markov Models were used for the run-time detection of the user intention to leave a guidance constraint to circumvent an obstacle. In this work, we present a novel, Neural Network (NN)-based method for the runtime classification of intentional and unintentional violations of ACs, that is trained on either statistical or frequency features from the enforced constraint forces. We investigate which set of parameters yield faster and more reliable classification results, both for guidance and regional constraints.

METHODS

Active Constraints

During cooperative assistance, intentional violations of ACs take place whenever the current action of the user is in disagreement with the purpose of the constraint, typically resulting from sensing limitations of the robotic system. In this case, the constraint is felt as a hindrance, resulting in disturbing interaction forces at the tip. Unintentional violations occur when the user shares the purpose of the constraint and accidental errors in the task execution are made. The classification of the user's intended action during the cooperative task would allow one to optimally adjust the assistance level provided by ACs. ACs can have two purposes [1]:

- *Guidance constraints* are enforced to guide the motion of the tool along a specified trajectory;
- *Regional constraints* are enforced to bound the motion of the tool into certain safe regions.

Both types of constraints were considered in this work, and modeled with a planar geometry according to a conventional viscoelastic constraint model:

$$\boldsymbol{f} = K(\boldsymbol{x} - \boldsymbol{x}_{eq}) - D\dot{\boldsymbol{x}} \qquad (1)$$

where $\boldsymbol{x}$ and $\dot{\boldsymbol{x}}$ are the position and velocity of the tool tip; K and D are the stiffness and damping parameters ($K > 0$, attractive fixture), $\mathbf{x}_{eq}$ is the equilibrium point that lies on the constraint where it is closest (Euclidian distance) to the current tool tip position. To enforce the constraints during the cooperative guidance, the commanded torque of the haptic master is computed from the resulting Cartesian force $\boldsymbol{f}$ according to the geometrical Jacobian.

Classification Method

Two NN-based binary classifiers were developed for the runtime identification of "intentional" and "unintentional" violations of ACs. The two approaches exploited different features, extracted from the interaction force signal across the tip-constraint interface, as follows:

1. Statistical (StNN): A feedforward NN was trained and validated on a dataset of 7 statistical features computed on the temporal evolution of the interaction force: mean, variance, energy, maximum value, integral, waveform length, average amplitude change;
2. Spectral (SpNN): A feedforward NN was trained and validated on a dataset of 10 spectral features computed on the time evolution of the force energy distribution using the Wavelet decomposition (9 levels) [4];

The structures of the StNN and SpNN were composed of one hidden layer (15 and 33 neurons respectively, "trial and error" optimization), and one output neuron (hyperbolic tangent activation functions).

EXPERIMENTAL DESIGN

Experimental setup

The Phantom Omni (Sensable Technologies, Inc.) haptic device was used during assisted cooperative tasks. The active constraint controller was implemented using the "PhanTorque"[1] Simulink-compatible library on Matlab/Simulink R2014b platform. Visual feedback of the task execution was provided with a 2-D monitor.

[1] https://sir.upc.edu/wikis/roblab/index.php/Projects/PhanTorqueLibraries

Experimental protocol

To evaluate task-independent properties of the two classifiers, two sets of tasks were considered (Fig. 1):

- *Following task.* The user was asked to accurately move along 2D spline-based paths, assisted by a *guidance constraint*. He/she was asked to circumvent any circular obstacles placed along the path by acting against the constraint;
- *Reaching task*. The user had to accurately place the pointer on several equally spaced targets, which lay within a forbidden region bounded by a *regional constraint* with 50% probability.

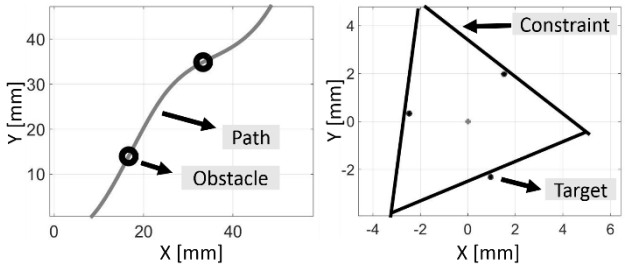

Fig. 1. Following Task (left) and Reaching Task (right)

We asked 12 subjects to perform 10 trials for each of the two tasks. The force signal was filtered, recorded, segmented to extract non-null interactions ($\mathbf{f} > 0$) and labeled as intentional or unintentional according to the known positions of obstacles/region boundaries. Two task-related datasets were built from all users across all trials. Both SpNN and StNN methods were cross-validated on each task dataset, and the performance were computed in terms of sensitivity (Se) and specificity (Sp) over time as:

$$Se(t) = TP(t)/(TP(t) + FN(t)) \qquad (2)$$

$$Sp(t) = TN(t)/(TN(t) + FP(t)) \qquad (3)$$

where TP and TN are the amount of correctly classified intentional (true positive) and unintentional violations (true negative), respectively; FN and FP are the amount of misclassified intentional (false negative) and unintentional violations (false positive), respectively.

RESULTS AND DISCUSSION

The classification threshold applied on the continuous output of the networks was optimized to achieve 90% asymptotic specificity. Consequently, the classifier was evaluated in terms of sensitivity-time profile (Fig. 2), and the minimum time interval to overcome a 90% sensitivity level was obtained. The Se index shows a sigmoidal profile in time for both tasks and methods. As reported in Table I, the 90% sensitivity was achieved for both methods within 1s for the *following* task (mean velocity 4.17 mm/s), and within 3s for the *reaching* task (mean velocity 8.36 mm/s). In the *following* tasks, as no motion limitation was imposed to the user during obstacle avoidance, a greater penetration was recorded with respect to the *reaching* task. Moreover, the StNN method resulted in higher performance with respect to SpNN method, yielding a 60% time reduction for the *following* task, and a 30% reduction for the *reaching* task. The proper classification timing is chosen based on the sensitivity level required by the specific application.

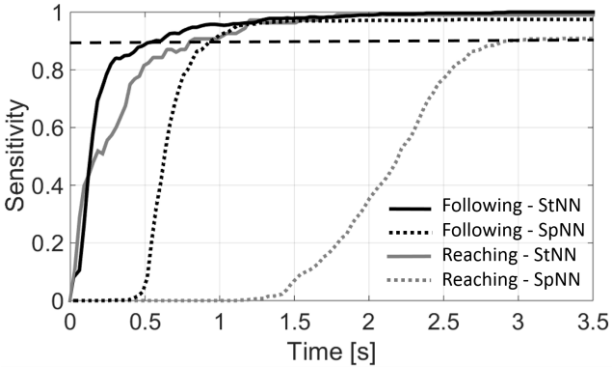

Fig. 2. Sensitivity profiles in time, across methods and tasks.

Table I Classification time and relative constraint penetration among methods and tasks ($\boldsymbol{Se = 90\%}$).

Task	Method	Time [s]	Penetration [mm]
Following	StNN	0.559	0.82
	SpNN	0.954	1.21
Reaching	StNN	0.816	0.51
	SpNN	2.911	0.52

CONCLUSIONS

NN-based algorithms were demonstrated to be suitable for the runtime task-independent classification of intentional and unintentional violations of ACs. Better performance was obtained for the *guidance constraints* with respect to regional constraints. Additionally, the use of statistical features yields a faster classification with respect to the use of spectral parameters. Future work could apply multi-objective model selection to find the optimal classifier, introduce data regularization (subsampling) to prevent class unbalance and combine statistical and spectral features. Moreover, some methods to exploit the continuous output of the NN could be investigated to optimally modulate the constraint assistance according to the probability of the user's intention classification in surgical manipulation tasks.

REFERENCES

[1] S. Bowyer, B. L. Davies, and F. Rodriguez y Baena. "Active constraints/virtual fixtures: A survey." In: Robotics, IEEE Transactions on 30.1 (2014): 138-157.

[2] B. Davies, et al. "Active-constraint robotics for surgery." Proceedings of the IEEE 94.9 (2006): 1696-1704.

[3] D. Kragic, et al. "Human-machine collaborative systems for microsurgical applications. In: " The International Journal of Robotics Research 24.9 (2005): 731-741.

[4] S. Pittner, and S. V. Kamarthi. "Feature extraction from wavelet coefficients for pattern recognition tasks." In: Pattern Analysis and Machine Intelligence, IEEE Transactions on 21.1 (1999): 83-88.

Autonomous Execution of Surgical Tasks: the Next Step in Robotic Surgery

R. Muradore[1], G. De Rossi[1], M. Bonfe[2], N. Preda[2], C. Secchi[3], F. Ferraguti[3], P. Fiorini[1]

[1] *Department of Computer Science, University of Verona, Italy*
{riccardo.muradore, giacomo.derossi, paolo.fiorini}@univr.it

[2]*Engineering Department, University of Ferrara, Italy*
{marcello.bonfe, nicola.preda}@unife.it

[3]*Department of Science and Methods for Engineering, University of Modena and Reggio Emilia, Italy*
{cristian.secchi, federica.ferraguti}@unimore.it

INTRODUCTION

Minimally invasive surgery first and, more recently, surgical robotics have brought new perspectives to surgery and have significantly improved the quality of many critical surgical tasks [1,2].

In this paper we go further by describing the design and testing of an architecture to control a robotic platform capable of executing in an autonomous way basic surgical tasks such as US-guided needle insertion and suturing. The results have been obtained during the FP7 European funded project Intelligent Surgical Robotics (I-SUR, grant agreement n. 270396). The main goal of the project was to demonstrate that autonomous surgical robotics can carry out simple surgical tasks effectively and without major intervention by surgeons. To fulfil this goal, we have developed an innovative approach (both in terms of technologies and algorithms) for planning and execution of movement of robot arms in contact with the deformable anatomical environment.

In [3,4] we described a methodology to collect requirements from surgeons, to translate the requirements in a formal and goal-oriented language, and to design sequence and state diagrams in Universal Model Language (UML) that can be implemented by an autonomous robotic platform. The trajectory planning based on pre-operative data (CT or MRI) is performed automatically as reported in [5]. The control and software architecture is described in [6]. Since the architecture of the system is modular and component-based by design, the same methodology can be applied to automate both the puncturing and suturing tasks.

With the proposed approach, the robotic system autonomously deals with the simplest tasks of a surgical procedure, whereas the surgeon can focus his/her attention on the most critical parts. The surgeon monitors the automatic execution of the task thanks to a user interface where all the relevant data of the procedure are clearly shown, and warning notices are displayed.

CASE STUDY AND ROBOTIC SETUP

To develop the system requirements we focus on surgical actions that would benefit mostly from the accuracy and repeatability levels achievable by intelligent robots. We selected percutaneous cryoablation of small tumors and automated suture of planar wounds as our case studies. Percutaneous cryoablation requires the use of pre- and intraoperative images (CT, MRI/US) to insert, through the skin, one or more cryoprobe needles into the tumoral mass to be destroyed and to check the real-time position of the tools inside the patient. Trajectory misalignments are usually due to the deformation of soft tissues and organ displacement because of breathing. Thanks to real-time image registration and accurately calibrated mechanical arms, needle insertion will be executed precisely by the robots and monitored via US images as described in [7].

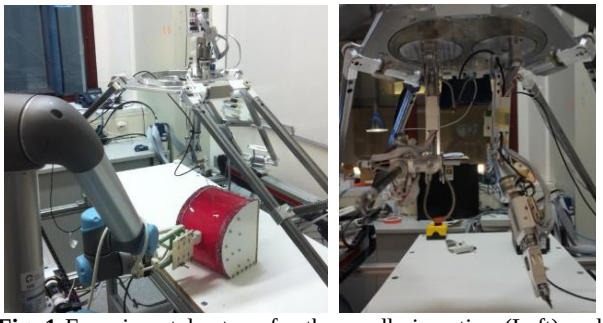

Fig. 1 Experimental setups for the needle insertion (Left) and for the suturing (Right).

To evaluate practical issues and benefits of cryoablation execution by means of automated robots, an experimental setup was prepared, as shown in Figure 1(Left). The setup includes two robotic manipulators: the ISUR micro-macro robot (developed by ETH) holds the needle, while the commercial UR5 robot holds the US probe. The end-effectors of both robots are equipped with specific tool adapters that integrate 6-DOF force/torque sensor. We used an Accutrack 500 from Atracsys LLC, Switzerland, to estimate the relative coordinate transformations among the robots, the phantom and the US images. Fig. 1(Right) shows the

setup for the suturing: the ISUR robot is equipped with two arms: the left arm holds the Covidien Endostich for performing the suture whereas the right arm is needed to grasp the thread to avoid knots during the procedure. In the experimental section we will focus on puncturing due to the space limitation and provide web link for videos related to suturing.

RESULTS

In this section the time series of forces and the states of the robots control logic recorded during the experimental phase are reported (see Figures 2 and 3). The proposed experimental setup goes through the following steps triggered by the surgeon through the user interface:

(1) The surgeon pushes the *Ready* button. Both robots move from their nest position to the ready position where the needle and the US probe are mounted.

(2) The robots receive their nominal trajectories and move the needle and the US probe in contact with the phantom.

(3) When the surgeon pushes the *InsertNeedle* button, the robot holding the needle starts the insertion until it reaches the target point as monitored by the US probe. In this case the state of the control logic is "WaitCryoCycle". However if the surgeon decides to stop the procedure (*Stop* button) because the needle is not visible in the US image any more, the robot holding the US probe performs a sequence of movements to bring the needle back on the US images.

(4) The surgeon pushes the button *Finish* to bring the robots back in the "Ready" state.

Figure 3(Top) shows the force measured by the F/T sensor located on the robot holding the needle along the main axis of the needle. The dashed vertical lines and the numbers help to understand what state of the control logic (Figure 2) is activated. Figure 3(Bottom) reports the Cartesian tracking error w.r.t. the nominal trajectory. At the following link a video of the US-based needle insertion can be seen:
http://1drv.ms/1F4z6v4
whereas the links:
http://1drv.ms/1F4zaLo
http://1drv.ms/1F4zbyN
refer to the on-going development of the suturing task.

DISCUSSION

In this paper we presented a robot control and coordination framework for the automation of simple surgical tasks. We formalized the design specifications using a requirements engineering approach and derived the state machines for the control of the robots. Then, we implemented the proposed architecture using component-based design tools, i.e. Orocos framework and rFSM, in order to properly handle the distributed nature of our system. The goal of these experiments was to show that the technology to execute autonomously basic surgical tasks is available and could be used to improve accuracy as requested by surgeons and radiologists involved in the ISUR project.

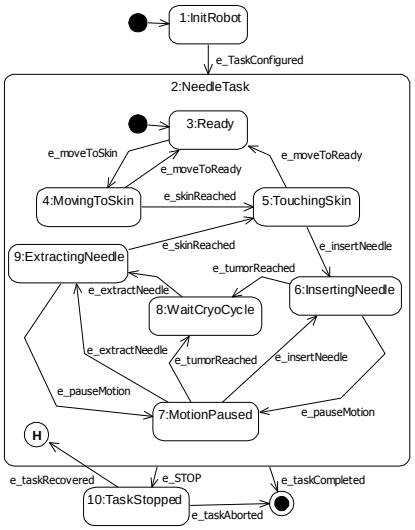

Fig. 2 UML State Diagram for the needle insertion task.

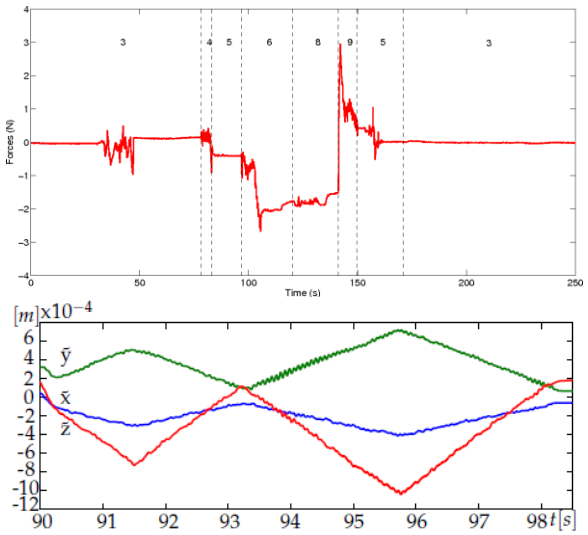

Fig. 3 Top. Force applied to the needle during the emulated cryoablation task**;** Bottom: tracking error (position) during the approach and insertion phase.

REFERENCES

[1] G.H.Ballantyne, "Robotic surgery, telerobotic surgery, telepresence, and telementoring," Surgical Endoscopy And Other Interventional Techniques, vol. 16(10), 2002.

[2] J.Rosen, B.Hannaford, and R.Satava, Surgical Robotics: Systems Applications and Visions. Springer, 2011.

[3] M.Bonfe, F.Boriero, R.Dodi, P.Fiorini, A.Morandi, R.Muradore, L.Pasquale, A.Sanna, and C.Secchi, "Towards automated surgical robotics: A requirements engineering approach," BioRob, 2012, pp. 56–61.

[4] R Muradore, P Fiorini, et al. "Development of a Cognitive Robotic System for Simple Surgical Tasks", Int J Adv Robot Syst, 2015

[5] M.Torricelli, F.Ferraguti, and C.Secchi, "An algorithm for planning the number and the pose of the iceballs in cryoablation," in EMBC, Osaka, Japan, July 2013.

[6] M.Bonfé, N.Preda, C.Secchi, F.Ferraguti, R.Muradore, L. Repele, G.Lorenzi, P.Fiorini, "Distributed Control Architecture for Automated Surgical Task Execution with Coordinated Robot Arms", IFAC-WC2014.

[7] K.Mathiassen, D.Dall'Alba, R.Muradore, P.Fiorini, and O.Elle, "Real-time Biopsy Needle Tip Estimation in 2D Ultrasound Images," in Proc. of ICRA, Germany, 2013.

Modular Fibre-optic Shape Sensor for Articulated Surgical Instruments

S. Sareh[1], Y. Noh[1], T. Ranzani[2], H. A. Wurdemann[1], H. Liu[1], K. Althoefer[1]

[1]*Centre for Robotics Research, Dept. of Informatics, King's College London*

[2] *Bio-Robotics Institute, Scuola Superiore Sant'Anna, Italy*

S.Sareh@kcl.ac.uk

INTRODUCTION

The rigid structure of laparoscopic instruments restricts manoeuvrability and reduces the possibility to reach surgical targets that are not situated along the line-of-sight of the entry point. In such a situation, the surgeon needs to reposition the laparoscopic instrument with the risk of damaging healthy tissue and organs.

In order to address this limitation, several articulated surgical instruments have been developed. Prominent examples of such flexible systems include the i-Snake [1], HARP [2], active-cannula based systems [3], and the STIFF-FLOP arm [4]. These robots often consist of curved segments joined serially, which enable a high degree of articulation and increased manoeuvrability in confined spaces such as the human body. It is noted though, that the control of these robots requires precise shape and position sensing. The purpose of this research is to achieve shape sensing through multi-segment curvature sensing. Review of similar studies reveals that the motion of these robots have been mainly tracked using vision [5] or electromagnetic tracking [6]. However, vision based systems are often restricted due to visual occlusion, and electromagnetic tracking is subject to magnetic field distortions, in addition to its spatial range being limited to the generated magnetic field [7]. Fibre Bragg Grating (FBG) sensors have been proposed for shape sensing in continuum robots [7]; nevertheless, these systems are highly sensitive to the change in environmental temperature. Also when subjected to a non-uniform strain field, the strain compensation becomes complex [8].

This paper presents a highly compact system composed of optical fibre bundles for multi-segment shape sensing based on light intensity modulation, with the capability of modular sensing.

MATERIALS AND METHODS

The proposed arrangement is 7.5 mm in diameter and comprises a flexible and stretchable Steiner chain section [9] with twelve housings at the tip which accommodates driving tendons and passive cables used for sensing. The Steiner chain section is followed by a basal rigid optical fibre sensing unit (Fig. 1), where the passive cables are mechanically coupled with optical fibres. The optical fibre sensing unit is integrated with a low-friction retractable distance modulation array (Fig. 2a). This mechanism uses a steel needle-spring double slider (Fig. 2c) connected to the base through an extension spring (Fig. 2e) to reduce the hysteresis and recover reference sensor values when the arm returns to its original straight configuration. In order to place the emitter and detector next to each other, the fibre was looped (Fig. 2d). Through the loopback design of the sensing system, all electronics are kept away from the sensing site.

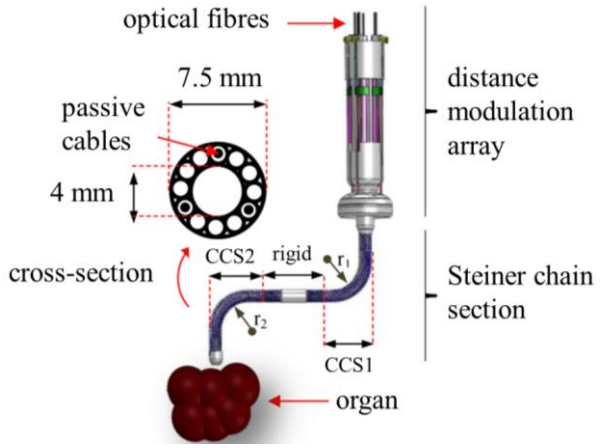

Fig. 1. The overall structure of the shape sensing system. Note that the flexible section also provides an empty central channel for end-effector instruments (CCS1 and CCS2 indicate constant curvature segments with radii of r_1 and r_2, respectively).

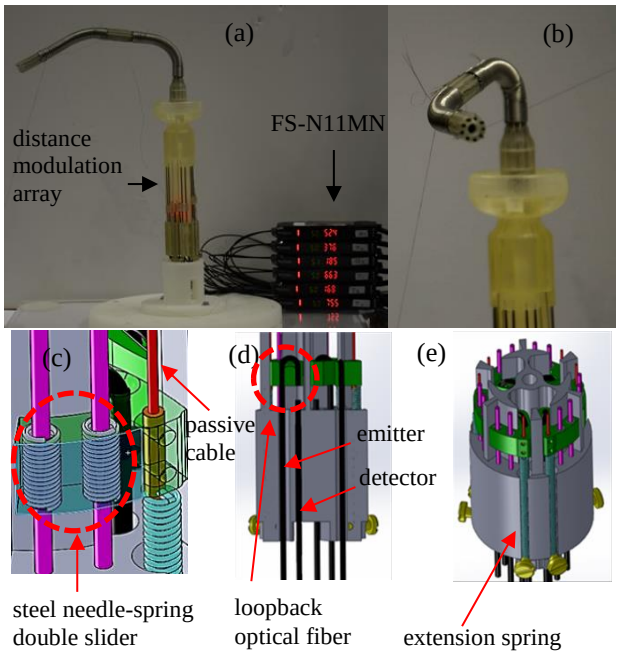

Fig. 2. The prototype of the arm and sensing system: (a) the finished configuration of the sensorized manipulation system, (b) close-up view of the top part, (c) the low-friction steel spring- needle double sliding mechanism (d) the loopback optical fibre arrangement, and (e) the recovery mechanism of the slider using an extension spring.

The curvature sensor of each segment of the arm consists of three passive cables. These cables are sliding inside flexible Steiner chain housings in the periphery of the arm, as shown in Fig.1, in parallel with driving tendons. When the arm bends, the cables' length portion inside the arm (s_1, s_2 and s_3) will change according to the pose of the arm. The changes in the length of these equally spaced cables modulate the position of the transmitting optical fibres (emitters) and, consequently, the intensity of light received by detectors (e.g. FS-N11MN, Keyence™). The received light is then converted into voltage $v = [v_1\ v_2\ v_3]$. By relating the voltage to the corresponding unique distance vector $s = f(v) = [s_1\ s_2\ s_3]$, the configuration parameters of the arm are acquired for each specific pose, which are computed as follows [10]:

$$S = \frac{1}{3}\sum_{i=1}^{3}(s_i),\ \ \theta = \frac{S - s_1}{d\cos(\frac{\pi}{2} - \varphi)},\ \ \varphi = \tan^{-1}(\frac{\sqrt{3}(s_2 + s_3 - 2s_1)}{3(s_2 - s_3)})$$

where S is the arc length of the central axis of the each segment, θ is the bending angle, φ is the orientation angle, and d describes the distance between the central axis of the manipulator and the parallel sensing tendons (here d=2.1mm).

This sensing arrangement uses only three Steiner channels out of twelve, extended along the whole length of the arm, for sensing. There are two passive cables sliding inside each of these three channels. One of the cables is fixed between two segments and the other one is fixed at the tip of the manipulator. This implementation allows measuring the bending angle in multi-segment arms in a modular way, in the sense that the Steiner chain structure remains the same for all segments.

RESULTS

In order to validate the design and implementation of the two-segment shape sensor, we have performed a set of experiments and measured the amount of bending curvature in each segment (Fig. 3). Two cameras were placed at the top and side of the manipulator to record ground-truth shape information.

DISCUSSION

This paper presents a novel shape sensing system for a multi-segment flexible manipulation arm. Three Steiner Chain channels were used for shape sensing in a two-segment articulated arm. A low-friction optical fibre distance modulation array based on a new spring-needle double slider was designed to precisely modulate the distance between emitter and detector optical fibres during the arm's bending. The design also employs a loopback optical method to keep all electronics away from of the sensing site. The complete sensing system is implemented and experimentally evaluated. A maximum error of 6° with respect to the camera ground-truth information was determined. From the experimental results, it can be seen that the sensing error can be reduced by increasing the initial stretch length of extension springs, hence, tightening the passive cables used for sensing.

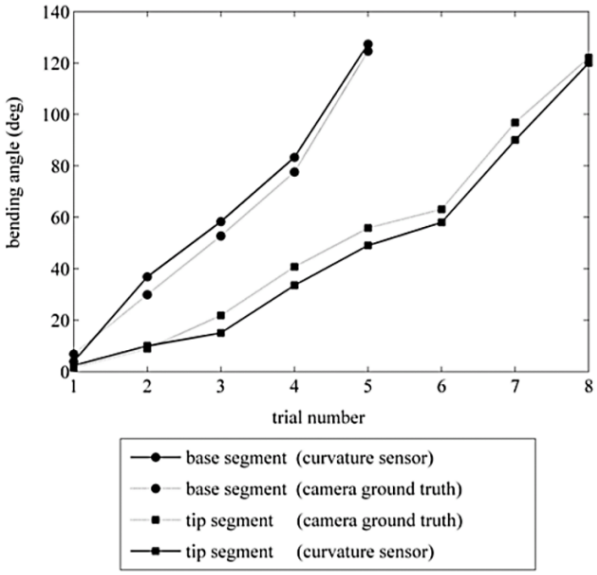

Fig. 3. The experimental results of curvature sensing in individual segments.

REFERENCES

[1] J. Shang et al. (2011) "An Articulated Universal Joint Based Flexible Access Robot for Minimally Invasive Surgery", IEEE Int. Conf. Robot. Autom. pp. 1147-1152, 2011.

[2] A. Degani et al., "Highly Articulated Robotic Probe for Minimally Invasive Surgery," in 30th Annual Int. IEEE EMBS Conference, Vancouver, British Columbia, Canada, August 2008.

[3] R.J. Webster et al., "Toward active cannulas: Miniature snake-like surgical robots, International Conf. on Int. Robots and Systems", 2857-2863, 2006.

[4] M Cianchetti et al. (2014) "Soft robotics technologies to address shortcomings in today's minimally invasive surgery: the STIFF-FLOP approach, Soft Robotics" 1 (2), 122-131, 2014.

[5] J.M. Croom, D.C. Rucker, J.M. Romano, R.J. Webster. "Visual sensing of continuum robot shape using self-organizing maps", IEEE International Conference on Robotics and Automation, 4591 – 4596, 2010.

[6] M. Mahvash, and D.E. Dupont, "Stiffness Control of a Continuum Manipulator in Contact with a Soft Environment", Conf Proc IEEE/RSJ International Conference on Intelligent Robots and Systems 2010:863-870, 2010.

[7] S. Ryu, P. E. Dupont, "FBG-based Shape Sensing Tubes for Continuum Robots", IEEE Int. Conf. Robotics and Automation, pp. 3531-3537, 2014.

[8] X. Zhang et al., "Experimental investigation on optical spectral deformation of embedded FBG sensors", Proc. SPIE 6478, Photonics Packaging, Integration, and Interconnects VII, 647808, 2007.

[9] P. Breedveld, J. Scheltes, , E. Blom, and J. Verheij, , "A New, Easily Miniaturized Steerable Endoscope", IEEE Eng. Med. Biol. Mag., pp. 40–47. 26, 2005.

[10] R. J. Webster III, and B. A. Jones, "Design and Kinematic Modeling of Constant Curvature Continuum Robots: A Review", International Journal of Robotics Research, vol. 29, no. 13, pp. 1661-1683, 2010.

Image Based Optical Multi-Axis Force Sensor for Medical Robotics

Y. Noh[1], S. Sareh[1], H. A. Wurdemann[1], J. Li[2], S. Wang[2], H. Liu[1], K. Althoefer[1]

[1]*Centre for Robotics Research, Department of Informatics, King's College London, UK*

[2]*School of Mechanical Engineering, Tianjin University, China*

yohan.noh@kcl.ac.uk

INTRODUCTION

The advent of surgical robot technologies has generated considerable impact on minimally invasive surgery. Equipped with multi-axis force sensors, surgical robots will endow surgeons with the essential feedback of touch to ensure the efficiency and safety of operations. Patients can also be protected from potentially excessive forces applied onto delicate internal organs. There are various miniaturized multi-axis force sensors that could potentially be considered for integrating with surgical tools, including those based on piezoresistive materials, strain gauges, polyvinylidene fluoride films, and fibre-optics. Commonly, two methods: (1) light intensity modulation or (2) Fibre Bragg Grating (FBG) have been utilized for developing fibre optic sensors [1-4]. In this paper, we propose a novel force sensing approach, making use of fibre optic technology and a CCD camera, which acquires light intensities transmitted from fibres. The light intensities are then modulated as a function of applied forces. As the cost of CCD chips has been dramatically reduced, this new approach provides a cost effective solution for fibre-optic sensing, especially when a large number of fibres are required. In this paper, we present the design and development of a three-axis force sensor using the proposed approach. This paper introduces the design, fabrication and calibration procedures. The experimental results show that the developed sensor achieved good performance.

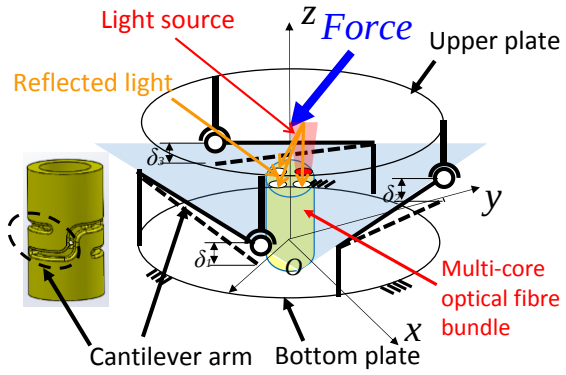

Fig. 1 The sensor mechanical structure based on the three cantilever beams

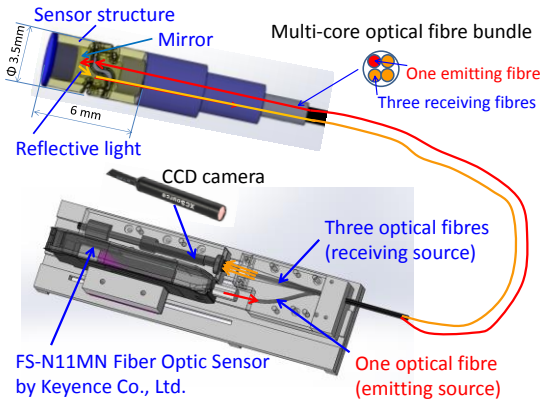

Fig. 2 The configuration of the sensor principle overview for multi-axis force sensor

MATERIALS AND METHODS

Sensor Principle: The proposed multi-axis force sensor consists of a CCD camera, a multi-core optical fibre bundle (FU-49X, Keyence Corp., Japan) and a light source. A light source (FS-N11MN, Keyence Corp., Japan) was used in this study. The sensor structure is designed to measure three force components F_x, F_y, and F_z; the three force components can be calculated by measuring the deflections δ_1, δ_2 and δ_3 of the three cantilever beams, Fig. 1.

The force measuring principle of our sensor is shown as follows. Light emitted from the light source travels via the emitting fibre; the light is then reflected by mirrors attached to the three cantilevers which bend in response to an applied force; the reflected light is then transmitted via three corresponding receiving fibres to three separate regions of the CCD camera; the light intensities in three sub regions of the CDD are interpreted into three corresponding cantilever beam deflections δ_1, δ_2 and δ_3 and the associated forces, Figs. 1 and 2.

Image Processing: The image with three sub-regions of reflected light is shown in Fig. 3a. To determine the light intensity of the three regions, signal processing approach first applied a median smoothing filter to the original RGB image reducing the original image noise. Then the image is converted into a greyscale image, Fig. 3b. To calculate each of the light intensity values of the three receiving fibres, the three corresponding regions of interest (ROIs) on the greyscale image are further processed. Each ROI has a pixel size of 320x240. The values of all pixels within the ROI are summed and divided by normalizer to obtain the reflected light intensity. From these normalised light intensity values (a_1, a_2, and a_3), the three cantilever beam deflections and the associated force components can be calculated, Fig. 1. To further reduce the noise, filtering techniques such as Kalman filter could be applied.

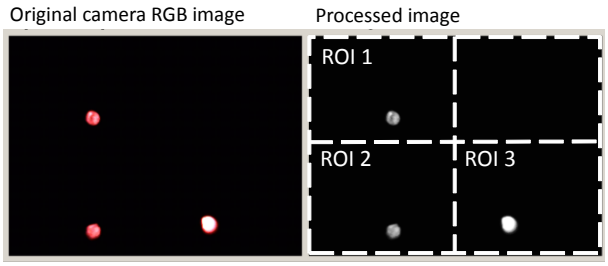

(a) (b)

Fig. 3 Original and processed images, the captured by the camera, from three light channels: a) the original RGB image b) the greyscale image converted after applying median smoothing filter on the original RGB image.

RESULTS

A set of the accuracy tests have been carried out with the multi-axis force sensor integrated into the catheter tip to compare the estimated forces with benchmark values (load cell) (Figure 5 left bottom). The results show that the estimated force components F_z, F_x and F_y

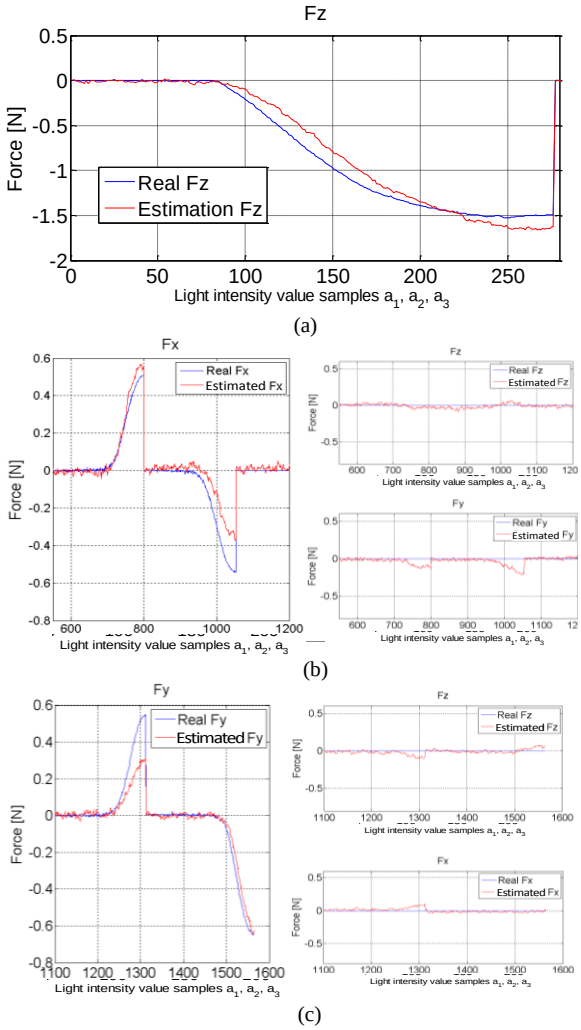

Fig. 4. Verification of sensor performance test: a) comparison between real F_z and estimated F_z b) comparison between real F_x and estimated F_x (cross-talk in other force components F_y and F_z) c) comparison between real F_y and estimated F_y (cross-talk in other force components F_x and F_z).

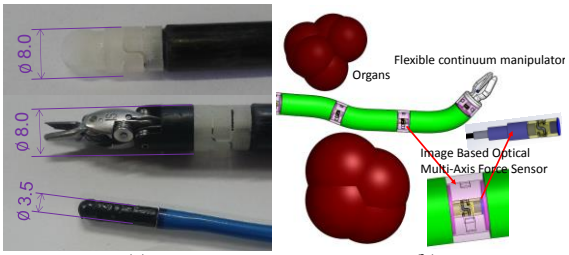

(a) (b)

Fig. 5 Possible medical devices for image based optical multi-axis force sensor: a) palpation tool (left top), da Vinci SutureCutTM Needle Drivers (left middle), and catheter tip (left bottom), b) flexible continuum manipulator**.**

closely align with the benchmark forces, Fig. 4. It can be noticed that F_y has slightly higher crosstalk when compared to the estimations of F_z and F_x, and has a higher error in comparison with F_x and F_y. This could possibly be due to an asymmetrical arrangement of the receiving fibres as shown in Fig. 2. When the maximum force is applied to the three-axis force sensor, the maximum error is 34% (F_x), 41% (F_y) and 13% (F_z), respectively.

DISCUSSION

The estimation of the force components calculated by the decoupling stiffness matrix has errors in comparison with the benchmark forces. We think these errors may be caused by the configuration of the asymmetrical optical fibre arrangement. As a future task, we will propose a symmetrical optical fibre arrangement (an optical fibre is located in the centre, and three are symmetrically located at 120° at the same radial distance) to reduce the observed estimation errors, and also further investigate sensor characteristics such as nonlinearity, crosstalk, repeatability and hysteresis. Furthermore, our proposed multi-axis force sensor will be integrated into many medical devices as shown in Fig. 5.

REFERENCES

[1] P. Polygerinos, L. D. Seneviratne, R. Razavi, T. Schaeffter, K. Althoefer, "Triaxial Catheter-Tip Force Sensor for MRI-Guided Cardiac Procedures," IEEE/ASME T. Mechatronics, 18(1), pp.386-396, 2013.

[2] J. Peirs, J. Clijnen, D. Reynaerts, H. V. Brussel, P. Herijgers, B. Corteville, S.Boone," A micro optical force sensor for force feedback during minimally invasive robotic surgery", Sensors and Actuators A: Physical, vol. 115, pp.447–455, 2014.

[3] S. Ryu, and P. E. Dupont, "FBG-based Shape Sensing Tubes for Continuum Robots", IEEE Int. Conf. on Robotics & Automation, pp. 3531-3537, 2014.

[4] H. Xie, H. Liu, Y. Noh, J. Li, S. Wang, K. Althoefer, "Fiber-Optics based Body Contact Sensor for a Flexible Manipulator", IEEE Sensors Journal, vol.15, Issue.6 pp. 3543-3550, 2015.

Robotic Technology and the Transformation of Epilepsy Surgery

D. R. Sandeman[1], K. A. Sieradzan[2], H. F. Faulkner [2]

[1]*Department of Neurosurgery, Southmead Hospital, Bristol, UK,*

[2] *Department of Neurology, Southmead Hospital, Bristol, UK*

david.sandeman@gmail.com

INTRODUCTION

Developments in the field of epilepsy surgery in the last 25 years have all been technology driven. MRI imaging of mesial sclerosis and the minimally invasive surgical techniques enhanced by the advent of image guided surgery have made temporal lobe surgery a routine procedure with greater than 70% cure rates in most centres. However imaging negative temporal lobe epilepsy and epilepsy of extratemporal origin remain a difficult challenge surgically. Historically, investigation techniques using subdural grids were imprecise, being a two dimensional solution to a three dimensional problem and carried unacceptably high risk for an investigative procedure [1]. The introduction of neurosurgical robotics and the order of magnitude greater accuracy that the technology provides has provided a solution to the investigation of extratemporal epilepsy.

RESULTS

This paper is an observational study comparng the results of conventional subdural grid placement for Video Electrocorticography (ECoG) recording with Robotic Stereo Electroencephalography (SEEG).

Between 2001 and 2011, 30 ECoG cases using subdural grids were performed out of a total of 149 craniotomies for epilepsy (20%) ECoG localised seizure onset sufficient to allow resective surgery in 27 cases (90%), A temporal focus was defined in 12 cases and an extra temporal focus defined in 15. Surgery lead to cure of epilepsy in 17 cases (63%), 9/12 temporal lobe cases (75%) and 8/15 extratemporal cases (53%) However seven patients suffered major complications from surgery – 4 haematomas, 2 infections and 1 stroke (23%) limiting the application of this technique as an investigative procedure.

Since 2011 ECoG has been replaced with robotic SEEG, carrying out 32 cases out of a total of 80 craniotomies for epilepsy (40%), In 17 cases SEEG was used to evaluate complex temporal epilepsy and extratemporal epilepsy in 14 cases. SEEG evaluation led to resective surgery in 20 cases with a cure of epilepsy in 16. (80%). Two patients are awaiting resective surgery. Seizures were shown not to be localizable in 9 cases. In two, repeat SEEG will be necessary as the epilepsy onset, although focal, was distant from the recording electrodes. A total of 402 electrodes – an average of 12 per case (range 6-17) have been implanted with one surgical complication, an intracerebral haematoma (3% of the SEEG cases)

CONCLUSIONS

The small numbers in this series, particularly of any sub group analysis do not allow for useful statistical analysis that might help to define the efficacy of SEEG over ECoG in the investigation of epilepsy. However the reduction in surgical complications allow us to conclude that robotic SEEG is a major technological advance in the investigation of intractable epilepsy, providing a definitive answer with respect to seizure localisation in 29/31 cases (94%) with subsequent curative surgery in 16/20 (80%) cases

DISCUSSION

Currently electrode placement is defined on an individual case basis by the preoperative hypothesis of epilepsy propagation. Analysis of the SEEG recording is qualitative. The field is ripe for the development of data mining algorithms using neuromorphometric methods to standardize electrode positioning to enhance automatic analysis of the onset and spread of complex epilepsy.

	ECoG	%	SEEG	%
Number of cases	30		31	
Total craniotomies	149	20	80	39
Temporal epilepsy	12	40	17	55
Extratemporal Epilepsy	18	60	14	45
Focus not localised	3	10	7	23
Wait listed for surgery	-	-	4	
Complications	7	23	1	3
Curative surgery	17	63	16	75

REFERENCES

[1] Abdinav K, Prakash S, Sandeman D R. Use of robot-guided stereotactic placement of intracerebral electrodes for investigation of focal epilepsy: initial experience in the UK. Brit J Neurosurg October 2013, Vol. 27, No. 5 , Pages 704-705

Cost Analysis across Therapeutic Boarders in Non-Metastatic Prostate Cancer

J. E. Jacobsen[1,2,4], E. S. Haug [1,2], T. Grotting [2], V. K. Mishra[1], S. Smeland[1], A. Stensvold[3], J. Cairns[4], H. Danielsen[1]

[1]*Institute for Cancer Bio-markers and Informatics, Oslo University Hospital Trust, Norway*

[2]*Department of Urology, Vestfold Hospital Trust, Norway*

[3]*Department of Urology, Ostfold Hospital Trust, Norway*

[4]*Public Health and Policy, HSRP, London School of Hygiene and Tropical Medicine, UK*

jorn.jacobsen@lshtm.ac.uk

ABSTRACT

A cost analysis has been carried out for more than 700 consecutive patients across therapeutic boarders in two Norwegian hospitals. Short and long term costs are calculated using a consistent homogeneous methodology. There are differences in costs between the management options as well as between patients within the same option. The cost information is an important prerequisite in cost-effectiveness analysis.

BACKGROUND

Non-Metastatic Prostate Cancer (n-MPCa) is the most common cancer in men. Radical prostatectomy (RP), Radiation therapy (RT) are standard curative approaches and Active Surveillance (AS) is increasingly accepted as a management option for localised n-MPCa. Comparative cost studies across therapeutic boarders are lacking. Methodological heterogeneity in existing cost studies is an obstacle for evidence synthesis as input to comparative HTA studies [1,2].

OBJECTIVE

To present costs components and cost structures for RP (Radical Retropubic Prostatectomy (RRP), Robot assisted Laparoscopic Prostatectomy (RALP)), RT (EB and HD-BRT) and AS as management options in n-MPCa with emphasis on initial costs and long term follow up costs.

METHODS

The study includes 711 consecutive patients diagnosed with n-MPCA managed with curative intent in 2011 - 2013. All patients are referred from GP's to two Norwegian hospitals. The cost data are derived from both administrative hospital records and electronic patient records data. The cost units were identified through literature search and a thorough patient care pathway analysis in close cooperation with clinicians. The follow-up costs include both hospital and GP visits. Costs are calculated from a health care provider perspective and presented in 2013 value of GB£. The study is carried out as a mixed micro-costing/case-mix method.

RESULTS

The immediate treatments (RP and RT) have high initial average costs per patient ranging from RRP at £4.304 to, RALP at £ 6063, RT-HD-Brachytherapy at £ 9.875 compared to AS at £119 for the first three months (see Figure 1).

The cost of yearly follow-up is higher and has a different distribution in AS than RT and RP and RT. The cost of AS is highly dependent on the cross-over rate to active treatment. The follow up cost of active treatment is dependent on the adverse effects from the treatment and the incidence of salvage treatment (see Figure 2).

The conversion rate from AS to active treatment plays a major role in this cost. In order to predict future cost from historic data a modelling process is required. In the present study the AS management option was the option accumulating the lowest costs over time followed by RRP, EB, RALP and HD-BRT. A transparent cost-model with natural cost units and unit costs can be adapted to local conditions and can therefore be generalizable with adaptation to local conditions and data. The results need to be seen in relation to oncological outcome and health state values.

There are few cost-analyses across therapeutic boundaries. One single centre study from Miami, US, based on clinical data for individual patients, Medicare fees for physicians and average hospital costs for as unit costs. The results are similar in the ranking order of costs for different modalities and the cost structure. The difference was that RALP and HD-BRT were similar in cost while external beam was calculated as the most expensive option [3].

CONCLUSIONS

In n-MPCa the main cost components and the cost structures in terms of onset of costs differ between the five management options included in the study. Active Surveillance incurs the least cost over time. The finding might be tested applying local results regarding treatment outcome, oncological outcome and adverse effects.

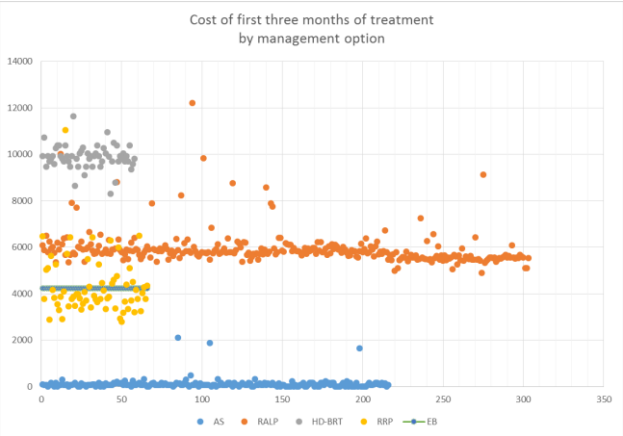

Fig. 1 Cost per patient for the different management options for n-MPCa. The cost is for three months of treatment. The x-axis represent single patients and the n per modality.

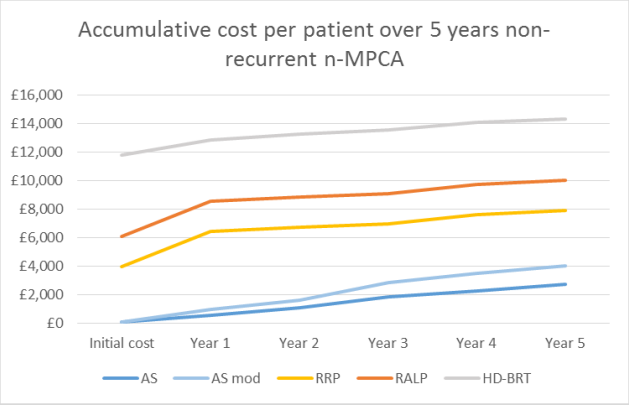

Fig. 2 AS=Active Surveillance as observed, AS mod= Active Surveillance according to the latest protocol.

REFERENCES

[1] Sanyal C, Aprikian AG, Chevalier S, Cury FL, Dragomir A. Direct cost for initial management of prostate cancer: a systematic review. Curr Oncol, Vol. 20, pp. e522-531; doi: http://dx.doi.org/10.3747/co.20.16302013.

[2] Molinier L, Bauvin E, Combescure C, Castelli C, Rebillard X, Soulie M, et al. Methodological considerations in cost of prostate cancer studies: a systematic review. Value in Health. 2008;11(5):878-85.

[3] Eldefrawy E, Katkori D, Abramowitz M, Soloway MS, Manoharan M, Active surveillance vs treatment for low-risk prostate cancer: a cost comparison.. Urologic Oncology Vol. 31, pp. 576-580

Spring Stiffness and Force Analysis in a Neurosurgical Spring-based Continuum Robot for MINIR-II

Y. Kim, S. S. Cheng, J. P. Desai

Robotics, Automation, and Medical Systems (RAMS) Laboratory,
Department of Mechanical Engineering,
University of Maryland, College Park, MD, USA
Ykim1212@umd.edu

INTRODUCTION

Brain tumors are one of the most feared complications of cancer and they can have a significant impact on the quality of life of an individual. Combining the intra-operative MRI system with an MRI-compatible robot with multiple degrees-of-freedom (DoFs) for higher dexterity, will enable us to develop a real-time MRI-guided robotic neurosurgical system that can provide neurosurgeons with the ability to remove the tumor more completely. Continuum robots have been extensively researched in robotics due to its flexibility and dexterity to work in confined spaces and also safely interact with its surrounding [1-3]. A soft continuum robot is an excellent choice of robot when a dexterous small-scale neurosurgical robot is needed to work in restricted space and avoid critical structures within the brain to prevent irreparable damage. We have developed a novel spring-based minimally invasive neurosurgical intracranial robot (MINIR-II), made of MRI-compatible plastic material. The robot body is a pair of parallel springs with an outer spring and an interconnected inner spring composed of multiple segments for better dexterity.

In this continuum robot, the spring backbone is the most important part which provides the flexibility and rigidity as well as force transmission capability. We need to determine the appropriate stiffness and consider tip force transmission required for neurosurgery. Yoon and Yi [3] studied the stiffness model of a spring backbone and designed a compressible beam structure with the same stiffness as that of the spring, and estimated deflection based on the beam model. Actuation force, especially at the manipulator tip, plays a major role in allowing a desired robot movement in the brain tissue. It has been reported that a spherical surgical probe with a diameter of 2.5 mm has to overcome 0.1-0.2 N of resistance force to advance through the brain tissue [4]. Our study on the tip force of the robot allows us to have a realistic expectation on the amount of tension we need to apply on the tendon to generate sufficient force for smooth robot motion in the brain environment.

ROBOT DESIGN AND TENDON ROUTING

Our robot has a spring that is divided into several segments (see Fig. 1) for the multiple DOFs needed in a neurosurgical procedure. It is made of a plastic material (VeroWhite, FullCure®, USA), commonly used in 3D printers. As shown in Figs. 1(a) and 1(b), together with the outer spring which acts as a flexible shell, the entire robot is assembled into a compact robotic device with the largest outer diameter being 13 mm. The inner spring is the main structure of the robot and at the same time offers flexibility and dexterity. The high DoFs of a flexible continuum robot make the tendon routing process complex. A slight movement of the tendons can easily deflect the robot links to a large extent when the tendons are routed using the 1st configuration shown in Fig. 1(c). Decoupled joint motion is important so that actuation of one robot joint does not cause deflection of any proximal robot links. The 2nd routing configuration shown in Fig. 1(c) leads to independent joint motion and therefore significantly improved robot performance. While tendon pulling generates moment at segment 3, it only causes normal compression in the other two segments. In this configuration, the tendons are routed along the central axis of the inner spring and start branching out to the respective robot joints at the base of the corresponding link. It is important to note that this design differs from the work of Bajo and Simaan [1], Jones and Walker [2], and Gravagne and Walker [5] because we can achieve independent control by routing the tendons central to the robot body and achieve motion in two independent directions for each link by using four tendons, spaced 90° apart.

STIFFNESS MODELING AND FORCE ANALYSIS

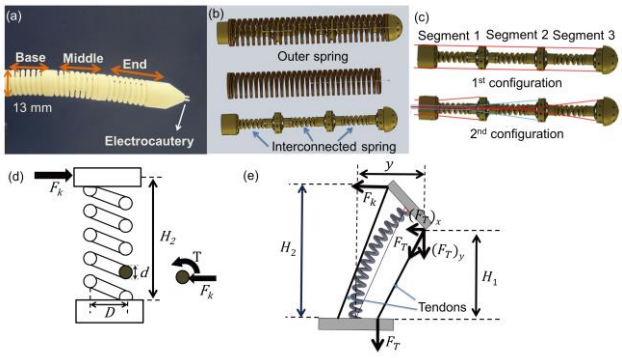

Fig. 1 (a) MINIR-II robot (b) Spring design with outer spring and interconnected inner spring. (c) Two different tendon routing configurations (d) Design parameters of interconnected spring (e) Relationship between lateral deflection and moment arm.

During modeling of the stiffness of our spring-based robot, we utilized an actual spring model. Figure 1(d) shows a single round-wire spring with mean spring diameter, *D*, and wire diameter, *d*, loaded by a lateral tip force, F_k. When force is applied at the tip of the spring to cause lateral deflection, there are two force components acting on it: direct shear force, which is equal to the tip force, F_k, and torsion, *T*. The spring stiffness that relates the lateral deflection and the tip force, can be expressed as:

$$k = \frac{d^4 G}{32 H_2^2 DN} \quad (1)$$

where *N*, H_2 and *G* are the number of spring coil, height of the tendon attachment point for tip force measurement and the shear modulus of the spring, respectively. The relationship between tip force, F_k and tension, F_T in the tendon can be expressed as:

$$\sum M = (F_T)_y y - (F_T)_x H_1 - F_k H_2 = 0 \quad (2)$$

where H_1 and y are the height and the lateral distance between the tendon attachment point and the center of rotation, respectively (See Fig 1(e)). To investigate the relationship between the spring deflection and different design parameters of the spring, a finite element (FE) model was developed. We assumed the material to be isotropic, homogeneous, and incompressible and we used ABAQUS (SIMULIA, USA) for our FE computation. The fixed boundary condition was applied on the bottom of the spring and a force in the lateral direction of 0.31 N was applied on the tip of the spring. For characterizing the spring constant, we performed a deflection experiment. The lateral motion at the end of a single robot segment was provided by a microstage (MP-285, Sutter instrument company, USA). While the end was moving laterally, the force exerted by the inner spring of the robot was captured by a force sensor (MDB-2.5, Transducer technology, USA).

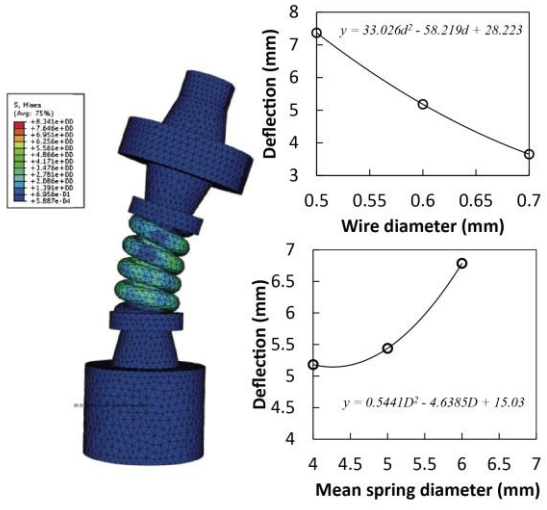

Fig. 2 Stress distribution of single segment of spring-based continuum robot and its tip deflection at various wire diameters and mean inner spring diameter.

RESULTS AND DISCUSSION

The simulation results from the FEM model (shown in Fig. 2) show that the deflection of the spring is nonlinearly dependent on the mean diameter of the inner spring and the wire diameter. From Eq. (1), stiffness of the inner spring, k, is 0.085 N/mm while it is determined to be 0.076 N/mm (R^2=0.9814) through experimental data (see linear fit in Fig. 3). Compared to that of the inner spring, the stiffness of the outer spring, which is 0.009 N/mm, is negligible. It can also be seen from Fig. 4 that the tension applied is 4.4 times the exerted tip force. Therefore, considering safety factor, we need to ensure that our actuators are able to generate and withstand around 5 times the amount of force we need at the robot tip. The theoretical data from Eq. (2) matches the experimental data well (R^2=0.9978). The robot can generate more than 1 N at the tip. In our future work, we will test the effect of stiffness changes on force transmission capability of our robot.

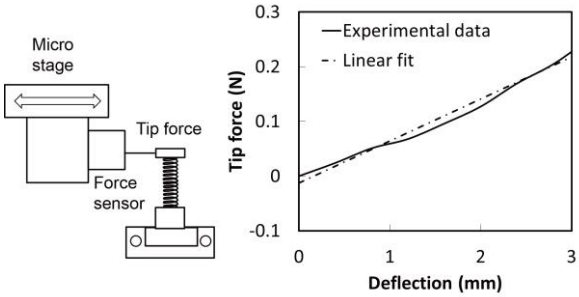

Fig. 3 Relationship between the tension force on the tendon and lateral deflection.

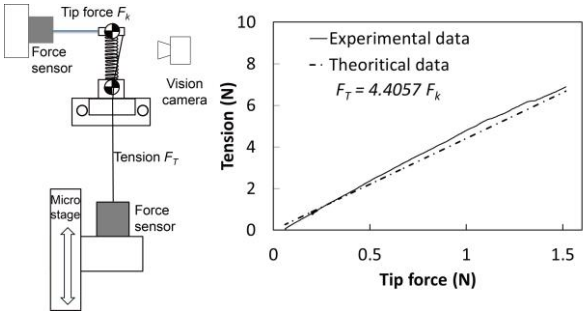

Fig. 4 Relationship between tip force and the tension force on the tendon.

ACKNOWLEDGEMENT

Research reported in this publication was supported by the National Institute Of Biomedical Imaging And Bioengineering of the National Institutes of Health under Award Number R01EB015870. This content is solely the responsibility of the authors and does not necessarily represent the official views of the National Institute of Health

REFERENCES

[1] Bajo A., Simaan N., Kinematics-based detection and localization of contacts along multi segment continuum robots, IEEE transactions on robotics, 2012; 28(2):291–302.

[2] Jones BA, Walker ID, Kinematics for multisection continumm robot, IEEE transaction on robotics, 2006; 22(1):43-57.

[3] Yoon HS, Yi BJ, A 4-dof flexible continuum robot using a spring backbone, in Mechatronics and Automation, 2009. ICMA 2009. International Conference on. IEEE, 2009; 1249–1254.

[4] Howard III MA, Abkes BA, Ollendieck MC, Noh MD, Ritter RC, Gillies GT, Measurement of the force required to move a neurosurgical probe through in vivo human brain tissue, Biomedical Engineering, IEEE Transactions on, 1999; 46(7): 891–894.

[5] Gravagne I, Walker ID, Kinematics and the implementation of an elephant's trunk manipulator and other continuum style robots , J Robot System, 2003; 20(2):45–63.

Author Index

P

Q

R

S

T

U

V

W

Y

Z

The Hamlyn Symposium on Medical Robotics

20-23 June 2015

The Royal Geographic Society and Imperial College London, UK